

# Multi-Constellation GNSS Estimation of Ocean Tide Loading Displacement

**Majid Abbaszadeh**

Thesis submitted for the Degree of  
Doctor of Philosophy

School of Engineering  
Newcastle University

January, 2020



*To my wife, Marjan*

## **Abstract**

For geodetic stations in proximity to intricate coastlines and shallow seas, the ocean tide loading (OTL) displacement, with up to decimetre level sub-daily peak-to-peak variations, is imperfectly modelled by the procedures recommended in the International Earth Rotation and Reference System Service (IERS) conventions. GPS Precise Point Positioning provides a means to measure OTL displacement, and about 0.3 mm accuracy for the GPS-estimated main lunar semidiurnal OTL displacement (M2) has been reported. Nonetheless, the GPS orbital and satellite constellation repeat periods are identical to those of the lunisolar K2 and K1 tidal constituents, respectively, which makes these constituents inseparable from the GPS orbit modelling and multipath errors. To help overcome the GPS problem of estimating K2 and K1 OTL displacement, the use of GLONASS data is investigated.

After processing GPS-only, GLONASS-only and combined GPS+GLONASS observations for 49 globally-distributed stations, which are affected marginally by OTL displacement forward modelling error, similar accuracy for the M2, N2, and O1 OTL displacement constituents estimated by GPS-only and GLONASS-only float ambiguity PPP is demonstrated. Combined GPS+GLONASS float ambiguity solutions show comparable precision to GPS-only fixed ambiguity solutions, and better accuracy than GPS-only and GLONASS-only for the aforementioned signals. The use of GLONASS data leads to about 2.0–2.5 mm accuracy improvement for the K2 and K1 OTL displacement estimation, compared with GPS-only estimates.

Finally, geophysical inferences of the OTL displacement in Alaska were investigated. The GPS-estimated OTL displacement at 87 stations in Alaska shows that FES2014b is the most accurate global ocean tide model in the region. It is also shown that including asthenosphere anelastic dispersion may improve OTL vertical displacement forward modelling in Alaska by up to 1–2 mm. Multi-GNSS OTL displacement investigation in Alaska also confirms the GLONASS data benefits which were found at the globally-distributed stations.



## **Acknowledgement**

I thank my supervisors Dr Nigel Penna and Professor Peter Clarke for their guidance during different parts of the project, including comments on the thesis draft. The GIPSY processing for the results shown in Chapter 5 was done by Dr Penna which is really appreciated. I also appreciate my examiners Professor Stuart Edwards and Professor Norman Teferle for their valuable comments and feedback.

I would like to thank GNSS Research Centre of Wuhan University for the PANDA software, and I also appreciate Dr Jing Guo for his useful advices in learning PANDA.

The GNSS data were gratefully obtained free-of-charge from the data providers listed in the text and Appendices, and the radiosonde data were obtained from the British Atmospheric Data Centre. I am grateful to ESA, CODE, GFZ and JPL of the IGS analysis centres for the satellite clock and orbit products used in this thesis.

I appreciate Professor Duncan Agnew for providing the SPOTL software, and Professor Geoff Blewitt for his online GPS data quality assessment product. I thank Dr Machiel Bos for providing anelastic Earth's Green's functions used in Chapter 6. I am also thankful for the free of charge generic mapping tools (GMT) software package which is used for the map generation in Chapter 5 and Chapter 6.

This project was sponsored by Doctoral Training Award from Newcastle University, UK.

# Contents

Chapter 1 Introduction .....	1
1.1 Research background .....	1
1.2 Research motivations and objectives .....	2
1.3 Research methodology .....	3
1.4 Thesis outline .....	4
Chapter 2 Ocean tides and loading .....	6
2.1 Introduction .....	6
2.2 Tide generation .....	6
2.3 Tidal potential .....	9
2.4 Earth body tide .....	13
2.5 Ocean tide loading displacement .....	16
2.5.1 Ocean tide models .....	16
2.5.2 OTL displacement forward modelling .....	18
2.6 Summary .....	23
Chapter 3 GNSS and tidal loading measurement.....	25
3.1 Introduction .....	25
3.2 GPS precise positioning methods.....	26
3.3 Spectral analysis of a time series.....	28
3.3.1 Fourier transformation .....	28
3.3.2 DFT main challenges .....	30
3.3.3 Least squares spectral analysis (LSSA) .....	31
3.4 OTL displacement measurement by GPS data.....	33
3.4.1 Relative OTL displacement .....	33
3.4.2 Absolute OTL displacement estimation.....	34
3.5 GLONASS enhancement for the OTL displacement measurement.....	37
3.6 Summary .....	42

Chapter 4 Multi-GNSS kinematic precise point positioning with PANDA.....	44
4.1 Introduction.....	44
4.2 Systematic errors in PPP.....	45
4.2.1 Phase centre offset (PCO)/ Phase centre variation (PCV).....	45
4.2.2 Instrumental delay .....	46
4.2.3 Relativistic effect.....	46
4.2.4 Antenna phase windup .....	47
4.2.5 Ionospheric delay.....	48
4.2.6 Tropospheric delay .....	48
4.2.7 Site displacement.....	49
4.3 Spurious periodicities in GNSS-derived time series.....	50
4.4 Observation modelling in PPP .....	51
4.4.1 Satellite clock/orbit interpolation .....	52
4.4.2 Observation least-squares adjustment .....	53
4.5 Running kinematic PPP in PANDA .....	58
4.5.1 Preparation of preliminary information.....	58
4.5.2 Pre-processing data quality assessment and cycle slip detection .....	59
4.5.3 Parameter estimation .....	60
4.5.4 Post-processed data snooping.....	61
4.5.5 Output files preparation.....	61
4.5.6 A summary of PPP in PANDA .....	61
4.6 Satellite clock/orbit selection for PPP .....	62
4.7 Day break error and session length.....	68
4.8 Synthetic tidal displacement signal in PPP .....	70
4.9 Noise tuning in kinematic PPP processing .....	73
4.10 Summary .....	77
Chapter 5 Benefits of combining GPS and GLONASS for measuring ocean tide loading displacement.....	78

5.1	Abstract .....	78
5.2	Introduction .....	79
5.3	OTL displacement estimation using multi-GNSS kinematic PPP .....	81
5.3.1	GNSS data selection.....	83
5.3.2	PANDA software validation .....	86
5.4	GLONASS data contribution to OTL displacement measurement .....	89
5.5	Comparison between GNSS-derived and modelled OTL displacements .....	96
5.6	Discussion and conclusions.....	104
Chapter 6 Ocean tide loading displacement in Alaska .....		106
6.1	Introduction .....	106
6.2	Modelled OTL displacement.....	107
6.3	Ocean tide models and OTL displacement modelling .....	111
6.3.1	Ocean tide model quality check with tide gauge data.....	113
6.3.2	GPS-derived OTL displacement residuals .....	117
6.4	Anelasticity effects on the GPS-estimated OTL displacement .....	123
6.5	GLONASS and GPS+GLONASS based OTL displacement assessment .....	129
6.6	Summary and conclusions.....	137
Chapter 7 Conclusions .....		139
7.1	Conclusions .....	139
7.2	Suggestions for future work .....	141
References.....		143
Appendix A: Satellite availability and GDOP calculation.....		152
Appendix B: Normal equation manipulation and input/output files in PANDA.....		154
B.1	Normal equation manipulation.....	154
Case 1: Similar phase connected arc.....		155
Case 2: Adding a new set of phase connected arc .....		156
Case 3: A set of phase connected arcs is lost.....		156
Case 4: A set of phase connected is added and a set of current arcs is lost .....		157

B.2 Local formats in PANDA .....	157
Appendix C: CODE, ESA and GFZ products comparison .....	166
Appendix D: GNSS stations, data availability and modelled OTLD used in Chapter 5.....	170
Appendix E: GNSS-derived vertical OTL displacement residuals in Chapter 5 .....	185
Appendix F: Modelled and measured (tide gauge) ocean tides in Alaska .....	195
Appendix G: GPS/GNSS-derived OTLD residuals in Alaska .....	203

## List of figures

Figure 2.1: Gravitational and tidal force.....	8
Figure 2.2: 2D layout of an observer and a tide generating body.....	10
Figure 2.3: Modelled EBT vertical displacement.....	15
Figure 2.4: Modelled EBT east displacement.....	15
Figure 2.5: Modelled EBT north displacement.....	15
Figure 2.6: Amplitude of the modelled OTL vertical displacement.....	22
Figure 2.7: Amplitude of the modelled OTL east displacement.....	23
Figure 2.8: Amplitude of the modelled OTL north displacement.....	23
Figure 3.1: Aliasing problem in spectral analysis.....	31
Figure 3.2: Mean number of available satellites within different longitude bands.....	41
Figure 3.3: Mean number of GDOP within different longitude bands.....	42
Figure 4.1: PPP flowchart in PANDA.....	62
Figure 4.2: Effect of satellite clock/orbit products in the GNSS-derived height.....	65
Figure 4.3: Ratio of GPS-estimated height RMS with ESA and CODE.....	66
Figure 4.4: Ratio of GLONASS-estimated height RMS with ESA and CODE products.....	67
Figure 4.5: Ratio of GPS-estimated height RMS with ESA and GFZ products.....	67
Figure 4.6: Ratio of GLONASS-estimated height RMS with ESA and GFZ products.....	68
Figure 4.7: Effect of the processing arc length on the GNSS-derived height time series.....	69
Figure 4.8: Cumulative distribution function (CDF) for the GPS-estimated height RMS with different processing length.....	70
Figure 4.9: Synthetic tidal signal recovery in PPP.....	72
Figure 4.10: Stations used for coordinate and ZWD process noise tuning.....	73
Figure 4.11: Zenith wet delay (ZWD) process noise tuning test.....	75
Figure 4.12: Station coordinate process noise tuning test.....	76
Figure 5.1: Effect of the ocean tide models for OTL displacement prediction.....	85
Figure 5.2: Statistical analysis of a synthetic signal recovery error in PPP.....	88
Figure 5.3: Power spectral density for the GPS-derived height time series from PANDA and GIPSY.....	89
Figure 5.4: Mean percentage of epochs with at least seven recorded satellites versus station absolute latitude.....	91
Figure 5.5: Cut-off angle effect on the PSD of the height time series from GPS-only kinematic PPP.....	92
Figure 5.6: Cut-off angle effect on the PSD of the height time series from GLONASS-only kinematic PPP.....	93

Figure 5.7: Comparison for the ambiguity-fixed and ambiguity float solutions .....	95
Figure 5.8: Vector differences between GNSS-derived and modelled OTL height displacement for global stations .....	99
Figure 5.9: Statistical analysis for the magnitude of vector differences between GNSS-derived and modelled M2 OTL height displacement .....	100
Figure 5.10: Statistical analysis for the magnitude of vector differences between GNSS-derived and modelled N2 OTL height displacement.....	100
Figure 5.11: Statistical analysis for the magnitude of vector differences between GNSS-derived and modelled K2 OTL height displacement.....	101
Figure 5.12: Statistical analysis for the magnitude of vector differences between GNSS-derived and modelled K1 OTL height displacement.....	101
Figure 5.13: Statistical analysis for the magnitude of vector differences between GNSS-derived and modelled O1 OTL height displacement.....	102
Figure 5.14: Statistical analysis for the magnitude of vector differences between GNSS-derived and modelled P1 OTL height displacement. ....	102
Figure 5.15: Statistical analysis for the magnitude of vector differences between GNSS-derived and modelled Q1 OTL height displacement.....	103
Figure 5.16: 95th percentile for the GNSS-derived OTL displacement residuals grouped by station latitude.. ....	104
Figure 6.1: Predicted OTL east displacement in Alaska. ....	108
Figure 6.2: Predicted OTL north displacement in Alaska. ....	109
Figure 6.3: Predicted OTL vertical displacement in Alaska .....	110
Figure 6.4: Ocean tide modeling error effect on the OTL displacement prediction in Alaska	112
Figure 6.5: Ocean tide in Alaska based on the FES2014b model .....	115
Figure 6.6: Ocean tide modelling error in Alaska .....	116
Figure 6.7: Comparison between modelled and observed M2 ocean tide in Alaska .....	117
Figure 6.8: Comparison between modelled and observed K1 ocean tide in Alaska .....	117
Figure 6.9: GPS-estimated M2 east OTL displacement residuals based on different ocean tide models.....	120
Figure 6.10: GPS-estimated M2 north OTL displacement residuals based on different ocean tide models.....	121
Figure 6.11: GPS-estimated M2 vertical OTL displacement residuals based on different ocean tide models.....	122
Figure 6.12: GPS-estimated M2 east OTL displacement residuals based on different Earth models.....	126

Figure 6.13: GPS-estimated M2 north OTL displacement residuals based on different Earth models .....	127
Figure 6.14: GPS-estimated M2 vertical OTL displacement residuals based on different Earth models .....	128
Figure 6.15: M2 OTL displacement residuals for the east component estimated by GPS-only, GLONASS-only, and GPS+GLONASS data .....	131
Figure 6.16: M2 OTL displacement residuals for the north component estimated by GPS-only, GLONASS-only, and GPS+GLONASS data .....	132
Figure 6.17: M2 OTL displacement residuals for the vertical component estimated by GPS-only, GLONASS-only, and GPS+GLONASS .....	133
Figure 6.18: K1 OTL displacement residuals for the east component estimated by GPS-only, GLONASS-only, and GPS+GLONASS data. ....	134
Figure 6.19: K1 OTL displacement residuals for the north component estimated by GPS-only, GLONASS-only, and GPS+GLONASS data .....	135
Figure 6.20: K1 OTL displacement residuals for the vertical component estimated by GPS-only, GLONASS-only, and GPS+GLONASS data .....	136
Figure B.1: Content of a ‘logYYYYDOY_stn’ file in PANDA.....	164
Figure B.2: Content of a ‘resYYYYDOY’ file in PANDA.....	164
Figure B.3: Format of a ‘kinYYYYDOY’ file in PANDA.....	165
Figure B.4: Format of a ‘ztdYYYYDOY’ file in PANDA.....	165



## List of tables

Table 2.1: Main Earth-Moon-Sun position changes.....	7
Table 2.2: Main diurnal and semi-diurnal lunisolar tides.....	9
Table 3.1: A summary of studies for the GPS-estimated OTL displacement .....	37
Table 3.2: Orbital features of GPS, GLONASS, Galileo, and BeiDou satellite systems.....	38
Table 3.3: Main tidal constituents focused in the thesis.....	43
Table 4.1: Preliminary files for a PPP run in PANDA.....	59
Table 4.2: Models and convention used for IGS ACs product comparison.....	65
Table 5.1: Principal semi-diurnal and diurnal tidal constituents of the tidal potential.....	79
Table 5.2: 95th percentile of the magnitude of the vector differences between GNSS-derived and modelled M2 OTL height displacement for the 49 stations .....	103
Table 6.1: RMS and 85th percentile of the GPS-estimated east M2 residuals in Alaska. ....	123
Table 6.2: RMS and 85th percentile of the GPS-estimated north M2 residuals in Alaska ....	123
Table 6.3: RMS and 85th percentile of the GPS-estimated vertical M2 residuals in Alaska. ....	123
Table 6.4: RMS and 85th percentile of the GPS-estimated east M2 residuals coastla stations in Alaska based on different Earth models. ....	129
Table 6.5: RMS and 85th percentile of the GPS-estimated north M2 residuals coastla stations in Alaska based on different Earth models .....	129
Table 6.6: RMS and 85th percentile of the GPS-estimated vertical M2 residuals coastla stations in Alaska based on different Earth models .....	129
Table 6.7: RMS and 85th percentile of the M2 OTL displacement residuals estimated by GPS-only, GLONASS-only and combined GPS+GLONASS data in Alaska.....	137
Table 6.8: RMS and 85th percentile of the K1 OTL displacement residuals estimated by GPS-only, GLONASS-only and combined GPS+GLONASS data in Alaska.....	137
Table C.1: IGS GNSS stations used for CODE, ESA and GFZ products comparison with the RMS ratio .....	169
Table D.1: GNSS stations used in Chapter 5 .....	171
Table D.2: Predicted M2 OTL displacement based on different ocean tide models and an elastic PREM Green's function .....	174
Table D.3: Predicted N2 OTL displacement based on different ocean tide models and an elastic PREM Green's function .....	176
Table D.4: Predicted K2 OTL displacement based on different ocean tide models and an elastic PREM Greens' function .....	178
Table D.5: Predicted K1 OTL displacement based on different ocean tide models and an elastic PREM Greens' function .....	180

Table D.6: Predicted O1 OTL displacement based on different ocean tide models and an elastic PREM Greens' function.....	182
Table E.1: GNSS-estimated vertical M2 OTL displacement residuals with respect to FES2014b and the elastic PREM model.....	186
Table E.2: GNSS-estimated vertical N2 OTL displacement residuals with respect to the FES2014b and elastic PREM model.....	188
Table E.3: GNSS-estimated vertical K2 OTL displacement residuals with respect to the FES2014b and elastic PREM model.....	190
Table E.4: GNSS-estimated vertical K1 OTL displacement residuals with respect to the FES2014b and elastic PREM model.....	192
Table E.5: GNSS-estimated vertical O1 OTL displacement residuals with respect to the FES2014b and elastic PREM model.....	194
Table F.1: List of tide gauge stations used in Chapter 6.....	196
Table F.2: Modelled and observed (tide gauge) M2 ocean tide in Alaska based on different ocean tide models.....	199
Table F.3: Modelled and observed (tide gauge) K1 ocean tide in Alaska based on different ocean tide models.....	202
Table G.1: GPS/GNSS stations in Alaska .....	204
Table G.2: GPS derived M2 OTL displacement residuals based on three ocean tide models in Alaska.....	207
Table G.3: GPS-estimated M2 vertical OTL displacement residuals in Alaska based on the FES2014b ocean tide model and three different Earth models.....	210
Table G.4: M2 OTL displacement residuals estimated by GPS-only, GLONASS-only and combined GPS+GLONASS.....	211
Table G.5: K1 OTL displacement residuals estimated by GPS-only, GLONASS-only and combined GPS+GLONASS.....	212

# Chapter 1 Introduction

## 1.1 Research background

Tidal forces, which originate predominantly from the Moon and the Sun, deform the solid Earth in two ways: the direct gravitational effect which is called the Earth Body Tide (EBT), and ocean tidal loading (OTL). Compared to the OTL displacement, EBT varies spatially smoothly, and from a knowledge of the Earth's layers' large scale physical heterogeneity and celestial bodies' position with respect to Earth, it is modelled with better than 1 mm accuracy (e.g., Yuan and Chao, 2012). However, OTL displacement forward modelling is more challenging as it demands both ocean tide and Earth layer physical models at high spatial resolution (e.g. Farrell, 1972; Agnew, 2007).

OTL displacement within ~500 km of a coastline may reach up to 100 mm. OTL displacement computed by forward modelling (Petit and Luzum, 2010) is typically corrected from Global Navigation Satellite Systems (GNSS), Very Long Baseline Interferometry (VLBI), Satellite Laser Ranging (SLR), and Doppler Orbitography and Radiopositioning Integrated by Satellite (DORIS) observations. However, in proximity to an intricate coastline or shallow oceans, in which ocean tide models are not sufficiently reliable, the uncertainty of the predicted OTL displacement can be several times larger than geodetic observation noise, and it is more accurate to estimate the unmodelled OTL displacement through observation adjustment. The estimated OTL displacement by geodetic data can evaluate the accuracy of the forward modelled OTL, and for areas such as Polar Regions with poorly modelled OTL, the OTL displacement estimated by geodetic data is an appropriate alternative. For a region with high quality ocean tide models, the discrepancy between the observed and predicted OTL displacement provides valuable information to constrain the Earth's lithosphere and upper mantle physical parameters (e.g., Bos *et al.*, 2015).

Although near 2 mm accuracy for the VLBI-estimated tidal displacement has been demonstrated (e.g., Sovers, 1994; Petrov and Ma, 2003; Thomas *et al.*, 2007), its poor geographical coverage, i.e. total 202 geodetic/astronomic stations across the globe (Dick and Thaller, 2017), limit its use. On the other hand, Global Positioning System (GPS), with its higher spatiotemporal resolution, e.g. more than 17000 stations processed by Blewitt *et al.* (2018), have been the main geodetic measurement used for tidal deformation assessment (e.g., Allinson *et al.*, 2004; King *et al.*, 2005; Yun *et al.*, 2007; Yuan *et al.*, 2009; Penna *et al.*, 2015; Bos *et al.*, 2015; Martens *et al.*, 2016). By employing International GNSS Service (IGS)

products, and processing GNSS data in precise point positioning (PPP) method, it is feasible to detect tidal displacement in the International Terrestrial Reference Frame (ITRF). Yuan and Chao (2012) and Penna *et al.* (2015) have reported ~0.3 mm accuracy for the lunar M2 and O1 tidal displacement constituents estimated by Global Positioning System (GPS) data. Nevertheless, due to the orbiting period of the satellites, GPS geodesy is intrinsically unreliable for measuring the lunisolar K2 and K1 constituents since they are modulated by satellite orbit/clock mismodelling error and daily repeating multipath effects at the ground station (e.g., King *et al.*, 2005; Yuan *et al.*, 2009).

In recent years, after the development of new global navigation satellite systems, PPP with multi-GNSS observations has been considered. At the moment, the Russian Globalnaya Navigatsionnaya Sputnikovaya Sistema (GLONASS) is another operational system with high quality data from 24 satellites. Therefore, with a simple logic of increasing observation redundancy and improving dilution of precision (DOP), GPS and GLONASS data integration has been considered. Cai and Gao (2007) and Li *et al.* (2015a) reported an improvement in convergence time as well as precision of the coordinate estimation in PPP with combined GPS+GLONASS data. Nonetheless, the capability of multi-GNSS PPP for OTL displacement measurement has not been considered yet.

## **1.2 Research motivations and objectives**

In a tidal displacement study, two main advantages for incorporating GLONASS data are expected. First, after verifying GLONASS-only PPP to detect the GPS-measurable tidal displacement constituents, e.g. M2, N2 and O1, the OTL displacement estimated by the former can be used for a quality check of the latter, and vice versa. In addition, evaluation of the modelled OTL displacement with observations from two independent systems is feasible. Moreover, mixed GPS+GLONASS data processing is likely to lead to a more robust estimation of the tidal displacement for the aforementioned constituents. Second, because of its different satellite constellation, GLONASS data are less likely affected by the GPS errors for the K2 and K1 constituents, and a more accurate estimation for these constituents with GLONASS is anticipated. Apart from the above benefits, GLONASS measurements are of critical importance when the transmitted GPS signal is degraded, e.g. ionospheric scintillation, environmental obstructions, and narrow sky view. Furthermore, the larger inclination angle of a GLONASS satellite orbit provides a bigger satellite elevation angle and longer satellite availability in high latitude areas, whereas GPS satellites may be less accessible.

The main objective of this research are therefore as follows:

- Investigate if GLONASS observations improve kinematic PPP OTL displacement estimation accuracy.
- Comparison between GPS-only, GLONASS-only, and combined GPS+GLONASS observation processing to detect lunar M2, N2 and O1 tidal deformation constituents.
- Investigation of GLONASS data capability to measure solar K2 and K1 tidal displacements.
- Applying the GPS and GLONASS OTL displacement estimation to validate ocean tide and Earth models, including for the GPS-problematic K1 constituent.

### 1.3 Research methodology

To process multi-GNSS data, the Positioning and Navigation Data Analyst (PANDA) software, which was originally created by Wuhan University, is used in kinematic PPP mode. Since PANDA has not been employed in any OTL displacement investigation, its performance is first tested in two ways: comparison between OTL displacement with PANDA and the GNSS-Inferred Positioning System (GIPSY) GPS processing software, and the evaluation of PANDA's accuracy to recover a synthetic tidal displacement signal. Then the most precise IGS satellite product with GPS/GLONASS 30 second satellite clock information is selected, followed by evaluating the quality of data needed for tidal displacement estimation.

After determining the most accurate PPP software and satellite clock/orbit products, the capability of GLONASS-only as well as combined GPS+GLONASS data for OTL displacement detection for a globally distributed set of stations are evaluated. For the station selection, two important criteria have been considered: daily and annual data coverage, and the quality of the predicted (modelled) OTL displacement. By processing GPS-only, GLONASS-only and combined GPS+GLONASS data at each station, and comparing the estimated M2, N2, O1, K2 and K1 vertical OTL displacements with the forward modelled values, the accuracy of the OTL displacement estimated by each GNSS data set is evaluated.

In the last part of this thesis, geophysical inference of the GNSS-estimated tidal displacement in Alaska is considered. Alaska has been chosen for several reasons: it has large M2 and K1 OTL displacement offering an opportunity to assess the asthenosphere anelasticity effect on the OTL displacement forward modelling (Bos *et al.*, 2015; Wang *et al.*, 2020). It also will be shown that GLONASS data coverage improves for higher latitude which enhances the GLONASS-only PPP solution. As part of a Continues Operating Reference Stations (CORS) network, there are more than 87 stations in Alaska with more than three years of GPS data, and 22 of them have been collecting GLONASS data from 2016.0 onwards.

## 1.4 Thesis outline

Chapter 2 describes ocean tides and the Earth's response to the periodic water surface loading. First of all, the theory of tidal potential with an explanation of the main tidal harmonics are described. Afterwards, EBT as well as ocean tide modelling are explained, and finally, OTL displacement forward modelling is reviewed.

Chapter 3 explains the application of GNSS geodesy for tidal displacement measurement. After an introduction to the most precise GNSS positioning techniques, a literature review about GPS-estimated tidal displacement is presented, and the main GPS problems for this subject are described. Then, the capability of GLONASS to support GPS in PPP, especially for OTL displacement measurement, is described.

In Chapter 4, the different steps of PPP implementation with the PANDA software are described. This chapter explains the systematic error mitigation, observation functional and stochastic modelling, and normal equation manipulation in PANDA. Useful setup files, commands and syntax for running PANDA in kinematic PPP mode are also introduced. Furthermore, the products from three IGS analysis centres which generate GLONASS as well as GPS satellite products are compared. Finally, tidal displacement signal simulation in PANDA processing, which is applicable for software verification and process noise tuning testing, is explained, and optimum process noise values in kinematic PPP are evaluated.

Chapter 5 highlights GLONASS observation benefits for tidal displacement measurement. Using GPS-only, GLONASS-only and combined GPS+GLONASS data for 49 globally distributed stations in which ocean tide modelling error was deemed marginal have been processed. After a least squares spectral analysis of the estimated time series, the main semi-diurnal and diurnal tidal displacement constituents, i.e. M2, N2, O1, P1, Q1, K2, and K1, from each GNSS data set per station are extracted. Finally, by statistical analysis of the estimated OTL displacement residuals, performance of GPS, GLONASS, and combined GPS+GLONASS measurement techniques are compared. This chapter forms a paper which is published in *Journal of Geodesy*.

To investigate the asthenosphere anelasticity effect, Chapter 6 focuses on the GNSS-estimated OTL displacement residuals in Alaska. That region is chosen as the M2 and K1 OTL vertical displacement near Alaskan southern coast are large enough (more than 15 mm) to contain GNSS-observable Green's function anelasticity effect. Furthermore, previous works (Khan and Tscherning 2001; Khan and Scherneck 2003) have only considered a GPS-estimation feasibility study, using relative GPS for a single baseline, whilst there are currently 65 GPS and 22

GPS/GLONASS stations with more than three years data. For studying the asthenosphere anelasticity effect in Alaska, first of all, seven modern ocean tide models are quality checked with tide gauge and GPS data. Thereafter, the modelled OTL displacement based on the most accurate ocean tide model and each elastic and anelastic Earth's Green's function are compared with the GPS-estimated OTL displacements, and the improved effect of applying asthenosphere anelasticity on the OTL displacement forward modelling is demonstrated. Finally, benefits of incorporating GLONASS data for measuring M2 and K1 OTL displacements are explained.

In Chapter 7, all conclusions of this research are reviewed, and some suggestions for the future works are presented.

## Chapter 2 Ocean tides and loading

### 2.1 Introduction

The difference between the gravitational attraction induced by celestial bodies at the Earth's surface and its centre of mass is known as the tidal force. Although this force is only about 1% of the Earth's self-gravitation, it has considerable consequences on the Earth system including the solid Earth, oceans and atmosphere. For instance, a peak-to-peak daily variation of the ocean tidal height in shallow water areas may reach up to several metres, which demands an accurate tidal current modelling for marine engineering and navigation. Tidal steering around islands can concentrate sediments and alter the ecosystem of the sea (e.g., Pingree, 2009). For estimating a national/international vertical datum, e.g. geoid or chart datum, the ocean level tidal variation should be taken into account (e.g., Vaníček, 1986). Ocean water tidal mass redistribution changes satellite trajectories, and needs to be corrected in the satellite orbit determination process (e.g., Tapley *et al.*, 1994). All geodetic data which are collected at the Earth's surface and its gravity field are modulated by the solid Earth tidal displacement which can be two orders of magnitude larger than measurement noise, and hence, for a robust parameter estimation, tidal signals should be resolved (e.g., Penna *et al.*, 2007; King *et al.*, 2008). From a geophysical perspective, the tide is the only well-modelled force acting on the Earth's surface. So, the Earth's tidal response, which is controlled by the mechanical properties of the Earth's layers, can be exploited for determining the Earth's interior tomography (e.g., Agnew, 2007).

Throughout this thesis, GNSS data will be used to measure solid Earth surface displacement induced by OTL. The observed discrepancy between the GNSS-derived OTL displacement and its predicted counterpart from forward modelling will be employed for the ocean tide as well as Earth model accuracy assessments. To pursue this objective, the current chapter is devoted to a theoretical discussion of the tidal force and its interaction with the Earth. After this introduction, tide generation and its main constituents are reviewed. Section 2.3 presents a mathematical formulation of the tidal potential, and in Section 2.4, Earth's body tide computation is explained. The last section of this chapter demonstrates forward modelling of the OTL displacement.

### 2.2 Tide generation

Based on Newton's law of universal gravitation, all the Earth's particles are being continuously pulled by other celestial bodies' gravitational attraction. The attraction varies throughout the



Earth due to the uneven distance from the Earth's particle to the attracting body. The gravitational force at the Earth's centre of mass, which is representative of the average gravitational force acting on the whole Earth, controls the Earth-body relative orbital motion. On the other hand, the difference between the gravitational attractions at any particle with respect to the average force is known as the tidal force, and deforms the solid Earth and its oceans. So, a tidal force at a point  $A$  on the Earth's surface can be written as:

$$\mathbf{F}_{tide}(A, t) = \mathbf{F}(A, t) - \mathbf{F}(C, t) \quad (2.1)$$

where  $\mathbf{F}(A, t)$  and  $\mathbf{F}(C, t)$  are the gravitational attraction from the celestial bodies at point  $A$  and the Earth's centre of mass  $C$ , respectively. The time dependence ( $t$ ) of the tidal force is due to the temporal relative position change in the Earth-body system. As the Moon and Sun generate more than 99% of the tidal force, it is typical to discard other celestial bodies' contributions. In Table 2.1, all major Earth-Moon-Sun relative position changes, which generate different periodicities in the tidal force, are listed. Modulations in amplitude as well as frequency, which will be reviewed later in this section, makes the resultant tidal force more complex.

Relative position change	Period
Earth daily rotation with respect to the Moon	24.84 hours
Earth daily rotation with respect to the Sun	24 hours
Orbital motion of the Moon around the Earth	27.2122 days
Earth's orbital motion around the Sun	365.2524 days
Lunar perigee progression	8.867 years
Lunar nodal point revolution	18.6 years
Solar perihelion progression	20941 years
Vernal equinox point revolution	26000 years

Table 2.1: Main Earth-Moon-Sun position changes

To have an intuitive comprehension for the main tidal constituents, as shown in Figure 2.1a, a synthetic stationary Moon in the Earth's equatorial plane is considered, and it is assumed that the Earth's surface is covered by water. In this figure, the gravitational force at a limited number of points on the Earth's surface and its centre of mass are shown with green and blue arrows,

respectively. In Figure 2.1b, the tidal force, i.e. the vector differences between each green and blue arrows in Figure 2.1a, are depicted. As can be seen in this figure, the two points which lie on the Earth-Moon centre of mass connecting line have high tides, and two other points with  $90^\circ$  longitude difference experience low tides. For a spinning Earth, it takes half a lunar day between two consecutive high tides for a specific point, and hence, the semidiurnal tide will be created. As can be seen in the figure, there is a secular low tide for the points at the Earth's pole. Figure 2.1 can be generalized for all particles at the Earth's surface.

It can be shown that, due to the non-zero declination of the Moon, the Earth's daily rotation generates a diurnal tidal signal for some regions (e.g., Melchior, 1966). Similar to the lunar tide, the Earth's daily rotation with respect to the Sun generates semi-diurnal and diurnal solar tides.

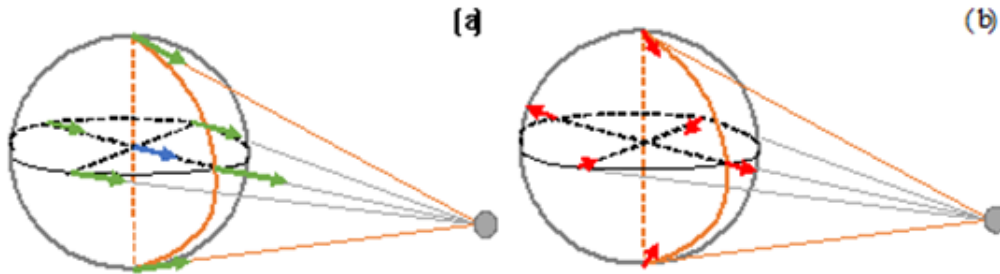


Figure 2.1: a) Gravitational force, and b) tidal force.

The Moon-Earth and the Earth-Sun orbits are not circular, so the distance between the Earth and the tide generating body also varies periodically. This is equivalent to an amplitude modulation on the fundamental tidal harmonics. Mathematically, the amplitude modulation of signal  $S_1 = A_1 \cdot \sin(\omega_1 t)$ , with another sinusoidal signal  $S_c = A_c \cdot \sin(\omega_c t)$  is expressed as:

$$S_{new} = [A_1 + A_c \cdot \sin(\omega_c t)] \cdot \sin(\omega_1 t) \quad (2.2)$$

After expanding the right hand side of Equation 2.2 and using a trigonometric identity for the sinusoid signals' multiplication, two new harmonics with frequencies at either sides of the original frequency will result:

$$S_{new} = S_1 + \frac{1}{2} A_c \cdot [\sin((\omega_1 + \omega_c)t) + \sin((\omega_1 - \omega_c)t)] \quad (2.3)$$

For example, if we consider the modulation of the main lunar semi-diurnal tidal constituent (M2 with angular speed of 28.9841 degree/hour) with the lunar orbital motion,  $\omega_1$  and  $\omega_c$  will be about 28.9855 and 0.55 degree/hour, respectively. As a result, two new constituents around M2 with angular speed of 28.4355 and 29.5355 degree/hour, respectively, will be generated.

Due to Kepler's second law, any orbiting motion around a central body occurs with a non-uniform speed. Hence, in addition to the amplitude modulation, a frequency modulation on the tidal signal is applied. Frequency modulation also creates tidal constituents around the main ones. For the oceans, the topography of the basin, coastline geometry, and the Coriolis force alter the tidal constituents from the theoretical tide. Therefore, a real ocean tidal signal is composed of thousands of constituents, and a thorough list of these constituents can be found in tidal catalogues (e.g., Hartmann and Wenzel, 1995).

This thesis focuses on the main diurnal and semi-diurnal tidal constituents, which are listed in Table 2.2. Similar to much tide literature, Darwin's naming convention for the tidal constituents is used. Table 2.2 also depicts the major tidal constituents with their period (in hours), their relative theoretical magnitude to the largest one, i.e. M2, as well as their source.

Constituent	Period (h)	Relative	Source
M2	12.4206	1	Earth's daily spin with respect to the Moon
S2	12.0000	0.46	Earth's daily spin with respect to the Sun
N2	12.6582	0.2	Modulation on M2 for elliptical orbit/speed change
K2	11.9673	0.13	Modulation on M2 and S2 due to orbital inclination
K1	23.9346	0.58	Earth's daily spin with respect to the Moon/Sun plus a modulation due to declination of the orbital plane
O1	25.8203	0.41	Earth's daily spin with respect to the Moon plus a modulation due to declination of the orbital plane

Table 2.2: Main diurnal and semi-diurnal lunisolar tides

### 2.3 Tidal potential

As the tidal force generates an irrotational field, replacing it with an equivalent potential scalar function facilitates tidal computation. Furthermore, the tidal potential is simply transferrable to the tide-induced observables, e.g. gravity change, vertical tilt, solid Earth deformation, as well

as ocean tidal currents. Hence, the tidal potential formulation and its main lunisolar constituents are reviewed in this section (following Melchior, 1966).

From classical mechanics, an arbitrary irrotational vector field  $\mathbf{F}$  can be shown with the gradient of its potential function  $W$ :

$$\mathbf{F} = \nabla W = \frac{\partial W}{\partial x} \mathbf{i} + \frac{\partial W}{\partial y} \mathbf{j} + \frac{\partial W}{\partial z} \mathbf{k} \quad (2.4)$$

It is important to realize that any constant term in the potential function has no physical meaning since it cannot produce any force. Therefore, Equation 2.4 can be generalized as:

$$\mathbf{F} = \nabla W = \nabla(W + W_c) \quad (2.5)$$

where  $W_c$  can be any constant function. Now, by replacing each term of Equation 2.1 with the gradient of the relevant potential function, and using the linear property of the gradient operator, the following form for the tidal potential can be written:

$$W_{tide}(A, t) = W(A, t) - W(C, t) \quad (2.6)$$

As can be seen from the above equation, the tidal potential at each point on the Earth's surface is the difference between the gravitational potential induced by the celestial bodies at that point and the Earth's centre of mass. In Figure 2.2, a two dimensional layout of the observer station (A), and Earth's centre of mass (C) and the celestial body (M), is shown. Again, for simplicity, the Moon is considered as the only body which induces the tidal potential.

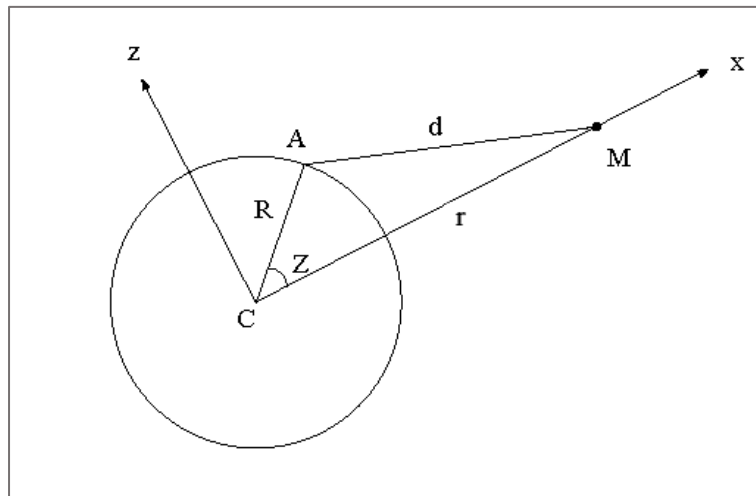


Figure 2.2: 2D layout of an observer (A) and a tide generating body (M), e.g. the Moon

From the global attraction law, the gravitational force from the Moon on a unit mass at point A can be written as a function of the distance from the Moon to the observer ( $d$ ), and the mass of the Moon ( $m$ ):

$$\mathbf{F} = \frac{G \cdot m}{d(t)^2} \mathbf{u}_d \quad (2.7)$$

where  $G$  is the global gravitational constant, and  $\mathbf{u}_d$  is the unit position vector of the Moon from the observer. So, the potential function for the gravitational force in Equation 2.6 can be computed by:

$$W(A, t) = \frac{G \cdot m}{d(t)} \quad (2.8)$$

On the other hand, by using the cosine rule in triangle AMC in Figure 2.2 ,  $d$  can be written based on the Moon's distance from the Earth's centre of mass ( $r$ ), its zenith angle at the observer station ( $Z$ ), and the Earth's mean radius ( $R$ ). Therefore, Equation 2.8 can be rewritten as:

$$W(A) = \frac{G \cdot m}{\sqrt{r^2 + R^2 - 2rR\cos Z}} \quad (2.9)$$

In the above formula, for clarity, the time dependency of  $W$ ,  $r$  and  $Z$  is dropped. After expanding the inverse square root in the denominator of Equation 2.9 to Legendre polynomials  $P_i(\cos Z)$ , the following formula results:

$$W(A) = \frac{Gm}{r} \sum_{i=0}^{\infty} \left(\frac{R}{r}\right)^i P_i(\cos Z) \quad (2.10)$$

where the Legendre polynomials can be generated by the following recursive formulae:

$$\begin{aligned} P_0(x) &= 1, \quad P_1(x) = x, \\ P_n(x) &= \frac{2n-1}{n} x P_{n-1}(x) - \frac{n-1}{n} P_{n-2}(x), \quad \text{for } n = 2, 3, \dots \end{aligned} \quad (2.11)$$

In the tidal potential expansion shown in Equation 2.10, the ratio of  $R$  to  $r$  for the Moon and the Sun is  $1.66 \times 10^{-2}$  and  $4.33 \times 10^{-5}$ , respectively, and the Legendre polynomials are always between -1 and 1 for  $-1 \leq \cos Z \leq 1$ . Therefore, all tidal potential terms with degree greater than three are negligible, e.g. the degree three lunar potential is about 0.03% of the whole lunar

potential. Hence, the tidal potential expansion for  $i = 0, 1, 2$ , is considered and their corresponding tidal forces are explained in the following paragraphs.

For  $i = 0$ , the first term of the series is  $W_0 = Gm/r$  which is independent of an observer's location. This constant potential cannot generate any tidal force. For  $i = 1$ , the second term of the potential function is:

$$W_1 = \frac{Gm}{r^2} R \cos Z \quad (2.12)$$

To understand the role of  $W_1$ , its gradient in the coordinate system which is shown in Figure 2.2, is illustrated here. In this frame,  $W_1$  and its gradient can be expressed in the form of Equations 2.13 and 2.14, respectively:

$$W_1 = \frac{Gm}{r^2} x \quad (2.13)$$

$$\nabla W_1 = \frac{\partial W_1}{\partial x} \mathbf{i} + \frac{\partial W_1}{\partial y} \mathbf{j} + \frac{\partial W_1}{\partial z} \mathbf{k} = \frac{Gm}{r^2} \mathbf{i} \quad (2.14)$$

Equation 2.14 is equivalent to the gravitational force from the Moon at the Earth's centre of mass. So,  $W_1$  can be realized as the contribution of the Moon-induced gravitational potential at point  $C$ . Therefore, for the tidal potential at point  $A$ , the first and second terms of Equation 2.10 are dropped, and the following equation for the tidal potential results:

$$W_{tide}(A) = W(A) - W(C) = \frac{Gm}{r} \sum_{i=2}^{\infty} \left(\frac{R}{r}\right)^i P_i(\cos Z) \quad (2.15)$$

As already explained, the tidal potential terms for  $i \geq 3$  are negligible, so the term corresponding to  $i = 2$  should be kept. After using the explicit form of the degree two Legendre polynomial, the following equation for the tidal potential is obtained:

$$W_{tide} \cong \frac{GmR^2}{2r^3} (3\cos^2 Z - 1) \quad (2.16)$$

For the Moon, the above formula gives around 98% of the tidal potential (Baker, 1984). It should be noted that parameters  $r$  and  $Z$  in Equation 2.16 vary spatio-temporally. To compute the periodicities in the tidal potential, precise astronomical information of the Moon/Sun's

location with respect to the rotating Earth is employed. In this approach, by applying spherical trigonometry, parameter  $Z$  in Equation 2.16 may be written as a function of declination and local hour angle  $(\delta, h)$  of the tide-generating body, plus the observer's latitude and longitude  $(\varphi, \lambda)$ . The following equation for the tidal potential results:

$$W_{tide}(t) \cong \frac{GmR^2}{4r^3} \left[ \cos^2\varphi \cdot \cos^2\delta(t) \cdot \cos 2h(t) + \sin 2\varphi \cdot \sin 2\delta(t) \cdot \cos h(t) \right. \\ \left. + 3 \left( \sin^2\varphi - \frac{1}{3} \right) \left( \sin^2\delta(t) - \frac{1}{3} \right) \right] \quad (2.17)$$

where  $\varphi$  is constant for a fixed station, but  $h$  changes with a period similar to the lunar/solar day, and  $\delta$  repeats for every relative Earth-body orbital motion. Therefore, a semidiurnal and a diurnal signal from the first and second terms of Equation 2.17 are expected, respectively. However, the extra factors in these two terms, i.e.  $1/r^3$ ,  $\cos^2\delta(t)$  and  $\sin 2\delta(t)$ , cause the two constituents to modulate with other signals, thereby, generating new constituents. The last term in Equation 2.17 can be realized as a long period signal in the tidal potential.

In addition to the temporal variation of the tidal potential, Equation 2.17 can also be used to understand its spatial pattern. For a given time  $t$ , the equation shows that the amplitude of a tidal constituent varies with the observer's latitude. For instance, both diurnal and semidiurnal constituents are zero at  $\varphi = 90$ , whilst the long-period constituent is maximized there. As another example, the semidiurnal and diurnal constituents have maximum power at latitudes 0 and 45, respectively. In Equation 2.17, the hour angle is a function of the station longitude, so a phase lag change for observers with identical latitude but different longitude is expected.

## 2.4 Earth body tide

The response of the solid Earth to the direct tidal force is the EBT. In almost all regions of the Earth, the EBT is large enough to be sensed by geodetic instruments. For instance, the peak-to-peak EBT displacement can reach up to 70 cm which is nearly a hundred times larger than the GNSS, VLBI or SLR observation error. EBT is typically computed from a forward modelling which solves the equation of motion of an oceanless Earth's particles against direct tidal force (e.g., Alsop, 1964; Agnew, 2007). In this approach, as a first approximation, a spherical, non-rotating, elastic, and isotropic (SNREI) Earth model is assumed.

Melchior (1966) explained that using Love numbers (Love, 1912) in the spherical elasticity problem simplifies the tidal deformation computation. In this method, for the 3D EBT displacement caused by the degree  $n$  tidal potential ( $W_n$ ), the following equations are used:

$$u_n = h_n \frac{W_n}{g}, \quad v_n = \frac{l_n}{g} \frac{\partial W_n}{\partial \theta}, \quad w_n = \frac{l_n}{g \cdot \sin \theta} \frac{\partial W_n}{\partial \lambda} \quad (2.18)$$

where  $u_n$  is the radial displacement, and  $v_n$  and  $w_n$  show the deformation components in the east-west and north-south directions, respectively. In this formula,  $h_n$  and  $l_n$  are degree  $n$  Love and Shida numbers, respectively, and  $g$  is the gravitational acceleration. Hereafter, Love and Shida numbers will simply be termed ‘Love’ numbers. As mentioned by Agnew (2007), the magnitude of  $h_n$  and  $l_n$  slightly changes among different standard Earth models. For instance,  $h_2$  estimated from the Guttenberg-Bullen model (Alterman *et al.*, 1961) is 0.6114 whilst it is 0.6032 based on the Preliminary Reference Earth Model (PREM) (Dziewonski and Anderson, 1981).

In theory, the contributions from all tidal potential terms should be summed to obtain the EBT displacement. However, as explained in the Section 2.3, the displacement attributed to the second and third degree lunisolar potential suffices. According to the IERS Conventions (Petit and Luzum, 2010), to achieve around 1 mm modelling accuracy for a GNSS station on the Earth's surface, the nominal values for  $h_n$  and  $l_n$ , which are derived from SNREI assumption, should be corrected for the Earth daily rotation, ellipticity and anelasticity. Wahr (1981) explained that for an elliptic rotating Earth,  $h_n$  and  $l_n$  change with latitude due to the Coriolis force. Furthermore, the Earth's free core nutation (FCN) produces a nearly diurnal free wobble (NDFW) which resonates the diurnal band of the tidal response. For the tidal forces with longer periods, the Earth's response tends to be anelastic, and it should be taken into account for the Love numbers' parametrization.

In the PPP software used in this thesis, the EBT is corrected according to the IERS 2010 Conventions (Mathews *et al.*, 1997). As an example, by using the DEHANTTIDEINEL routine, which is from the IERS software collection<sup>1</sup>, EBT 3D displacements at UTC midnight, 21 March, 2018, for a  $1^\circ \times 1^\circ$  grid has been computed, and the results are shown in Figure 2.3 to 2.5. Figure 2.3 exhibits a tidal bulge (nearly 30 cm vertical displacement) for the areas close to the equator with longitude  $45^\circ E$  as well as  $135^\circ W$ . The long wavelength spatial change for the EBT in Figure 2.3 is mainly controlled by the elastic/inelastic properties of the deep mantle and the global structure of the Earth's layers. In Figure 2.4 and Figure 2.5, the computed EBT east-west and north-south displacements are shown, respectively.

---

<sup>1</sup> <http://iers-conventions.obspm.fr/content/chapter7/software/dehanttideinel/DEHANTTIDEINEL.F>



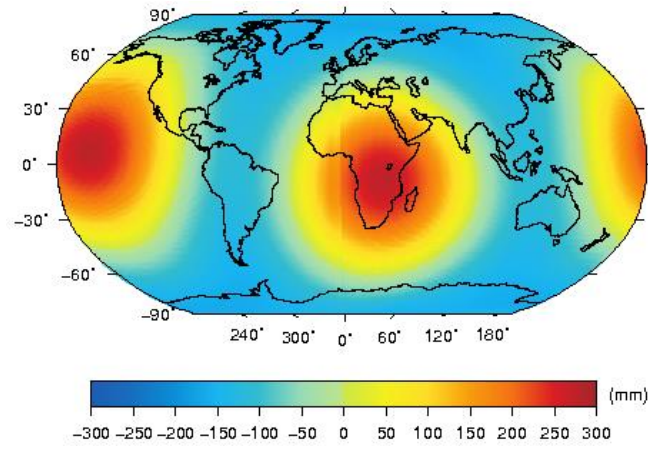


Figure 2.3: Modelled EBT vertical displacement at UTC midnight on 21 March 2018 for a  $1^\circ \times 1^\circ$  grid (based on the DEHANTTIDEINEL program)

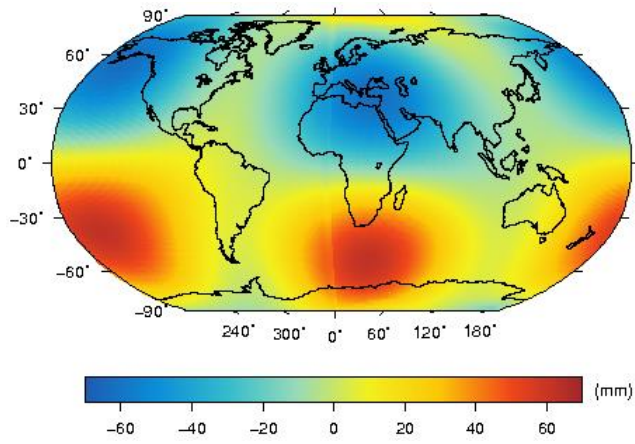


Figure 2.4: Similar to Figure 2.3 but for the east-west direction

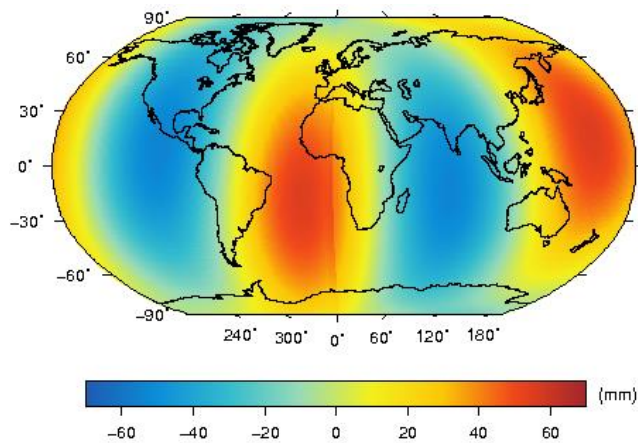


Figure 2.5: Similar to Figure 2.3 but for the north-south direction

## 2.5 Ocean tide loading displacement

OTL displacement is the response of the solid Earth to the ocean tidal loading, and geodetic instruments are sensitive to OTL displacement up to hundreds of kilometre away from coastlines. The OTL displacement spatial variation and its forward modelling is more complicated than EBT as it is influenced by the ocean tidal pattern. Due to a more rapidly varying spatial distribution of the ocean tidal load, OTL displacement varies with a shorter wavelength than EBT. Hence, loading potential spherical harmonics with  $n > 3$  cannot be discarded any longer, and it is typical to expand the loading potential up to  $n = 10000$  which is equivalent to a wavelength for about 4 km at the equator. Clearly, for each potential term the corresponding Love numbers should be computed. On the other hand, the regional variation of the Earth's surface response to the OTL is mainly controlled by the mechanical properties of the Earth's lithosphere and upper mantle. So, the anelasticity as well as lateral heterogeneities for these layers, which were largely ignorable for EBT prediction, may need to be taken into account.

In the following subsection, a brief review of ocean tide modelling, the available recent models and their accuracy are described. Thereafter, the theoretical as well as practical aspects of the Earth's response to OTL are addressed.

### 2.5.1 Ocean tide models

Due to the speed of the ocean wave propagation, irregularities in the shape of the ocean basin and coastlines, oscillation of the ocean basin, and the tidal potential resonance, the ocean response to the tidal force is not as straightforward as the body tide. However, to achieve a partial understanding of the ocean tidal currents, the hydrodynamic equations for the ocean particles can be considered. Equations of motion of the ocean particles due to the tidal force, which comprise three distinct equations formally known as Laplace Tidal Equations (LTEs), are developed and described in classic tide literature (e.g., Cartwright, 1977; Pugh, 1987), and a summary is presented here.

The first equation of the LTEs, which is called the conservation of mass or continuity equation, is based on the fact that the net flux of water into or out of an area must be compensated by a corresponding change in the water level. This equation is written in the form:

$$\frac{\partial \xi}{\partial t} + D \left( \frac{\partial u}{\partial x} + \frac{\partial v}{\partial y} \right) = 0 \quad (2.19)$$

where  $\xi$  is used for the ocean tidal height and  $D$  refers to the ocean depth. It is conventional to express both  $\xi$  and  $D$  with respect to mean sea level (MSL). In the equation above,  $x$  and  $y$  are the coordinate axes directing to the local east-west and north-south directions, respectively, and the water flow speed in the two directions is shown by  $u$  and  $v$ , respectively.

The two other LTEs are derived by the motion formulation of an infinitesimal element of the ocean water on the rotating Earth. In reality, the force system on the element is very complicated, but the tidal force, horizontal pressure gradient, and shear force are typically considered in the first approximation. Furthermore, to express the particle motion in an inertial frame, the Coriolis effect caused by the fluid flow on the rotating Earth should be taken into account. Therefore, the particle acceleration is decomposed to its local acceleration within the non-inertial fluid field, and the field acceleration, which is known as advection and is expressed in an inertial frame. The second and third LTEs for a particle at latitude  $\varphi$  are as follows:

$$\frac{\partial u}{\partial t} + v \frac{\partial u}{\partial y} + u \frac{\partial u}{\partial x} - (2\omega_e \sin\varphi)v = -\frac{\partial W_{tide}}{\partial x} - \frac{1}{\rho} \frac{\partial P}{\partial x} - \frac{1}{\rho} \frac{\partial F}{\partial z} \quad (2.20)$$

$$\frac{\partial v}{\partial t} + u \frac{\partial v}{\partial x} + v \frac{\partial v}{\partial y} + (2\omega_e \sin\varphi)u = -\frac{\partial W_{tide}}{\partial y} - \frac{1}{\rho} \frac{\partial P}{\partial y} - \frac{1}{\rho} \frac{\partial G}{\partial z} \quad (2.21)$$

where  $\omega_e$  is the Earth's daily rotation angular speed,  $W_{tide}$  is the direct lunisolar tidal potential,  $P$  is the horizontal pressure, and  $F$  and  $G$  are the shear stress at the interested point in the  $x$  and  $y$  directions, respectively. In the above equations, the left hand sides represent the particle accelerations, which are equivalent to the resultant force acting on the particle's unit mass shown on the right hand side. By assuming a uniform density for the ocean water, the horizontal pressure gradient in the above equations can be replaced with the horizontal gradient of the tidal height  $\xi$ , multiplied by density.

To solve LTEs, some boundary conditions as well as direct tidal potential, horizontal shear stresses, and ocean depth information are required. Although the boundary conditions can be provided by direct observation and the tidal potential is calculable from the formulae explained in the Section 2.3, bathymetry data may have a sparse distribution especially in the far oceans. The incomplete shear stress model can also be another source of uncertainty of the ocean tide hydrodynamic modelling.

Schwiderski (1980) computed one of the first hydrodynamic ocean tide models called Naval Surface Weapons Centre (NSWC) based on the LTEs solution constrained by tide gauge data.

Although NSWC was the most realistic description for the ocean tide at its time, an error larger than 10 cm for this model in some open oceans, in which no tide gauge data was employed, has been reported (Cartwright and Ray, 1990). FES94.1 (Le Provost *et al.*, 1994) is another pure hydrodynamic tide model which employed a finite element solution (FES) to provide a finer resolution for the shallow ocean tide. With the development of the TOPEX/POSEIDON satellite altimeters, more accurate data of the open ocean surface variation was provided, and the FES99 model (Lefèvre *et al.*, 2000) was constructed. By quantity and quality improvement in the tide data from satellite altimetry, more tide gauge and bottom pressure measurements, and the development in computation resources, the ocean tide models have been considerably enhanced in accuracy, resolution, as well as coverage. The result of an accuracy assessment among historic, modern data-constrained and purely hydrodynamic models is presented in Stammer *et al.* (2014). By comparing the ocean tide models with tide gauge and bottom pressure data, they report that the RMS accuracy of the best altimeter-constrained model for the M2 constituent in pelagic and shelf sea areas have been reduced from 1.64 and 23.0 cm to 0.51 and 3.5 cm, respectively, over the last two decades. However, they highlight that accurate tide modelling in shallow seas and Polar Regions is still a big challenge.

In this thesis, the FES2014b tide model (Carrère *et al.*, 2016) is used for OTL displacement forward modelling. This model, which is prepared at a  $1/16^\circ$  resolution, is fed by satellite altimetry data from TOPEX/POSEIDON, Jason-1, Jason-2, and ERS-1/ERS-2. Compared to FES2012 (Carrère *et al.*, 2012), FES2014b employed more tide gauge data in shallow waters and Antarctica. By using seven years of GRACE inter satellite range-rate observation, Ray *et al.* (2019) demonstrated an improvement for FES2014b compared to FES2012 especially for the K1 and S2 constituents in the Arctic Ocean, although they found a degradation for the O1 and M2 constituents in the Ross Sea and Weddell Sea, respectively.

### **2.5.2 OTL displacement forward modelling**

To compute the solid Earth response to the OTL, a similar technique to the EBT modelling can be implemented. As the ratio of the celestial bodies' radius to their distance from the Earth is very small, e.g. 0.0045 and 0.0047 for the Moon and the Sun, respectively, they could be assumed as point masses for the EBT potential formulation. However, in the OTL forward modelling, the whole ocean water is partitioned to columns with equal base area  $dA$  and tidal height  $\xi$ , located at distance  $r$  from the observer. Then, by assuming a uniform density for the ocean water, the total tide loading potential is the integrated potential induced by all small volume elements:

$$W_{OTL}(\varphi, \lambda, t) = \int G \frac{dm(\varphi', \lambda', t)}{r} \xrightarrow{dm_{OTL} = \rho_w \xi dA} G \rho_w \int \frac{\xi(\varphi', \lambda', t)}{r} dA \quad (2.22)$$

Agnew (2007) explains that both the tidal height ( $\xi$ ) and distance reciprocal ( $1/r$ ) in Equation 2.22 can be replaced with their spherical harmonic expansions, and after some mathematical manipulation, the following equation arises:

$$W_{OTL}(\varphi, \lambda, t) = \sum_{n=0}^{\infty} \sum_{m=-n}^n G \cdot R \cdot \rho_w \frac{4\pi}{2n+1} \xi_{nm}(t) Y_{nm}(\varphi', \lambda') = \sum_{n=0}^{\infty} W_{OTL,n} \quad (2.23)$$

where  $\xi_{nm}$  is the coefficient for the tidal height spherical harmonics which are estimated in the ocean tide modelling,  $Y_{nm}$  is the normalized spherical surface harmonic which is generated by:

$$Y_{nm}(\varphi, \lambda) = (-1)^m \left[ \frac{2n+1}{4\pi} \frac{(m-n)!}{(m+n)!} \right]^{0.5} P_{nm}(\cos\varphi) e^{im\lambda} \quad (2.24)$$

$$P_{nm}(\cos\varphi) = (-1)^m (1-x^2)^{\frac{m}{2}} \times \frac{d^m}{dx^m} \{P_n(x)\} \quad (2.25)$$

Similar to the direct tidal potential, Equation 2.23 shows a decomposition of the loading potential base on different wave numbers. Therefore, by using appropriate Love numbers (known as loading Love numbers), the solid Earth response to the OTL at each wave number may be calculated:

$$u'_n = h'_n \frac{W_{OTL,n}}{g}, \quad v'_n = \frac{l'_n}{g} \frac{\partial W_{OTL,n}}{\partial \theta}, \quad w'_n = \frac{l'_n}{g \cdot \sin\theta} \frac{\partial W_{OTL,n}}{\partial \lambda} \quad (2.26)$$

where  $h'_n$  and  $l'_n$  are the loading Love numbers (Farrell, 1972).

Baker (1984) and Agnew (2007) explain that to compute the OTL response at a limited number of points, e.g. GNSS stations, the spherical harmonic expansion method is computationally inefficient, and they explain that the convolution technique is an alternative. To understand the convolution method, the concept of a Green's function, which facilitates the solution of ordinary differential equations (ODEs) solution, should be realized.

In general, the state of a system which is acted on by an external force  $f(x)$  can be expressed in the form of a second order ODE:

$$p(x) \cdot \frac{d^2 y}{dx^2} + q(x) \cdot \frac{dy}{dx} + r(x) \cdot y = f(x) \quad (2.27)$$

where  $p(x)$ ,  $q(x)$  and  $r(x)$  are continuous functions for  $x \in [a, b]$ , and  $f(x)$  is bounded in this interval. Mathematically, a Green's function for Equation 2.27 is a solution of the equation after replacing  $f(x)$  by a Dirac-delta function  $\delta(x - \eta)$ . In a physical perspective, the Green's function  $G(x; \eta)$  shows the response of a system to a point force at  $x = \eta$ . The instruction of finding an ODE Green's function is beyond the scope of this thesis, but the response of a system with a known Green's function to an external force  $f(x)$  can be formulated by a convolution integral (e.g., Stakgold, 1998):

$$y(x) = \int_a^b G(x; \eta) \cdot f(\eta) d\eta \quad (2.28)$$

In two dimensional space, this may be generalized as:

$$y(x_1, x_2) = \iint G(x_1, x_2; \eta_1, \eta_2) \cdot f(\eta_1, \eta_2) d\eta_1 d\eta_2 \quad (2.29)$$

To compute OTL displacement with Equation 2.29, the ocean tidal loading force and the Earth's surface loading Green's function should be available. Furthermore, the above integral needs to be calculated over the entire oceans. By assuming a uniform density  $\rho_w$  for ocean water and using vector representation for the location of the point load and the observer station in the form of  $\vec{r}'$  and  $\vec{r}$ , respectively, Equation 2.29 can be simplified to:

$$L(\vec{r}) = \rho_w \iint G(\vec{r}; \vec{r}') \xi(\vec{r}') dA \quad (2.30)$$

where  $L$  is the OTL displacement and  $\xi(\vec{r}')$  is the tidal height.

For the first time, Longman (1963) proposed the Green's function approach to predict the loading effect on the Earth's surface. Thereafter, Farrell (1972) formulated Green's functions for the Guttenberg-Bullen (Alterman *et al.*, 1961) Earth model. He showed that the Earth's Green's function can be computed through a weighted sum of the Love numbers, and proposed the following equations for the vertical and horizontal displacement Green's functions, respectively:

$$G_u(\psi) = \frac{R}{m_e} \sum_{n=0}^{\infty} h'_n P_n(\cos\psi) \quad (2.31)$$

$$G_v(\psi) = G_w(\psi) = \frac{R}{m_e} \sum_{n=0}^{\infty} l'_n \frac{\partial P_n(\cos\psi)}{\partial\psi} \quad (2.32)$$

where  $\psi$  is the angular distance between the point load and the observer's location,  $R$  and  $m_e$  are the mean radius of the Earth and its mass, respectively.

The OTL displacement convolution integral is typically calculated by a discrete summation over the ocean cells. To resemble a point load for the open oceans or near regular coastlines, Farrell (1972) suggested a ratio of a tenth for the radius of a cell to the load-observer distance, but near non-regular coastlines, a smaller ratio should be selected. However, the ocean tidal models are generated for a regular grid with a resolution about than 7 km or more. So, the OTL software packages, e.g. OLFG/OLMPP (Scherneck, 1991), SPOTL (Agnew, 1997), GOTIC2 (Matsumoto *et al.*, 2001), have to approximate the tidal height at the centre of each cell. By comparing the predicted OTL displacement with the GPS-measured one, Penna *et al.* (2008) concluded that bilinear interpolation without local mass redistribution is the most appropriate approach to estimate the tidal height in each ocean cell.

The OTL displacement computation in the forward modelling can be with respect to the centre of mass of the Earth's system (CM), i.e. the entire solid Earth plus oceans and atmosphere, or the centre of mass of the solid Earth (CE). Regarding the coordinate frame for the geodetic observation adjustment, an appropriate frame for the predicted OTL displacement should be used. For instance, the satellite products generated by the IGS analysis centres consider the centre of the GNSS network (CN) as the origin of the coordinate frame. At semi-diurnal and diurnal timescales, CN is equivalent to CE, and the modelled OTL displacement with respect to the CE can be used for the GNSS data processing with the IGS products. However, it is worthwhile to note that the Jet Propulsion Laboratory (JPL) disseminates precise GPS satellite orbit information in a JPL (native) as well as IGS (SP3) formats. Although the latter is computed with respect to CE, the former is expressed with respect to CM. So, JPL satellite product users adopting the precise point positioning (PPP) technique should be aware of the origin difference, otherwise, their estimated station coordinates will be modulated with the CE-CM relative periodic motion.

The forward modelled OTL displacement used in this thesis is computed by solving the convolution integral in the SPOTL software. SPOTL provides the flexibility to compute OTL by a mixture of local and global ocean tide models. It can also use loading Green's functions which are based on the Love numbers computed in either CE or CM frames. To correct the modelled OTL displacement from GNSS data, the FES2014b ocean tide and PREM Green's function are used in Chapter 5, and several ocean tide models and Earth's Green's functions in Alaska are compared in Chapter 6.

In Figure 2.6 to 2.8, global distribution of M2 OTL displacement amplitude based on the FES2014b and PREM models for a  $1^\circ \times 1^\circ$  grid are shown. It can be seen in Figure 2.6 that the OTL vertical displacement in many coastal regions, e.g. western Europe, southern Africa, northeast of South America, west of central America, south of Alaska, and northern New Zealand, is larger than 30 mm. Similar to EBT, Figure 2.7 and 2.8 indicate that the horizontal OTL displacement is smaller than the vertical component, but it may reach up to 5-7 mm in the aforementioned regions. The OTL displacement pattern is not as regular as the EBT pattern shown in Figure 2.3 to 2.5, and it varies with shorter spatial wavelength than the EBT.

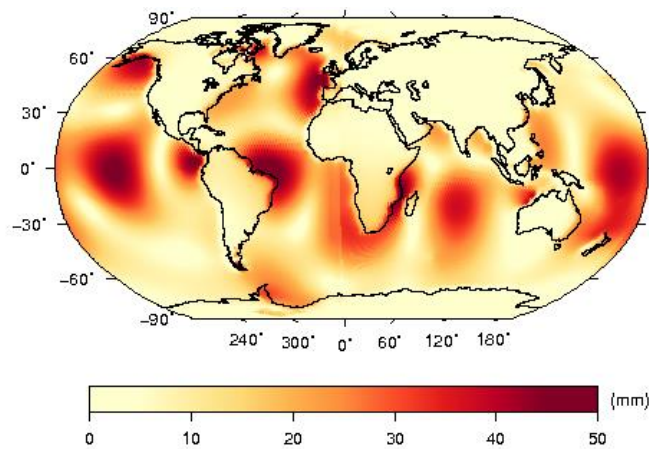


Figure 2.6: Amplitude of the modelled OTL vertical displacement for M2 based on the FES2014b ocean tide model and the PREM Earth model



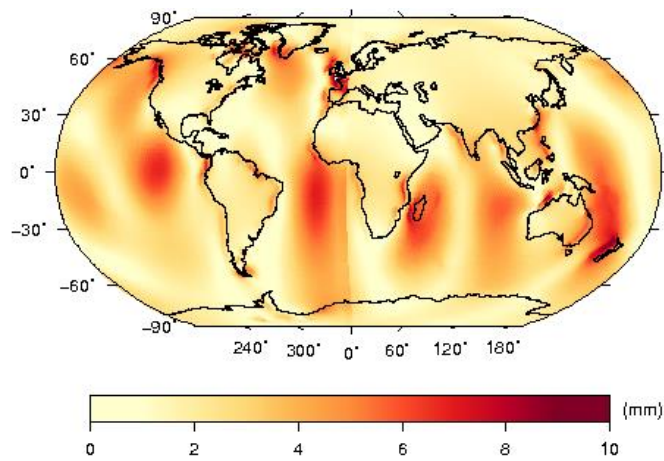


Figure 2.7: Similar to Figure 2.6 but for the east-west direction

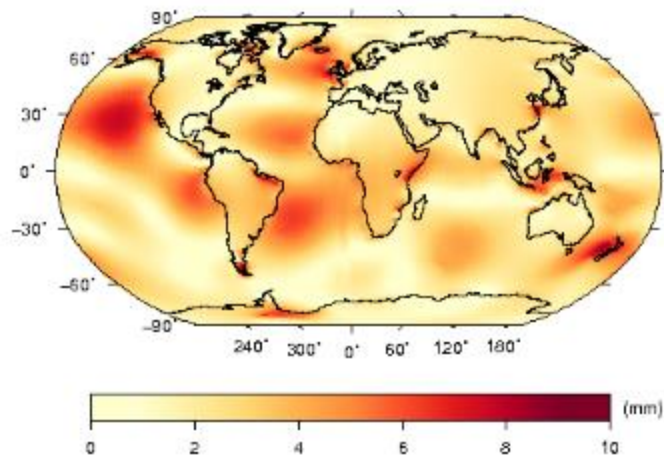


Figure 2.8: Similar to Figure 2.6 but for the north-south direction

## 2.6 Summary

This chapter has addressed the solid Earth tidal displacement modelling. First of all, tide generation and its main diurnal and semidiurnal constituents have been introduced. It is also described that by having precise information of the Moon and Sun positions, the total tidal potential can be formulated as an infinite sum of the potential functions with different spatial wavelengths. After introducing the correspondence between Love numbers and the tidal potential terms, tidal displacement modelling has been explained. For the EBT modelling with 1 mm accuracy, it was described that the lunisolar tidal potential up to degree three should suffice, whilst for the oceans, especially near coastlines, the response to the tidal force is more complicated. After reviewing the ocean tide modelling techniques, the OTL displacement

forward modelling using ocean tide models and Earth's physical models has been described. It was explained that the concept of Green's functions is useful for the surface loading displacement prediction, and it is computationally more convenient to use a convolution of the ocean tide and Earth Green's function to compute OTL displacement at geodetic stations. Because of its reliance on the ocean tide models, the OTL displacement forward modelling is more challenging than EBT. Alternatively, as will be discussed in Chapter 3, OTL displacement may be measured with GNSS data.

## Chapter 3 GNSS and tidal loading measurement

### 3.1 Introduction

The forward modelled OTL displacement is contaminated by the ocean tide and Earth's physical model error. The ocean tide modelling error near intricate coastlines and shallow seas, can introduce up to 5 mm error in the forward modelling (Melachroinos *et al.*, 2007), and at stations with larger than about 15 mm OTL displacement, about 1-2 mm uncertainty in the predicted OTL displacement induced by the Earth model error may be expected (e.g., Ito and Simons, 2011; Bos *et al.*, 2015). The unmodelled OTL displacement propagates into estimated parameters by GNSS, VLBI, SLR, and DORIS. Schuh and Moehlmann (1989) showed VLBI-estimated station coordinates and baseline length change up to 1 cm when OTL displacement correction is applied. Dach and Dietrich (2000) showed that about 20% of the unmodelled OTL displacement is absorbed with GPS-derived zenith tropospheric delay, and Vey *et al.* (2002) demonstrated that to satisfy near 1 mm accuracy for GPS-estimated precipitable water vapor, OTL displacement with less than 3 cm uncertainty should be known. Ray *et al.* (2004) demonstrated that tidal displacement should be included in the instantaneous position of ITRF stations, and King *et al.* (2008) demonstrated that a sub-daily unmodelled Earth's surface harmonic deformation may produce artificial signals with annual and semi-annual periods which can bias seasonal geophysical loading estimation. After applying OTL displacement corrections to SLR observations, Sośnica *et al.* (2013) obtained about 19% and 30% reductions in the stations' 3D coordinates and annual amplitude of the station height, respectively. DiCaprio and Simons (2008) suggest that OTL displacement near coastlines generates a spatial gradient which is larger than InSAR observation noise. Therefore, it is necessary to understand the errors in OTL displacement, and geodetic measurements of OTL displacement are usable for this objective.

Sovers (1994) estimated eight nearly diurnal and semidiurnal constituents of OTL vertical displacement using VLBI measurements collected from 1984 to 1992 at six stations in Europe and North America. He concluded an overall 1-2 mm uncertainty for the estimated OTL displacement. By processing VLBI data collected at 40 global stations from 1980 to 2002, Petrov and Ma (2003) distinguished between different ocean tide models used for M2 OTL displacement forward modelling. They also compared the estimated OTL displacements from VLBI and GPS data with modelled values, and reported smaller residuals for the VLBI solution. Thomas *et al.* (2007) compared a GPS-derived OTL displacements with the VLBI estimates

listed in Petrov and Ma (2003). They demonstrated no statistically significant difference between the results obtained by the two techniques. GPS has attracted more attention than VLBI for the tidal displacement investigation as its continuous data collecting networks are several orders of magnitude denser than VLBI networks. Therefore, GPS and GLONASS data will be used for OTL displacement assessment in this thesis.

In the next section, GPS precise positioning methods, which are applicable for tidal displacement detection and estimation, are briefly described. Thereafter, spectral analysis of a time series is introduced, followed by a literature review on the main GPS-derived OTL displacement studies. Finally, the potential benefits of GLONASS data for OTL displacement investigation is explained.

### 3.2 GPS precise positioning methods

The GPS constellation is comprised of at least 24 satellites which are equally distributed in six nearly-circular orbits with radius of 26559 km, and each orbital plane is inclined at about 55° to the equatorial plane. There is a 60° longitude separation between the ascending nodes of two adjacent orbits. With this arrangement, which results in an orbital period of 11h 58min, at least four GPS satellites are always above the horizon anywhere on the Earth's surface. To determine a GPS receiver's coordinates, distances from the satellites to the receiver are measured. Then, by knowing the satellite coordinates, a multi-lateration problem is solved. However, the immediate solution for this problem is accurate at the level of several metres. To satisfy centimetre or millimetre accuracy level for GPS positioning, high quality satellite positions as well as the receiver-satellite ranges are required. Comprehensive details for GPS precise positioning algorithms can be found in several textbooks (e.g., Seeber, 2003; Hofmann-Wellenhof *et al.*, 2007; Teunissen *et al.*, 2017). Only an overview of the subject is provided in this section.

Any GPS receiver used for geodetic applications records two types of observables: pseudorange and carrier phase. Whilst the former represents the receiver-satellite distance unambiguously with decimetre level accuracy, the latter with millimetre level precision but ambiguous nature have to be used for a GPS precise positioning. In a very simplified form, an observation equation for the phase data with frequency  $f_j$  can be written as:

$$\varphi_{r,j}^s = \{(x_s - x_r)^2 + (y_s - y_r)^2 + (z_s - z_r)^2\}^{0.5} + d_r + d^s + d_{atm} + \lambda_j \cdot b_j + \varepsilon_\varphi \quad (3.1)$$

where  $\varphi_{r,j}^s$  is the observed carrier phase with wavelength  $\lambda_j$ ;  $(x_r, y_r, z_r)$  are the receiver coordinates which should be determined;  $(x_s, y_s, z_s)$  are the satellite's coordinates which are known with some uncertainty;  $d_r$  and  $d_s$  are lumped receiver-based and satellite-based ranging errors, respectively;  $d_{atm}$  is the total error induced by the atmospheric physical deviation from a standard calibration environment;  $b_j$  is an integer number of cycles which is traveled by the carrier signal from a satellite to a receiver and is called the phase ambiguity;  $\varepsilon_\varphi$  is the measurement noise. As the above equation indicates, error treatment and integer ambiguity resolution make the GPS precise positioning a complicated problem. In general, GPS precise positioning can be performed in two ways: relative positioning and precise point positioning (PPP). For both techniques, the most robust solution is achievable in a post-processing mode.

Relative positioning uses measurement differencing between satellites, receivers, data collection epochs or their combination, to treat positioning errors. For instance, in a double differencing (DD) approach, following a subtraction between simultaneous recorded observations at two receivers from two satellites, the errors in the receiver and satellite clocks as well as satellite orbit errors are eliminated, and the atmospheric error is mainly reduced. Hence, the observation adjustment leads to precise baseline coordinates and real-valued phase ambiguities which may then be resolved to integers through ambiguity searching techniques (Teunissen, 1995). It should be noted that, to overcome the datum deficiency in relative positioning, at least one station with known coordinates is needed. The precision of the relative positioning decreases directly with increasing baseline length due mainly to uneven atmospheric error at two ground stations.

Unlike the relative positioning technique, PPP is an undifferenced (UD) coordinate determination technique which requires the mitigation of observational error by using external precise information, modern systematic error models, and data combination over more than one frequency (Zumberge *et al.*, 1997; Kouba and Heroux, 2001). For the satellite clock and orbit errors, PPP uses satellite orbits and clocks obtained from the analysis of a global network, and the ionospheric error is mainly eliminated by the ionospheric-free data combination. The predictable part of the tropospheric delay is corrected with standard models which are included in the IERS Conventions, and its residual part is estimated together with the station coordinates, receiver clock offset, and real-valued phase ambiguities. As the satellite coordinates used in PPP are generated in the ITRF (Altamimi *et al.*, 2016), the estimated station position is also tied to the ITRF.

Ambiguity fixing in PPP is more challenging than relative positioning as it is more likely to miss its integer nature due to the satellite and receiver uncalibrated phase delay (UPD). Ge *et al.* (2007) proposed that the estimated fractional part of the single differenced (SD) UPD from a global network can be used to give an integer nature to the SD ambiguities in PPP. They showed that when a global network is used, narrow-lane (NL) UPDs for satellite pairs should be estimated every 15 min. Geng *et al.* (2009) described that the NL UPD for a satellite pair over a regional network is more stable, and it is sufficient to estimate them within each full pass of the pair over the network. Bertiger *et al.* (2010) suggested that, in addition to estimating satellite clock/orbit corrections in a global network solution, phase bias and wide-lane (WL) information can be archived, and subsequently, they can be integrated with a single-receiver point positioning run to construct double differences (DD) between the interested receiver and the global network. Thereby, the estimated DD phase biases can be used for the PPP solution. This technique is applied for the PPP ambiguity fixed solution in GIPSY which is used in Chapter 5. More theoretical and practical details for the PPP technique will be provided in Chapter 4.

### 3.3 Spectral analysis of a time series

Instead of looking at a signal behaviour in the time or space domain, it is more informative in some applications to see its variation with frequency, which is called spectral analysis. For instance, by spectral analysis of a tide gauge measurement, the tidal constituent amplitudes and phase lags can be obtained. Thereafter, the physical tidal signal can be mathematically formulated as a function of time which may be usable for a later tide prediction.

#### 3.3.1 Fourier transformation

The Fourier transformation is one of the most popular techniques to split a signal  $s(t)$  to some sinusoids with pre-defined frequencies, and it can be written as:

$$S(\omega) = \int_{-\infty}^{+\infty} s(t). e^{-2\pi i\omega t} dt \quad (3.2)$$

where  $\omega$  is the frequency of the interested sinusoid constituent. A Fourier transformation is analogous to an inner product between a vector and its orthonormal base vectors in Euclidean space in which the orthogonal components of the vector are extracted. However, for the function space, infinite number of base functions, e.g. sinusoids, can be theoretically considered, although a limited number of constituents are computed in practice. If there is no clue for the frequency of the signal's main constituents, it is conventional to select the highest and lowest

resolvable frequencies based on the sampling rate and the length of the data span, respectively, and with a constant increment from the minimum to the maximum frequency, the intermediate ones are selected. Next, for a signal which is sampled discretely at  $t_1, t_2, \dots, t_N$ , the Fourier transformation integral will be replaced with a series which is shown in the following equation and is called the Discrete Fourier Transformation (DFT).

$$\begin{aligned}
 S(\omega_{min}) &\cong \sum_{k=1}^N s(t_k) \cdot e^{-2\pi i \omega_{min} t_k} \\
 &\vdots \\
 S(\omega_{max}) &\cong \sum_{k=1}^N s(t_k) \cdot e^{-2\pi i \omega_{max} t_k}
 \end{aligned} \tag{3.3}$$

Each computed  $S$  in Equation 3.3 is a complex number of the form  $S = a + i \cdot b$ ,  $i = \sqrt{-1}$ , and the amplitude  $A$  of a signal  $S$  can be computed as:

$$A = \sqrt{a^2 + b^2} \tag{3.4}$$

The amplitude spectrum, i.e. an amplitude versus frequency plot, is a useful tool to demonstrate the contribution of each frequency in the total signal, but it cannot indicate the nature of noise, i.e. white or coloured, of a time series. Instead, power spectral density (PSD), which is calculable from amplitude as shown in Equation 3.5 (e.g. Leon-Garcia, 1994), is an alternative and it is used in Chapter 5:

$$PSD(f) = E \left\{ \frac{1}{k} \cdot A_k(f)^2 \right\} \tag{3.5}$$

where  $k$  is the number of points which are used to compute amplitude  $A$  at frequency  $f$ , and  $E$  is the expectation (mean) operator. To practically compute the PSD of a time series, the whole data should be divided into segments with equal length  $k$ , and then the amplitude spectrum in each segment (at pre-defined frequencies) computed. Thereafter, the square of the amplitude spectra are normalized by the segment length and then averaged over the number of segments. It should be noted that, to increase the number of segments, an overlap between them is allowed. The Fast Fourier transformation (FFT) (Rao, 2010) is a computationally efficient algorithm to perform the DFT. However, the accuracy of the DFT may be decreased by spectral aliasing and leakage, which are explained in the following subsection. Furthermore, DFT is prone to any

trend or non-sinusoidal behavior of a time series, and it is usable only for equally-spaced data. Alternatively, for the spectral analysis of a tidal signal, as the frequency of its main constituents are known, least squares spectral analysis (LSSA) is the most appropriate option (Vaniček, 1973). The LSSA technique is discussed in more detail later in this section.

### **3.3.2 DFT main challenges**

As mentioned before, DFT implementation may be biased by two main errors: aliasing and leakage. Aliasing arises when the sampling interval is not small enough to cover high frequencies in the signal. As shown in Figure 3.1 (bottom pane), all theoretical spectra with frequency higher than  $1/(2dt)$ , where  $dt$  is the sampling rate, are aliased to lower frequencies (transformation of the blue dash line to the black dash line), and the estimated spectrum (solid black line) results. By increasing the sampling rate and undertaking data low-pass filtering, the aliasing effect may be reduced. For example, the GNSS-derived station coordinates in Chapter 5 are sampled at 0.5 hour rate which is sufficiently smaller than the main diurnal and semidiurnal tidal period. Furthermore, by applying a moving average filter the random white noise in the time series is reduced.

Spectral leakage is due to applying DFT over a non-integer number of cycles of a signal. For instance, in a DFT of a GNSS-derived coordinate time series with a length of one year (365 days), the M2 tidal spectrum will be leaked to either side as there are 705.3 cycles of the M2 signal in the time series. In many spectral analysis applications, it is typical to use window function, e.g. a Hanning window, to taper the non-integer part of the sample toward zero.



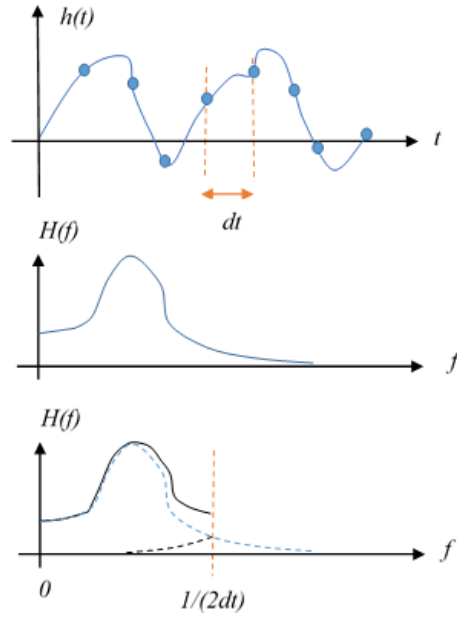


Figure 3.1: Signal sampling (top), theoretical spectrum (middle), and estimated (aliased) spectrum (black curve in the bottom pane)

### 3.3.3 Least squares spectral analysis (LSSA)

LSSA is resilient against aliasing and leakage problems, and it is also applicable for time series with gaps, jumps and trends. Furthermore, given the covariance matrix of the input time series, LSSA can compute the covariance matrix of the estimated amplitude and phase, and hence, the statistical significance of the estimated spectra can be evaluated. In this subsection, more details of the method are reviewed.

In LSSA, a linear (or quadratic, exponential, etc.) function and a collection of sinusoids with pre-defined frequencies but unknown amplitudes and phases are fitted to the time series. Hence, the following functional model may be used in LSSA:

$$s(t) = p + q \cdot t + \sum_{i=1}^n c_i \cdot \sin(\omega_i \cdot t + \varphi_i) \quad (3.6)$$

where  $p$  and  $q$  are the intercept and gradient of the (assumed) linear trend of the time series, respectively;  $c_i$  and  $\varphi_i$  are the unknown amplitude and initial phase of a signal with known frequency  $\omega_i$ , respectively, and  $n$  is the number of considered constituents in the spectral analysis. To construct the observation-equation, the sinusoidal term in Equation 3.6 may be expanded as:

$$c_i \cdot \sin(\omega_i \cdot t + \varphi_i) = c_i \cdot \cos(\varphi_i) \cdot \sin(\omega_i \cdot t) + c_i \cdot \sin(\varphi_i) \cdot \cos(\omega_i \cdot t) \quad (3.7)$$

Thereafter, by defining  $a_i = c_i \cdot \cos(\varphi_i)$  and  $b_i = c_i \cdot \sin(\varphi_i)$ , a new form for Equation 3.6 can be found:

$$s(t) = p + q \cdot t + \sum_{i=1}^n a_i \cdot \sin(\omega_i \cdot t) + b_i \cdot \cos(\omega_i \cdot t) \quad (3.8)$$

So, for a time series sampled at  $t_1, \dots, t_N$  time epochs, the following linear observation equation can be written:

$$\begin{aligned} s(t_1) &= p + q \cdot t_1 + a_1 \cdot \sin(\omega_1 \cdot t_1) + b_1 \cdot \cos(\omega_1 \cdot t_1) + \dots + a_n \cdot \sin(\omega_n \cdot t_1) \\ &\quad + b_n \cdot \cos(\omega_n \cdot t_1) \\ &\quad \vdots \end{aligned} \quad (3.9)$$

$$\begin{aligned} s(t_N) &= p + q \cdot t_N + a_1 \cdot \sin(\omega_1 \cdot t_N) + b_1 \cdot \cos(\omega_1 \cdot t_N) + \dots + a_n \cdot \sin(\omega_n \cdot t_N) \\ &\quad + b_n \cdot \cos(\omega_n \cdot t_N) \end{aligned}$$

The matrix representation of Equation 3.9, which is required for the least squares computation, is:

$$\begin{bmatrix} s(t_1) \\ \vdots \\ s(t_N) \end{bmatrix} = \begin{bmatrix} 1 & t_1 & \sin(\omega_1 \cdot t_1) & \cos(\omega_1 \cdot t_1) & \dots & \sin(\omega_n \cdot t_1) & \cos(\omega_n \cdot t_1) \\ \vdots & \vdots & \vdots & \vdots & \vdots & \vdots & \vdots \\ 1 & t_N & \sin(\omega_1 \cdot t_N) & \cos(\omega_1 \cdot t_N) & \dots & \sin(\omega_n \cdot t_N) & \cos(\omega_n \cdot t_N) \end{bmatrix} \begin{bmatrix} p \\ q \\ a_1 \\ b_1 \\ \vdots \\ a_n \\ b_n \end{bmatrix} \quad (3.10)$$

Equation 3.10 can be encapsulated in the form of  $\mathbf{l} = \mathbf{A} \cdot \mathbf{x}$  after using the following matrix definitions:

$$\mathbf{l} = [s(t_1) \dots s(t_N)]^t,$$

$$\mathbf{x} = [p \ q \ a_1 \ b_1 \ \dots \ a_n \ b_n]^t,$$

$$\mathbf{A} = \begin{bmatrix} 1 & t_1 & \sin(\omega_1 \cdot t_1) & \cos(\omega_1 \cdot t_1) & \dots & \sin(\omega_n \cdot t_1) & \cos(\omega_n \cdot t_1) \\ \vdots & \vdots & \vdots & \vdots & \vdots & \vdots & \vdots \\ 1 & t_N & \sin(\omega_1 \cdot t_N) & \cos(\omega_1 \cdot t_N) & \dots & \sin(\omega_n \cdot t_N) & \cos(\omega_n \cdot t_N) \end{bmatrix}$$

Now, by using least squares formulae, the unknown parameters and their covariance matrix can be estimated:

$$\hat{\mathbf{x}} = (A^t \cdot P \cdot A)^{-1} A^t \cdot P \cdot \mathbf{l}$$

$$C_{\hat{\mathbf{x}}} = (A^t \cdot P \cdot A)^{-1}$$
(3.11)

where  $P$  is the observation weight, i.e. the inverse of the time series covariance matrix. Since the covariance matrix of the full GNSS-derived station coordinate time series (through kinematic PPP) is not available, the covariance matrix of the estimated spectra will not be calculated in this study.

### 3.4 OTL displacement measurement by GPS data

The coordinates of a GPS receiver, which is fixed to the solid Earth, are modulated by the tidal surface displacement. The tidal displacement for each east, north and vertical component, can be written as the following summation (e.g., McCarthy and Petit, 2004):

$$\Delta c_k = \sum_{i=1}^{\infty} A_{k,i} \cos(\omega_i t + \chi_i(t_0) - \varphi_{k,i})$$
(3.12)

where  $\Delta c_{j=1,2,3}$  is the tidal displacement for component  $j$ ,  $A_{j,i}$  and  $\varphi_{j,i}$  are the amplitude and Greenwich phase lag, respectively, for component  $j$  and constituent  $i$ ,  $\omega_i$  is the constituent's angular frequency, and  $\chi_i(t_0)$  is the constituent's astronomical argument at reference time  $t_0$ .

As was explained in Chapter 2, EBT with a long wavelength spatial variations is more accurately and reliably modelled than OTL displacement. So, it is typical to correct GPS data from EBT, and the OTL displacement is retained in the estimated coordinates. Regarding to the GPS precise positioning method, OTL displacement can be observed relatively or absolutely which are reviewed in the following subsections.

#### 3.4.1 Relative OTL displacement

For the relative GPS positioning baseline solution, the estimated OTL displacement exhibits the periodic motion of the rover station with respect to a base station. To ensure a minimum OTL effect on the base station, it is conventional to select it far from coastlines. Khan and Tscherning (2001) and Khan and Scherneck (2003) processed GPS data for 49 days at two stations in Alaska: one at Fairbanks which is several hundred kilometres away from the coast and another on an island between Prince Williams Sounds and Gulf of Alaska, to estimate the relative OTL displacement. Their hourly relative estimated positions revealed about  $21.3 \pm 1.0$  mm amplitude and  $99.7 \pm 2.8^\circ$  phase lag for the differential M2 OTL vertical displacement which were close to the amplitude of 19.3 mm and phase lag of  $110.2^\circ$  computed

by forward modelling. Compared to the predicted 4.5 mm amplitude and  $-77^\circ$  phase lag for the north-south component, they estimated  $5.4 \pm 0.3$  mm and  $-106.3^\circ \pm 3.3^\circ$  with GPS. They also explained that the east-west relative OTL displacement was not large enough to be sensed with GPS measurements. In Chapter 6 of this thesis, OTL 3D displacement in Alaska will be investigated in more detail.

Yun *et al.* (2007) estimated relative positions for 12 coastal stations with respect to an inland station in 1-hour batches for 57 days in Korea. They observed about 1 mm RMS for the difference between the GPS-estimated and the predicted M2 vertical OTL displacement based on the NAO.99Jb regional tide model, but using the GOT002 and FES99 global ocean tide models increased the RMS to 3.6 mm and 4.6 mm, respectively. However this and the above-mentioned studies can only estimate relative OTL displacement, and it is preferred to use absolute estimation techniques, which will be described in the following subsection.

### **3.4.2 Absolute OTL displacement estimation**

OTL displacement at a single point can be determined by PPP which can be implemented in two ways. In the first approach, the tidal displacement and other parameters, i.e. receiver clock, phase bias, station coordinate, tropospheric delay, are estimated together in a (usually) daily batch adjustment (e.g., Allinson *et al.*, 2004; King *et al.*, 2005), whilst the second method uses sub-daily estimated coordinate solutions and then a spectral analysis. Similar to Penna *et al.* (2015), the first and second methods are termed harmonic estimation and kinematic PPP approach, respectively, for the rest of this document.

#### *Harmonic estimation*

The harmonic estimation method was initially used for VLBI data analysis (Schuh and Moehlmann, 1989; Sovers, 1994). In this approach, the observation adjustment model comprises a set of station coordinates, zenith tropospheric delay and gradients, receiver clock offset, ambiguity parameters, as well as the amplitudes and phase lags of the OTL displacement for some predefined constituents. For instance, if the M2, S2, N2, K2, K1, O1, P1 and Q1 tidal constituents were of interest, 48 tidal displacement parameters, i.e. 16 for each direction, with their covariance matrix are estimated in a daily data processing batch. The daily-based estimates of the tidal parameters may then be combined in a Kalman filter with a zero process noise, which is equivalent to a weighted averaging, to generate the final solution. In practice, to avoid any instability in the adjustment procedure, it is typical to consider a loose constraint for the tidal displacement amplitude (King, 2006). Regarding the frequency separation between the

interested tidal constituents, the length of the time series should satisfy the Rayleigh criterion (Godin, 1972):

$$|f_i - f_j| \times T > 1 \quad (3.13)$$

where  $f_i$  and  $f_j$  (in cycles/day) denotes the frequency of the adjacent constituents and  $T$  (in days) is the minimum length of the data span needed for the two constituents to be resolved. For example, to decouple K2 from S2, at least ~200 days of continuous observations are needed, and any gap in the coordinate time series increases the minimum length requirement.

The harmonic estimation approach has been employed in many OTL displacement studies. Schenewerk *et al.* (2001) used this technique in a relative positioning of 353 globally distributed sites which were processed using the PAGES software. They demonstrated smaller than 5 mm residual OTL displacement at 90% of the tested stations, although around the Gulf of Alaska with the complex coastline and large OTL vertical displacement (up to 50 mm), about 10-24 mm amplitude difference between the GPS-estimated OTL vertical displacement and those predicted by the forward modelling was obtained. Allinson *et al.* (2004) used the GIPSY software to apply harmonic estimation in PPP mode. By processing nearly 1000 days of GPS data, they found 0.5 mm agreement between the GPS-estimated and the forward modelled M2 OTL vertical displacement at station LEED in the British Isles. King *et al.* (2005) also processed GPS observations at 15 permanent stations (using 300 to 1500 days of continuous data) in Antarctica with GIPSY to estimate OTL displacement for assessing ocean tide model accuracy. Apart from the K2 and K1 constituents, they found submillimetre agreement between the GPS-estimated and modelled OTL displacement in Eastern Antarctica where the tides are accurately modelled. King (2006) and Yuan *et al.* (2009) demonstrated that phase ambiguity fixing in PPP can lead to a better decorrelation of the east-west, north-south and vertical components of the OTL displacement in the harmonic estimation approach, and they found around 1 mm discrepancy for the GPS-derived M2 displacement compared to the modelled one in Antarctica and Hong Kong, respectively. Yuan and Chao (2012) processed GPS observations for 1075 stations of the Plate Boundary Observatory (PBO) project network in western USA, with at least 1000 days data, by GIPSY. They observed submillimetre residual tidal displacement but with spatial patterns over 669 inland stations located more than 200 km away from coastline, and attributed it to EBT modelling error.

### *Kinematic PPP*

In the kinematic PPP approach, which is used in this thesis, a station position is estimated with sub-daily resolution, e.g. 1 hour, and then a concatenated coordinate time series is analyzed spectrally. Kinematic PPP has been employed for OTL displacement estimation in many studies. King (2006) used this approach to measure OTL displacement at the AMUN station near the South Pole where theoretical diurnal and semidiurnal EBTs are negligible ( $\sim 0.1$  mm). After processing GPS data from 1998.5 to 2003.5, it was found that the estimated amplitude of the M2 vertical component derived by kinematic PPP and harmonic approach differed from the modelled value by around  $-0.9$  mm and  $0.8$  mm, respectively. By processing 4 months of data from 1200 stations of the Japanese GEONET GPS network in the kinematic PPP mode, Ito *et al.* (2009) produced a high resolution map of the Earth's response field to the tidal force in Japan. The GPS-derived M2 vertical tidal displacement was on average 0.7% larger than its theoretical values. They inferred the observed discrepancy to an inelastic response of the Earth to the tidal forces. Ito and Simons (2011) processed one year of GPS data at 702 stations in western US, and found 1-2 mm differences with a regional pattern between the M2 OTL vertical displacement estimated by GPS observation and those predicted by forward modelling. After assuring the sensitivity of the GPS-estimated OTL displacement residuals to the physical parameters of the Earth's layers, i.e. bulk modulus, shear modulus, and density, they fitted a 1D Earth model for western US (called PBO-1D/M) to the observed residuals. Penna *et al.* (2015) investigated kinematic PPP accuracy for OTL displacement measurement by simulating a tidal displacement signal in GPS data processing with GIPSY. After tuning appropriate process noise for the time-variant parameters in kinematic PPP, they verified  $\sim 0.2$ - $0.4$  mm height accuracy for the technique to recover a pre-defined tidal synthetic signal for more than 20 stations in western Europe. They also suggested that at least 2.5 years of the GPS data with minimum 70% availability is required to recover the synthetic signal by around  $0.2$ - $0.4$  mm accuracy. Bos *et al.* (2015) focused on a 2-3 mm discrepancy revealed between GPS-derived and predicted M2 vertical OTL displacement in Cornwall and Brittany. They showed that the observed residuals are larger than the total uncertainty which may be induced by the GPS data processing, ocean tide modelling, and local variation in the crustal physical conditions, and also no elastic global Earth model could reduce the residuals to the kinematic PPP noise level. Thereby, they investigated the effect of the asthenosphere anelasticity, and realized that a reduction around 8-10% in the seismic shear modulus enabled the reduction of the OTL displacement residuals to the  $0.2$ - $0.4$  mm level. Martens *et al.* (2016) used GPS-derived position time series with 5 minutes resolution spanning up to 14 years in South America, to look at residual M2 vertical

OTL displacement. They concluded that the overall observed spatial pattern for the displacement residuals may be due to a deficiency in the global Earth's elastic model in that region. Wang *et al.* (2020) processed 96 GPS stations of GEONET Japan plus six IGS sites in the East China Sea region from 2013.0 to 2017.0, and observed 1-1.5 mm difference between the GPS-derived M2 OTL vertical displacements and those computed by forward modelling. Similar to Bos *et al.* (2015), they showed that using anelastic PREM-based Earth model, with about 8-10% smaller shear modulus compared to the elastic PREM model, can reduce the OTL displacement residuals to below 0.8 mm. In Table 3.1, the above literature review is summarized. As this table indicates, the M2 OTL displacement constituent has been of main interest for different studies possibly for two reasons: M2 has the largest magnitude among all constituents, and its spectrum is separate enough from the spurious periodicities in the GPS-estimated coordinate time series which are explained in Section 4.3. Hence, M2 OTL displacement is the focus of this thesis. However, due to the potential benefits of GLONASS data in OTL displacement investigation, which is discussed in the next section, N2, K2, K1, O1, P1 and Q1 constituents are also investigated in this study.

<b>Region</b>	<b>M2 OTL displacement residual</b>	<b>Reference</b>
South Pole	0.9 mm	King (2006)
Japan	1.0-2.0 mm	Ito <i>et al.</i> (2009)
western USA	1.0-2.0 mm	Ito & Simons (2011)
western Europe	Up to 2-3 mm at Cornwall and Brittany	Penna <i>et al.</i> (2015)
		Bos <i>et al.</i> (2015)
South America	0.5-1.0 mm	Martens <i>et al.</i> (2016)
East China Sea	1.0-1.5 mm	Wang <i>et al.</i> (2020)

Table 3.1: A summary of studies for the GPS-estimated OTL displacement with kinematic PPP approach

### 3.5 GLONASS enhancement for the OTL displacement measurement

GPS has been the only global navigation satellite system with long data archives and high quality satellite clock/orbit products until recent years. To the best of the author's knowledge, all published studies on GNSS-estimated OTL displacement have used GPS-only data.

Although the main lunar semidiurnal and diurnal tidal constituents have been accurately determined with GPS, the GPS satellites' mismodelling error repeats every 11.96 hour which is equal to the period of the K2 tidal constituent. Furthermore, the GPS satellites repeat their sky constellation, and consequently the multipath error at a ground station, every 23.93 hour which is identical to the period of the K1 tidal signal. Therefore, K2 and K1 OTL displacement cannot be reliably resolved by GPS-only data to enable OTL model validation, and a system with different satellite constellation characteristics may be helpful.

GLONASS was the second global navigation satellite system, with fully operational satellite availability since 2011. In addition to GPS and GLONASS, the European and Chinese global navigation systems, known as Galileo and BeiDou, respectively, are partially operational. Unlike other GNSSs, BeiDou comprises three different orbits: geostationary Earth orbit (GEO), inclined geosynchronous orbit (IGSO), and medium elevation orbit (MEO). A summary of the main constellation features of the four GNSSs is presented in Table 3.2.

GNSS type		Altitude <sup>a</sup> (km)	Inclination	Orbital period	Ground track repeat	Number of satellites	Number of orbital
GPS		20180	55°	11h58min	23h56min	24 <sup>b</sup>	6
GLONASS		19100	65°	11h16min	8 days	24 <sup>b</sup>	3
Galileo		23200	56°	14h04min	10 days	24 <sup>c</sup>	3
BeiDou (BDS-3)	GEO	36000	0°	23h56min	NA	5	1
	IGSO	36000	55°	23h56min	23h56min	5	3
	MEO	21500	55°	12h56min	8 days	27 <sup>c</sup>	3

Table 3.2: Some orbital features of GPS, GLONASS, Galileo, and BeiDou satellite systems (*a*: Mean (nominal) altitude, *b*: Number of operational satellites, *c*: Full operational capability is expected for 2020).

To inspect the potential impact of using multi-GNSS data in PPP, satellite global availability and geometrical DOP (GDOP) are considered here. To compute these parameters at a given point, the 3D coordinates of that point and the satellites are required. Whilst the former is definable by the users, IGS Multi GNSS Experiment (MGEX) satellite orbit information was employed for the latter. Further details of the satellite availability and GDOP computation are provided Appendix A.



Since 24 hour arc lengths of GNSS data are processed in kinematic PPP in this work, the quality of the GNSS-derived coordinate time series is affected by the observation redundancy and receiver-satellite geometrical configuration within the data arc. As a representative value for the abovementioned parameters, the mean number of available satellites and GDOP (for a  $10^\circ$  mask angle) were computed in two steps. In the first step, the hourly value of the parameters were calculated and then averaged throughout 24 hour for a global  $1^\circ \times 1^\circ$  grid. Afterwards, since the number of available satellites and GDOP are weakly correlated to the station longitude (except for BeiDou), the computed parameters in the first step were averaged within longitude bands (with a width of  $60^\circ$ ) per latitude. In Figure 3.2 and Figure 3.3, the mean number of available satellites and GDOP for GPS-only, GLONASS-only and their combinations with Galileo and BeiDou on 1<sup>st</sup> January 2018 are shown, respectively. To examine the effect of different ground track repeat period (shown in Table 3.2), the mean number of available satellites and GDOP for 10 consecutive days, i.e. maximum ground track repeat period (for Galileo), were computed, and similar pattern (not shown here) to Figure 3.2 and Figure 3.3 was found.

As can be seen in Figure 3.2, using combined GPS+GLONASS observation may increase the number of recorded data by around 60-100% compared to the GPS-only and GLONASS-only cases. Furthermore, the figure indicates that the majority of the world has access to more than 20 satellites when Galileo is added to the combined GPS+GLONASS. By including BeiDou to the three aforementioned GNSSs, the number of available satellites increases to more than 21-22 in almost all parts of the world. Figure 3.2 also confirms a better regional accessibility to BeiDou in Asia and Pacific as planned, i.e. for longitudes between  $60^\circ$  and  $180^\circ$ .

Figure 3.3 depicts that the satellite geometrical configuration for the GPS-only and GLONASS-only constellations is not ideal in many areas, i.e. mean GDOP around two or more. However, combining GPS and GLONASS reduces the mean GDOP to around 1.5 in almost all regions, and incorporating Galileo and BeiDou leads to further improvement. After accomplishment of the Galileo and BeiDou satellite mission in the upcoming years, a more distinct enhancement for the number of available satellites and GDOP is expected.

It should be noted that the GLONASS satellites' low availability and poor GDOP for regions within latitudes  $\sim 50^\circ S$  and  $\sim 50^\circ N$  (shown in Figure 2.2 and 2.3) may lead to a weak GLONASS-only kinematic PPP performance in that region. This issue is investigated in more detail in Chapter 5.

By increasing observation redundancy as well as improving the receiver-satellite geometrical configuration, using GPS+GLONASS+Galileo+BeiDou data offers the potential for an enhanced positioning solution. However, at the time of writing, IGS analysis centres only provide high rate 30 second precise clock correction for GPS and GLONASS satellites. Currently, 423 out of 506 stations of the IGS network are collecting GPS+GLONASS observation, and five IGS analysis centres, i.e. Centre for Orbit Determination in Europe (CODE), Natural Resource Canada (EMR), European Space Agency (ESA), German Research Centre for Geosciences (GFZ), Geodetic Observatory Pecny (GOP), and Wuhan University (WHU), are computing and disseminating both GPS and GLONASS precise satellite clock/orbit products. Hence, for a tidal displacement application, a more robust estimation of the GPS-detectable constituents with a combined GPS+GLONASS data is anticipated. Furthermore, due to the different satellite orbiting period of GLONASS, its data have the potential to estimate K2 and K1 tidal displacements more accurately than GPS.

In spite of the aforementioned advantages, a GLONASS-based PPP solution may have several challenges. First of all, GLONASS frequency division multiple access (FDMA) makes its integer phase ambiguity resolution complicated. Therefore, GLONASS-only and mixed GPS+GLONASS data processing are carried out in the float ambiguity solution in this thesis. Second, only a few IGS analysis centres, i.e. CODE, ESA and GFZ, are generating high rate 30 second GLONASS precise satellite clock information which is needed for accurate kinematic PPP. Furthermore, based on the IGS website ([www.igs.org/products](http://www.igs.org/products)), the accuracy of the GLONASS satellite final orbit products is about 0.5 cm poorer than the GPS ones. It also will be discussed in Chapter 5 that the poor availability of the GLONASS satellites for regions with latitude between  $50^{\circ}S$  and  $50^{\circ}N$  may reduce GLONASS-only PPP performance in some part of a PPP data processing arc.

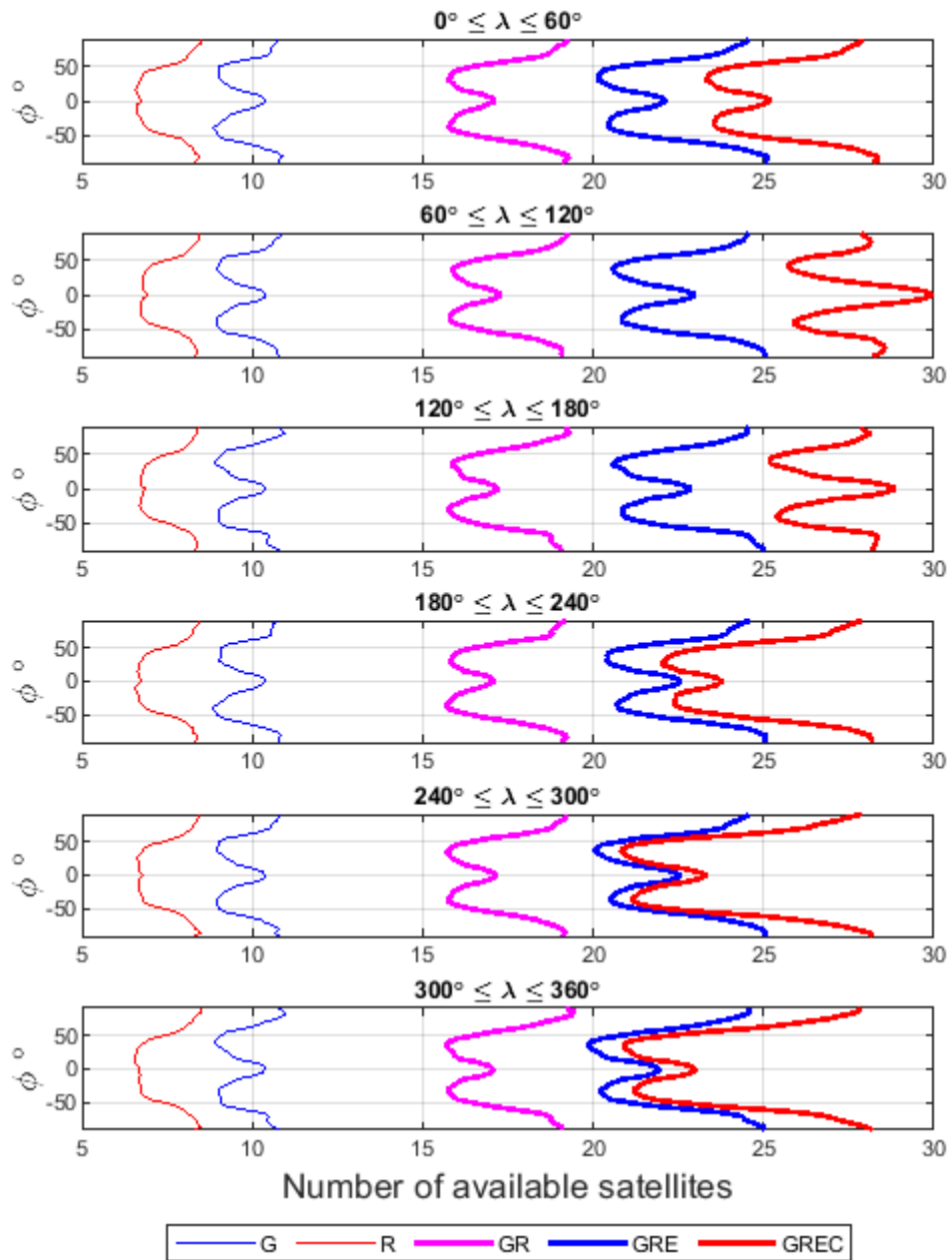


Figure 3.2: Latitude vs. mean number of available satellites (with elevation angle greater than  $10^\circ$ ) within different longitude bands on 1<sup>st</sup> January, 2018. Different constellations are labelled as: G for GPS, R for GLONASS, GR for GPS+GLONASS, GRE for GPS+GLONASS+Galileo, and GREC for GPS+GLONASS+Galileo+BeiDou.

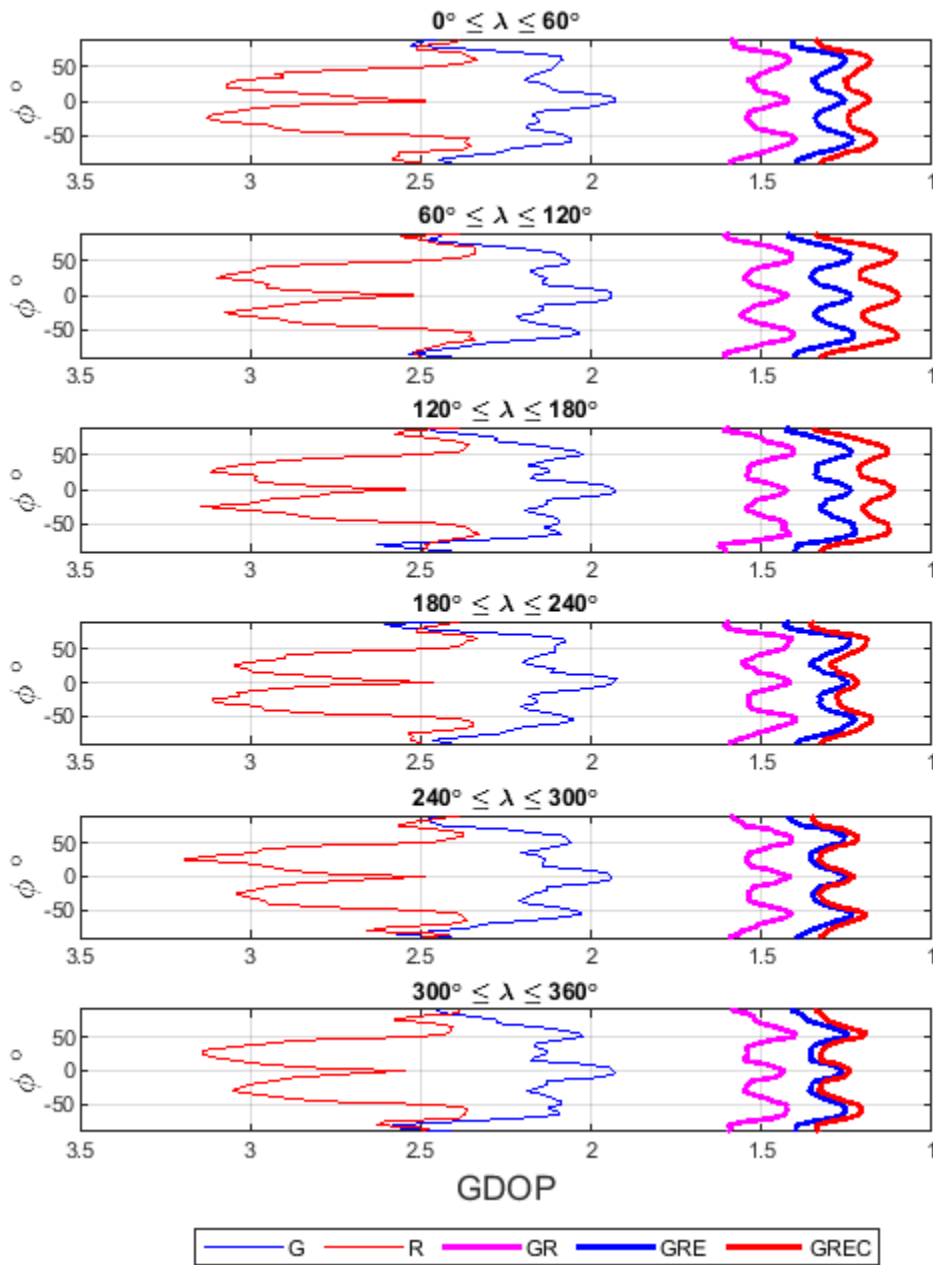


Figure 3.3: Similar to Figure 3.3 but for mean geometrical dilution of precision (GDOP).

### 3.6 Summary

This chapter has outlined GNSS positioning approaches which have obtained centimetre to millimetre level accuracy, and their application for the OTL displacement assessment is described. It has been explained that OTL displacement may be estimated with GNSS data either by incorporating the tidal harmonic signals in the observation model or a spectral analysis of the GNSS-estimated station coordinates which are modulated by the OTL displacement signals. For each method, relevant literature has been described including how submillimetre accuracy of GPS kinematic PPP is achieved for measuring M2 OTL displacement. Thereafter,

the main problem of GPS geodesy for K2 and K1 OTL displacement assessment is explained, and the potential role of GLONASS data for resolving the GPS problem for these two constituents as well as competing with GPS for the M2 OTL displacement estimation is explained. In Table 3.3, the estimability of the main diurnal and semidiurnal OTL displacement constituents with GPS and GLONASS data is summarized. To follow in Chapter 4, the theoretical background and practical steps of a multi-GNSS kinematic PPP are described. Chapter 4 also focuses on assessment for the multi-GNSS data processing, i.e. software verification, satellite product accuracy assessment, and tests describing process noise optimization.

<b>Constituent</b>	<b>Period (h)</b>	<b>Expected GPS/GLONASS contribution for OTL assessment</b>
M2	12.4206	Detectable by GPS and GLONASS
S2*	12.0000	Neither estimable by GPS nor by GLONASS
N2	12.6582	Detectable by GPS and GLONASS
K2	11.9673	Problems for GPS but potential for GLONASS
K1	23.9346	Problems for GPS but potential for GLONASS
O1	25.8203	Detectable by GPS and GLONASS

Table 3.3: Main tidal constituents considered in this thesis, and the expected capability of GPS/GLONASS to measure them

(\* OTL signal cannot be resolved from atmospheric tidal loading displacement).

## Chapter 4 Multi-GNSS kinematic precise point positioning with PANDA

### 4.1 Introduction

Although reduction in processing time of global GPS networks in relative positioning and reference frame maintenance were the initial motivation and objectives of PPP (Zumberge *et al.*, 1997), it has been used effectively for crustal deformation monitoring, precise orbit determination, precision farming, sensor positioning in support of seafloor mapping, marine construction, airborne mapping, atmospheric remote sensing (e.g., Bisnath and Gao, 2009). Several data analysis centres are cooperating under the IGS umbrella to produce precise satellite clock/orbit information. This information with the different levels of reliability and latency is freely available from the IGS product archives (Villiger and Dach, 2018). To reach centimetre level accuracy for PPP, very accurate IGS final products (especially the high-rate satellite clocks) and receiver-satellite centimetre level ranges are required. Hence, range error reduction, which will be discussed later in this chapter, has always been a high priority for the PPP community. It has also been shown that ambiguity fixing can improve PPP accuracy and precision (e.g., Ge *et al.*, 2007; Geng *et al.*, 2009; Bertiger *et al.*, 2010; Collins *et al.*, 2010; Loyer *et al.*, 2012). However, PPP with ambiguity resolution relies on the hardware delay information or needing a network of ground stations which makes it less practical. As well as accuracy enhancement, manipulation of the large normal equation systems in global and local parameter estimation has been a research interest in PPP studies (e.g., Ge *et al.*, 2006; Blewitt, 2008; Chen *et al.*, 2014; Gong *et al.*, 2017). Furthermore, by increasing the number of global navigation satellite systems from GPS to GPS, GLONASS, Galileo, and BeiDou, new thoughts for the accuracy improvement as well as latency reduction in PPP have emerged (e.g., Li *et al.*, 2015b; Geng *et al.*, 2016).

In this thesis, PPP is implemented with the PANDA software (Liu and Ge, 2003). Since its creation at Wuhan University around the year 2000, the PANDA software has been used for precise orbit determination (POD) of low earth orbits (LEOs) (Zhao *et al.*, 2011), IGS satellite clock/orbit preparation (Guo *et al.*, 2015), and multi-GNSS huge networks as well as PPP solution (Li *et al.*, 2015b). As PANDA is used for kinematic PPP, this chapter is devoted to theoretical as well as practical features of the kinematic PPP approach. Hence, within the following sections, PPP systematic errors and their treatment with PANDA are reviewed. Then, the kinematic PPP observational model, its normal equation manipulation, and a practical instruction to run PANDA in kinematic PPP are described. Next, the proficiency of the satellite

products from three IGS analysis centres with high rate GPS/GLONASS satellite clock information is evaluated, and the effect of the processing session length on the estimated coordinates around UTC midnight is investigated. Finally, after assessing PANDA's performance for recovering a simulated tidal displacement signal, station coordinate and ZWD optimum process noise values are determined.

## **4.2 Systematic errors in PPP**

From signal creation at a satellite oscillator to its reception by a receiver correlator, both pseudorange and carrier phase observables are contaminated with different types of errors. A thorough discussion of GNSS measurement errors is provided in several textbooks (e.g., Seeber, 2003; Hofmann-Wellenhof *et al.*, 2007; Teunissen *et al.*, 2017), and in the following subsections, a summary of the main systematic errors affecting PPP together with their treatment in PANDA is provided.

### **4.2.1 Phase centre offset (PCO)/ Phase centre variation (PCV)**

The measured satellite-receiver range should represent the geometrical distance between the antenna phase centres at the transmitter and receiver. However, the phase centre is not generally located at the antenna's geometrical/mechanical centre, and it is not even a fixed point. Furthermore, the position of a satellite's centre of mass is provided in the IGS orbit products, and the coordinates of a receiver's antenna reference point (ARP) is of interest in GNSS positioning. Therefore, it is typical to express the deviation of the phase centres from the aforementioned physical fixed points at the satellite and receiver as a superposition of a constant and a variable vector. The fixed vector, which is a long term average of the phase centre location, is known as the phase centre offset (PCO), and the temporary variation of the real phase centre from the PCO is called the phase centre variation (PCV). For example, the magnitude of PCO and PCV for GPS satellites may be 0.5-3 m and 5-15 mm, respectively, and for a receiver, PCO may change from 5 cm to 15 cm, whilst PCV can reach up to 3 cm (e.g. Kouba *et al.*, 2017).

For GNSS satellites as well as a variety of receiver antennas, PCO and PCV are determined through calibration techniques (Görres *et al.*, 2006), and they are accessible from the IGS in antenna exchange (ANTEX) format (Rothacher and Mader, 2003; Schmid *et al.*, 2005). In PANDA, after reading an IGS ANTEX file, the phase centre variation (correction) in the satellite-receiver line-of-sight direction is computed and removed from the carrier phase observation.

### 4.2.2 Instrumental delay

Both code and phase measurements are delayed in the satellite as well as the receiver's hardware. An absolute value for the pseudorange delay in satellites is not accessible, but their relative delay, which is called the differential code bias (DCB) is estimable by using global ionospheric map (Montenbruck *et al.*, 2014). For a GPS-based PPP, the receiver code bias can be absorbed as part of its clock parameter, but, for a GLONASS signal which is transmitted with its specific frequency per satellite, an additional term in the observation model should be considered.

The instrumental phase delay disturbs the integer nature of the phase ambiguity. In a PPP solution with integer ambiguity resolution, an instrumental phase bias correction, which is based on a previous GNSS double difference (DD) network adjustment, is applied, whilst for a PPP with float ambiguity solution, the phase delay is absorbed by the real-valued ambiguity parameter. For a multi-GNSS PPP without GLONASS data, the intersystem bias may be estimated as a constant parameter during a daily processing session. When GLONASS observations are incorporated, the inter-channel biases caused by the GLONASS satellite frequency division multiple access (FDMA) and intersystem bias are lumped together, and their resultant effect may be estimated. Either being estimated as an individual parameter or absorbed with the estimated real-valued phase bias, the instrumental phase delay and intersystem bias can be deemed constant during GNSS data processing.

### 4.2.3 Relativistic effect

The onboard satellite clock is moving with a speed around 3.9 km/s, and it is subject to a different gravitational field compared to the receiver clock at the ground station. Consequently, the frequency of the satellite clock oscillator is reduced which causes a dilation in the measured time. By assuming a circular orbit for the GNSS satellite, the relativistic effect on the satellite clock is computed, and a fractional rate offset is removed. However, the satellite orbit eccentricity and Earth's oblateness introduce a periodic dilation effect on the satellite clock, which is computed by:

$$\delta_{rel} = -\frac{2}{C^2} \boldsymbol{\rho}^s \cdot \dot{\boldsymbol{\rho}}^s \quad (4.1)$$

where  $\boldsymbol{\rho}^s$  is a location vector from the receiver to the satellite,  $\dot{\boldsymbol{\rho}}^s$  is the temporal rate of change of  $\boldsymbol{\rho}^s$ , and  $C$  is the speed of light. Furthermore, due to the Earth's rotation relative to an inertial frame, the receiver clock is also moving with a considerable speed, e.g. at the equator it is



around 0.5 km/s. Due to this motion, a receiver clock may be delayed by up to 10 ns after 3 hours of its installation, which is equivalent to around a 300 cm ranging error. The estimated receiver clock offset in PPP includes the relativistic error on the receiver's timing system. The rotating receiver clock is also biased by the Sagnac effect which can be computed with the following formula:

$$\delta_{rel} = \frac{1}{C} (\boldsymbol{\rho}^S \times \boldsymbol{\rho}_r) \cdot \boldsymbol{\omega}_e \quad (4.2)$$

where  $\boldsymbol{\rho}^S$  and  $\boldsymbol{\rho}^r$  are the satellite and receiver position vectors, respectively, and  $\boldsymbol{\omega}_e$  is the Earth's daily rotation vector. Finally, the satellite signal is also affected by space-time curvature. The correction to convert the curved path to a straight line is computed by:

$$\delta_{rel} = -\frac{2\mu}{C^2} \cdot \text{Ln} \left( \frac{\rho^S + \rho_r + \rho_r^S}{\rho^S + \rho_r - \rho_r^S} \right) \quad (4.3)$$

In PANDA, by extracting the satellite and receiver position vectors from the IGS satellite orbit and observation file, respectively, all relativistic errors are computed and removed from the raw data.

#### 4.2.4 Antenna phase windup

Due to the circular polarization of the GNSS signals, any rotation either for the transmitter or receiver antenna around their boresight axis alters the received carrier phase angle, and this is known as phase wind-up (Wu *et al.*, 1993). Even for a stationary GNSS receiver, phase wind-up is unavoidable as satellites have to change their attitude to maintain their solar panel and antenna towards the Sun and the Earth, respectively (Bar-Sever, 1996). To formulate phase wind-up ( $\omega$ ), the transmitter-receiver relative position unit vector ( $\mathbf{k}$ ) should be computed. Thereafter, by using the satellite attitude model, the phase wind-up can be computed through the following formulae:

$$\mathbf{D} = \mathbf{x} - \mathbf{k}(\mathbf{k} \cdot \mathbf{x}) + \mathbf{k} \times \mathbf{y} \quad (4.4)$$

$$\mathbf{D}' = \mathbf{x}' - \mathbf{k}(\mathbf{k} \cdot \mathbf{x}') + \mathbf{k} \times \mathbf{y}' \quad (4.5)$$

$$\boldsymbol{\gamma} = \mathbf{k} \cdot (\mathbf{D} \times \mathbf{D}') \quad (4.6)$$

$$\omega(rad) = sign(\gamma) \arccos\left(\frac{\mathbf{D}' \cdot \mathbf{D}}{\|\mathbf{D}'\| \cdot \|\mathbf{D}\|}\right) \quad (4.7)$$

where  $\mathbf{x}, \mathbf{y}$  are the receiver's unit vectors in the east-west and north-south directions, respectively, and  $\mathbf{x}', \mathbf{y}'$  are the satellite body unit vectors in a plane perpendicular to its boresight axis.

#### 4.2.5 Ionospheric delay

The ionized layer of the atmosphere, which is called the ionosphere, has a dispersive effect on the GNSS signal. In PPP, it is typical to use the ionospheric-free linear combination of dual-frequency observations, shown in the following equations, to remove the first order ionospheric error:

$$\Phi_{IF} = \frac{f_1^2 \Phi_{L1} - f_2^2 \Phi_{L2}}{f_1^2 - f_2^2} \quad (4.8)$$

$$R_{IF} = \frac{f_1^2 R_{P1} - f_2^2 R_{P2}}{f_1^2 - f_2^2} \quad (4.9)$$

where  $\Phi_{L1}$  and  $R_{P1}$  are the carrier phase and pseudorange observation at frequency  $f_1$ , respectively, and  $\Phi_{L2}$  and  $R_{P2}$  are the corresponding measurements at frequency  $f_2$ . For the ignored higher-order ionospheric delay, which may be around 1% of the total error, a negligible effect on the estimated station coordinates is expected.

#### 4.2.6 Tropospheric delay

The speed of the electromagnetic signal transmitted by satellites in the neutral part of atmosphere, which comprises the troposphere and stratosphere layers, is less than its speed in a vacuum, and it is called tropospheric delay. To correct this error in a range measurement, it is usual to compute the zenith hydrostatic delay (ZHD) and zenith wet delay (ZWD) components (Saastamoinen, 1972; Davis *et al.*, 1985), and then, by using an appropriate mapping function (e.g., Hopfield, 1969), the tropospheric total delay (TTD) in any direction is calculated:

$$ZHD = \frac{0.002277p}{1 - 0.00266 \cos(2\varphi) - 0.0028 \times 10^{-3}h} \quad (4.10)$$

$$ZWD = \left(\frac{1255}{T} + 0.05\right) \frac{0.002277e}{1 - 0.00266 \cos(2\varphi) - 0.0028 \times 10^{-3}h} \quad (4.11)$$

$$TTD(E) = m_{ZHD}(E).ZHD + m_{ZWD}(E).ZWD \quad (4.12)$$

In the above formulae,  $\varphi$  is the station latitude and  $h$  is its height, and  $T$ ,  $p$ , and  $e$  are the station temperature, hydrostatic as well as wet pressure, respectively, and  $E$  is the satellite elevation angle. Furthermore,  $m_{ZHD}$  and  $m_{ZWD}$  are mapping functions for ZHD and ZWD, respectively. In PANDA, the Global Mapping Function (GMF) (Boehm *et al.*, 2006) is used for computing  $m_{ZHD}$  and  $m_{ZWD}$ . For the temperature and pressure data, PANDA uses the global pressure and temperature (GPT2) model (Lagler *et al.*, 2013). Given surface pressure data with 0.3 mbar precision, ZHD can be modelled with 1 mm accuracy (Elgered *et al.*, 1991), whilst the ZWD computation depends on the tropospheric water vapor content, which is difficult to model from ground surface observations. Hence, the unmodelled part of the ZWD is usually estimated in PPP. Furthermore, to incorporate azimuthal asymmetry of the troposphere in the ranging error, troposphere horizontal gradients are also parametrized in PPP (Bar-Sever *et al.*, 1998).

Due to a strong correlation between station height and zenith tropospheric delay, particularly for observations collected at high elevation angles (e.g. Rothacher and Beutler, 1998), accurate modelling of the vertical OTL displacement is a prerequisite for the accurate GNSS estimation of tropospheric delay. In a simulation study, Dach and Dietrich (2000) showed that nearly 20% of the unmodelled vertical ocean tide loading displacement may propagate into the estimated tropospheric zenith path delay. They also demonstrated a 99% correlation between the estimated zenith tropospheric delay and a synthetic ocean tide loading displacement in the GPS data. Vey *et al.* (2002) computed zenith tropospheric delay differences with and without applying OTL corrections for a GPS baseline in Brittany. Their investigation showed that the estimated zenith tropospheric delay difference (from the two approaches) contains a signal with OTL displacement character.

#### **4.2.7 Site displacement**

The IERS Conventions (Petit and Luzum, 2010) define two groups of displacement for a station established at the Earth's surface: conventional and non-conventional. The conventional displacements (described below), which are mainly due to the Earth's tidal potential variation and its polar motion, can be modelled by standard geophysical models, and then be removed from geodetic observations. However, non-conventional displacements are induced by hydrological as well as non-tidal ocean and atmospheric loadings, and the IERS Conventions recommend not to include their modelled values in operational solutions that support products of the IERS. So, the non-conventional displacements are discarded here, and conventional ones are considered as follows.

EBT and OTL displacements are the first part of the conventional displacements. In Chapter 2, the EBT and OTL modelling with their maximum range and expected modelling error were discussed. Atmospheric pressure oscillations, which are caused by the solar heating of the atmosphere, act as loading with tidal S1, S2 and higher harmonic periods, and displace the solid Earth by up to 3 mm. The IERS Conventions recommend the model proposed by Ray and Ponte (2003) to calculate the atmospheric loading displacement. Earth's polar motion, which is mainly composed of the ~14-month Chandler Wobble and annual variations, changes the centrifugal force on the Earth's surface. As a result, geodetic stations displace with similar periods to the polar motion by up to 25 mm which is the pole tide. As described in the IERS Conventions, the pole tide is modelled by the Earth's daily rotation speed, mean and instantaneous pole location, and Love numbers. The centrifugal force variation caused by the polar motion also generates an ocean tide loading which may displace the solid Earth by up to 1.8 mm (Desai, 2002).

### **4.3 Spurious periodicities in GNSS-derived time series**

The GNSS satellite constellation and systematic errors described in Section 4.2 may introduce some periodic signals in the GNSS-estimated coordinate time series. In a simulation, Penna and Stewart (2003) addressed the effect of an unmodelled OTL displacement on annual and semi-annual constituents of the GPS-estimated height time series. Stewart *et al.* (2005) have analytically explained the propagation of the systematic errors into the GPS-derived station coordinate. In that study, it is shown that truncation of the non-linear terms in the GPS range observation equation causes some spurious periodic signals in the station coordinate time series when periodic systematic errors are ignored. It was also demonstrated that the period and amplitude of the spurious signals are dependent on: period/amplitude of the input signal; period/amplitude of the satellite orbit; location of the ground station relative to satellites; and length of the observation processing session. The abovementioned GPS simulation and theoretical prediction of the spurious signal in the GPS-estimated time series are confirmed by Penna *et al.* (2007) who verified spurious signals in fortnightly, semi-annual and annual period caused by unmodelled M2, S2, K1, and O1 tidal displacement. Tregoning and Watson (2009) have demonstrated that deficiency in the atmospheric tidal load modelling may cause two periodic artefacts with a period of one and one-half of the GPS draconitic year, i.e. the time period required to repeat the satellite constellation with respect to the Sun, in the GPS-estimated time series. It is also addressed by King and Watson (2009) that harmonics of the GPS draconitic year may arise in the estimated ground station coordinates due to multipath and the time-variable satellite constellation. Rodriguez *et al.* (2012) showed that Earth radiation pressure mismodelling introduces perturbation in the GPS satellite orbit with a repeat period of

the GPS draconitic year and its harmonics. A similar study by Griffiths and Ray (2012) indicated that the effect of the mismodelled sub-daily Earth orientation parameters (EOP) tides enters in the IGS orbits with harmonic signal at the GPS draconitic year and its overtones. Both the abovementioned orbit mismodelling periodicities are manifested in the ground station coordinate time series estimated by GPS observation.

It should be noted that GNSS-estimated coordinate time series, especially in the PPP method, may contain some periodic signals with a period of the GNSS satellite constellation change (relative to the ground station). For instance, as shown by Abraha *et al.* (2017), there is a signal with a period of the GLONASS satellites ground track revisit period, i.e. 8 days, in the coordinate time series estimated by GPS-only, GLONASS-only, and combined GPS+GLONASS data when GPS and GLONASS satellite products, which are fixed in PPP, are computed from the combined GPS+GLONASS data.

#### 4.4 Observation modelling in PPP

To perform PPP for a dual frequency GNSS receiver, the ionospheric-free combination of the pseudorange ( $p_{r,IF}^S$ ) and phase ( $\varphi_{r,IF}^S$ ) observables, which are corrected for the systematic errors beforehand, is constructed. Then, the following equations for the observation modelling are used:

$$p_{r,IF}^S = \rho_r^S(x_r, y_r, z_r) + c \cdot dt_r + m_{ZTD}(E) \cdot ZTD + m_{ZTD}(E) \cdot [G_N \cdot \cos(A) + G_E \cdot \sin(A)] \quad (4.13)$$

$$\varphi_{r,IF}^S = \rho_r^S(x_r, y_r, z_r) + c \cdot dt_r + m_{ZTD}(E) \cdot ZTD + m_{ZTD}(E) \cdot [G_N \cdot \cos(A) + G_E \cdot \sin(A)] + \lambda_{IF} \cdot b_{IF} \quad (4.14)$$

where  $\rho_r^S$  is the receiver-satellite geometric distance,  $x_r, y_r, z_r$  are the coordinates of the GNSS station,  $dt_r$  is the receiver clock error,  $ZTD$  is the zenith total tropospheric delay,  $G_N$  and  $G_E$  are the tropospheric horizontal gradient in the north-south and east-west directions, respectively, and  $b_{IF}$  is the phase bias which includes the instrumental delay. Since satellite clock/orbit parameters are assumed to be known, they are not presented in the above equations.

GLONASS data processing is slightly complicated by the inter-frequency channel bias (IFCB). For precise phase positioning, the fractional part of the IFCB, which differs between satellites and may reach up to 5 cm, makes GLONASS phase ambiguity fixing nontrivial. In GLONASS-only PPP with a float ambiguity solution, the IFCB is absorbed with the phase bias and can be

ignored. On the other hand, in a combined GPS+GLONASS PPP, the GPS-GLONASS system time difference needs to be estimated (Cai and Gao, 2007).

#### 4.4.1 *Satellite clock/orbit interpolation*

The reliability of PPP is strongly dependent on the accuracy of satellite clock and orbit information. For the IGS analysis centres, it is usual to generate satellite orbit information at 15 min temporal resolution which is much larger than the typical 30 second data collection rate at a ground station. Even for satellite clock corrections with 30 second or higher resolution, their time tag may differ from the signal transmission instant (which is used to construct the PPP observation equation). Hence, interpolation of the satellite clock/orbit information is unavoidable in PPP software packages.

In PANDA, to interpolate the satellite clock correction to time  $t$ , two points at either side of  $t$  are selected, and then a linear interpolation is applied. However, each component of the satellite 3D coordinates is interpolated after fitting a high degree polynomial to a few points of the orbits at either side of the interested time. Lagrange interpolation, which is one type of polynomial fitting and is employed in PANDA, is explained here.

The Lagrange polynomial with degree  $n-1$ , which passes through  $n$  points  $(x_1, y_1), \dots, (x_n, y_n)$ , is a summation of  $n$  polynomials with degree  $n-1$ :

$$P(x) = \sum_{i=1}^n P_i(x) \quad (4.15)$$

where each polynomial  $P_i(x)$  is defined as:

$$P_i(x) = y_i \cdot \prod_{\substack{j=1 \\ j \neq i}}^n \frac{x - x_j}{x_i - x_j} \quad (4.16)$$

After constructing the Lagrange polynomial, the value of the parameter  $y$  at point  $x^*$  is computed by substituting  $x = x^*$  in the polynomial.

In PANDA, satellite orbit files for three consecutive days are imported and then merged into one arc. Then, to extract the satellite coordinates at the signal transmission time, a nine-degree Lagrange polynomial is fitted to 10 points, i.e. five points at either side of the interested point.

#### 4.4.2 Observation least-squares adjustment

In kinematic PPP, the non-ambiguous pseudorange measurement, with metre to decimetre-level precision, is used to compute initial values for the station coordinates, receiver clock correction and phase biases. Furthermore, by using the pseudorange observation, a signal transmission time from a satellite is calculated. As the observation model relies on the satellite clock/orbit correction information which are interpolated to the time of signal transmission, any error in computing the signal transmission time introduces large uncertainty in PPP, e.g.  $10^{-3}$  s uncertainty in the time of transmission computation may be equivalent to nearly 3.9 m error for the satellite orbit interpolation. In PANDA, the signal arrival time  $t_{arriv}$  and receiver approximate coordinates at the time of signal arrival  $\boldsymbol{\rho}_r(t_{arriv})$  are extracted from the observation RINEX<sup>2</sup> file. Then, to estimate the time of transmission  $t_{trans}$  and the satellite position at that time  $\boldsymbol{\rho}^s(t_{trans})$ , the following simultaneous equations are solved in an iterative approach:

$$\rho_r^s = |\text{Rot}(t_{arriv} - t_{trans}) \cdot \boldsymbol{\rho}^s(t_{trans}) - \boldsymbol{\rho}_r(t_{arriv})| \quad (4.17)$$

$$t_{trans} = t_{arriv} - \frac{\rho_r^s}{c} \quad (4.18)$$

In Equation 4.17,  $\text{Rot}(t_{arriv} - t_{trans})$  is a rotation matrix which applies the Earth's rotation to convert the satellite position vector at the time of signal transmission to its location at the time of signal arrival. To solve the above system, an initial value of 20000 km is selected for  $\rho_r^s$ , and after a few iterations,  $t_{arriv}$  converges.

To enable parameter estimation with few centimetre precision in PPP, the phase observation model (Equation 4.14), must be used in the least squares adjustment. Matrix representation of the linearized observation equation for the ionospheric-free phase data for S satellites at epoch  $i$  is shown below:

---

<sup>2</sup> Receiver Independent Exchange (RINEX) Format

$$\begin{bmatrix} \delta\varphi_1 \\ \vdots \\ \delta\varphi_S \end{bmatrix}_i = \begin{bmatrix} [u_{r,x}^s & u_{r,y}^s & u_{r,z}^s & 1 & m_{ZTD} & m_{ZTD} \cdot \cos(A) & m_{ZTD} \cdot \sin(A) & 1 & 0 \cdots 0]_1 \\ \vdots \\ [u_{r,x}^s & u_{r,y}^s & u_{r,z}^s & 1 & m_{ZTD} & m_{ZTD} \cdot \cos(A) & m_{ZTD} \cdot \sin(A) & 0 & 0 \cdots 1]_S \end{bmatrix}_i \begin{bmatrix} \delta x_r \\ \delta y_r \\ \delta z_r \\ c \cdot \delta dt_r \\ \delta ZTD \\ \delta G_N \\ \delta G_E \\ \lambda \cdot \delta b_1 \\ \vdots \\ \lambda \cdot \delta b_S \end{bmatrix}_i \quad (4.19)$$

Defining  $\delta l_i$  as the difference between the observed and expected observation,  $\delta x_i$  as the correction to the initial value of the station coordinates,  $ZTD$  and receiver clock (which vary per epoch),  $\delta y$  for the phase bias corrections which are constant within a phase connected arc, and  $A_i$  and  $I$  for the design matrix relevant to  $\delta x_i$  and  $\delta y$ , respectively, Equation 4.19 can be rearranged as:

$$\delta l_i = [A_i \ I] \cdot \begin{bmatrix} \delta x_i \\ \delta y \end{bmatrix} \quad (4.20)$$

To solve the above equation using least squares, observation weights should be defined. By assuming no covariance between individual phase observables, and implementing variance propagation on Equation 4.8, the variance of an ionospheric-free phase observable is found:

$$\sigma_{\Phi_{IF}}^2 = \left( \frac{f_1^2}{f_1^2 - f_2^2} \sigma_{\Phi_1} \right)^2 + \left( \frac{f_2^2}{f_1^2 - f_2^2} \sigma_{\Phi_2} \right)^2 \quad (4.21)$$

In PANDA, 2 mm standard error for the phase data uncertainty (collected from a satellite located at the observer's zenith) is defined. It is also assumed that undifferenced measurements are uncorrelated. However, due to the variable nature of the atmospheric delay, multipath and PCV errors in different elevation angles, it is unrealistic to consider equal error to all measurements.

The signal to noise ratio (SNR) of each GNSS measurement, which can sometimes be found in the observation RINEX file, is the best indicator for the quality of the data, but SNR cannot be easily applied for the observation variance computation (e.g. Lou *et al.*, 2014). Hence, it is typical to relate observation variance to the satellite elevation angle ( $E$ ) (e.g. Jin *et al.*, 2014). For instance, in the Bernese GNSS software, it is recommended to scale phase observation variance with  $1/\sin^2(E)$ . In PANDA, for observations which are recorded from satellites with



elevation angle less than  $30^\circ$ , following Gendt *et al.* (2003), the user-defined observational error is scaled by  $1/2 \sin(E)$ . The variance-covariance matrix of the ionospheric-free observation and their weight in PANDA are constructed as:

$$Q_i = \text{diag}\left(\sigma_{\Phi_{IF,1}}^2, \sigma_{\Phi_{IF,2}}^2, \dots, \sigma_{\Phi_{IF,S}}^2\right) \quad (4.22)$$

$$W_i = Q_i^{-1} \quad (4.23)$$

Therefore, the normal equations (NEQ) for the overdetermined system shown in Equation 4.20 can be written in the following form:

$$\begin{bmatrix} A_i^t \cdot W_i \cdot A_i & A_i^t W_i \\ W_i A_i & I \end{bmatrix} \cdot \begin{bmatrix} \delta \mathbf{x}_i \\ \delta \mathbf{y} \end{bmatrix} = \begin{bmatrix} A_i^t \cdot W_i \cdot \delta \mathbf{l}_i \\ W_i \cdot \delta \mathbf{l}_i \end{bmatrix} \quad (4.24)$$

In PANDA PPP post-processing, recursive least squares is employed, and parameter estimation is implemented through two steps: elimination and backward substitution. The estimated parameters in the elimination/substitution algorithm and a batch least squares adjustment are equivalent, but the former deals with smaller matrices which makes it a computationally efficient method. For instance, kinematic PPP in a daily session with GPS-only data (collected with 30 second resolution), may include around 30,000 ionospheric-free phase measurements and 12,000 unknown parameters comprising epoch-dependent station coordinates and receiver clock corrections, hourly tropospheric corrections, and phase biases in the phase-connected arcs. Hence, the normal equation matrix construction and its inversion is a time demanding task for the above example. In recursive least squares, on the other hand, the number of rows/columns of the normal equation matrix is equivalent to the number of unknown parameters only at each epoch.

In the first step of the elimination/substitution algorithm, by rearranging Equation 4.24,  $\delta \mathbf{x}_i$  is eliminated, and the equations system will be written only in terms of  $\delta \mathbf{y}$ . Then, the NEQ at epoch  $i+1$ , which is constructed by updating  $i$  to  $i+1$  in Equation 4.24, will be combined with the eliminated NEQ at epoch  $i$  (ENEQ<sub>*i*</sub>). Thereafter, the augmented NEQ at epoch  $i+1$  (ANEQ<sub>*i+1*</sub>) undergoes an elimination, and by removing  $\delta \mathbf{x}_{i+1}$ , the eliminated NEQ at epoch  $i+1$  (ENEQ<sub>*i+1*</sub>) will be obtained. This NEQ contains information for  $\delta \mathbf{y}$  which is gathered from the two epochs. The elimination procedure continues to the last epoch of the session, and hence, the eliminated NEQ in the last epoch (ENEQ<sub>last</sub>) can be used to estimate all phase biases in the processing session. It is important to realize that, if there were a cycle slip for satellite  $k$  at epoch

$j$ , the arrays of  $\text{ENEQ}_j$  (which contains information for this satellite) will be stored in a temporary file, and from epoch  $j+1$ , those arrays will be re-initialized. Moreover, after finding a new satellite, its phase bias parameter will be placed to a new row and column of the NEQ. The NEQ manipulation during each elimination step is explained in more detail in Appendix B. The estimated phase bias within each phase connected arc in the elimination method benefits all observations and satellite-receiver geometry changes through the arc.

After estimating all phase biases ( $\widehat{\delta\mathbf{y}}$ ), they are substituted to Equation 4.20, and a new set of observation equations in terms of station coordinates, tropospheric parameters and the receiver clock are constructed:

$$\delta\mathbf{l}_i - \widehat{\delta\mathbf{y}} = \delta\mathbf{l}_i^* = A_i \cdot \delta\mathbf{x}_i \quad (4.25)$$

To solve the above equation for the entire processing session, a recursive rather than a batch least squares adjustment is used in PANDA. In addition to its computational efficiency, the recursive approach can exploit filtering equations when appropriate dynamic models for the time variant parameters are presumed. PANDA implements Kalman Filtering in two steps to estimate  $\delta\mathbf{x}_i$  at each epoch. Firstly, the state of the system at the previous epoch ( $\delta\mathbf{x}_{i-1}$ ) is used in the dynamic model to predict the current state ( $\widehat{\delta\mathbf{x}}_i^-$ ). For the initial state, some approximate values, e.g. approximate station coordinates from the observation RINEX file, and zero for the tropospheric parameters and receiver clock offset, are used. In the second step, by combining the predicted state with the new observations, the updated current state  $\widehat{\delta\mathbf{x}}_i^+$  is computed. Clearly, the predicted and updated parameter covariance matrix is also computed in each epoch.

In PANDA, all phase bias parameters for the whole session are estimated at the last epoch of the forward elimination ( $i=N$ ). Then, backward substitution in the form of Kalman filtering starts from the last epoch towards the first data epoch ( $i=1$ ). Hence, the last epoch state vector ( $\widehat{\delta\mathbf{x}}_N$ ) and its covariance matrix ( $C_{\widehat{\delta\mathbf{x}}_N}$ ) are estimated in a classical least squares adjustment:

$$\widehat{\delta\mathbf{x}}_N = (A_N^t \cdot W_N \cdot A_N)^{-1} \cdot A_N^t \cdot W_N \cdot \delta\mathbf{l}_N^* \quad (4.26)$$

$$C_{\widehat{\delta\mathbf{x}}_N} = (A_N^t \cdot W_N \cdot A_N)^{-1} \quad (4.27)$$

Next, by knowing the linear or linearized dynamic model in the form of a transition matrix ( $\Phi_{N-1,N}$ ) and its imperfectness ( $Q_N$ ), the predicted state vector ( $\widehat{\delta\mathbf{x}}_{N-1}^-$ ) as well as its covariance matrix ( $C_{\widehat{\delta\mathbf{x}}_{N-1}^-}$ ) at epoch  $N-1$  are calculated:

$$\widehat{\delta x}_{N-1}^- = \Phi_{N-1,N} \widehat{\delta x}_N \quad (4.28)$$

$$C_{\widehat{\delta x}_{N-1}^-} = \Phi_{N-1,N}^t C_{\widehat{\delta x}_N} \Phi_{N-1,N} + Q_N \quad (4.29)$$

Then, observations at epoch  $N-1$  are used to compute the estimated state vector ( $\widehat{\delta x}_{N-1}^+$ ) and its covariance matrix ( $C_{\widehat{\delta x}_{N-1}^+}$ ) at this epoch:

$$\mathbf{v}_{N-1} = \delta \mathbf{l}_{N-1}^* - A_{N-1} \widehat{\delta x}_{N-1}^- \quad (4.30)$$

$$C_{\mathbf{v}_{N-1}} = C_{\delta \mathbf{l}_{N-1}^*} + A_{N-1}^t C_{\widehat{\delta x}_{N-1}^-} A_{N-1} \quad (4.31)$$

$$G_{N-1} = C_{\widehat{\delta x}_{N-1}^-} A_{N-1}^t C_{\mathbf{v}_{N-1}} \quad (4.32)$$

$$\widehat{\delta x}_{N-1}^+ = \widehat{\delta x}_{N-1}^- + G_{N-1} \mathbf{v}_{N-1} \quad (4.33)$$

$$C_{\widehat{\delta x}_{N-1}^+} = (I - G_{N-1} A_{N-1}) C_{\widehat{\delta x}_{N-1}^-} \quad (4.34)$$

Equations 4.30 to 4.34 are recursively updated to estimate the state vector at each epoch. As can be seen from the above formulae, an explicit form of the transition matrix ( $\Phi_{i,i+1}$ ) and its uncertainty ( $Q_i$ ) should be defined. For a permanent GNSS ground station, it is typical to assume a random walk model for the position and tropospheric variation, whilst for the receiver clock disturbance, a white noise process is used in PANDA. Based on this assumption, the transition matrix ( $\Phi_{i,i+1}$ ) and its covariance ( $Q_i$ ) for the time varying parameters can be written as:

$$\Phi_{i,i+1} = \text{diag}([1 \ 1 \ 1 \ 0 \ 1 \ 1 \ 1]) \quad (4.35)$$

$$Q_i = \text{diag}([s_x^2 \cdot \Delta t \ s_y^2 \cdot \Delta t \ s_z^2 \cdot \Delta t \ s_{clk}^2 \ s_{ZWD}^2 \cdot \Delta t \ s_{G_N}^2 \cdot \Delta t \ s_{G_E}^2 \cdot \Delta t]) \quad (4.36)$$

where  $\Delta t$  is the time interval between consecutive recorded data, and  $s_k$  where  $k: x, y, z, clk, ZWD, G_N, G_E$  is the process noise. As will be shown in Chapter 5, for a continuously operating reference station which is far from active tectonic areas, a coordinate process noise of around  $1-3 \text{ mm}/\sqrt{s}$  may be suitable. On the other hand, ZWD varies more smoothly and it is typical to estimate it every 30 or 60 min. The very slow temporal variation

of the troposphere azimuthal asymmetry are deemed constant in the PANDA processing, and to cover receiver clock potential violent variation, a clock process noise of  $3 \text{ ms}/\sqrt{s}$  is assigned.

#### 4.5 Running kinematic PPP in PANDA

PANDA, which is written in FORTRAN 90, is a combination of binary programs which need to be run with some time conversion programs. To have automatic and manageable PANDA runs, it is recommended to put all required commands in a LINUX shell script. Running kinematic PPP with PANDA starts with reading preliminary files, e.g. a list of the important directory addresses, observations and their uncertainties, satellite clock/orbit information, and tables of the IERS recommended models. Afterwards, data preprocessing removes outliers and detects cycle slips. Thereafter, parameter estimation is executed, followed by post-fit residual checks to find undetected outliers and cycle slips. The parameter estimation and residual assessment steps can be iterated. In the following subsections, some key practical details of a PANDA run will be outlined.

##### 4.5.1 Preparation of preliminary information

As its input, PANDA reads several files which are listed in Table 4.1. Furthermore, for 24 hour data processing of a daily observation file, it merges three consecutive daily orbit/clock information files to enable an accurate interpolation of the satellite positions near to the boundaries of the middle day. It also converts the merged file format from SP3 to a PANDA local format. For the files whose formats are not mentioned in Table 4.1, PANDA local format is used. More details for the local format of input/output files in PANDA are in Appendix B.

File Name	Application
ssssddd0.yyo	Raw GNSS observation in RINEX format. <ul style="list-style-type: none"> <li>▪ ssss: 4 character identifier for the station</li> <li>▪ ddd: 3 digit day of year</li> <li>▪ yy: 2 digits year, e.g. 15 for year 2015</li> </ul>
accwwwd.sp3 accwwwd.clk_30s	Precise satellite orbit/clock products in IGS SP3 format. <ul style="list-style-type: none"> <li>▪ acc: 3 letters IGS analysis centre name</li> <li>▪ www: 4 digits GNSS week number</li> <li>▪ d: 1 digit day of week</li> </ul>

file_table	Directory address of the IERS recommended models used to correct systematic error.
gnss.cfg	The user-defined settings for the session length, observation type, etc.
session.obj	Information for the dynamic model, PCV model, tropospheric mapping function, observation and initial state vector uncertainty.
gnss.sit	Station approximate coordinates.
Antnam	List of the receivers' antenna names with PCO/PCV information in the IGS ANTEX file.
igs14.atx	PCO/PCV information for different types of receiver/satellite antenna (IGS ANTEX format).
gpt2_5.grd	Temperature/pressure information to be used in the GPT2 model.
leap.sec	Leap second instances which are needed for TAI to UTC conversion.
Oceanload	Modelled OTL displacement coefficients in BLQ format.
poleut1	Daily information of the pole coordinate and UT1 in IGS format which are needed to transform the terrestrial to celestial reference system.
ut1t10	Zonal tide correction on the UT1 which is applicable for terrestrial to celestial frame transformation
panda_file_name	File name conventions in PANDA
p1c1bias.hist	DCB correction history

Table 4.1: Preliminary files for a PPP run in PANDA

#### ***4.5.2 Pre-processing data quality assessment and cycle slip detection***

Estimated parameters from a least squares adjustment must be free from outliers, and in kinematic PPP the effect of an undetected blunder propagates through the whole PPP session if using recursive least squares. Pre-process data cleaning is therefore essential, notably to isolate and detect cycle slips.

Both outlier and cycle slip detection in PANDA are based on the TurboEdit algorithm (Blewitt, 1990), which uses the Melbourne-Wübbena (Melbourne, 1985; Wübbena, 1985) and geometry-free (e.g., Hofmann-Wellenhof *et al.*, 2007) observation linear combinations at each data collection epoch. TurboEdit is suitable where a dual frequency receiver is available and ionospheric conditions are smooth. By computing the difference between the Melbourne-Wübbena and geometry-free combinations between each consecutive epoch, unusual jumps e.g. a difference larger than one carrier phase wavelength, may be found by TurboEdit. Any single jump with smooth phase bias variations at either side is considered a cycle slip, and other types of jump are assumed to be outliers. In PANDA, the data quality assessment is performed by the ‘qc’ program which can be used with the following form:

```
qc -file_table -option1 argument1 -option2 argument2 ...
```

The ‘file\_table’ is described in Table 4.1, and the options and their arguments can be seen in the terminal window by typing the ‘qc’ command. The output of the ‘qc’ program is a file with a ‘log’ prefix which contains information for the start/end times of each satellite phase connected arc, as well as deleted data arcs. The following example shows the most important options/arguments for a ‘qc’ run:

```
qc -file_table -short 600 -gap 400 -lc_check no -elev 10 -renew
```

In this example, observations in phase connected arcs which are shorter than 600 s will be removed. Also, if the time interval between two consecutive points for a satellite is greater than 400 s, ‘qc’ considers them as two separate arcs with different phase ambiguities. In this example, to detect cycle slips and outliers, ‘qc’ programs uses geometry-free and wide-lane combinations and discards the ionospheric-free combination, as ‘lc\_check’ option with ‘no’ argument is used. Furthermore, observations with an elevation angle less than 10° are not incorporated in the data quality check. To overwrite the result of each ‘qc’ run to a previous output, the ‘renew’ option is added in the above example.

### 4.5.3 *Parameter estimation*

By running the ‘lsq’ program, PANDA estimates the unknown parameters in kinematic PPP mode. This program can be used with the following syntax:

```
lsq -file_table
```

Consequently, a file with a ‘res’ prefix will be generated which contains the estimated PPP parameters and the observation post-fit residuals.

#### **4.5.4 *Post-processed data snooping***

To find cycle slips and blunders which were undetected within the ‘qc’ program, the ‘edtres’ program is executed on the post-fit observation residuals. This program can be run in the form below to update a current observation ‘log’ file:

```
edtres -file_table -res res.file -option1 argument1 ...
```

Similar to ‘qc’, a complete description for the options and arguments of ‘edtres’ can be seen by typing ‘edtres’ in LINUX terminal. However, the most standard syntax to run the program is:

```
edtres -file_table -res res.file -jump 50 -bad 50 -nshort 600
```

For this example, any inter-arc jump larger than 50 mm for the phase data is considered a cycle slip, and a jump bigger than 50 mm for an isolated point is assumed to be an outlier. In addition, arcs shorter than 600 s will be deleted.

#### **4.5.5 *Output files preparation***

Since the files output by the ‘lsq’ program contain a variety of information on the estimated parameters, observation post-fit residuals, involved satellites, etc., it is useful to prepare individual files for each class of unknown parameters. For instance, the ‘extxyz’ and ‘extztd’ programs extract the receiver coordinate and tropospheric zenith total delay (ZTD), respectively.

#### **4.5.6 *A summary of PPP in PANDA***

Different steps of the PPP implementation in PANDA, which were described in previous subsections, are summarized in Figure 4.1. In this figure, the program which is responsible for running each step is mentioned in brackets.

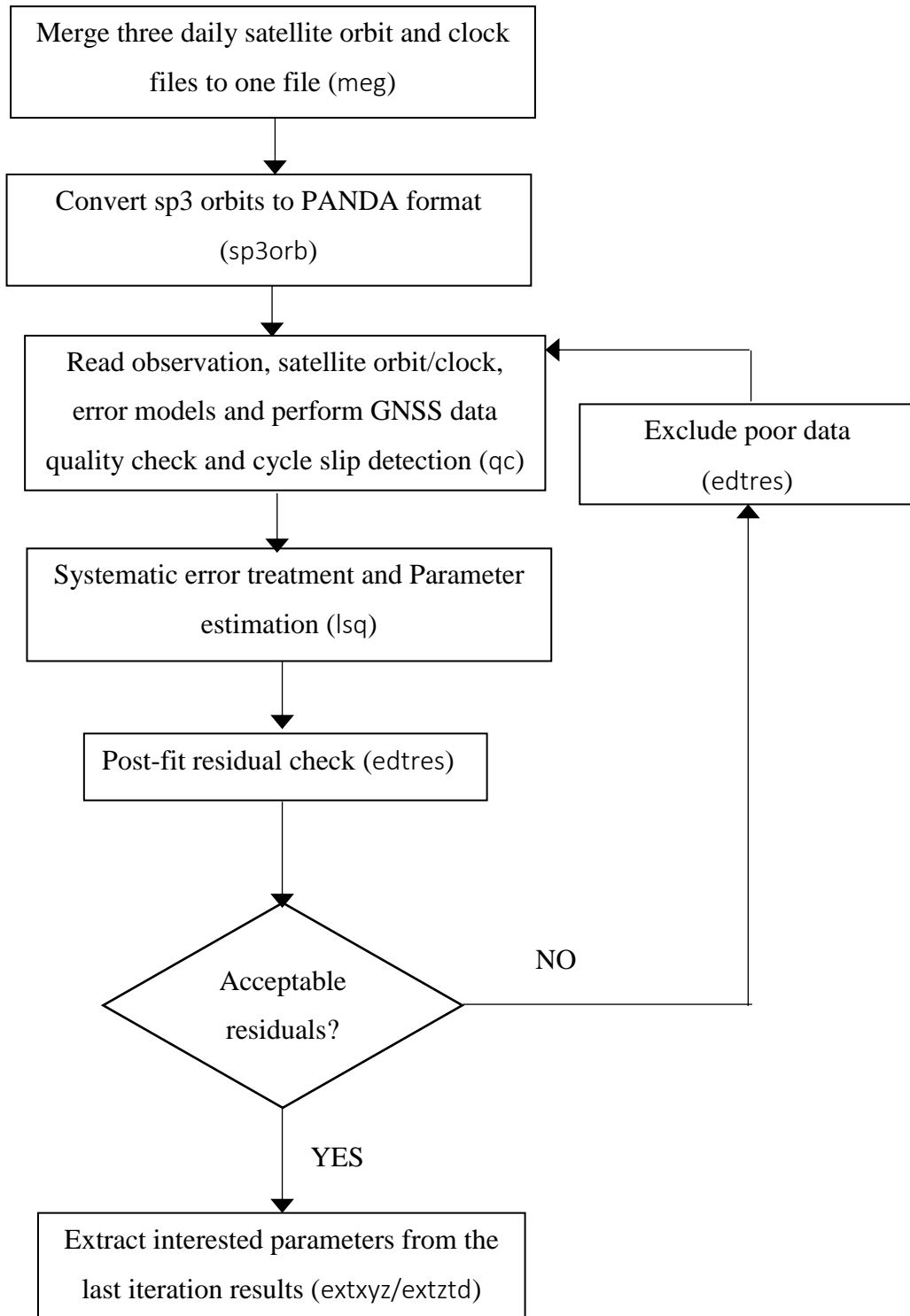


Figure 4.1: PPP flowchart in PANDA (with relevant program name inside bracket).

#### 4.6 Satellite clock/orbit selection for PPP

Since their establishment in the 1990s, all IGS ACs have been involved in generating GPS satellite clock/orbit information. However, GLONASS satellite products, especially satellite clock corrections at high resolution (e.g. 30 second), are only generated by CODE, ESA and



GFZ. Details of each AC estimation strategy, systematic error treatment and employed ground track stations are included in the IGS Technical Reports (e.g., Villiger and Dach, 2018), standard textbooks (e.g. Weiss *et al.*, 2017) and the IGS analysis centres description files<sup>3</sup>. A short introduction for the topic, which is mainly from Weiss *et al.* (2017), is presented in the following paragraphs.

By processing GNSS phase and pseudorange observation at globally distributed tracking stations, IGS different products, e.g. transmitter/receiver clock corrections, satellite 3D positions, stations 3D daily coordinates, tropospheric delay, Earth rotation parameters (ERP), global ionospheric correction map, and DCBs are generated. Due to their different variability nature during the observation collection arc, the abovementioned variables are parameterized in one of the following forms: offset, piecewise constant, piecewise linear, and epoch dependent. For instance, in 24 hour data processing, station coordinates, DCBs and PCOs are parametrized as constant offsets whilst phase ambiguities are piecewise constant, and tropospheric delays and receiver/transmitter clock are considered as piecewise linear and epoch dependent parameters, respectively.

In general, IGS products are computed via two estimation strategies. In the first approach, double difference data are used to remove clock parameters and then estimate orbits, EOPs, station coordinates, tropospheric delays, and phase ambiguities. Thereafter, by fixing the computed parameters and processing undifferenced observations, all clock parameters are estimated. In the second method, undifferenced observations are used to estimate all parameters in one step. In both methods, all systematic error corrections mentioned in Section 4.2 should be applied before observation adjustment. Hence, it is important to use consistent error correction models when IGS products are employed in a follow-up PPP application.

The Bernese GNSS software package, which is developed by the Astronomical Institute of University of Bern, is used for the CODE products generation. CODE provides two types of final products: one is processed from three days of observations and then estimated parameters for the middle day are extracted, whilst another is computed from data in one-day-arc. In this thesis, the former which is accessible from <ftp://ftp.aiub.unibe.ch> is used. To process GNSS observations in generating ESA satellite orbit/clock products, the NAPEOS software package is used. ESA products, which are based on 24 hour data processing, can be downloaded from <http://navigation-office.esa.int/products/gnss-products/>. GFZ satellite clock/orbit products are

---

<sup>3</sup> [igsb/center/analysis/](ftp://ftp.igsb/center/analysis/)  
[igsb/center/data/](ftp://ftp.igsb/center/data/)  
[igsb/center/oper/](ftp://ftp.igsb/center/oper/)

based on GNSS data processing via the EPOS.P8 software package, and similar to ESA, these products are estimated from a 24 hour observation arc, and they are accessible from <ftp://ftp.gfz-potsdam.de/GNSS/products>.

It is typical to compare the RMS of individual IGS AC satellite clock/orbit products with the IGS combined solution for the accuracy assessment of the products. The RMS of the clock/orbit final products generated by CODE, ESA and GFZ are within 1-2 cm. To select the most appropriate clock/orbit products, the performance of kinematic PPP using the satellite products generated by the aforementioned analysis centres is considered here. It is worthwhile to mention that, at the time of writing this thesis in January 2020, the GLONASS clock 30 second information from day 1 to day 210, 2015 for the CODE final product is not available. As it is aimed to process GNSS data from 2012.0 to 2019.0 in Chapter 5, the CODE final product is discarded in the satellite orbit/clock check in this section, and instead, its final rapid product together with ESA and GFZ final products are considered. As mentioned in the CODE analysis centre description file at <ftp://ftp.aiub.unibe.ch/CODE/>, a final rapid solution for a day is estimated from rapid solutions for that day and its previous day with an ultra-rapid solution of the next day.

For comparing the three products, 101 globally distributed stations were selected. Thereafter, 30 second kinematic PPP using each satellite product at each station at 36 uniformly distributed days through 2016 (DOY= 10, 20, ..., 360) was run. Station names and their coordinates are shown in Appendix C. In Table 4.2, the models and conventions which were used for the kinematic PPP are shown. After coordinate estimation at each 30 second epoch, suspected outliers were removed, and the time series is detrended. In Figure 4.2 the resulted height time series for day 200, 2016 at three sample stations: HERT, DRAO and HRAB is presented. As this figure demonstrates, GPS-derived time series (left panel) are less noisy than their counterpart from GLONASS (right panel). It also seems that GPS satellite clock/orbit products from CODE, ESA and GFZ are at the same accuracy level, whilst different accuracy of the GLONASS satellite clock/orbit information among the three centres can be seen.

To inspect the role of the GNSS satellite clock/orbit products in the quality of PPP more thoroughly, Root Mean Square (RMS) per day of the estimated height time series using satellite orbit/clock information from each centre (for all stations) are computed. For each site then the 36 RMSs were internally checked, and any RMS which differed from the median RMS by larger than five times the median absolute deviation (MAD) was excluded. Finally, the mean RMS for the remaining RMSs at each site was calculated.

Earth Orientation Parameters (EOP)	IERS bulletins
Antenna PCO/PCV	IGS14 ANTEX file (Rothacher and Schmid, 2010)
Ionospheric correction	Ionospheric free data combination
Tropospheric delay	Saastamoinen formulas with GMF (Saastamoinen, 1972)
EBT/OTL displacements	IERS2010 Conventions (Petit and Luzum, 2010)
Station position dynamic model	Random walk with $10 \text{ mm}/\sqrt{s}$ noise
ZWD dynamic model	Random walk with $10 \text{ mm}/\sqrt{h}$ noise
Receiver clock dynamic model	White noise with $3 \text{ ms}/\sqrt{s}$

Table 4.2: Models and convention for the kinematic PPP used for IGS ACs product comparison

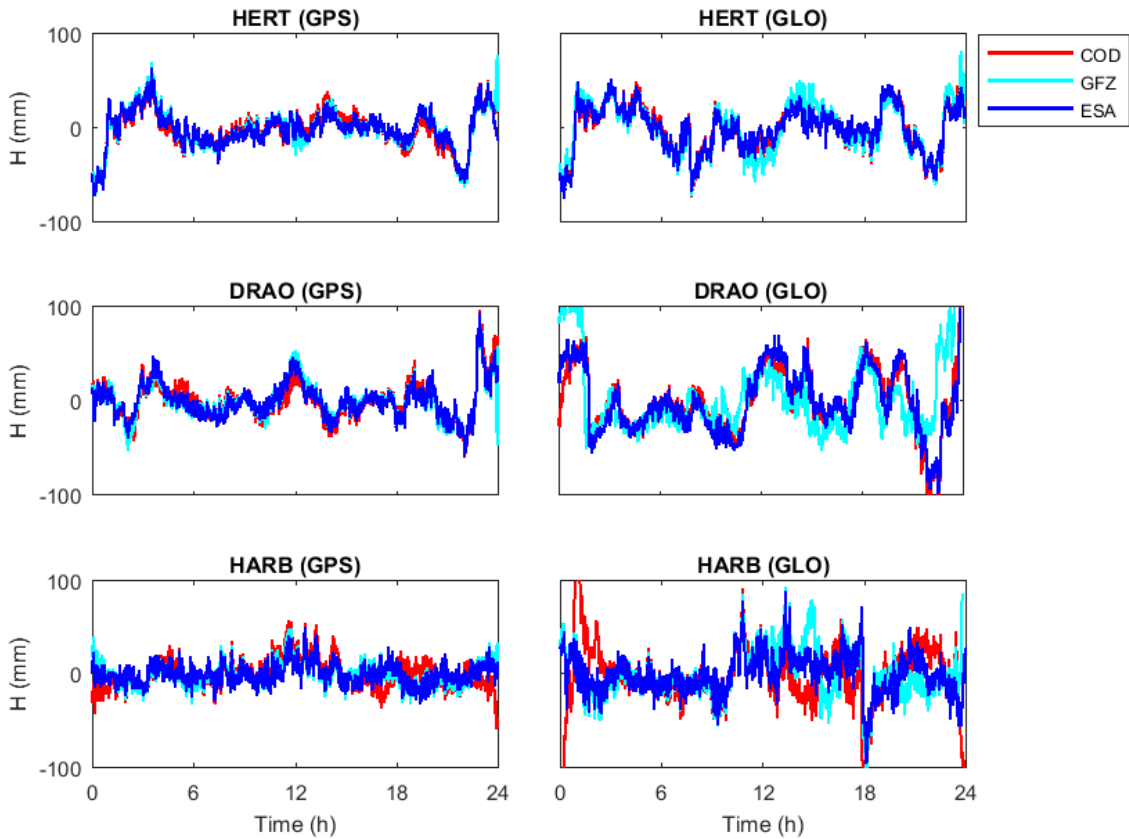


Figure 4.2: Detrended height time series estimated from kinematic PPP of GPS-only and GLONASS-only data with different satellite clock/orbit products

In Figure 4.3 to Figure 4.6, the ratio of the mean RMS (for the height component) between PPP results using different satellite products in GPS-only and GLONASS-only PPP are shown. Station names, their latitudes and longitudes, and the computed ratio at each point are in Appendix C. In these figures, a ratio between 0.9 and 1.1 is considered as a slight difference

between the RMSs whilst a ratio out of this band is interpreted as a distinctive RMS change. Figure 4.3 and Figure 4.4 indicate that for the majority of stations, time series generated using the ESA final products have smaller or equal RMS (green, blue, and orange circles) to those generated using the CODE final rapid product. In some parts of South America, the height RMS from GPS as well as GLONASS PPP with ESA is about 50% smaller, and in Antarctica a distinct higher precision for the GLONASS solution with the ESA product can be seen. By this comparison, it is concluded that the ESA final product should be preferred to the CODE final rapid product in kinematic PPP. Figure 4.5 shows a slightly smaller or equal RMS for the GPS estimated height time series using ESA final products compared to those estimated using the GFZ final product. However, GLONASS data processing with ESA product leads to smaller RMS values almost for all stations as shown in Figure 4.6. In some parts of Europe, South America, and Africa, the GLONASS-derived time series generated using ESA products exhibits about a 50% smaller RMS compared to those based on GFZ products. Therefore, for GPS-only, GLONASS-only and combined GPS+GLONASS data processing in PANDA, the ESA (operational) satellite clock/orbit final products are used in all tests in the rest of this thesis.

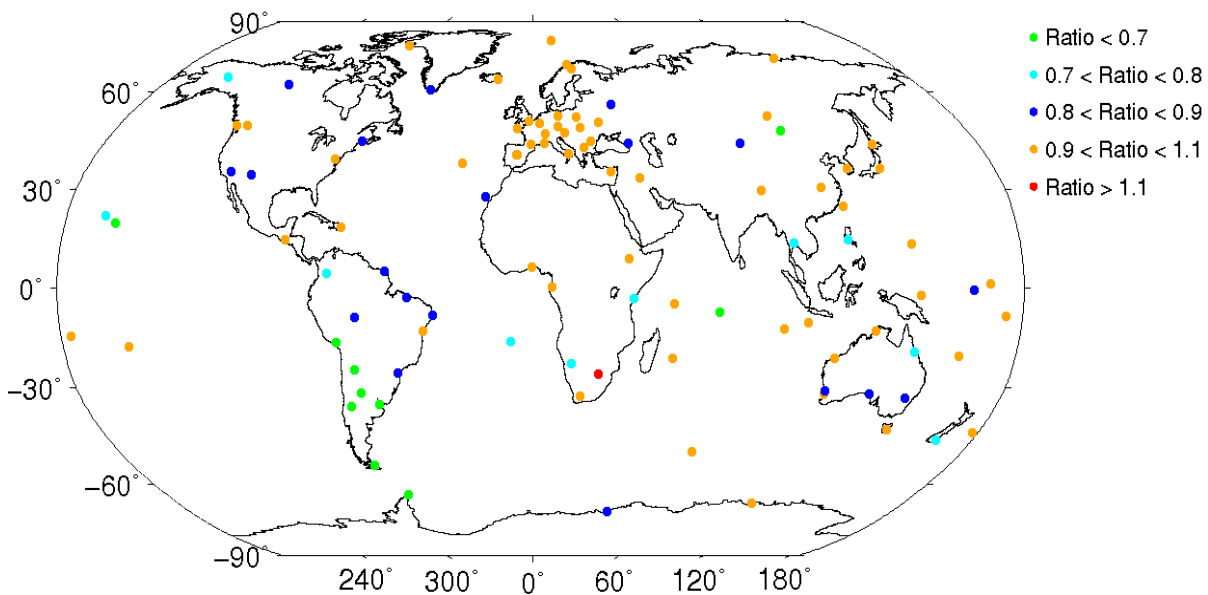


Figure 4.3: Ratio of GPS-estimated height RMS with ESA final and CODE final rapid products.

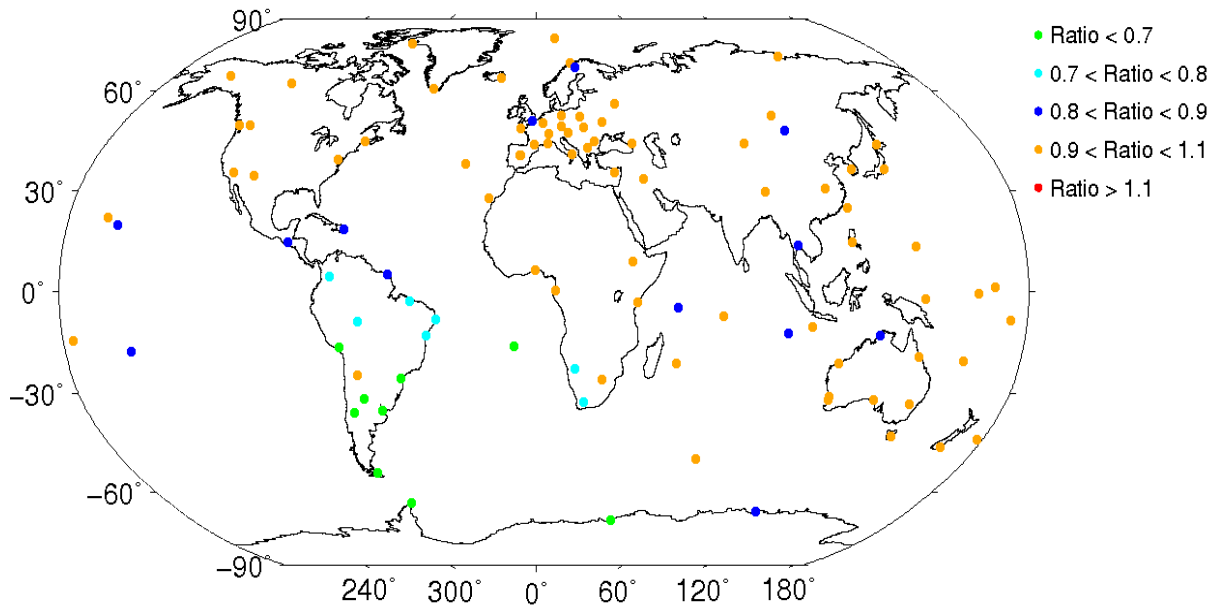


Figure 4.4: Ratio of GLONASS-estimated height RMS with ESA final and CODE final rapid products

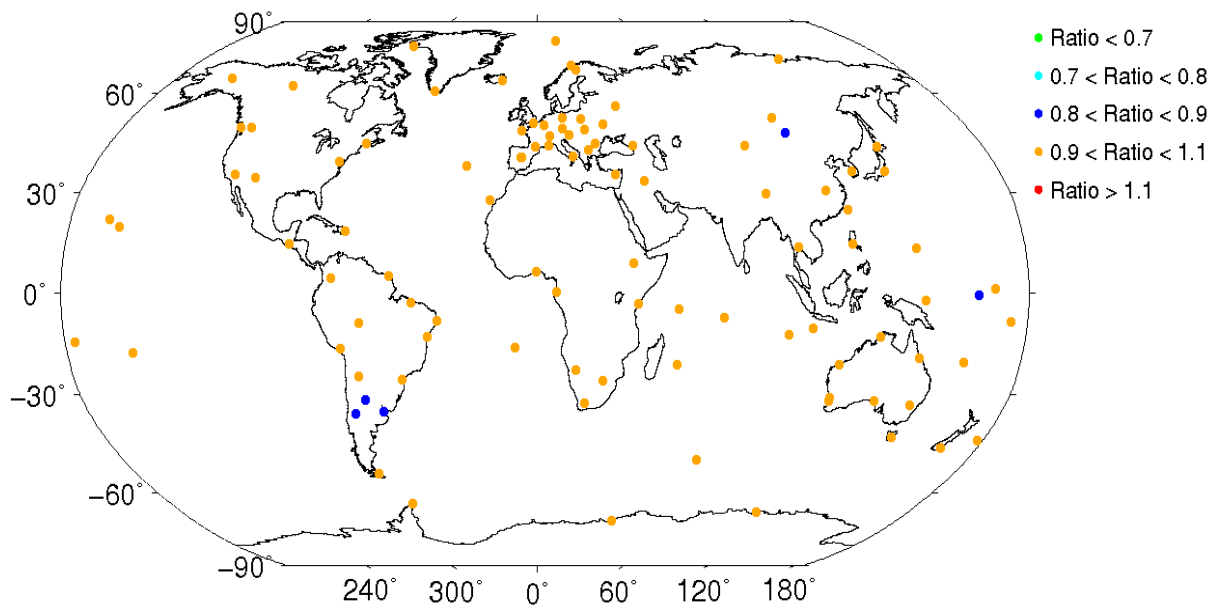


Figure 4.5: Ratio of GPS-estimated height RMS with ESA and GFZ final products

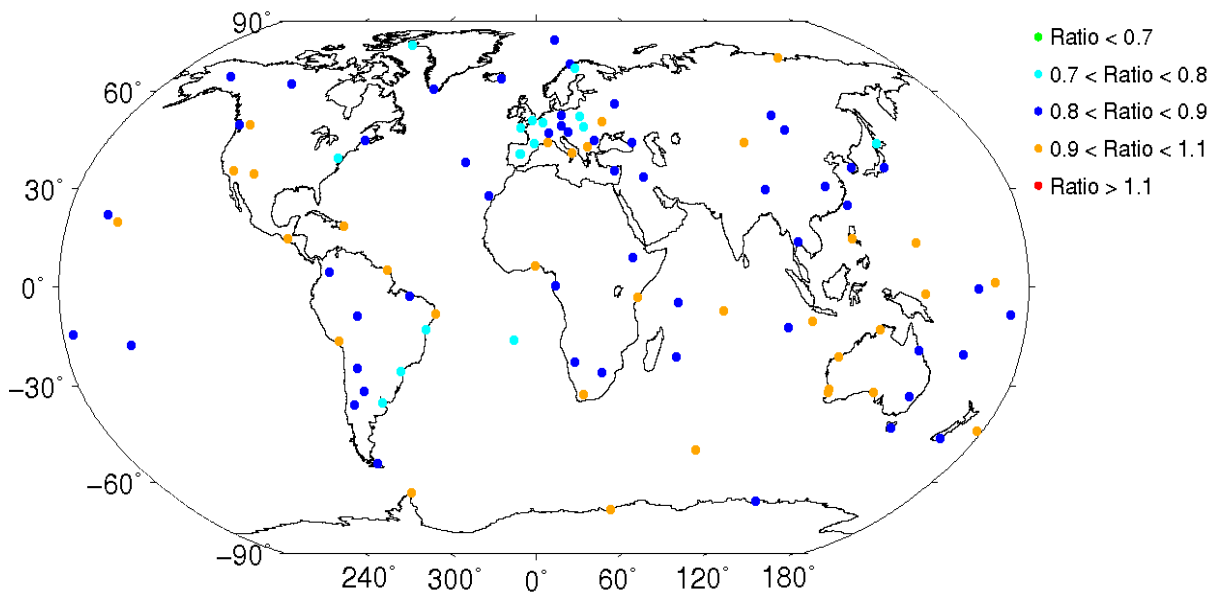


Figure 4.6: Ratio of GLONASS-estimated height RMS with ESA and GFZ final products

#### 4.7 Day break error and session length

For a given phase connected arc of a satellite in kinematic PPP, it would be ideal to engage all observations of that satellite within the arc to estimate the corresponding phase bias. However, it is unavoidable to miss some observations of the phase connected arc when it extends to outside of the data processing window. ESA satellite clock and orbit products are generated from a 24 hour data processing, and there is a discontinuity for the estimated products at the UTC midnights. Hence, the estimated coordinates in kinematic PPP may experience an unusual jump at the edge of the data processing window, which is called the day break error when observations between two UTC midnights are processed.

PANDA can process GNSS data in any arc length, but data processing in 24-hour or longer arcs prevents sub-daily discontinuities in the coordinate time series. To see the effect of data arc length on the day break error, 30 second kinematic PPP data processing in 24 and 30-hour batches using ESA orbits and clock products are compared in this section. All kinematic PPP models used in Section 4.6 are also used here. In the 24-hour processing, data between two consecutive UTC midnights are used, whilst in the 30 hour processing the data arc is enlarged to three hours before and after the UTC midnight, and then the estimated coordinate time series for the middle day is extracted. In this test, GPS data for the stations and days mentioned in Section 4.6 were used.

The detrended height time series generated with GPS data processing in 24 and 30 hour sessions at three sample stations on day 200, 2016 are shown in Figure 4.7. This figure depicts that around the middle of the session arc, the estimated height is not affected by the session length, whilst near the edges, different results may arise. To quantify height time series variations due to observation processing length changes, the RMS of the height time series within three bins near UTC noon and midnights, i.e. 00:00 to 04:00, 10:00 to 14:00, and 20:00 to 24:00, were computed. Figure 4.8 shows the experimental cumulative density function for the computed RMSs over different aforementioned bins in 24 and 30 hour data processing. This figure demonstrates that the estimated height around UTC noon is not affected by the data processing length. However, the 95th percentile of the day break error for 30 hour data processing session is about 4 mm and 9 mm larger at the beginning and end parts of the data arc, respectively, compared with 24 hour arcs. Therefore, it can be concluded that kinematic PPP with 24 hour data processing is less susceptible to daybreak error with ESA satellite products, which are computed in 24 hour sessions.

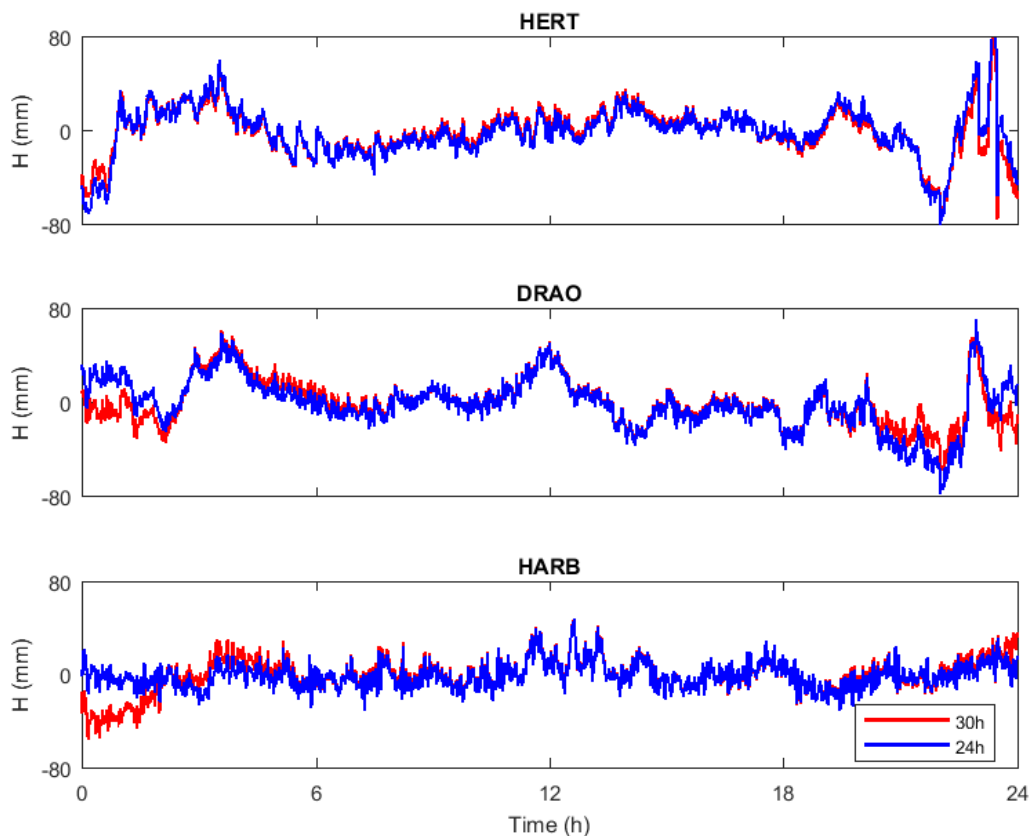


Figure 4.7: Detrended height time series estimated from 24 and 30 hour kinematic PPP at three sample station on day 200, 2016

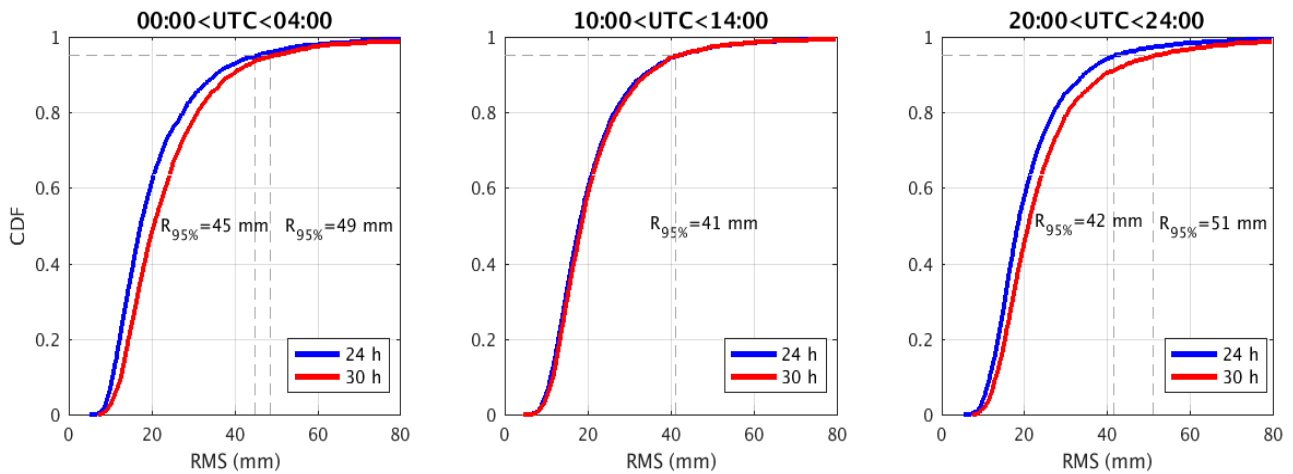


Figure 4.8: Cumulative distribution function (CDF) for the GPS-estimated height RMS at three time bins with 24 and 30 hour data processing using ESA final satellite orbit/clock products.

#### 4.8 Synthetic tidal displacement signal in PPP

As proposed by Penna *et al.* (2015), the absolute accuracy of the GNSS-derived OTL displacement may be obtained by introducing a known synthetic tidal displacement signal in kinematic PPP processing. By using this idea, they evaluated the effect of the GNSS-derived time series length as well as observation gaps on the OTL displacement estimation. They also found the optimum process noise for the station coordinate and tropospheric parameters which minimized the synthetic signal recovery error. In Chapter 5, the synthetic tidal displacement signal for the software validation and process noise tuning test, is also adopted.

To construct the artificial tidal displacement signal, Penna *et al.* (2015) computed a sinusoid function at each data collection epoch, and inserted it to the a priori station coordinates in the observation adjustment. They demonstrated around 0.2-0.4 mm accuracy for the recovery of the artificial signal when at least 2.5 years of high quality GPS data was provided. Rather than adding the simulated signal to the station approximate coordinate, its equivalent effect is applied to the satellite 3D coordinates here, and then PPP solution are run with the altered orbit. This algorithm may have two main advantages to the approach used in Penna *et al.* (2015). First, the effect of any satellite-oriented mismodelling error, e.g. solar radiation pressure, satellite antenna PCV, etc. can be simulated and added to the satellite 3D coordinates, and their effect on either PPP or relative GNSS positioning outputs may be inspected. Second, to compare the robustness of different IGS analysis centres' orbit products, their degree of sensitivity to an artificial noise or signal can be computed. More detail about inserting a simulated signal to the satellite orbit is now described.



In general, a 3D tidal displacement signal in a local coordinate frame can be expressed as:

$$e_s(t) = a_1 \cdot \sin(\omega t + \theta_1) \quad (4.37)$$

$$n_s(t) = a_2 \cdot \sin(\omega t + \theta_2) \quad (4.38)$$

$$u_s(t) = a_3 \cdot \sin(\omega t + \theta_3) \quad (4.39)$$

where  $e_s$ ,  $n_s$ , and  $u_s$  are the simulated tide-induced station coordinate change in the east-west, north-south, and up-down directions, respectively. In the above equations,  $\omega = 2\pi f$  is the angular frequency of the signal, and  $a_j, \theta_j$  ( $j = 1,2,3$ ) are the amplitude of the signal and its initial phase, respectively. By assigning constant values to  $\omega$ , and  $\theta_j$ , the tidal signal at each data collection epoch  $t_i$  is constructed. For simplicity, only the vertical component is considered, and hence the tidal displacement at each epoch is  $[0 \ 0 \ u_s(t_i)]^t$ . Similar to Penna *et al.* (2015), for the amplitude and period of the vertical synthetic signal, 5 mm and 13.96 hour are considered, respectively. The 5 mm amplitude is chosen as it is at the level of the expected residual tidal signal in GPS data processing (Penna *et al.*, 2007), and the selected 13.96 hour period is sufficiently far from the minor and major tidal periods.

By using the following transformation, the synthetic signal in an Earth Fixed Earth Centred (EFEC) coordinate system at a GNSS station with approximate coordinate of  $(\lambda_{stn}, \varphi_{stn})$  is computed:

$$\begin{bmatrix} x_s(t_i) \\ y_s(t_i) \\ z_s(t_i) \end{bmatrix} = R_3(\lambda'_{stn})R_2(\varphi'_{stn})P_2 \begin{bmatrix} 0 \\ 0 \\ u_s(t_i) \end{bmatrix} \quad (4.40)$$

where

$$R_3(\lambda'_{stn}) = \begin{bmatrix} \cos(180 - \lambda_{stn}) & \sin(180 - \lambda_{stn}) & 0 \\ -\sin(180 - \lambda_{stn}) & \cos(180 - \lambda_{stn}) & 0 \\ 0 & 0 & 1 \end{bmatrix} \quad (4.41)$$

$$R_2(\varphi'_{stn}) = \begin{bmatrix} \cos(90 - \varphi_{stn}) & 0 & -\sin(90 - \varphi_{stn}) \\ 0 & 1 & 0 \\ \sin(90 - \varphi_{stn}) & 0 & \cos(90 - \varphi_{stn}) \end{bmatrix} \quad (4.42)$$

$$P_2 = \begin{bmatrix} 1 & 0 & 0 \\ 0 & -1 & 0 \\ 0 & 0 & 1 \end{bmatrix} \quad (4.43)$$

The corresponding effect of the generated synthetic signal may then be added to the satellite coordinates from IGS products:

$$\begin{bmatrix} x_{sat}(t_i) \\ y_{sat}(t_i) \\ z_{sat}(t_i) \end{bmatrix} = \begin{bmatrix} x_{sat-IGS}(t_i) \\ y_{sat-IGS}(t_i) \\ z_{sat-IGS}(t_i) \end{bmatrix} + \begin{bmatrix} x_s(t_i) \\ y_s(t_i) \\ z_s(t_i) \end{bmatrix} \quad (4.44)$$

The altered orbit was used to process 30 second GPS data from the IGS station ONSA from 2012.0 to 2017.0. Kinematic PPP models and conventions which were used in Section 4.6 are also employed here. It will be shown in the next section that the coordinates and ZWD process noise may be selected more precisely in a noise tuning test. The estimated station coordinates time series in PANDA is then de-trended and cleaned for blunders. Thereafter, a moving average with window size of 1800s is used, and Fourier spectral analysis is applied. The result of the spectral analysis is shown in Figure 4.9. As this figure depicts, the synthetic tidal displacement is recovered with around 0.1 mm accuracy, which confirms PANDA's ability for GNSS data processing in an OTL displacement investigation. Similar results were also observed in different stations which are not shown here. In Chapter 5, a statistical analysis for the artificial tidal displacement signal recovery error, and a comparison between PPP results with PANDA and GIPSY will be explained.

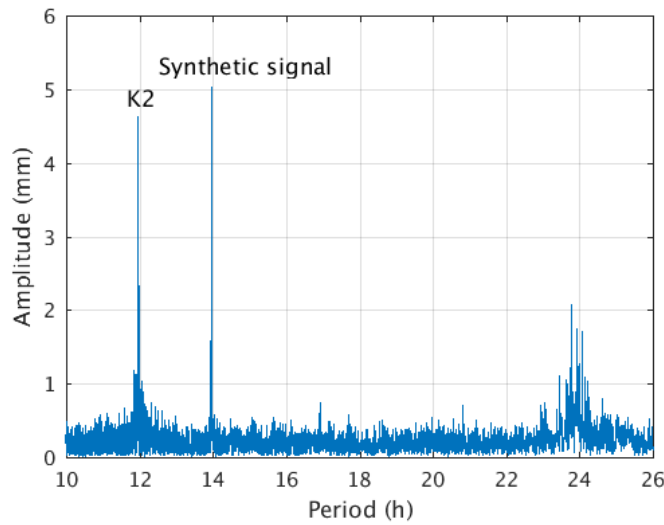


Figure 4.9: Amplitude spectrum for the GPS-estimated height time series at the ONSA IGS station from 2012.0 to 2017.0. The satellite orbit fixed in PPP was modulated by a synthetic tidal signal with amplitude 5 mm and period 13.96 hours.

#### 4.9 Noise tuning in kinematic PPP processing

In Section 4.4, it was explained that PANDA assumes a random walk model for the station coordinates as well as ZWD temporal variation in Kalman filtering. As the degree of epoch to epoch variability of the parameters, which is called process noise, is not known. Penna *et al.* (2015) proposed a noise tuning test based on assessing the PPP performance versus process noise variation, and Hadas *et al.* (2017) used numerical weather prediction models to compute the expected ZWD temporal variation which is directly proportional to the ZWD process noise. As the noise tuning method used in Penna *et al.* (2015) is applicable for both station coordinates and ZWD parameters, it is preferred here.

The noise tuning test in Penna *et al.* (2015) is based on investigating the effect of process noise on the GPS-estimated parameters, and five statistics for the estimated parameters are considered in the test: standard deviation of the height time series, median of the daily RMS values of the phase observation residuals, standard deviation of the difference between estimated tropospheric zenith total delay (ZTD) by GPS and those from radiosondes, residual M2 OTL vertical displacement, and synthetic signal recovery error. Since the water vapour content of the troposphere varies with latitude, six stations with different latitudes, which are shown in Figure 4.10 and Appendix C, were selected. For all tested stations, GPS observations were processed in 30 second epochs and, after outlier removal, averaged in 30 min bins from 2012.0 to 2017.0. For the kinematic PPP models, Table 4.2 is used.

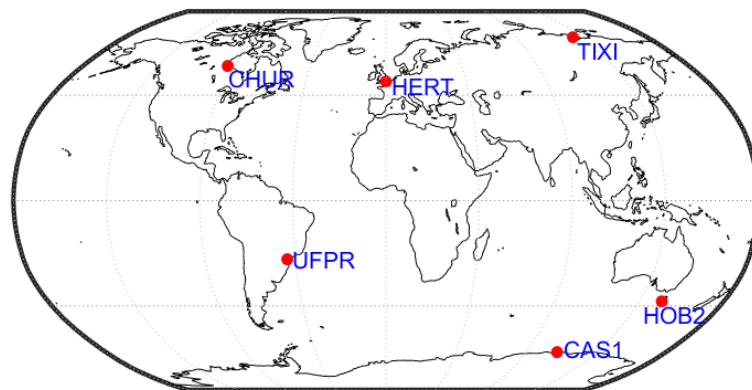


Figure 4.10: Stations used for coordinate and ZWD process noise tuning

In Figure 4.11, the graphs of the tested parameters which are estimated by different ZWD process noise are shown, with the station coordinate process noise held fixed to  $10 \text{ mm}/\sqrt{\text{sec}}$ . For the station names, the IGS four-letter naming convention is used. This figure indicates that a ZWD process noise value of around  $1 \text{ mm}/\sqrt{\text{hour}}$  is the optimum lower level value to

minimize the RMS of the height time series, the median of the daily RMS observation phase residuals, the difference between estimated ZWDs by GPS and radiosondes, and synthetic signal recovery error. The optimum ZWD process noise value for all stations except UFPR and HOB2 (which are located in lower latitudes compared to other stations) matches well to the values shown in Figure 2 of Hadas *et al.* (2017). Figure 4.11 indicates that the  $3\text{-}6\text{ mm}/\sqrt{\text{hour}}$  ZWD process noise values at UFPR and HOB2 in Hadas *et al.* (2017) can minimize the discrepancy between the estimated ZWD from GPS and radiosonde data, but this may adversely affect the accuracy of the estimated height, i.e. increased height RMS for larger process noise values.

Now, the optimum  $1\text{ mm}/\sqrt{\text{hour}}$  for ZWD process noise is used for the GPS data processing with different candidates of coordinate process noise. Figure 4.12 demonstrates that a coordinate process noise around  $3\text{ mm}/\sqrt{\text{sec}}$  minimizes phase observation residuals as well as the artificial signal recovery error. Furthermore, the residual M2 OTL displacement and height time series RMS are stabilized at this point. Hence, for any GNSS data processing in Chapter 5 and Chapter 6,  $1\text{ mm}/\sqrt{\text{hour}}$  and  $3\text{ mm}/\sqrt{\text{sec}}$  for the ZWD and coordinates process noise values are assigned, respectively.

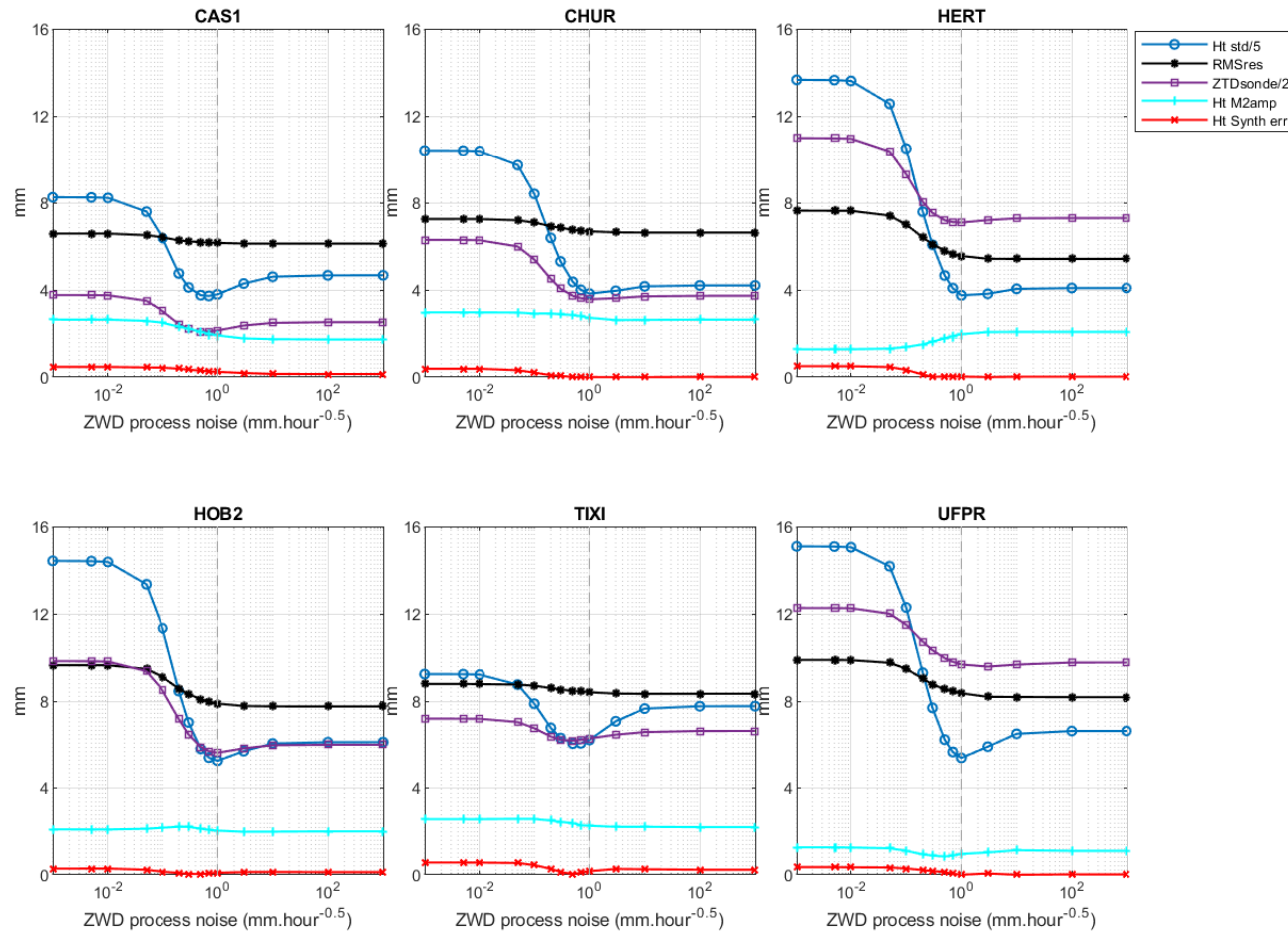


Figure 4.11: Zenith wet delay (ZWD) process noise tuning at six globally distributed stations. In each panel, the following parameters are shown: standard deviation of the height time series divided by 5 (Ht std/5), median of daily RMS values of the phase observation residuals (RMSres), standard deviation of the difference between estimated ZTD by GPS and those from radiosondes divided by 2 (ZTDsonde/2), residual M2 OTL vertical displacement amplitude (Ht M2amp), and synthetic signal recovery error (Ht Synth err). For station coordinate process noise,  $10 \text{ mm}/\sqrt{\text{sec}}$  is assigned.

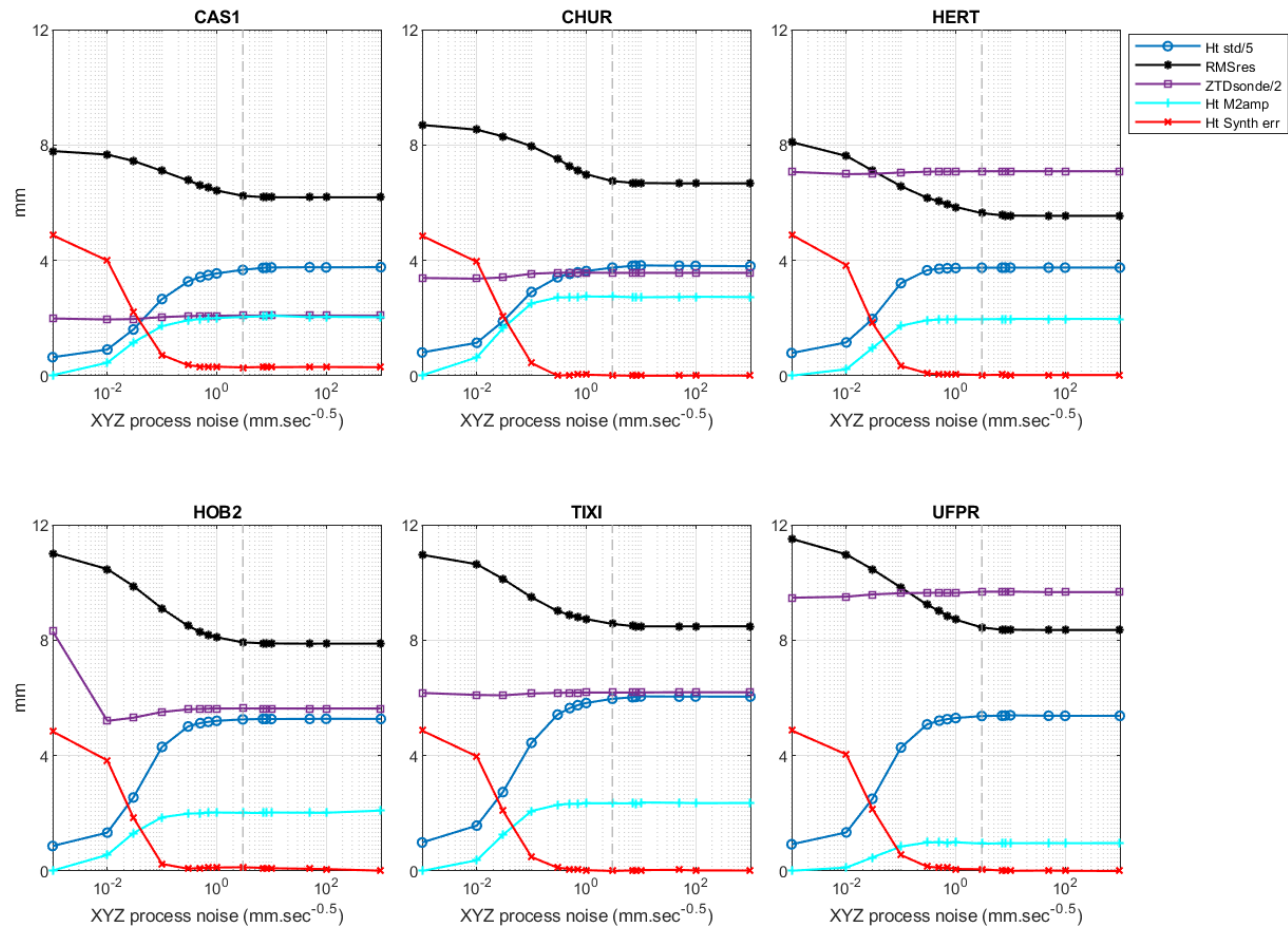


Figure 4.12: Station coordinate process noise tuning test with the optimized ZWD process noise achieved in Figure 4.7. All parameters in Figure 4.7 are used in this figure.

#### 4.10 Summary

This chapter has explained the different steps of kinematic PPP approach and their implementation in the PANDA software. A short instruction for running kinematic PPP in PANDA has also been presented. By checking the height time series RMS at 101 globally distributed stations, it has been demonstrated that ESA offers the highest quality satellite orbit and high rate 30 second clock products for the kinematic PPP with GPS and GLONASS data. Furthermore, it is shown that 24 hour data processing is less affected by the day break edge error than 30 hour data processing when IGS satellite products were used. Tidal displacement simulation in kinematic PPP, which is applicable for the quality check of the GNSS-estimated OTL displacement, has been explained, and an accuracy about  $\sim 0.2$  mm for recovery of a synthetic signal is verified. Finally, process noise tuning test for six globally distributed stations has suggested  $1 \text{ mm}/\sqrt{\text{hour}}$  and  $3 \text{ mm}/\sqrt{\text{sec}}$  as the optimum ZWD and station coordinates process noise values in kinematic PPP, respectively. All results in this chapter for the satellite clock/orbit assessment, data processing arc length, and optimum process noise values will be used in Chapter 5 to investigate the potential advantages of GLONASS data for the OTL displacement estimation.

## Chapter 5 Benefits of combining GPS and GLONASS for measuring ocean tide loading displacement

This chapter is published in Journal of Geodesy as:

*Abbaszadeh, M., Clarke, P.J. & Penna, N.T. Benefits of combining GPS and GLONASS for measuring ocean tide loading displacement. J Geod 94, 63 (2020). <https://doi.org/10.1007/s00190-020-01393-5>.*

Clarke and Penna provided supervisory input, which included refinement of the text, and the GIPSY GPS data processing was done by Penna.

To have a consistent writing format throughout the thesis, the numbering style of the other chapters is used in this chapter.

### 5.1 Abstract

GPS has been used to estimate ocean tide loading (OTL) height displacement amplitudes to accuracies of within 0.5 mm at the M2 frequency, but such estimation has been problematic at luni-solar K2 and K1 frequencies because of multipath and satellite orbit errors. We therefore investigate the potential of using the GLONASS constellation (with orbital period 11.26 hours and true site geometry repeat period of 8 sidereal days distinct from K2 and K1) for OTL displacement estimation, analysing 3-7 years of GPS and GLONASS data from 49 globally-distributed stations. Using the PANDA software in kinematic precise point positioning mode with float ambiguities, we demonstrate that GLONASS can estimate OTL height displacement at the M2, N2, O1 and Q1 lunar frequencies with similar accuracy to GPS: 95th percentile agreements of 0.6-1.3 mm between estimated and FES2014b ocean tide model displacements. At the K2 and K1 luni-solar frequencies, 95th percentile agreements between GPS estimates and model values of 3.9-4.4 mm improved to 2.0-2.8 mm using GLONASS-only solutions. A combined GPS+GLONASS float solution improves accuracy of the lunar OTL constituents and P1 (but not significantly for K1 or K2) compared with a single constellation solution, and results in hourly-to-weekly spectral noise very similar to a GPS ambiguity-fixed solution, but without needing uncalibrated phase delay information. GLONASS estimates are more accurate at higher compared with lower latitudes because of improved satellite visibility, although this can be countered by using a lower elevation cut-off angle.



## 5.2 Introduction

Geodetic measurements, for example from Global Navigation Satellite Systems (GNSS), Very Long Baseline Interferometry (VLBI), Satellite Laser Ranging (SLR) and Doppler Orbitography Integrated by Satellite (DORIS), are sensitive to ocean tide loading (OTL) deformation of the solid Earth which is caused by the periodic change in ocean mass distribution arising from the gravitational attractions of the moon and Sun. The IERS Conventions (Petit and Luzum 2010) provide utilities to correct geodetic measurements for this OTL deformation, requiring as input OTL displacement coefficients at the dominant tidal periods (including those listed in Table 1). These are generated by convolving a global model of the ocean tides with a loading Green's function, which is dependent on the material properties of the Earth's interior. Because any errors in these OTL displacement coefficients will propagate to the normally estimated geodetic parameters and degrade, for example, resultant coordinate time series used for reference frame definition and the monitoring of millimetre-level land movements, it is important that accurate models are used for their derivation. One way in which the accuracy of these Earth and numerical ocean tide models can be verified is by independent geodetic analysis in which the OTL displacements are the parameters of interest.

Constituent	Frequency (cycles per day)	Relative magnitude of tidal potential
M2	1.936	1.00
S2	2.000	0.46
N2	1.896	0.20
K2	2.006	0.13
K1	1.003	0.58
O1	0.929	0.41
P1	0.997	0.19
Q1	0.893	0.08

Table 5.1: Principal semi-diurnal and diurnal tidal constituents of the tidal potential (after Kudryavtsev, 2004)

VLBI data were first shown to be able to estimate OTL displacement by Schuh and Moehlmann (1989) and then Sovers (1994), who included harmonic parameters at the dominant tidal frequencies in the primary least squares estimation. Schenewerk *et al.* (2001) showed this was also possible with global solutions of double differenced Global Positioning System (GPS) data but to an accuracy of  $\sim 5$  mm for 90% of the sites studied, whereas Allinson *et al.* (2004) used Precise Point Positioning (PPP) for at least 90 days of GPS data to obtain M2 OTL displacement

agreements with geophysical models within  $\sim 1$  mm. Thereafter King *et al.* (2005) used the PPP GPS method of Allinson *et al.* (2004) to obtain OTL displacements to validate ocean tide models around Antarctica. Thomas *et al.* (2007) compared VLBI and PPP GPS analyses (each using several years of data), and concluded similar millimetre-level agreement for GPS and VLBI when compared with OTL computed from existing Earth and ocean tide models, for the majority of tidal constituents. An alternative approach was followed by Khan and Tscherning (2001) and Melachroinos *et al.* (2008), who undertook harmonic analysis of GPS coordinate time series to estimate the OTL displacement, obtaining observed versus model differences of several millimetres but using only 7-15 weeks of GPS data. Penna *et al.* (2015) refined this time series analysis technique by determining the optimum tropospheric and coordinate process noise through comparisons with radiosonde tropospheric delays and synthetic harmonic ground displacements. This led to the estimation of OTL displacement using GPS to an accuracy of around 0.4 mm when using time series from 2.5 years of data, improving to about 0.2 mm with 4 years or more of data. While ocean tide model errors have historically been assumed to be the limiting accuracy factor in the modelling of OTL displacement (e.g., Bos and Baker 2005), recent advances in ocean tide modelling (e.g., Stammer *et al.* 2014) have led to GPS-estimated OTL displacements being used to not only validate and identify deficiencies in ocean tide models, but also to measure the elastic and anelastic properties of the Earth's interior (e.g., Ito and Simons 2011; Bos *et al.* 2015).

Studies to date on probing the Earth's interior properties at tidal frequencies using GPS have mostly considered the M2 constituent only (e.g., Bos *et al.* 2015; Yuan and Chao 2012; Martens *et al.* 2016), and validation of ocean tide models using GPS-estimated OTL displacements has proved especially problematic at the K2 and K1 frequencies (e.g., Allinson *et al.* 2004; King *et al.* 2005; Thomas *et al.* 2007). This is because K2 and K1 coincide with the GPS orbital period and sidereal geometry repeat period respectively, so any orbit errors and multipath effects degrade the OTL displacement estimates even over time spans of several years (e.g., Thomas *et al.* 2007). The completion of the GLONASS satellite constellation replenishment in 2010, the subsequent upgrade of networks of GNSS receivers worldwide such that there are now over five years of both GLONASS and GPS dual frequency observations widely available, together with IGS Analysis Centres generating high accuracy GPS and GLONASS satellite orbits and high-rate clocks, now facilitate the estimation of OTL displacement using GLONASS. This is particularly desirable, as the GLONASS orbital period of 11.26 hours ( $\sim 2.131$  cycle per day) and the sidereal geometry repeat period of 8 days (0.125 cycle per day) are distinct from any major tidal frequencies, so K2 and K1 OTL displacement estimation becomes potentially

feasible. This complements the promise shown by GLONASS for longer period crustal deformation studies, with Abraha *et al.* (2018) demonstrating that GLONASS can result in reductions compared with GPS in artificial longer period signals arising from the propagation of unmodelled semi-diurnal and diurnal tidal displacements, because of the different geometry repeat period.

This paper investigates how well OTL displacement may be estimated using GLONASS observations, in particular for the GPS-problematic K2 and K1 frequencies. We also investigate whether combining GPS and GLONASS observations can lead to more accurate OTL displacement estimation than when using either GPS or GLONASS observations alone. A globally-distributed set of GPS+GLONASS continuous receiver data spanning at least three years at carefully selected stations is used, with validation undertaken by comparison with forward geophysical model OTL displacement values. We focus on the height component, as these OTL displacements are typically three times the size of the horizontal components (Baker 1984).

### **5.3 OTL displacement estimation using multi-GNSS kinematic PPP**

As described by Penna *et al.* (2015), OTL displacement can be estimated by the GNSS Precise Point Positioning (PPP) technique in two ways, which they termed harmonic estimation and the kinematic approach. In kinematic PPP (which we use here, following Penna *et al.* 2015), satellite positions and clock offsets are held fixed, and a variety of systematic errors, including antenna phase centre variations (PCV), phase windup, atmospheric propagation effects, and tidal displacements, are corrected. Then, parameters of interest are estimated which include time-varying 3D station coordinates, receiver clock offsets (at each data collection epoch), unmodelled time-varying tropospheric delays, and phase biases for each satellite during each phase-connected arc. Thereafter, the station coordinates in each processing session, e.g. 24 hours, are concatenated to form a time series and then screened to remove blunders. In addition, a low pass filter in the form of a window average may be used to eliminate time series noise with periods much shorter than the diurnal and semidiurnal tidal bands. Finally, by least squares spectral analysis of the time series for each desired coordinate component and tidal constituent, the amplitude and phase lag of the tidal displacement signals are estimated.

Here, for the kinematic PPP data processing, we use the Position and Navigation Data Analyst (PANDA) software (Liu and Ge 2003), as it not only has a proven capability in kinematic PPP combined multi-GNSS processing (e.g., Penna *et al.* 2018) but also allows the processing of either GPS or GLONASS data separately. To fix the satellite positions and their clock offsets

at each data collection epoch, we use the ESA final (operational) products as they have the longest continuous record of high-rate (30-second) GPS+GLONASS satellite clock availability (2010 onwards) of all the IGS Analysis Centres, and they are of high quality throughout this interval,  $\sim 1$  cm weighted root mean square difference from the IGS combined solution (Villiger and Dach 2018). We use EOP information provided by IERS bulletins as fixed values for each daily kinematic PPP batch. We apply IGS receiver and satellite antenna phase centre variation models and we use the ionosphere-free combination of dual frequency data to mitigate ionospheric effects. The predictable parts of the tropospheric delay and tidal displacement (including the perturbation due to the Free Core Nutation) are removed from GNSS observations according to the IERS Conventions 2010 (Petit and Luzum 2010), using the Saastamoinen (1972) formula and the Global Mapping Function (GMF) (Boehm *et al.* 2006) to reduce the hydrostatic and wet tropospheric delays. Due to their simpler modelling approach (e.g., Mathews *et al.* 1997), Earth body tide calculations are typically performed within PPP software packages. However, OTL displacement computations, which require information for the ocean tidal height and coastline geometry (e.g., Farrell 1972; Baker 1984), require a separate computation procedure. We input the FES2014b ocean tide model (Carrère *et al.* 2016), and an elastic Earth response Green's function computed from the Preliminary Reference Earth Model (PREM) (Dziewonski and Anderson 1981) by Wang *et al.* (2020), to the NLOADF (SPOTL) software (Agnew 1997; 2012) to compute a priori OTL displacements. These are then applied in the GNSS processing via the hardisp program of the IERS Conventions 2010. Thus, the tidal displacement signals we estimate are residuals to this a priori model. We focused our study on the M2, N2, K2, K1, O1, P1 and Q1 constituents which typically have the largest semi-diurnal and diurnal OTL displacements (Table 1). We disregarded S2 OTL despite its typically large magnitude, as GNSS observations are also affected by S2 atmospheric loading displacement (e.g., Tregoning and van Dam 2005) and these two physical signals cannot be separated in the frequency domain. Because ESA satellite orbit/clock information is provided in the centre of GNSS network (CN) reference frame, which is a realisation of the Earth's centre of figure (CF) frame (e.g. Dong *et al.* 2003), we compute the predicted OTL displacement with respect to the centre of mass of the solid Earth (CE), which closely resembles CF.

We adopt a dynamic model for the estimated time-varying kinematic PPP parameters consisting of white process noise for receiver clock offsets, and random walk process noise for the station coordinates and tropospheric zenith wet delay (ZWD) and its northward and eastward horizontal gradients. As described below, we use the method of Penna *et al.* (2015) to tune appropriate process noise values. The unknown parameters in the GPS-only solutions, namely

3D station coordinates and receiver clock corrections every 30 seconds, ZWD every 30 minutes and its horizontal gradients every 60 minutes, and a real-valued phase bias for each phase-connected arc, are estimated in a recursive least squares adjustment, over 24-hour sessions (chosen to minimise any additional errors from day break effects when concatenating 24-hour ESA orbits and clocks). The GLONASS-only and GPS+GLONASS solutions were parameterised as for GPS except: for GLONASS, also a time-constant inter-frequency bias is estimated per satellite (except for a reference satellite); for GPS+GLONASS, also a time-constant inter-system time and inter-frequency bias is estimated per satellite. As precise satellite orbit products for GPS and GLONASS are both computed in the International Terrestrial Reference Frame (ITRF), a coordinate frame transformation between them is not required in combined GPS+GLONASS PPP. Gross outliers were removed from the resulting 30-second detrended height coordinate time series if they were more than ten times the median absolute deviation from the median, before coordinate averaging in 30-minute bins, which were then used to estimate harmonic displacements at specific, defined tidal frequencies using least squares.

### **5.3.1 GNSS data selection**

The GNSS stations used to assess the benefit of GLONASS for OTL displacement estimation were selected according to (i) GNSS data availability and quality, and (ii) the suitability of using forward geophysical models for the validation of the estimated OTL displacements. As the quality of a kinematic PPP solution will be directly dependent on the quality of satellite orbits and high-rate clocks, as well as how well ionospheric and tropospheric effects are mitigated, we selected a globally-distributed set of GNSS stations to assess the impact of these effects on the OTL displacement estimation. In total, 49 globally-distributed GNSS stations were selected (shown in Figure 5.1 and listed in Appendix D along with the data availability and spans used) which fulfilled the criteria now described.

The accuracy of a GNSS-estimated tidal displacement is a function of data completeness within each daily PPP session, and the entire data processing window size. Penna *et al.* (2015) found that if at least 2.5 years of data are used, a harmonic displacement in the semi-diurnal tidal band may be estimated to within about 0.4 mm. They also found that at least 70% data coverage is needed over the given time span. Therefore to be conservative in selecting our data set, we used globally-distributed stations which had 90% annual coverage for at least three consecutive years between 2012.0 and 2019.0. Daily station data files were only considered as candidates if there were at least 20 hours of GPS and GLONASS continuous data and if the GPS analyses of Blewitt *et al.* (2018) for the station per day resulted in sub-3 cm values both for the RMS of the

daily post-fit residuals from all satellites and for the formal error of the estimated daily 3D coordinates ([ftp://data-out.unavco.org/pub/products/unr\\_qa](ftp://data-out.unavco.org/pub/products/unr_qa)). For validation of the GLONASS-estimated OTL displacements, GPS-derived OTL displacements using established methodology could be used for most constituents, but for the K2 and K1 constituents which are expected to be problematic for GPS, we must validate using OTL displacements computed by forward modelling. Therefore, after assuring data completeness as described above, we further restricted our choice of GNSS stations to locations where precise and accurate tidal displacement modelling is possible. This must in principle include the modelling of the Earth body tide, but referring to Yuan *et al.* (2013), we expect sub-millimetre uncertainty for this at any station. Therefore we are concerned only with the accuracy of predicted OTL displacement, which is a function of errors in each of the ocean tide model, the Green's function incorporating the Earth model, and the computational strategy for convolving these. Penna *et al.* (2008) found sub-millimetre agreement for the convolution integral computation using different OTL software packages, even in the worst case of coastal stations, and agreement better than 0.2 mm for stations more than 150 km inland. On the other hand, Bos *et al.* (2015) reported 0.2-0.4 mm disagreement between GPS observations and the predicted M2 OTL height displacement using a Green's function that accounted for anelasticity effects, commensurate with the effects of the established GPS observation error and uncertainties in the ocean tide models that they used. This suggests that computational and Earth model errors can be reduced to negligible amounts provided a suitable Green's function and ocean tide model are used. Hence, we believe ocean tide model error remains the main source of potential uncertainty for OTL displacement prediction.

To determine the GNSS station locations at which ocean tide model errors are minimised, OTL displacements based on eight global ocean tide models, FES2014b (Carrère *et al.* 2016), GOT4.10c (Ray 2013), TPXO8-Atlas (Egbert and Erofeeva 2002), NAO.99b (Matsumoto *et al.* 2000), HAMTIDE11a (Taguchi *et al.* 2014), DTU10 (Cheng and Andersen 2011), and EOT11a (Savcenko and Bosch 2012), were computed using NLOADF, and the phasor differences from the mean of the displacements for each cell of a  $0.25^\circ \times 0.25^\circ$  global grid were generated. The RMS magnitudes of these phasor (vector) differences for the modelled height component for the M2 and K1 constituents are shown in Figure 5.1, and similar maps for the smaller constituents N2, K2, O1, P1 and Q1 are provided in Appendix D. The largest inter-model discrepancies of about 3 mm arise around the Weddell Sea, the Ross Sea, Baffin Bay, Baffin Island (outside the TOPEX/POSEIDON and Jason altimetry satellite data coverage and where the ice grounding zone is poorly determined) and the Philippines, while there are further

more localised areas where the discrepancies are about 1 mm, such as in the Arctic Ocean, northern Australia, the Gulf of Alaska and the north coast of Brazil. Therefore we only considered GNSS stations away from these areas, and selected 49 stations for GNSS processing which all fulfilled the criterion  $Max\{RMS_i, i = M_2, N_2, K_2, K_1, O_1, P_1, Q_1\} < 1mm$  as well as fulfilling the GNSS data criteria described above. As stated above, we used an elastic Green's function based on PREM for all of our computations, and at our 49 stations, the M2 constituent height component displacements differ by only 0.16 mm RMS from when the anelastic Green's function of Wang *et al.* (2020) is used. Ocean tide model variations caused 0.7-0.8 mm RMS inter-model agreement for the predicted M2 OTL height displacements at OHI2, TOW2, TRO1, VARS, and WARK (labelled in Figure 5.1), which is mostly caused by 0.8-1.5 mm discrepancies arising from the NAO.99b model. If this model is excluded, the RMS inter-model agreement per station is reduced to 0.4-0.7 mm, but these stations are still the worst-performing. All other stations' predicted OTL displacements agree better than 0.5 mm regardless of ocean tide model choice.

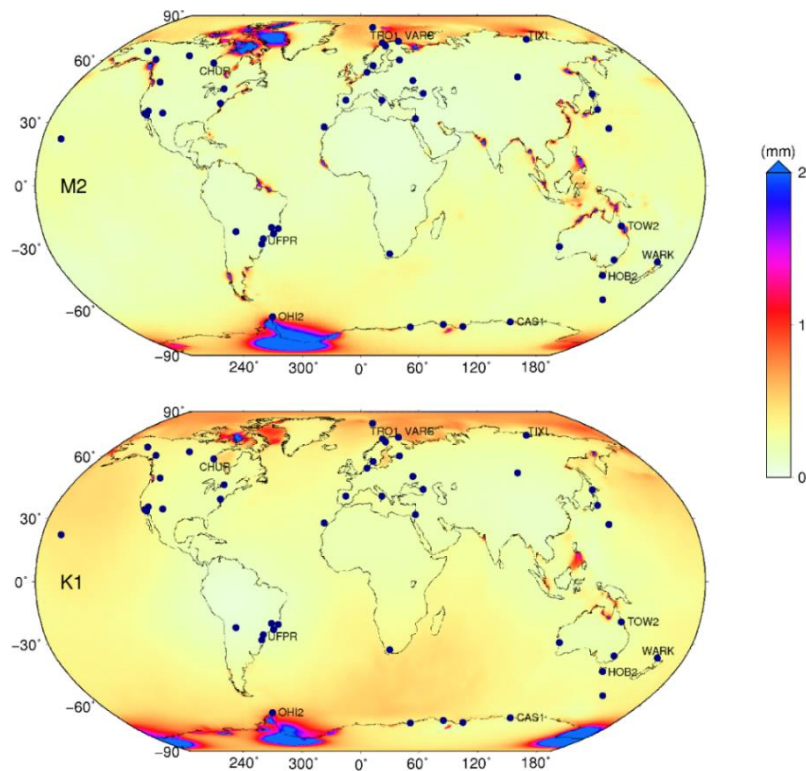


Figure 5.1: RMS agreement of the magnitudes of the vector differences for the predicted OTL height displacement (in mm) per cell of a  $0.25^\circ$  global grid for the M2 and K1 constituents based on seven recent ocean tide models (FES2014b, GOT4.10c, TPX08-Atlas, NAO.99b, HAMTIDE11a, DTU10, and EOT11a), with GNSS stations used in this paper shown as dark blue dots. The colour scale saturates at 2 mm RMS (maximum RMS for both M2 and K1 is 3 mm). The five stations with the largest (0.7-0.8 mm) inter-model disagreement (OHI2, TOW2, TRO1, VARS and WARK) are labelled, as are the five stations co-located with radiosonde observations (CAS1, CHUR, HOB2, TIXI and UFPR).

### 5.3.2 PANDA software validation

As we are not aware of any previous publications using PANDA kinematic PPP to estimate OTL displacements, we initially assessed its GPS-only capability using two tests. First, we introduced a synthetic harmonic displacement signal and assessed how well it may be recovered using our PANDA kinematic PPP estimated GPS height time series. Second, the power spectral density (PSD) from GPS kinematic PPP height time series from PANDA were compared with those using the GNSS-Inferred Position System (GIPSY) software, which is regarded as valid because GIPSY height time series have been shown by Penna *et al.* (2015), Bos *et al.* (2015) and Martens *et al.* (2016) to estimate OTL displacement to an accuracy of better than 0.5 mm.

All data from all stations marked on Figure 5.1 (and listed in Appendix D) were processed using PANDA in GPS-only mode with a  $10^\circ$  elevation angle cut-off, and a 5 mm amplitude (phase assigned as zero at J2000) synthetic harmonic height displacement with 13.96 hour period was applied to the data in order to test the harmonic displacement measurement accuracy and precision. This follows the validation methodology of Penna *et al.* (2015), except here we implemented this by changing the satellite instantaneous position rather than the nominal reference coordinate of the ground station. At each data epoch, we generated a height displacement signal in the GNSS station's local topocentric frame. Then the station's approximate latitude and longitude were used to construct the matrices to convert from the topocentric frame to the geocentric Earth fixed frame of the orbits. After converting the synthetic signal 3D coordinates (with zero values for the east-west and north-south components) to the IGS orbit coordinate frame in this way, the displacements were applied to the satellite positions. Similar to Penna *et al.* (2015), we then varied the process noise values of the station coordinates and the ZWD, to minimise the synthetic signal recovery error, estimated height repeatability, RMS of the observation post-fit residuals, and RMS discrepancy between GPS-estimated tropospheric delay and that estimated from nearby radiosonde data where available. Based on analysis of five of the stations in different parts of the world (CAS1, CHUR, HOB2, TIXI and UFPR, labelled on Figure 5.1), we found optimum values of  $1.0 \text{ mm}/\sqrt{h}$  and  $3.0 \text{ mm}/\sqrt{s}$  for the ZWD and coordinate process noise, respectively, and hence these values are used for the GNSS kinematic PPP data processing throughout the rest of this paper. In Figure 5.2a, the phasor differences between the true synthetic signal and its estimated values at all stations are shown. As this figure indicates, the residual vectors are randomly distributed with a very small mean  $\mathbf{R}_m = (0.02, 0.01) \text{ mm}$ . Therefore, we applied the Rayleigh distribution (e.g., Maymon 2018) for the statistical assessment of the synthetic signal recovery error, and the best fit probability distribution function (PDF) and its equivalent cumulative



distribution function (CDF) are shown in Figures 5.2b and 5.2c, respectively. For more than 95% of the tested GNSS stations the synthetic signal was recovered with an error less than 0.5 mm in magnitude. This is approximately equivalent to the 0.2-0.4 mm RMS reported by Penna *et al.* (2015) for GIPSY, but uses more stations (49 rather than 21) which are distributed globally, not just in western Europe. The PANDA solution uses float not fixed carrier phase ambiguities. The similarity between the PANDA synthetic signal displacement recoveries and those of Penna *et al.* (2015) also suggest that for tidal constituents with periods clearly distinct from 12 or 24 hours, there is no significant degradation in using 24 hour session lengths with concatenated 24 hour orbits and clocks rather than 30 hour GPS processing session lengths with 30 hour orbit and clocks.

To compare directly with the PANDA GPS height time series, GPS data over the same time span from all 49 stations were processed using GIPSY v6.4 in kinematic PPP mode, with the processing method following that described in Bos *et al.* (2015). The key differences between the PANDA and GIPSY processing are that in GIPSY: the VMF1 mapping function was used; the data were processed in 30-hour sessions and the central 24 hours of estimated coordinates extracted and concatenated; JPL repro3 fiducial satellite orbits and 30-second clocks computed in the IGB14 reference frame were held fixed; and the nominal FES2014b / PREM Green's function OTL displacements applied were computed in the CM frame to ensure compatibility with the JPL orbits and clocks. The resulting mean (stacked) PSD plot for the ambiguity-float GIPSY height time series for all 49 stations is shown in Figure 5.3, and superimposed on it is that from the PANDA GPS-only processing. It can be seen that they are very similar, with the PANDA results showing slightly (11-18%) more noise PSD averaged across the non-tidal bands 0.2-0.8 cycles per day (cpd), 1.2-1.8 cpd and 2.2-2.8 cpd. This confirms that PANDA GPS-only processing gives commensurate kinematic float PPP results to GIPSY. This similarity exists despite these solutions using different orbit and clock products which have different reference frames (the ESA products are operational and initially in the IGS08 frame but switched to IGB14 at GPS week 1934, whereas the JPL ones are repro3 products in the IGB14 frame) and may be subject to changes in ESA processing strategy over time for the operational products. However, this similarity further substantiates the findings of Penna *et al.* (2015) who noted that OTL displacement estimates are not sensitive to reference frame changes.

Previous studies (e.g., Penna *et al.* 2015; Bos *et al.* 2015; Martens *et al.* 2016) have used ambiguity-fixed GPS kinematic PPP within GIPSY (Bertiger *et al.* 2010) as the most robust solution for the GPS-derived OTL displacement, so this will be taken as the reference solution for comparison of the ambiguity-float PANDA GPS-only, GLONASS-only and combined

GPS+GLONASS solutions later in this paper. To illustrate the effect of ambiguity fixing, Figure 5.3 also compares the stacked PSDs of our ambiguity-fixed and ambiguity-float GIPSY GPS solutions. Ambiguity fixing leads to a reduction in noise across the entire frequency range (35-45% smaller noise PSD in the three non-tidal bands mentioned above), although this reduction is marginal at the highest frequencies. We will in the next section investigate to what extent the addition of GLONASS data can mitigate the lack of ambiguity resolution in our PANDA solutions, and constellation-related GPS errors. A notable feature of all solutions shown in Figure 5.3 is the frequency comb of increased noise at frequency multiples of K1 (23h56m period) and K2 (11h58m period), arising from errors in GPS which are sidereally-repeating (station-satellite geometry and multipath) and orbitally-repeating (satellite orbits and clocks) respectively. These errors, resulting from the 11h58m orbital period of GPS satellites, are a principal motivating factor for including GLONASS in our analysis, although they are accompanied by some daybreak noise, centred on frequency multiples of S1 (24h period), which we would expect to persist in all solutions based on 24-hour data segments.

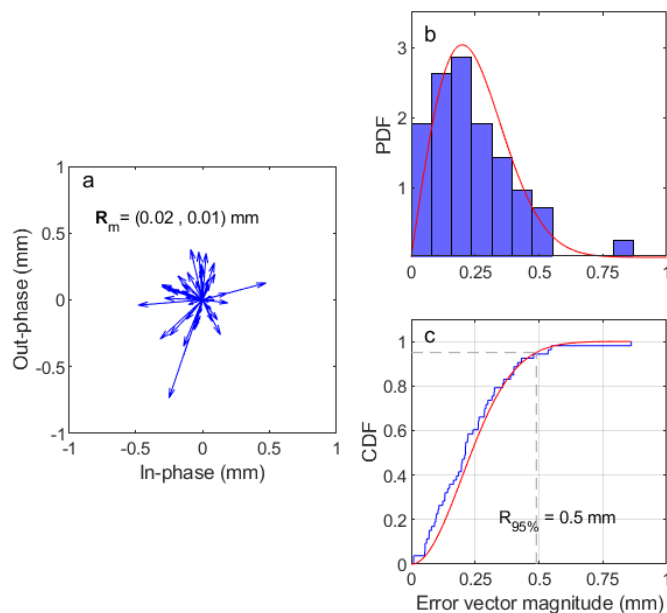


Figure 5.2: a) Signal recovery error phasors from the introduction of a 13.96 hour harmonic height displacement for the PANDA GPS-only height solutions, b) normalised probability distribution function (PDF) histogram of their vector magnitudes, and c) cumulative probability distribution (CDF) over all 49 GNSS stations listed in Appendix D. The smooth red curves in (b) and (c) are for the fitted distribution functions.

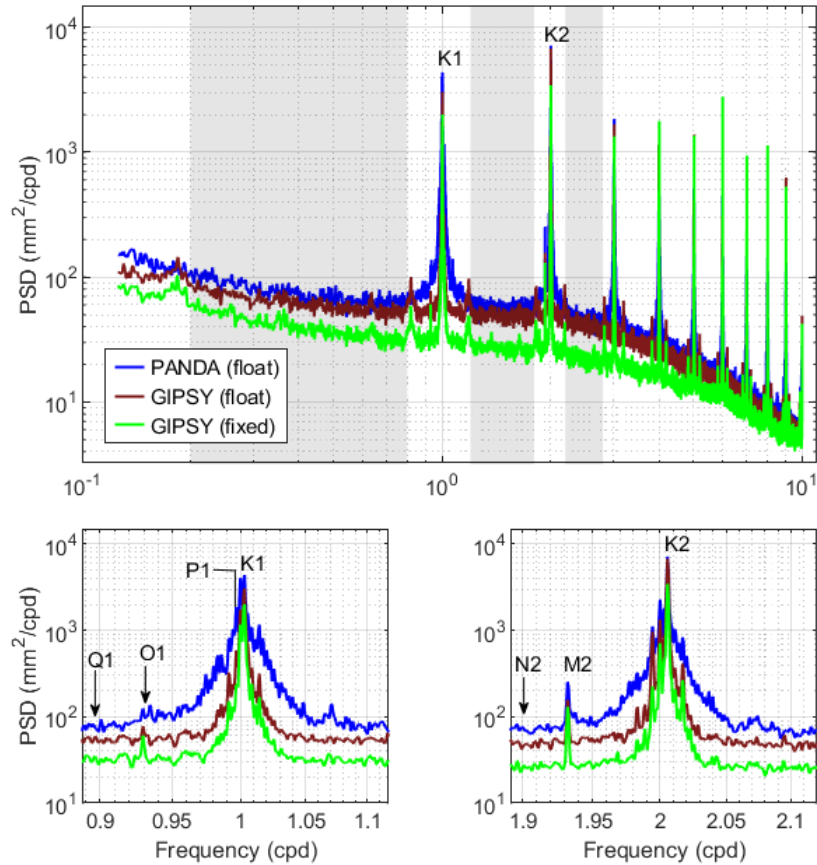


Figure 5.3: Mean stacked power spectral density (PSD) for the GPS-derived height time series for the 49 globally-distributed GNSS stations processed using both PANDA (ambiguity-float) and GIPSY (ambiguity-float and ambiguity-fixed). All solutions used a  $10^\circ$  elevation cut-off angle. The shaded bandwidths (0.2-0.8 cpd, 1.2-1.8 cpd and 2.2-2.8 cpd) are used for the noise PSD comparisons. The lower panes show enlargements of the diurnal and semi-diurnal frequency bands.

#### 5.4 GLONASS data contribution to OTL displacement measurement

The quality of kinematic PPP solutions is very sensitive to the number of satellites and their geometric distribution at each epoch (e.g., Li *et al.* 2015). The GPS constellation consists of at least 24 satellites distributed in six near-circular orbits of approximate radius 26559 km, inclined at  $55^\circ$  to the equatorial plane, with a  $60^\circ$  longitude separation between their ascending nodes. The GLONASS constellation also consists of 24 operational satellites, but they are distributed evenly across three near-circular orbits with approximate radius 25471 km, inclination angle  $65^\circ$ , and longitude separation of  $120^\circ$  for the ascending nodes. These differences in satellite constellation change the temporal and spatial variation in GNSS satellites' availability and viewing geometry, and the consequent dilution of precision (DOP) in different locations; thus kinematic PPP performance is affected (Pan *et al.* 2017). In particular, to estimate independent coordinates and receiver clock terms at each epoch within a phase-connected data arc, a minimum of four satellites is required for a single-constellation solution, or five satellites for a dual-constellation solution where the GPS-GLONASS system

time offset also needs to be estimated. Epochs when this minimum is approached, or when the geometric dilution of precision is high, may not achieve reliable outlier identification and hence the position estimates may be unreliable (especially as 30-minute tropospheric parameters and constant ambiguity parameters are also estimated in our solutions).

Using the initial elevation cut-off angle of  $10^\circ$ , we noted particularly poor performance of some GLONASS-only PPP solutions, which we investigated as follows. We used the TEQC program (Estey and Meertens 1999) to inspect the RINEX observation files of all stations from 00:00 UTC on 15 January to 00:00 UTC on 21 January 2016, a sample time span during which all stations recorded all 30-second data epochs with no receiver tracking outages. The average daily percentage of epochs for which at least seven GPS or seven GLONASS satellites were recorded is shown in Figure 5.4. It can be seen that when a  $10^\circ$  mask angle is used, all stations obtain data from at least seven GPS satellites at virtually all epochs, whereas for GLONASS data this success rate varies with station latitude, from around 50% for latitudes between  $20^\circ$ - $30^\circ$  rising to at least 95% at latitudes of  $50^\circ$  and above. Figure 5.4 also indicates that for stations with latitudes less than  $50^\circ$ , reducing the mask angle to  $5^\circ$  can significantly increase the percentage of epochs with ample GLONASS observations. Although satellites at lower elevation angles will have lower quality observations because of increased atmospheric propagation errors and multipath, this is mitigated by elevation angle dependent data weighting. In PANDA, for any observation collected at an elevation angle ( $E$ ) less than  $30^\circ$ , the pre-defined standard error is scaled by  $\{2\sin(E)\}^{-1}$ , following Gendt *et al.* (2003).

Hence, we classified stations into two groups based on their latitude: stations within  $50^\circ$  of the equator, and those at higher latitudes, to evaluate the impact of the data mask angle on kinematic PPP performance. After running kinematic PPP solutions for all stations with  $5^\circ$  and  $10^\circ$  elevation cut-off angles for GPS-only as well as GLONASS-only data, the mean PSDs of the estimated height time series for each region were computed. Figure 5.5 demonstrates slightly lower performance for the GPS-only kinematic PPP solution for stations in the equatorial band, compared with the high-latitude group. For GPS, mean vertical DOP improves slightly at lower latitudes, but we hypothesise that this is offset by greater atmospheric delay variability which impacts the position estimates. Reducing the elevation cut-off angle improves the time series precision very slightly in both regions, which can be explained by the typically increased number of recorded GPS measurements and reduced DOP at each data collection epoch. In Figure 5.6, we present the mean stacked PSDs for the estimated height time series from GLONASS-only data, which also show larger noise for the lower-latitude group. However, in this case there is much smaller latitudinal variation in mean DOP, and we hypothesise that the

effects of atmospheric delay variability are more extensively compounded because of the smaller number of satellites typically observed. As can be seen in Figure 5.6 (middle and bottom panels), the amplitude modulation of the K2 and K1 constituents on the GLONASS satellite ground track repetition signal ( $K_{1/8}$ ) causes peaks which are symmetrically distributed around K2 and K1, but which are not present in the equivalent plots for GPS shown in Figure 5.5. Figure 5.6 also indicates that a reduction in data processing elevation cut-off angle enhances GLONASS-only kinematic PPP performance more for lower than for higher latitude stations. Therefore because of this improved precision with a  $5^\circ$  instead of  $10^\circ$  elevation cut-off angle for both GPS and GLONASS constellations and across all latitude bands, we use a  $5^\circ$  cut-off angle for all PANDA GPS-only, GLONASS-only and combined GPS+GLONASS data processing for the remainder of this paper.

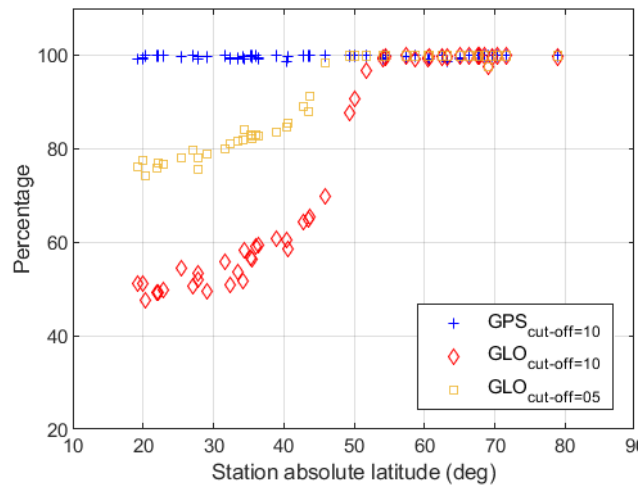


Figure 5.4: Mean percentage of epochs with at least seven recorded satellites, as a function of station absolute latitude, for six consecutive days in January 2016 for all 49 stations, for different elevation cut-off angles.

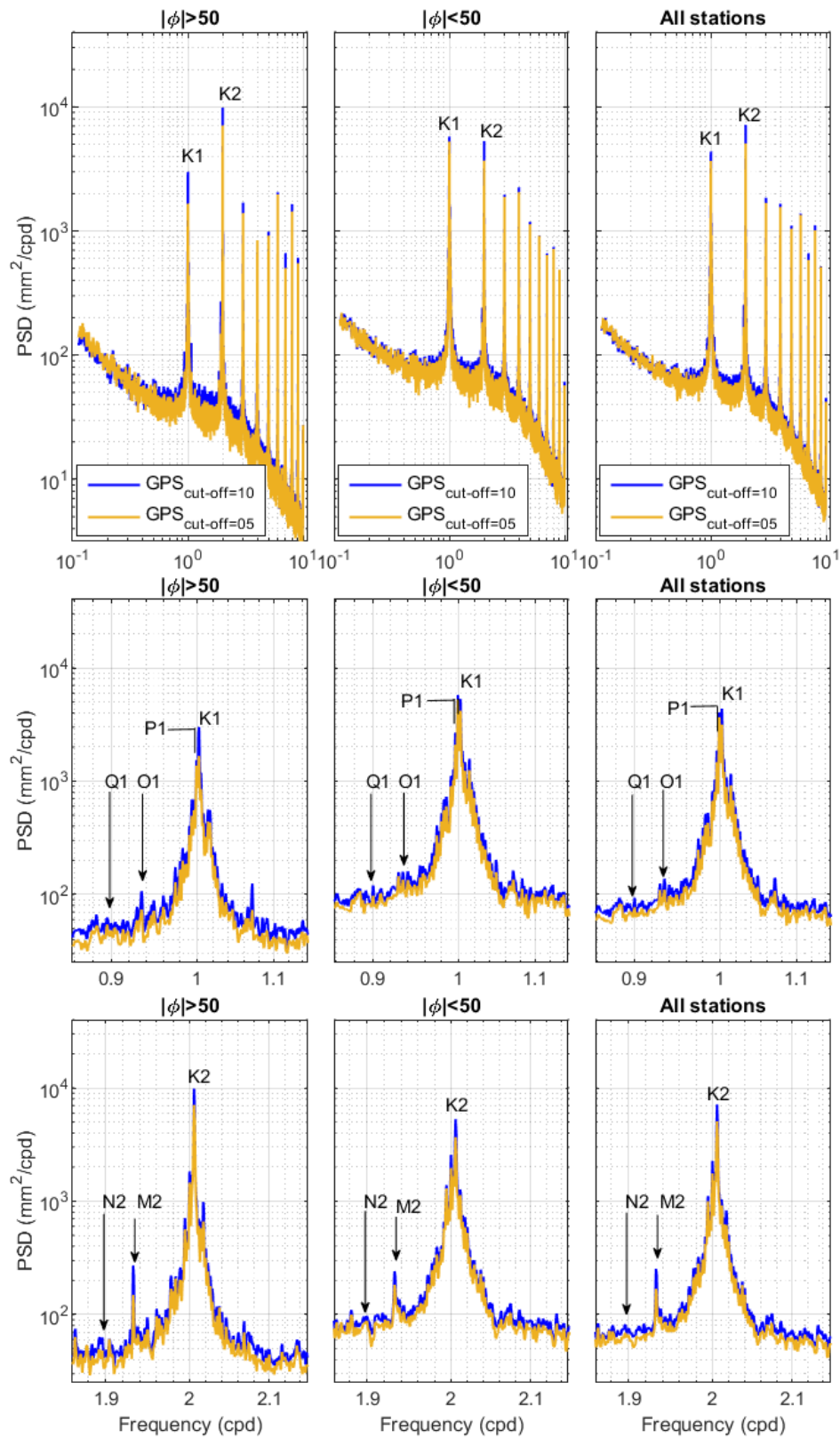


Figure 5.5: Mean stacked PSD of the height time series from PANDA GPS-only kinematic PPP ambiguity-float solutions with different elevation cut-off angles. Stations with absolute latitude ( $\phi$ ) greater than  $50^\circ$  are in the left panel, lower-latitude stations are in the centre panel, and the right panel is for the entire dataset.

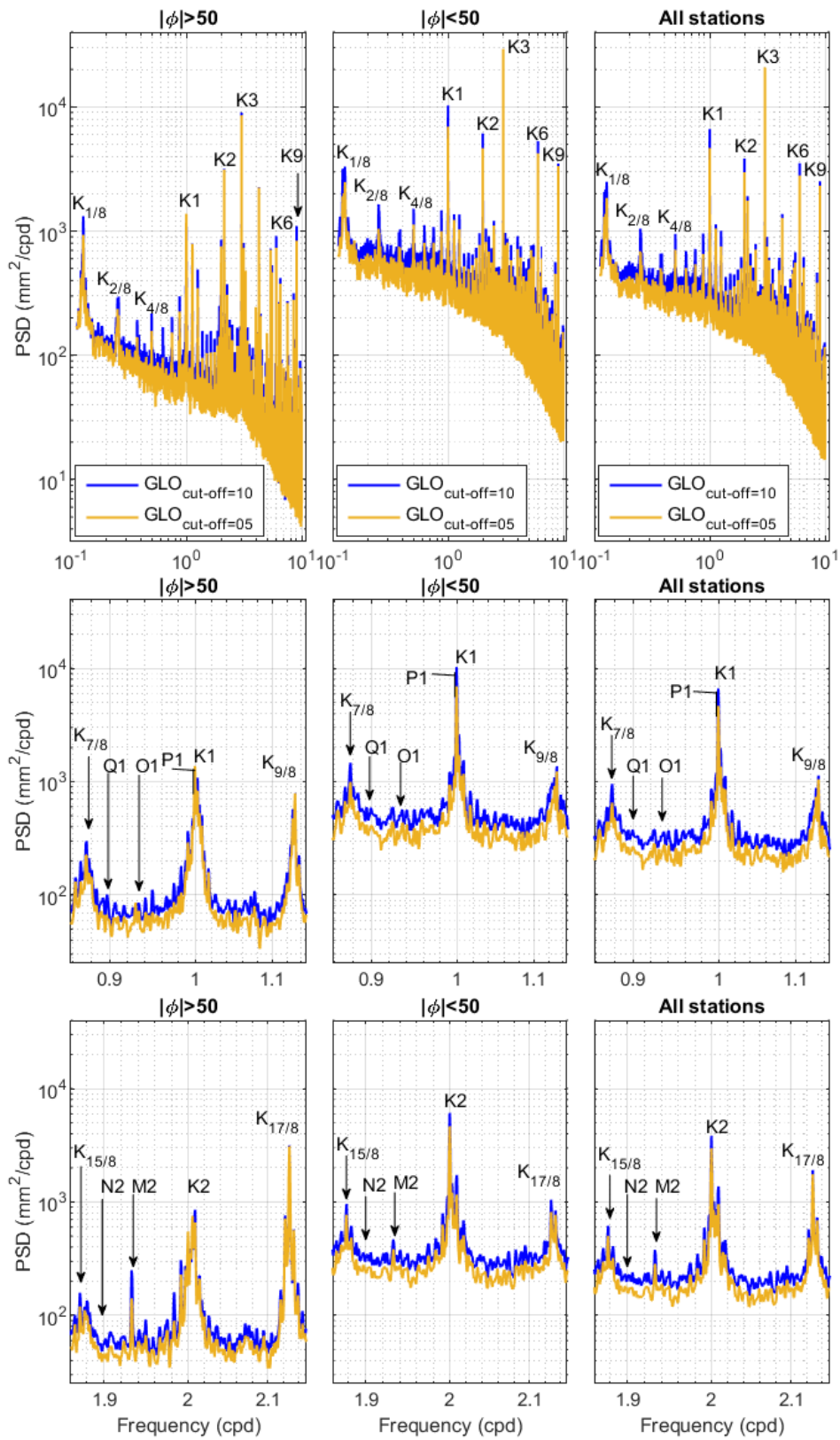


Figure 5.6: Similar to Figure 5.5 but for GLONASS-only data.

In Figure 5.7, the mean stacked height time series PSDs of the GPS ambiguity-fixed solutions from GIPSY, and those for the GPS, GLONASS, and combined GPS+GLONASS ambiguity-float solutions from PANDA are compared. The GLONASS-only solution has generally greater noise than GPS-only, likely because of fewer available GLONASS satellites especially in mid-latitude areas, and lower quality GLONASS satellite clock/orbit products (e.g., Prange *et al.* 2017). However, by combining GPS and GLONASS data in a float solution, the noise level of the estimated height time series is considerably reduced, and it shows generally similar or even smaller noise compared with the GPS-only ambiguity-fixed solution in GIPSY (0-8% reduction in noise PSD across the 0.2-0.8 cpd, 1.2-1.8 cpd and 2.2-2.8 cpd non-tidal bands). This demonstrates the benefit of incorporating GLONASS data if an ambiguity-fixing algorithm is not implemented in a PPP software package, or when uncalibrated phase delay (UPD) information, which is required for PPP ambiguity fixing, is not available.



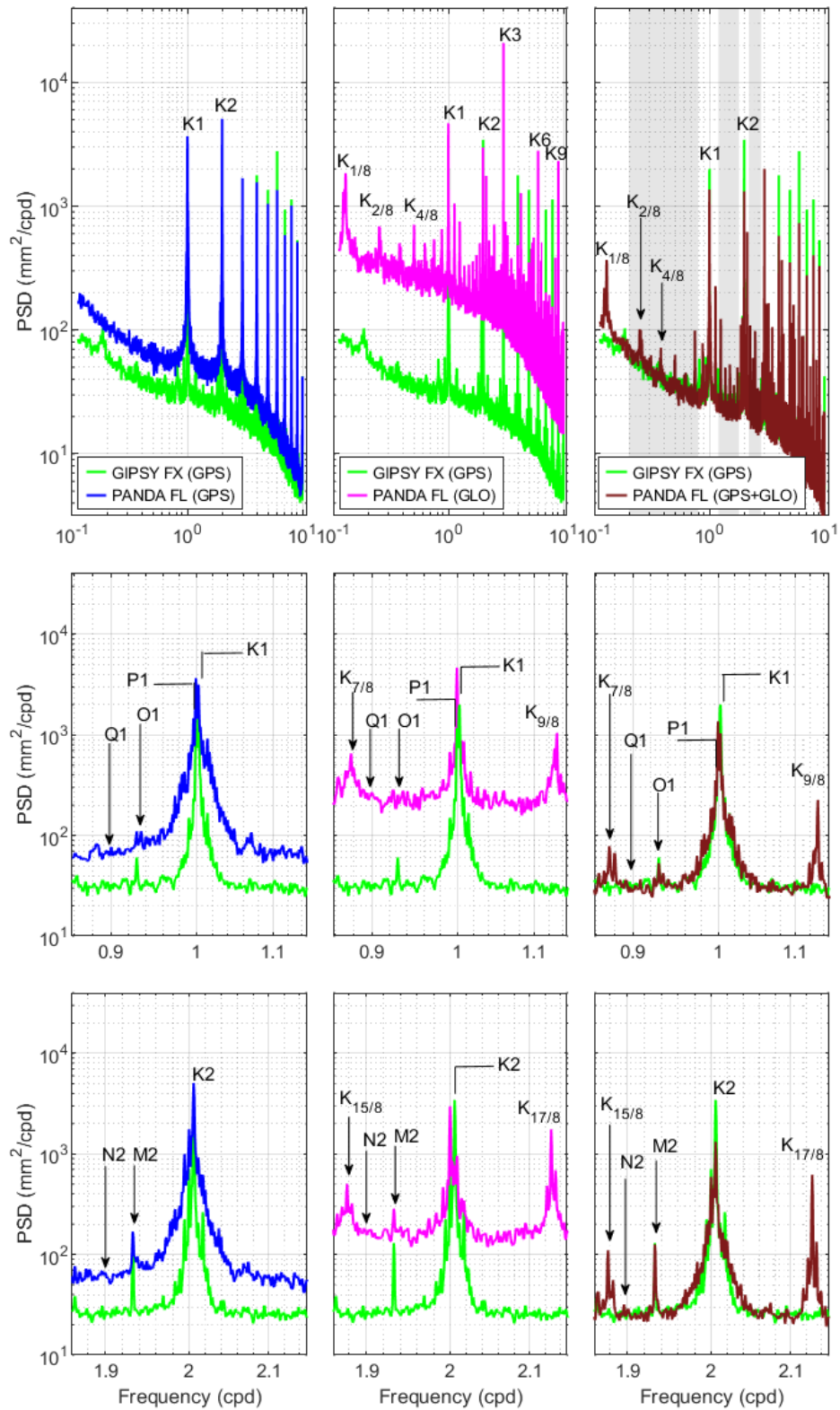


Figure 5.7: Mean stacked height time series PSDs from GIPSY ambiguity-fixed GPS-only solutions and GPS-only, GLONASS-only and combined GPS+GLONASS ambiguity-float solutions in PANDA. For all PANDA solutions a  $5^\circ$  elevation cut-off angle is used. The shaded bandwidths (0.2-0.8 cpd, 1.2-1.8 cpd and 2.2-2.8 cpd) are used for the noise comparison.

Although the noise level is generally higher, most of the peaks at frequencies  $n \cdot K1$  in the GLONASS-only PSD are smaller in absolute terms than those in any of the GPS-only solutions. This is because the 11h16m orbital period of GLONASS satellites does not combine with the sidereal rotation of the Earth to create an exact station-satellite geometry repeat as it does for GPS, so sidereally-repeating errors such as multipath are much reduced in a GLONASS-only solution. However, small errors remain because there does exist a weak approximate geometry repeat arising from the interaction between the  $2\frac{1}{8}$  GLONASS satellite orbits per sidereal day and the equal separation of eight satellites per GLONASS orbital plane. This means that after one sidereal day the satellite geometry as seen from a station will repeat, although different satellites will be involved. These small peaks can be seen in the GLONASS spectrum, with larger peaks at  $3 \cdot K1$  (K3) and  $9 \cdot K1$  (K9) caused by the  $120^\circ$  longitude separation of the three GLONASS orbital planes. Also, the GLONASS solution shows slightly increased noise at period  $K_{1/8}$  and its frequency multiples, caused by the true GLONASS geometry repeat interval of 8 sidereal days. The combined ambiguity-float GPS+GLONASS PANDA solution is still contaminated by the sidereally-repeating errors arising principally from GPS, but whereas overall noise levels are similar, the magnitude of all  $n \cdot K1$  peaks is reduced compared with any of the GPS-only solutions.

### **5.5 Comparison between GNSS-derived and modelled OTL displacements**

We inspect OTL height displacements for the M2, N2, K2, K1, O1, P1 and Q1 constituents obtained from GPS-only, GLONASS-only and combined GPS+GLONASS solutions at each of the 49 stations. The vector differences between the predicted (modelled) and GNSS-derived OTL displacements are shown in Figure 5.8, and their statistics summarised in Table 2. The largest M2 residuals (of about 1.2 mm even for the combined GPS+GLONASS solution) are for the stations TOW2, TRO1, VARS and WARK, for which 0.7-0.8 mm inter-model disagreement for the predicted M2 OTL height displacement was noted in Section 5.2. Figure 5.8 demonstrates that the vector differences for all constituents are distributed randomly around zero with a mean well below 0.5 mm, which again leads us to use the Rayleigh distribution for their statistical analysis. The estimated OTL height displacement residuals with their best-fitted Rayleigh CDF are presented in Figures 5.9-5.15.

As depicted in Figure 5.9 for the M2 constituent, the estimated OTL height displacement residuals with GPS-only and GLONASS-only measurements are smaller than 1.2 mm and 1.3 mm, respectively, at about 95% of the processed stations. When excluding the five stations at which the largest M2 disagreements arose (OHI2, TOW2, TRO1, VARS and WARK), these 95% limits are slightly reduced to 1.0 mm and 1.2 mm (not shown in Figure 5.9). This indicates

the near-similarity in capability of GPS-only and GLONASS-only data to estimate OTL displacement for M2. The slight improvement in vector difference residuals by a factor of 1.2 with GPS rather than GLONASS is also commensurate with the PSD differences around the M2 frequency shown in Figure 5.7. Also in accordance with the PSD GPS+GLONASS noise reductions over GPS-only and GLONASS-only, the combined GPS+GLONASS data provides the smallest residuals for M2: for the 44 better-modelled stations the 95th percentile is reduced to 0.9 mm for this estimate and the mean magnitude of these residuals is 0.4 mm, commensurate with the ambiguity-fixed GPS results of Bos *et al.* (2015). In comparison, Figure 5.10 shows that for N2 OTL height displacement, which is only marginally affected by ocean tide model uncertainty, the estimated residual with combined GPS+GLONASS is smaller than 0.3 mm at 95% of the 49 stations, compared with 0.5 mm and 0.6 mm for GPS-only and GLONASS-only respectively. Similar behaviour for the estimated O1 height residual can be seen in Figure 5.13 and, as for N2 and M2, the improvements in the residuals with GPS+GLONASS are commensurate with the PSD reductions over GPS-only and GLONASS-only shown in Figure 5.7. We suggest that these results, for constituents whose OTL modelling uncertainty is low, are indicative of the inherent GNSS measurement error budget at frequencies well separated from the sidereal and satellite orbit and geometry repeat periods. Poorer agreement at M2 is at least partly due to the greater OTL modelling uncertainty, but might also indicate systematic lunar-origin errors in satellite orbit and clock or Earth body tide modelling.

Figure 5.11 clearly demonstrates the problem of measuring OTL displacement at the K2 frequency from GPS data. The 95th percentile of the estimated K2 height residuals estimated by GPS is 4.4 mm, which is much larger than any uncertainty in OTL modelling and more than two times larger than its counterpart estimated by GLONASS (2.0 mm). Hence, the ability of GLONASS to partially overcome GPS problems in measuring K2 tidal displacement is confirmed. However, the lack of GLONASS agreement to within the level of OTL modelling uncertainty that is indicated by the results for N2 and O1 implies that systematic errors remain, which we suggest may be due to overtones of sidereally-repeating errors such as multipath arising from the approximate geometry repeat of the GLONASS constellation. Figure 5.11 also indicates that the increase in satellite availability and better DOP in the combined GPS+GLONASS kinematic PPP can compensate GPS-specific error in the estimated K2 tidal displacement to some extent, but the latter error dominates and so a combined solution (95th percentile residual 2.4 mm) is not as accurate as GLONASS-only. For the K1 tidal constituent shown in Figure 5.12, the 95th percentiles of the GLONASS-derived and combined GPS+GLONASS estimated K1 residuals are 2.8 mm and 2.6 mm respectively, roughly two-

thirds of the GPS-derived value of 3.9 mm. In comparison to K2, these larger discrepancies might imply further systematic errors in addition to the fundamental sidereally-repeating geometry related errors. Such errors may arise from the 24-hour data segments used in processing and/or orbit integration, as evidenced by the larger discrepancies also noted for the P1 constituent (Figure 5.14) which is similarly close to 24 hours in period. The discrepancies at P1 are identical for GPS-only and GLONASS-only solutions (95th percentile 2.4 mm), indicating that they are not related to orbital or geometry repeat period, but reduce to a 95th percentile of 1.3 mm for the combined solution as expected in accordance with the decreased overall noise level.

It was anticipated from the noise reductions shown in Figure 5.6 that a more robust kinematic PPP solution would arise for the GLONASS-only solutions at higher latitude stations. Therefore in Figures 5.9 to 5.15, we grouped the residuals into two latitude bands, with smaller GLONASS-only M2, N2, O1, P1 and Q1 residuals seen for the higher latitude band than the lower. To quantify this, we computed the 95th percentiles for the estimated OTL displacement residuals by latitude band, and plot these in Figure 5.16 for each of the GPS-only, GLONASS-only and GPS+GLONASS solutions. It can be seen that the M2, N2 and O1 OTL displacements can be measured by GLONASS data with similar accuracy to the GPS observations for high latitude stations, whereas the accuracy of the GLONASS-derived M2, N2, O1, P1 and Q1 estimates is reduced by around 0.2-1.9 mm for the low latitude stations. For K2 and K1, the station latitude effect cannot be seen because the K2 and K1 error sources discussed above dominate.

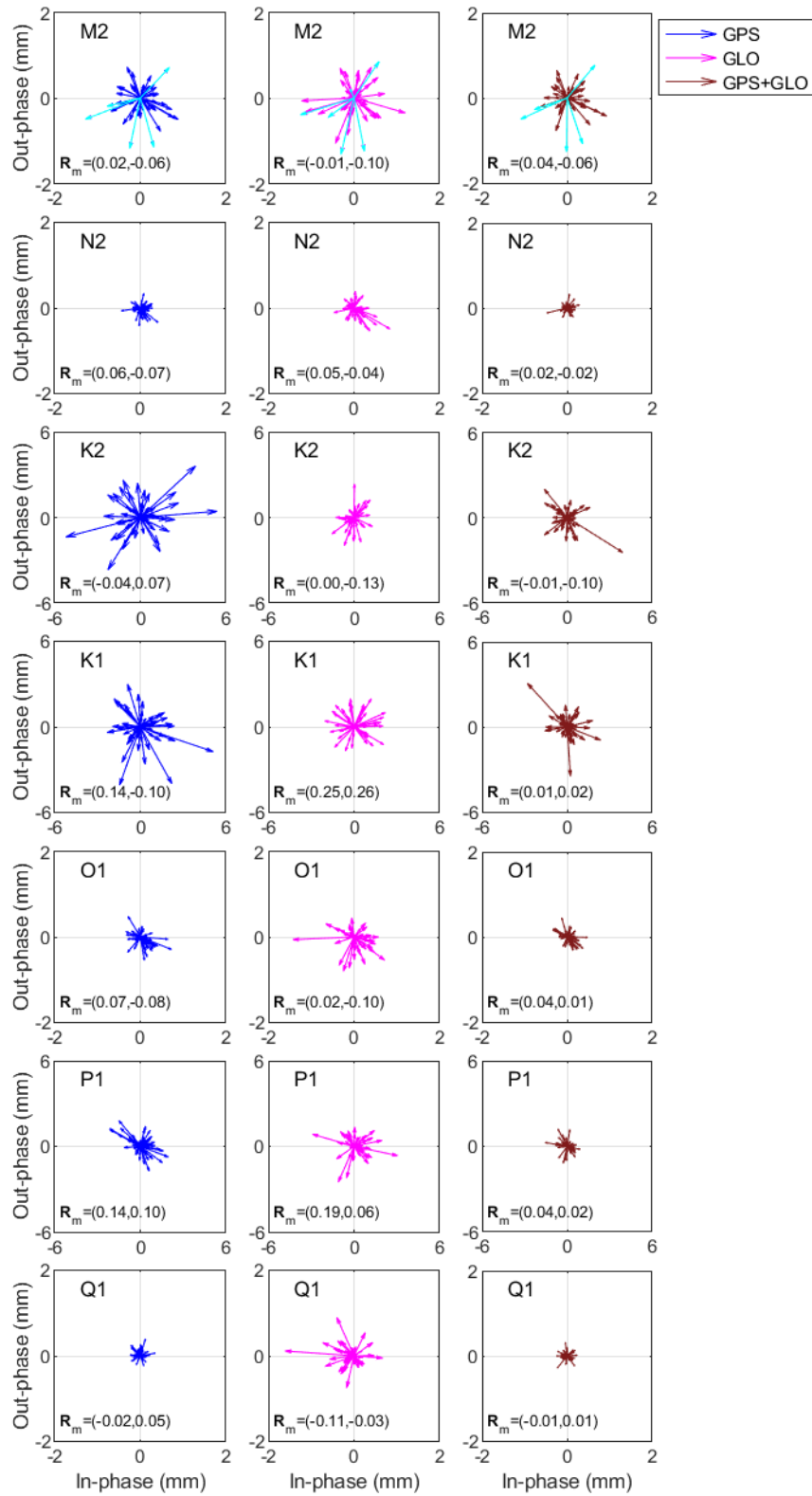


Figure 5.8: Vector differences between GNSS-derived and modelled OTL height displacement for all 49 stations for M2, N2, K2, K1, O1, P1 and Q1. In each panel, the mean of all vector differences ( $R_m$ ) is provided. Note that K2, K1 and P1 are plotted with a different scale to the other constituents. For M2, phasors are highlighted in cyan for stations OHI2, TOW2, TRO1, VARS and WARK, which show larger disagreement among ocean tide models.

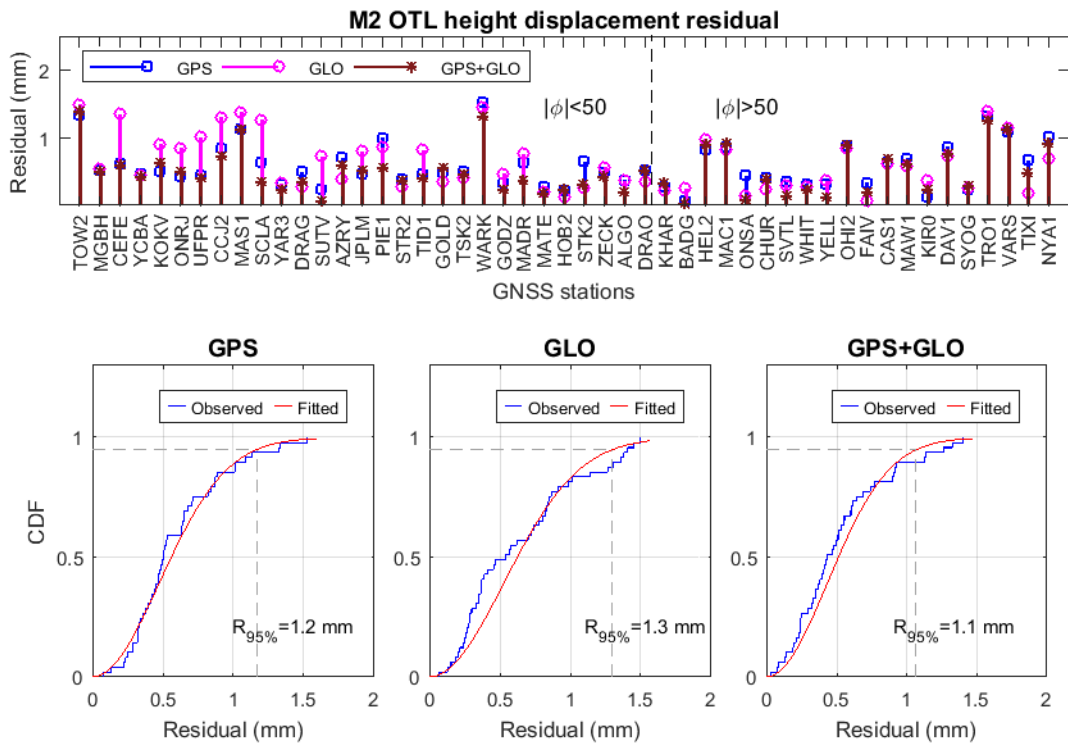


Figure 5.9: Magnitude of vector differences between GNSS-derived and modelled M2 OTL height displacement. In the lower panels, the observed cumulative distribution function (CDF) with its fitted counterpart (based on the Rayleigh probability distribution function (PDF)) is shown and the 95th percentile of the fitted CDF is labelled.

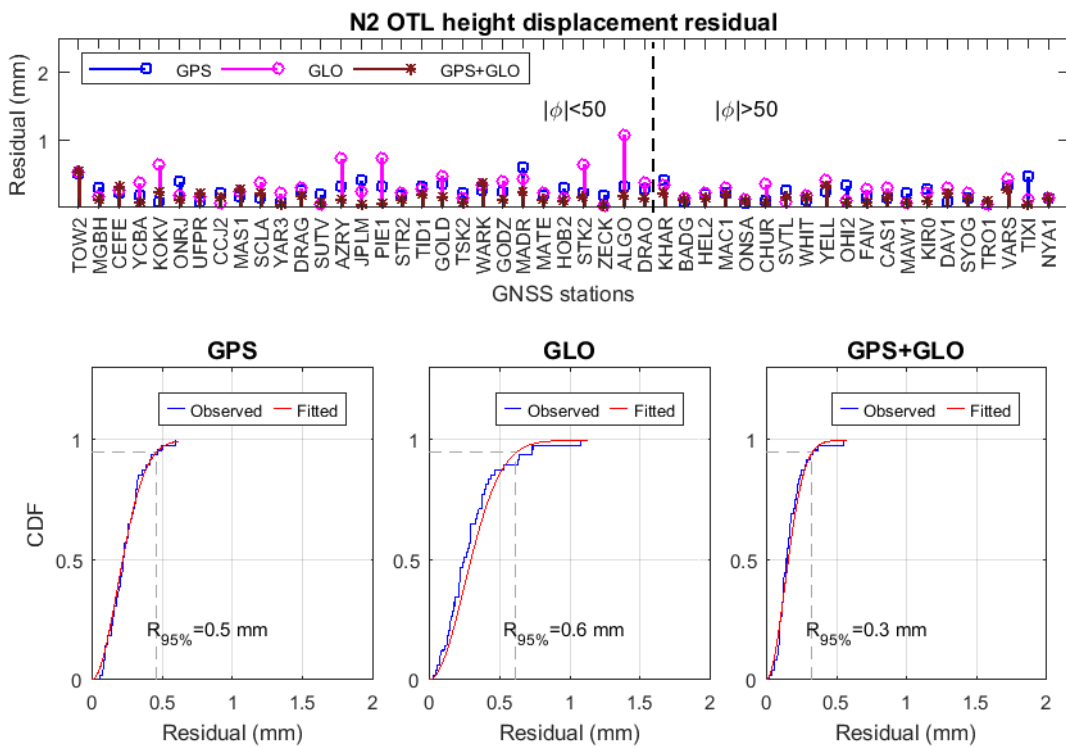


Figure 5.10: Similar to Figure 5.9 but for the N2 constituent.

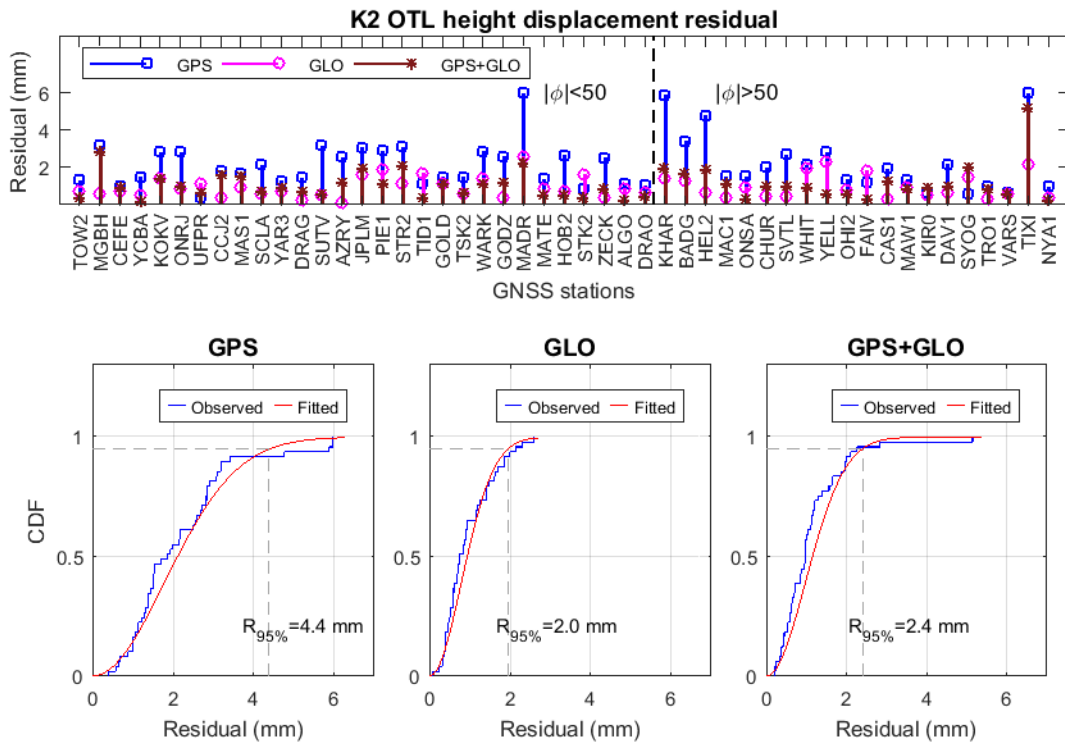


Figure 5.11: Similar to Figure 5.9 but for the K2 constituent (note the different scale matching K1 and P1).

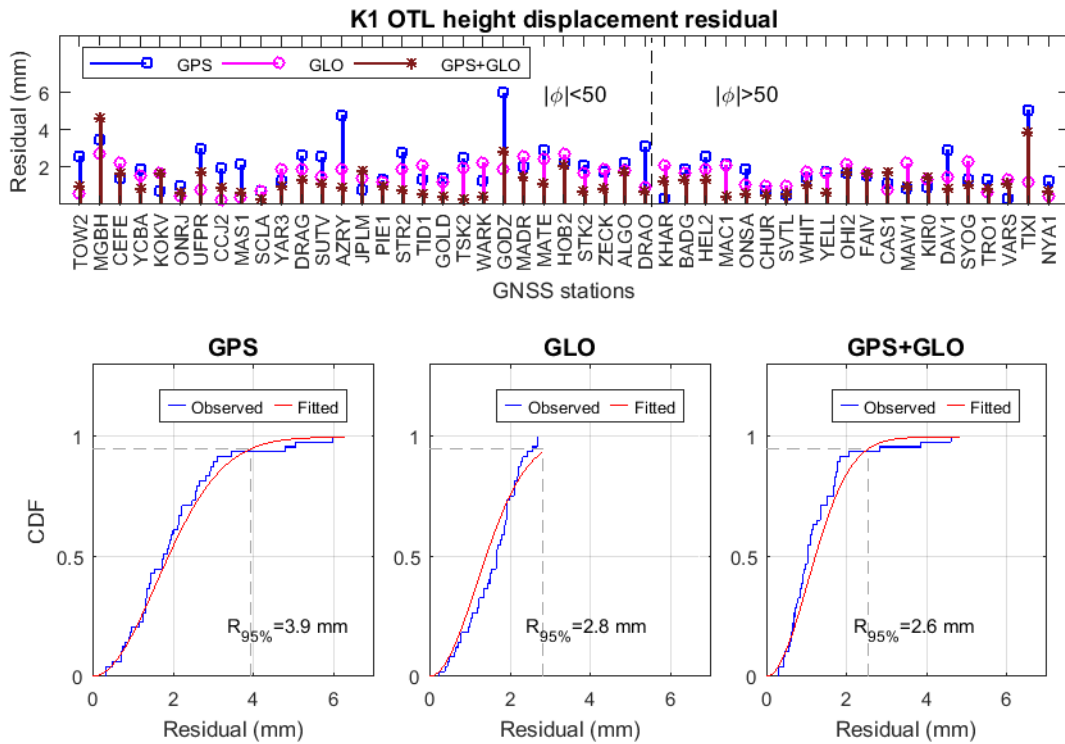


Figure 5.12: Similar to Figure 5.9 but for the K1 constituent (note the different scale matching K2 and P1).

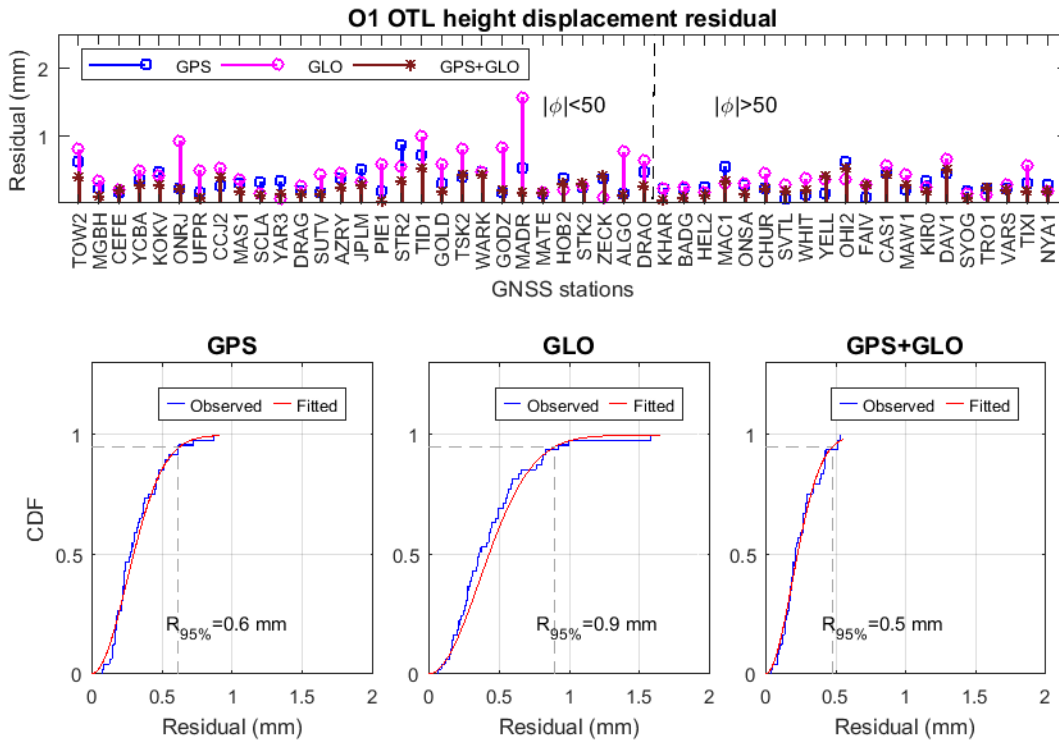


Figure 5.13: Similar to Figure 9 but for the O1 constituent.

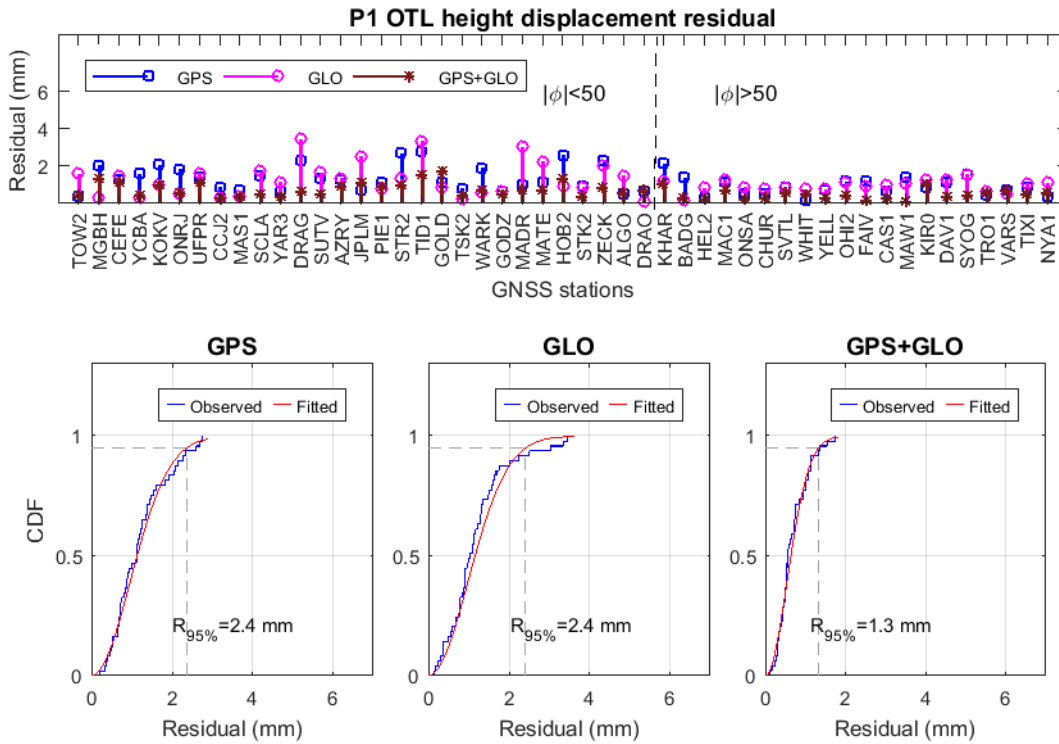


Figure 5.14: Similar to Figure 5.9 but for the P1 constituent (note the different scale matching K2 and K1).



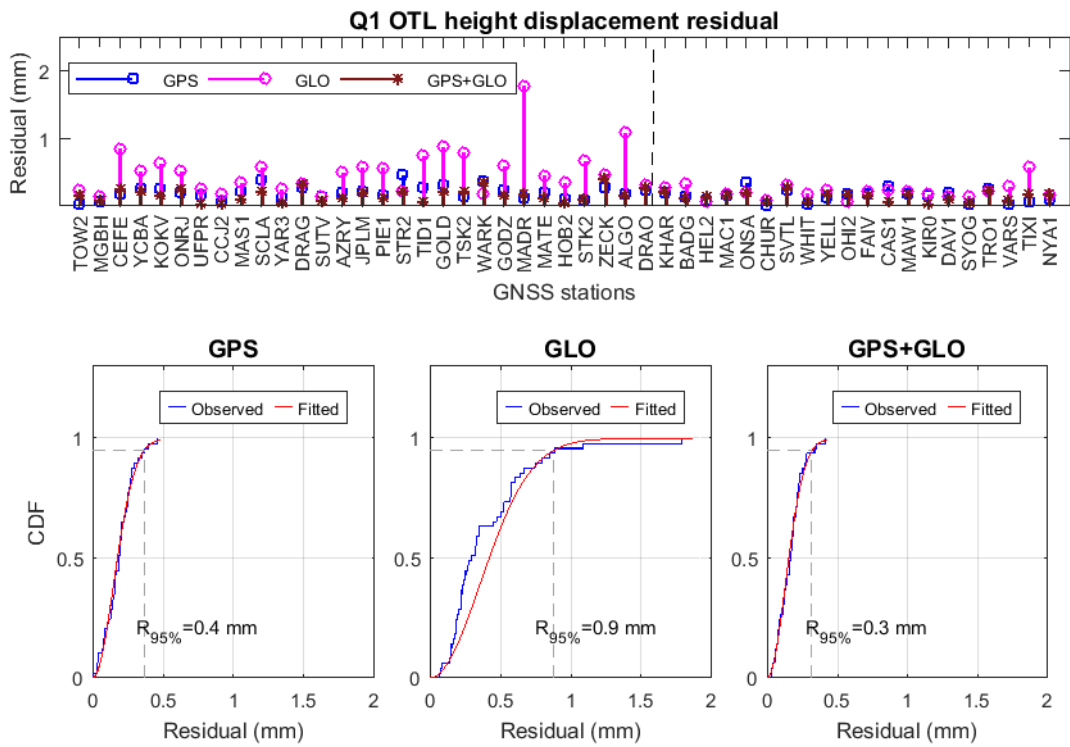


Figure 5.15: Similar to Figure 5.9 but for the Q1 constituent

	95th percentile (mm)		
	GPS	GLO	GPS+GLO
M2	1.2	1.3	1.1
N2	0.5	0.6	0.3
K2	4.4	2.0	2.4
K1	3.9	2.8	2.6
O1	0.6	0.9	0.5
P1	2.4	2.4	1.3
Q1	0.4	0.9	0.3

Table 5.2: 95th percentile of the magnitude of the vector differences between GNSS-derived and modelled M2 OTL height displacement for the 49 stations, for GPS-only, GLONASS-only and GPS+GLONASS solutions

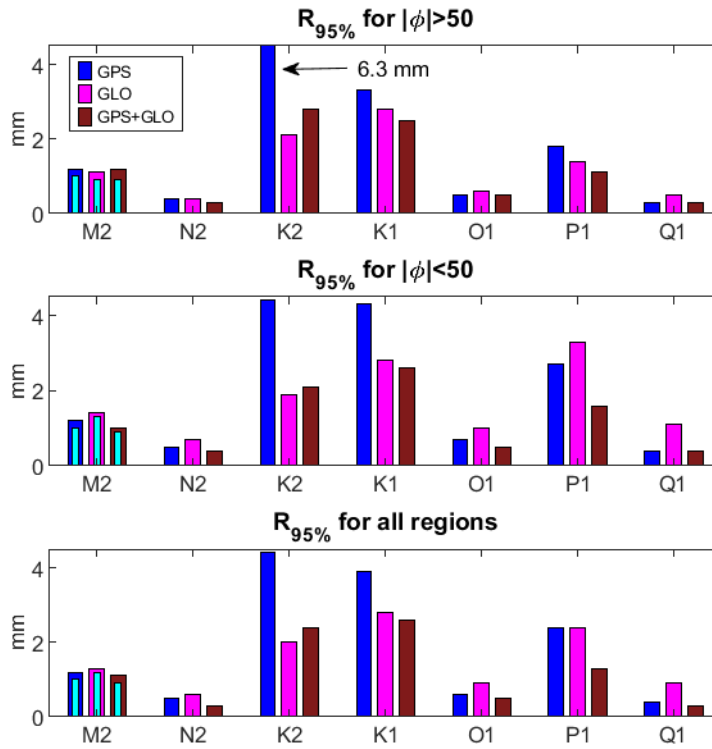


Figure 5.16: 95th percentile for the GNSS minus model M2, N2, K2, K1, O1, P1 and Q1 OTL height displacement residuals grouped by station latitude. The cyan bars shown for M2 were computed after excluding the poorly-modelled stations mentioned in the Figure 5.8.

## 5.6 Discussion and conclusions

We have validated PANDA's robustness as a kinematic PPP displacement estimation software by comparing the spectral characteristics of its height time series noise to those from GIPSY, at hourly to weekly periods. We used a network of globally-distributed GNSS stations fulfilling daily and annual data completeness, located in regions with sub-millimetre consistency in predicted OTL height displacement when computed with different ocean tide models. We found that a low ( $5^\circ$  instead of  $10^\circ$ ) elevation cut-off angle mask was especially beneficial for processing lower-latitude GLONASS-only solutions, and had small but positive impact in other situations. Our investigation of GPS-only, GLONASS-only and combined GPS+GLONASS observation processing in kinematic PPP mode demonstrates three main benefits of incorporating GLONASS data, with particular relevance for measuring OTL displacement.

First, combined GPS+GLONASS kinematic PPP with float ambiguity estimation is as precise as GPS-only fixed ambiguity PPP. However, the former is more flexible, as it is independent of UPD corrections. Even with available UPD information, the ambiguity fixing success rate will decrease when estimated float ambiguities are not precise enough (Teunissen 2017), for

instance in the situation of poor DOP, extreme ionospheric activity, or short phase-connected arcs.

Second, in addition to noise reduction in the combined GPS+GLONASS kinematic PPP compared with single-constellation solutions, it is verified that GLONASS-only float solutions are able to measure the M2, N2, O1 and Q1 constituents of OTL height displacement with almost similar accuracy to GPS-only float solutions. With GLONASS-only, 95% of tidal displacements agreed with forward geophysical models to within 0.6-1.3 mm for the M2, N2, O1 and Q1 constituents, compared with 0.4-1.2 mm for GPS-only. Hence, GLONASS-derived M2, N2, O1 and Q1 OTL displacements can be used as a check for GPS-derived ones and vice versa. Furthermore, OTL displacement estimation from a float solution using combined GPS+GLONASS observations can be as robust as a GPS-only ambiguity fixed solution for these constituents.

Third, we have demonstrated the improved ability of GLONASS data to resolve OTL height displacements at the luni-solar semi-diurnal and diurnal periods (K2 and K1) which are not reliably measurable by GPS on account of the latter's orbital period and station-satellite geometry repeat interval. We found very distinct improvement for purely GLONASS-derived K2 tidal displacement compared to its GPS-derived counterpart (2.0 mm rather than 4.4 mm 95th percentile residual values), and also improved compared with the combined GPS+GLONASS estimate (2.4 mm 95th percentile) which appears to be dominated by GPS-related errors. For the K1 constituent, the GLONASS-only and combined solutions are of comparable quality. However, even the best solutions at K1 and K2 do not agree with the modelled OTL at the level achieved for M2, N2, O1 and Q1. This disagreement may be caused by sidereally-repeating errors which also exist for GLONASS because of its approximate sidereal station-satellite geometry repeat, and errors arising from the use of 24-hour data segments which also affect the nearby P1 constituent. When several years of complete constellation data together with corresponding high accuracy satellite orbits and high rate clocks are available for the Galileo and BeiDou systems (which have further differences in orbital and geometry repeat periods), a combined GPS+GLONASS+Galileo+BeiDou kinematic PPP solution may achieve a further reduction in the K1 and K2 residuals. For example, Abraha *et al.* (2018) showed that even limited Galileo data when added to GPS+GLONASS data reduced the amplitude of spurious propagated tidal signals in GPS coordinate time series. Hence a full, four-constellation kinematic PPP solution using longer data segments could in future provide the potential to be utilised for the refinement of solid-Earth Green's functions and numerical ocean tide models including the K1, K2 and P1 constituents.

## Chapter 6 Ocean tide loading displacement in Alaska

### 6.1 Introduction

GNSS data has been shown in Chapter 5 to be able to recover a synthetic OTL displacement signal with sub-millimetre accuracy. Therefore such GNSS-estimated OTL displacements are sensitive to millimetre level errors in modelled OTL displacement. King *et al* (2005) and King *et al.* (2011) used GPS-estimated OTL displacement to quality control ocean tide models in Antarctica, and Ito and Simons (2011) adapted lithosphere physical parameters based on the GPS-estimated OTL displacement residual in the western United States. Bos *et al* (2015) used GPS to measure asthenospheric anelasticity at the M2 tidal period in western Europe, and Wang *et al* (2020) suggest the other regions where such effects are likely to be observable, including Alaska, south east Africa, north-west Australia, New Zealand, eastern China, west of Central America, and Greenland.

In this chapter, it is aimed to use GPS/GLONASS data from Alaska to validate ocean tide models, Earth's Green's functions, and to probe the Earth's interior, e.g. measure anelasticity effects in the asthenosphere. This region is chosen as many of the other candidate regions where asthenospheric anelasticity is likely to be observable do not have that many GPS stations, and few have GLONASS. Due to their latitude being greater than  $50^{\circ}N$ , Alaska's stations track sufficient GLONASS satellites to enable an accurate kinematic PPP solution, and Alaska is also subject to the largest K1 OTL displacement signal in the world. Since 2016, the GPS-only receivers in Alaska are beginning to be replaced with multi-GNSS ones so the benefits of multi-GNSS data processing for the OTL displacement measurement can be tested in that region.

This chapter is comprised of five sections. In Section 6.2, to recognize those OTL displacement semi-diurnal and diurnal constituents with a potentially GNSS-observable asthenosphere anelasticity effect, the modelled OTL displacements using the convolution integral are considered. Section 6.3 considers quality assessment of ocean tide models in Alaska, and Section 6.4 investigates the GPS-derived OTL displacement residuals based on the most accurate ocean tide model selected in Section 6.3 and different Earth Green's functions. Asthenospheric anelasticity effects on the 3D OTL displacements at the GPS stations are then considered in Section 6.4. Finally, GLONASS data benefits for estimating M2 and K1 OTL displacements are investigated in Section 6.5.

## 6.2 Modelled OTL displacement

As explained by Bos *et al.* (2015), OTL vertical displacement can be affected by the asthenosphere anelasticity up to 8%. Similar to Penna *et al.* (2015) and Wang *et al.* (2020), an accuracy better than 0.5 mm for the GNSS-detected OTL vertical displacement has been demonstrated in Chapter 5 of this thesis. Therefore, for stations with OTL vertical displacement larger than 7 mm, asthenospheric anelasticity effects may be detectable with GNSS observations. To ascertain areas where such effects may be observable, the modelled OTL displacement for M2, N2, S2, K2, K1, and O1 tidal constituents in the east, north and vertical directions for a  $0.0625^\circ \times 0.0625^\circ$  grid across Alaska were computed with SPOTL using the FES2014b ocean tide model and an elastic PREM Green's function. These constituents are considered as they are the largest semi-diurnal and diurnal OTL displacements. The amplitude and phase lag of the modelled OTL displacement are shown in Figures 6.1 to 6.3. As can be seen in Figure 6.1 and Figure 6.2, in some parts of Alaska, the M2 horizontal OTL displacement is larger than 7 mm which makes it testable for the asthenosphere anelasticity. In Figure 6.3, the M2 and K1 vertical OTL displacement are shown to be about 25 mm and 15 mm respectively for almost all the southern Alaskan coastline, which makes them large enough for the anelasticity investigation. This figure also indicates that the S2 and O1 constituents, which are around 10 mm, may contain some GNSS-detectable anelasticity effect. However, atmospheric loading displaces the solid Earth at the S2 frequency which cannot be readily separated from the S2 OTL displacement. For the O1 constituent, the ~8% anelasticity effect (which is around 0.8 mm) is marginal for detection. So, for the rest of this chapter, M2 and K1 OTL vertical and horizontal displacements are considered for further investigation.

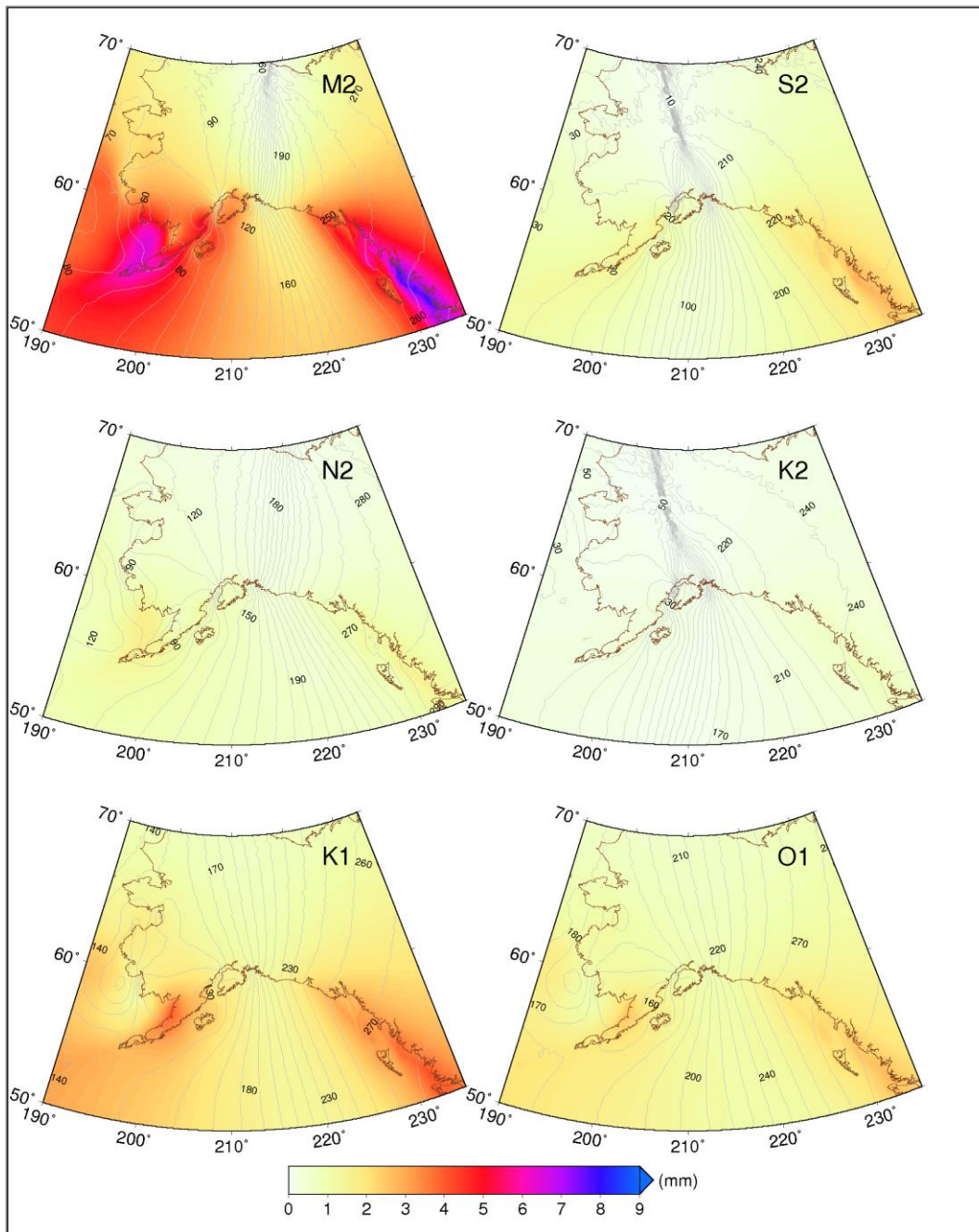


Figure 6.1: Predicted OTL east displacement amplitudes and Greenwich phase lags across Alaska for the M2, S2, N2, K2, K1 and O1 constituents based on the FES2014b ocean tide model and a PREM elastic Green's function.

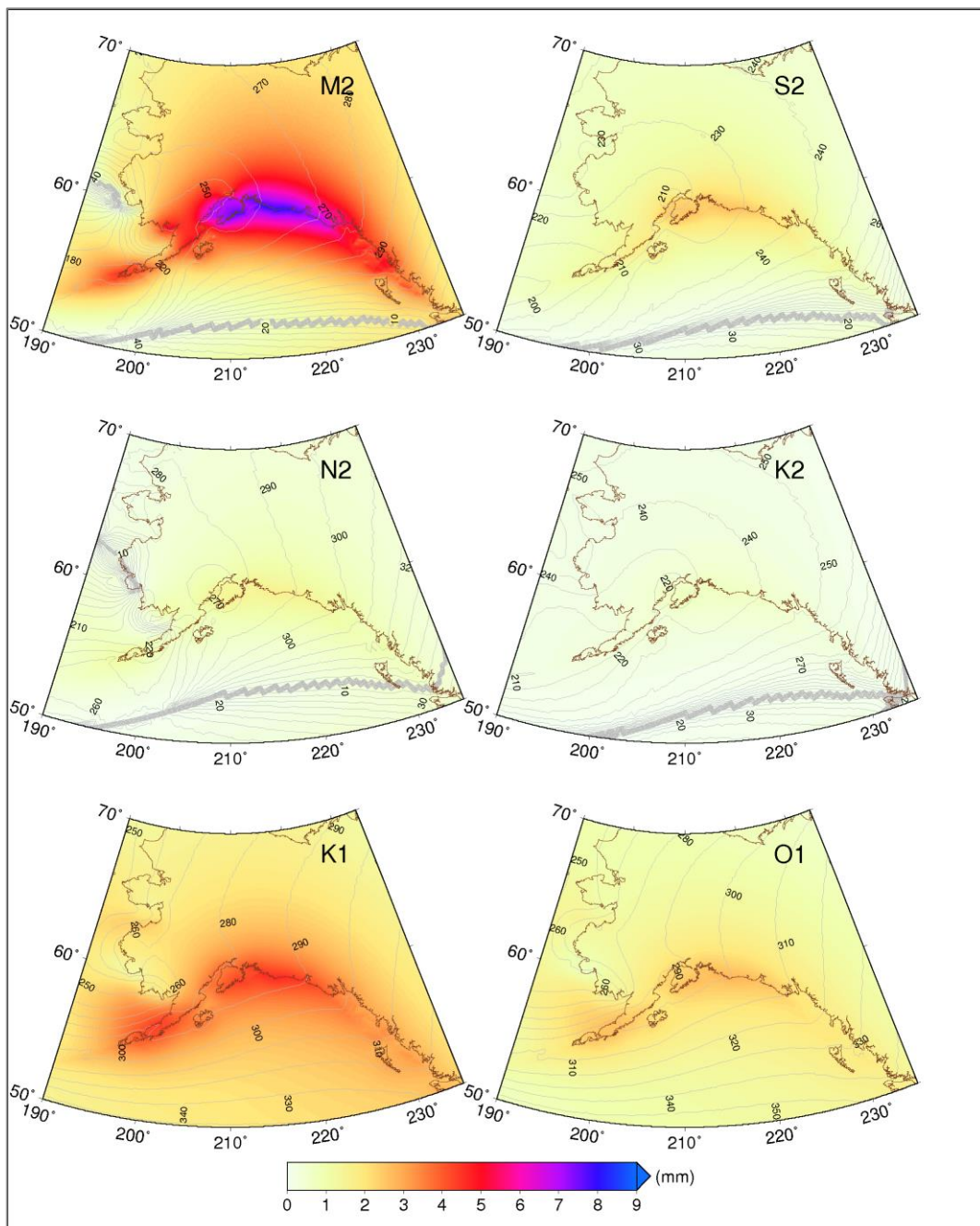


Figure 6.2: Similar to Figure 6.1 but for the north component.



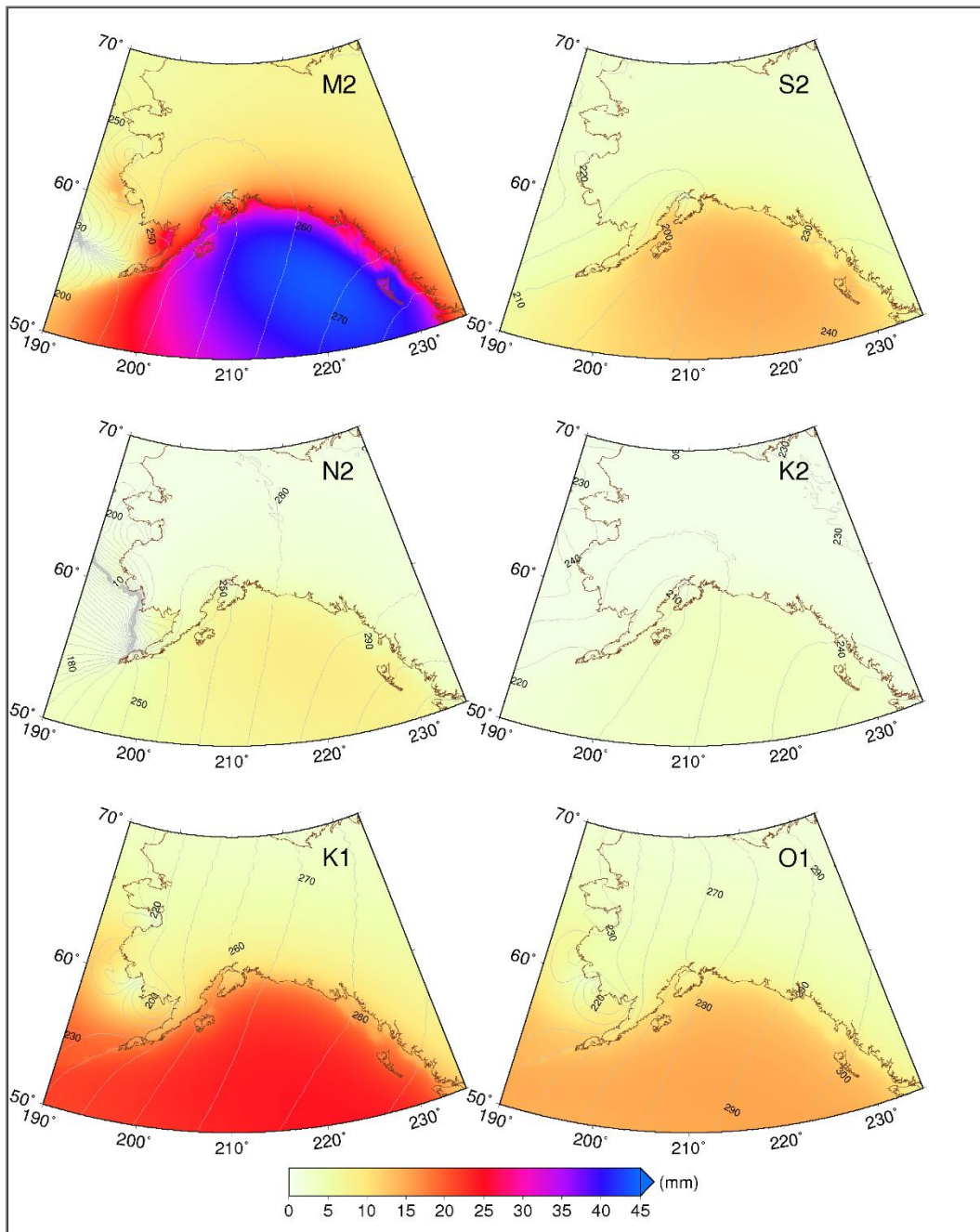


Figure 6.3: Similar to Figure 6.1 but for the vertical component (different scale is used for the amplitude)



### 6.3 Ocean tide models and OTL displacement modelling

Based on Bos *et al.* (2015) and Wang *et al.* (2020), the difference between the GNSS-estimated OTL displacements and those predicted by elastic Green's functions may be used for asthenospheric anelasticity assessment. However, the accuracy of the modelled OTL displacement is affected by the ocean tide model and Earth model errors, and when the latter is under investigation, errors in the former should be minimized. For Alaska with its fairly complicated coastlines, selecting the most appropriate ocean tide model is crucial. To help with this, OTL 3D displacement amplitude and phase lags for the M2 and K1 tidal constituents based on seven modern global ocean tide models, i.e. DTU10, EOT11a, FES2014b, GOT4.10c, HAMTIDE, NAO-global, and TPXO8-atlas, and the elastic PREM Green's function were computed for a  $0.0625^\circ \times 0.0625^\circ$  grid across Alaska with the NLOADF subroutine of the SPOTL software. Thereafter, the phasor differences from the mean of the displacements in each cell were computed, and finally, the RMS magnitudes of these phasor (vector) differences was calculated, as shown in Figure 6.4. This figure indicates that the RMS inter-model agreement for the predicted K1 OTL horizontal components is less than 0.3 mm, but it may reach up to 1.0 mm for the K1 vertical component. For the M2 constituent, a few areas with inter-model OTL RMS larger than 0.5 mm and 2.5 mm for the horizontal and vertical directions, respectively, can be seen in Figure 6.4. The inter-model M2 vertical disagreement in this figure is rather larger than the expected asthenosphere anelasticity effect of about 1.5 mm for some areas, and hence, ocean tide models need to be further quality checked which is considered next.

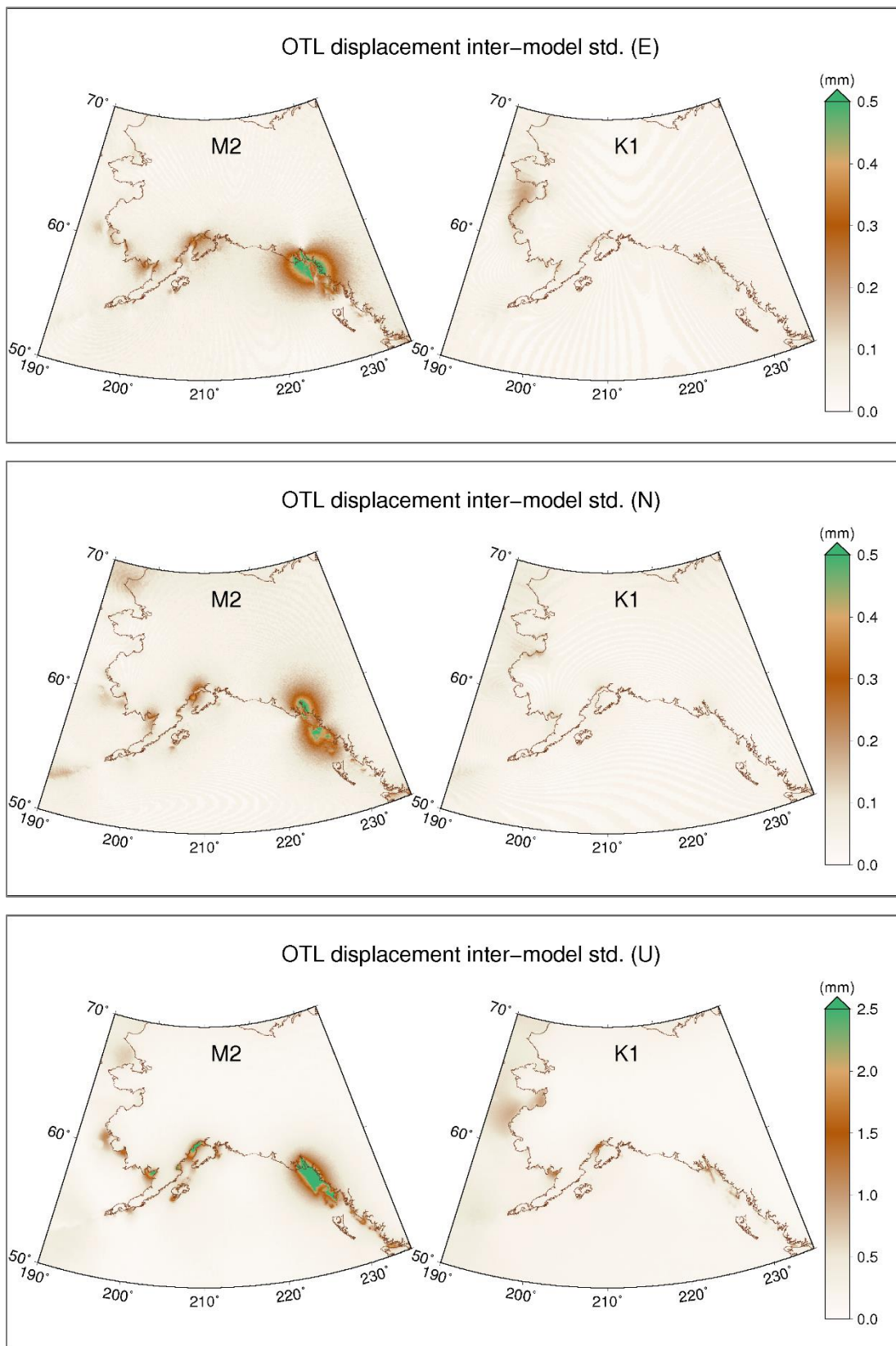


Figure 6.4: RMS agreement of the magnitudes of the vector differences for the predicted OTL displacement (in mm) for a  $0.0625^\circ \times 0.0625^\circ$  grid for the east (top), north (middle), and vertical (bottom) components based on seven ocean tide models (DTU10, EOT11a, FES2014b, GOT4.10c, HAMTIDE, NAO-global, and TPXO8-atlas) and an elastic PREM Green's function. The background maps for the horizontal and vertical components are shown in different scales.

### **6.3.1 Ocean tide model quality check with tide gauge data**

Alaska has one of the largest ocean tidal currents in the world. As is shown in Figure 6.5, even several hundred kilometres away from the Alaskan southern coast, the tidal height peak-to-peak subdaily variation is more than 2 m and it can exceed 4 m near the coast. Furthermore, intricate coastline geometry makes satellite-based ocean tide modelling challenging. To see the consistency among the aforementioned global ocean tide models, by using the OCLOOK subroutine of the SPOTL software, the amplitude and phase lags of the ocean tide for the M2 and K1 constituents based on each model were computed for a  $0.0625^\circ \times 0.0625^\circ$  grid, and similar to Figure 6.4, the inter-model RMS agreement of the magnitudes of the vector differences was generated per cell, as shown in Figure 6.6. This figure demonstrates that, although the models are consistent over the deep oceans (shown by white colour), their disagreement is around 20 cm within shallow waters, e.g. between islands in the southeast coast, which causes the OTL displacement discrepancies in the same region as shown in the left panels of Figure 6.4.

Ocean tide model accuracy can be accessed from comparisons with tide gauge measurements, and the US National Oceanic and Atmospheric Administration (NOAA) offers more than 193 historical and active tide gauge stations in Alaska. However, many of the tide gauges are installed in narrow bays and rivers which the ocean tide models do not cover. Therefore, 81 tide gauges were selected for the accuracy assessment of the ocean tide models, and the M2 and K1 ocean tidal constituent amplitudes and phase lags, which were computed from spectral analysis of the ocean water level time series, were used. In Figure 6.6, the tide gauge stations and six sub-regions (labelled by letters A to F), which were selected based on the ocean tide model disagreement and facilitate a local investigation of the global ocean tide models, are shown. Further details for the location of the tide gauge stations and observed plus modelled ocean tide values are provided in Appendix F. In Figure 6.6, the number of tide gauges per sub-region (from A to F) are: 15, 22, 25, 4, 7, and 7.

For the quality assessment of the ocean tide models, the modelled M2 and K1 harmonics at the tide gauge stations were interpolated from a  $0.0625^\circ \times 0.0625^\circ$  grid with which was generated in SPOTL, and the vector difference between the tide gauge observation and the modelled tide was computed. Thereafter, vector differences which deviated more than 5 times the median absolute deviation (MAD) from the median vector difference were removed as outliers, and the RMS of the remaining vector differences in each sub-region was computed. Figures 6.7 and 6.8 depict the computed RMS for the M2 and K1 harmonics, respectively. As can be seen from Figure 6.7, a single model cannot be chosen as the most accurate model for the M2 constituent

in all sub-regions, but FES2014b and TPXO8-atlas show better than 22 cm and 17 cm agreement with the tide gauge data in all sub-regions, respectively, and except in sub-region A, GOT4.10c shows comparable accuracy with the two aforementioned models. Figure 6.8 indicates a general similar accuracy for the ocean tide models at the K1 frequency in all sub-regions. Hence, FES2014b, TPXO8-atlas and GOT4.10c will be used as a priori models when computing GPS-estimated OTL displacement residuals in the next section.

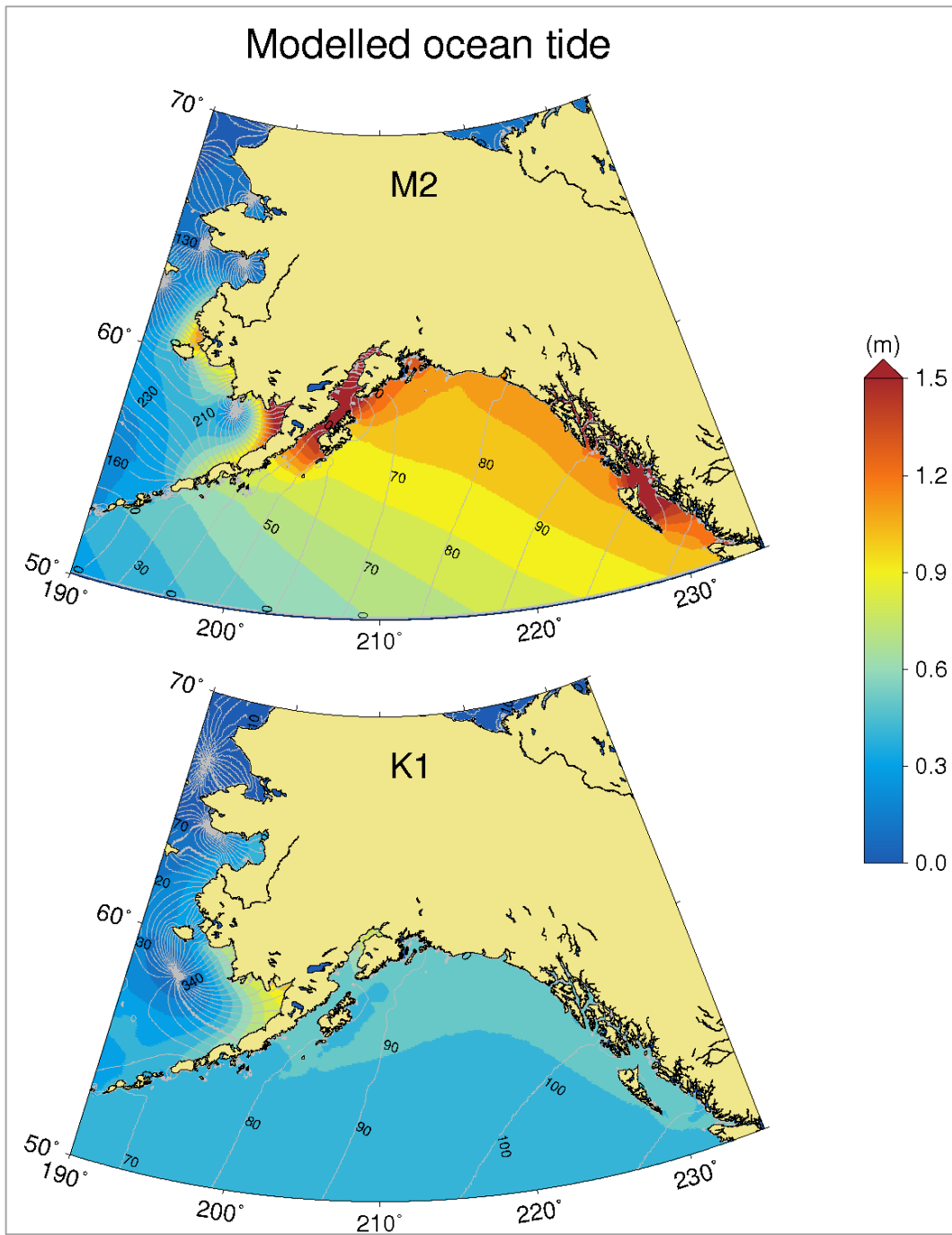


Figure 6.5: Ocean tide amplitude and Greenwich phase lags based on the FES2014b mode for M2 and K1 constituents, for a  $0.0625^\circ \times 0.0625^\circ$  grid

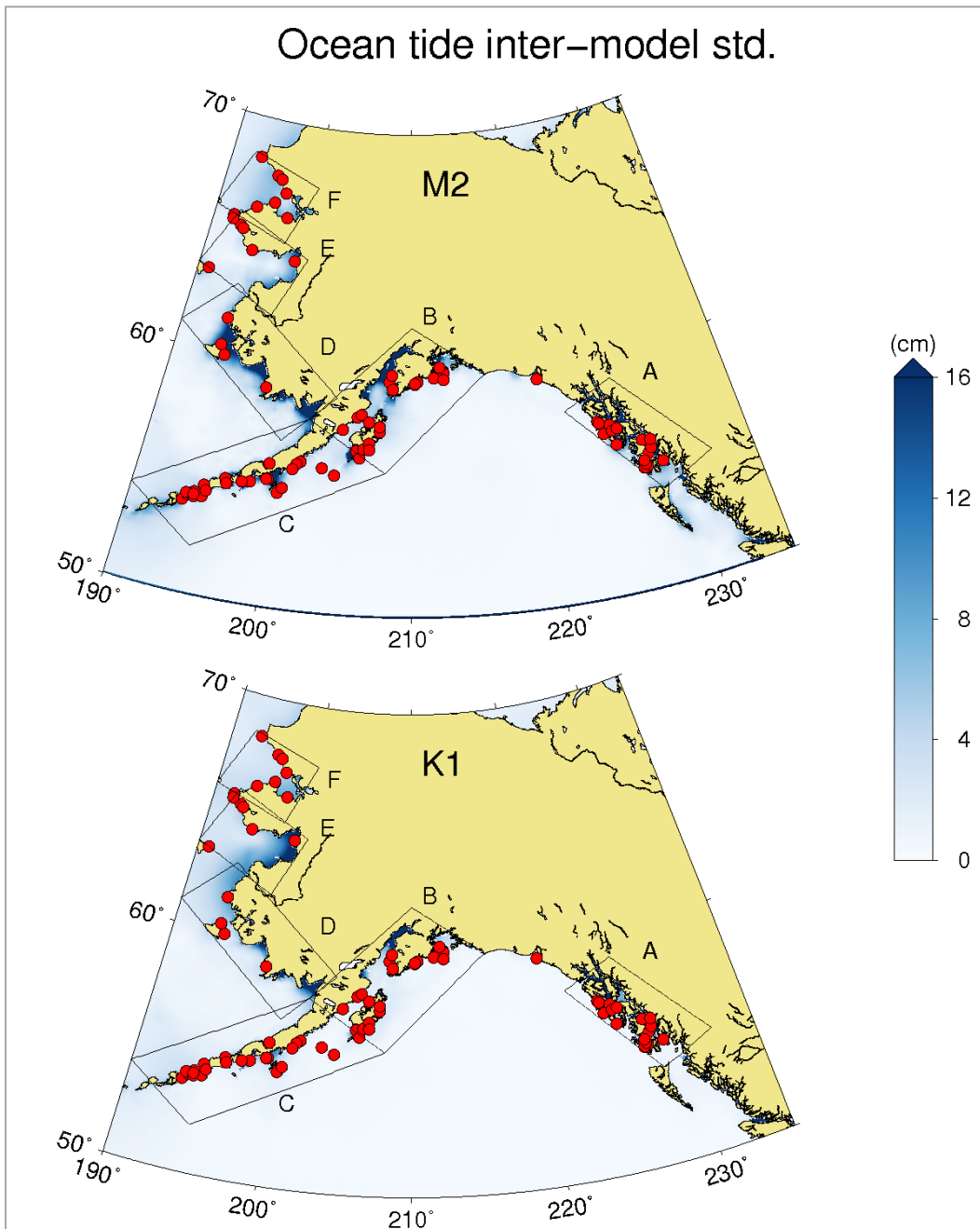


Figure 6.6: RMS agreement of the magnitudes of the vector differences for the predicted ocean tide (in cm) for a  $0.0625^\circ \times 0.0625^\circ$  grid based on seven ocean tide models (DTU10, EOT11a, FES2014b, GOT4.10c, HAMTIDE, NAO-global, and TPXO8-atlas), and tide gauge stations (red circles). Each model is compared with tide gauge data within the sub-regions A to F.

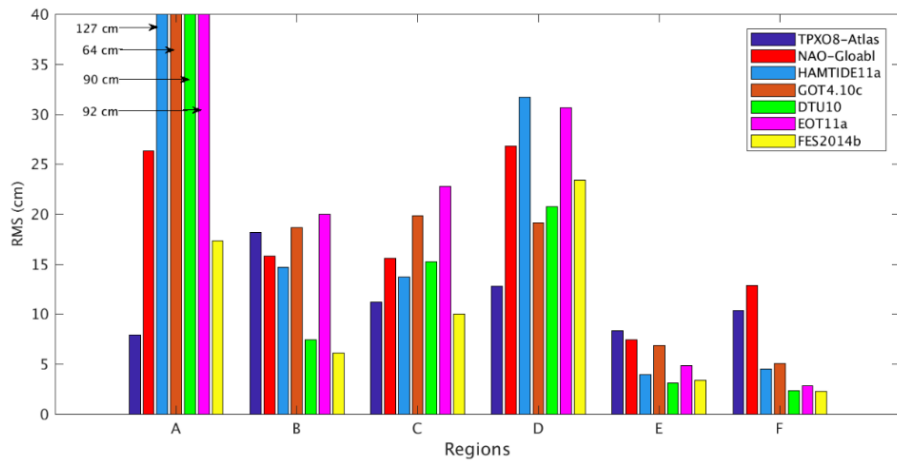


Figure 6.7: RMS of the vector difference for the M2 ocean tide constituent of the ocean tide models and tide gauge data in the sub-regions shown in Figure 6.6

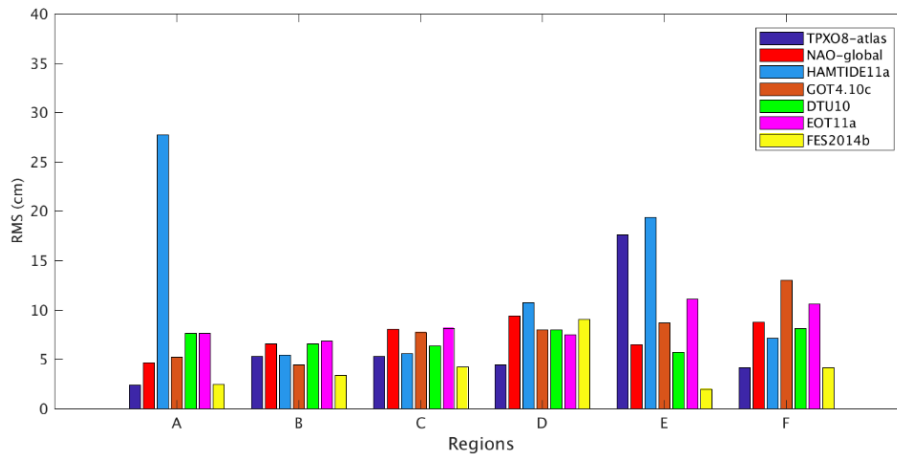


Figure 6.8: Similar to Figure 6.7 but for the K1 constituent

### 6.3.2 GPS-derived OTL displacement residuals

NOAA provides 151 continuous operating reference stations (CORS) which collect GPS observations in Alaska, and 87 of these stations, which satisfy the 90% daily and annual data availability standards explained in Chapter 5, are used for the OTL displacement assessment in this section. However, to have a more consistent time series for the later geophysical interpretation, a GPS data span from 2016.0 to 2019.0 was used. The list of stations with their coordinates is provided in Appendix G. Similar data processing to Chapter 5 was used to estimate OTL 3D displacement residuals with respect to the modelled ones (based on the FES2014b ocean tide model and elastic PREM Earth model Green's function). To obtain the total observed OTL displacement, the GPS-estimated residual was added to the priori modelled value which was used in the data processing in PANDA. Then, by subtracting the modelled

OTL displacement computed by another model from the total displacement, the residual with respect to that model could be computed. Therefore, the GPS-estimated OTL displacement residuals based on the FES2014b ocean tide and elastic PREM Earth model were converted to the residuals which are estimable with regard to the modelled OTL displacement based on the GOT4.10c or TPXO8-atlas ocean tide models and elastic PREM Green's function. In Figures 6.9 to 6.11, the estimated residuals for the east, north, and vertical components based on the three ocean tide models are shown, and the numerical values for the residuals are shown in Appendix G. All these figures suggest that the inland stations are affected by the ocean tide model change by less than 0.2 mm. Furthermore, along the west coast, i.e. sub-regions E and F in Figure 6.6 in which similar accuracy for the tide models was reported in Figure 6.7, the OTL displacement residual is insensitive to the ocean tide model selection. From Figure 6.9, it is evident that M2 OTL displacement residuals for the east component are at the observation/computation noise level at inland stations, but may reach up to 0.8 mm in coastal areas which is clearly larger than the 0.2 mm uncertainty explained in the synthetic signal recovery test. In Figure 6.10, a common M2 displacement signal for the north component at almost all stations, except those near the west coast, can be seen. This common mode signal may indicate a radial Earth model problem, induced by the Pacific plate northwards 40 mm/year motion, for the forward modelling of the OTL north displacement. However, to validate this hypothesis, more investigation is required.

For the coastal stations in southern Alaska, the OTL displacement residuals, especially for the vertical component shown in Figure 6.11, are clearly correlated with the applied ocean tide model in the OTL displacement forward modelling. For instance, the top panel of Figure 6.11 demonstrates that using the GOT4.10c ocean tide model generates larger OTL displacement residuals at stations with longitude between  $220^\circ$  and  $225^\circ$  than those when using FES2014b, whilst the bottom panel indicates similar results for the TPXO8-atlas and FES2014b models for those stations. The larger RMS difference (listed in Tables 6.1 to 6.3) between the GOT4.10c ocean tide model and tide gauge data in sub-region A matches the bigger OTL displacement residuals resulting from that model. In addition, Figure 6.11 shows smaller GPS-estimated OTL displacement residuals when the FES2014b ocean tide model is used in sub-region B with longitude between  $201^\circ$  and  $215^\circ$ , which is also confirmed by the better agreement between FES2014b and tide gauge data in that sub-region.

In Tables 6.1 to 6.3, the RMS and 85th percentile of the GPS-estimated OTL M2 displacement residuals, which are shown in Figures 6.9 to 6.11, are presented for models FES2014b, GOT4.10c and TPXO8-atlas. To explain the upper bound of the displacement residuals in each



sub-region, the 85th percentile is preferred as the number of points in some sub-regions is not enough to compute the 95th percentile, e.g. seven stations in sub-regions A and C. Sub-regions D, E, and F, which contain only four, five and two GPS stations, respectively, are not considered separately, but their contributions in the overall statistical analysis are included. Table 6.1 indicates that the east component of the OTL displacement residual is not greatly affected by the ocean tide model selection in sub-regions A and C, but using FES2014b reduces the RMS and 85th percentile in sub-region B by around 0.5 mm and more than 0.8 mm, compared with using GOT4.10c and TPXO8-atlas, respectively. These values are clearly larger than the 0.2 mm error in recovering the synthetic signal in the east direction. It can be seen in Table 6.2 that for sub-region B, GOT4.10c leads to about 0.2 mm and 0.5 mm larger respective RMS and 85th percentile values for the north component, compared to FES2014b and TPXO8-atlas, but the estimated residuals from the three models for other sub-regions are similar at the 0.1 mm level. Table 6.3 indicates that there is no apparent difference for using FES2014b or TPXO8-atlas to model the vertical OTL displacement in sub-region A, but using GOT4.10c leads to about 1.5 mm and 2 mm larger RMS and 85th percentile values, respectively. Table 6.3 also shows that in sub-region B, using FES2014b reduces the discrepancy between modelled and GPS-estimated OTL vertical displacement more than 1.0 mm compared to TPXO8-atlas and GOT4.10c, and it also leads to smaller residuals in sub-region C for the vertical OTL displacement. So, similar to the tide gauge observation, GPS-estimated OTL displacement confirms a better accuracy for the FES2014b ocean tide model for Alaska, and for the rest of this chapter, this model is used for the OTL displacement forward modelling.

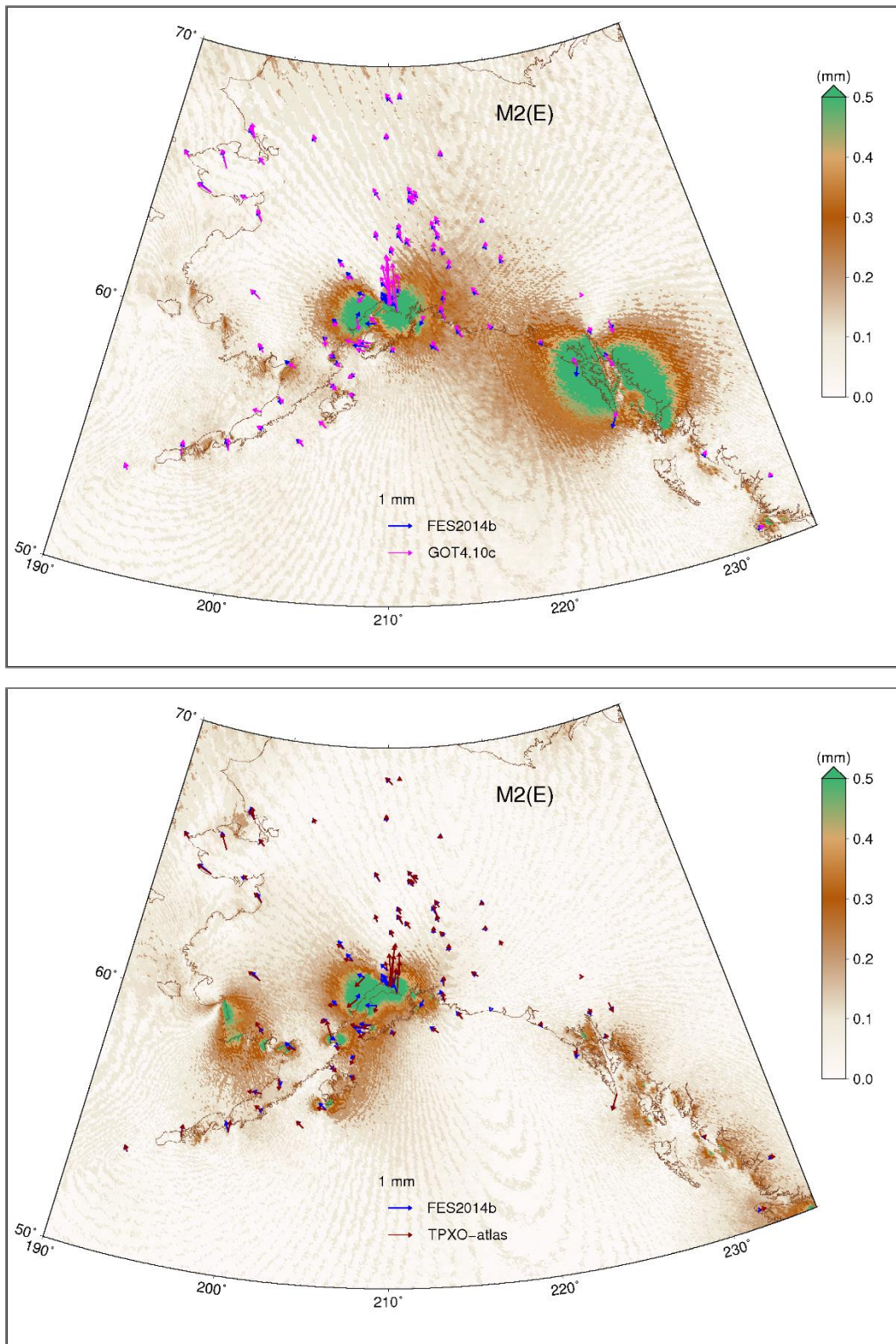


Figure 6.9: GPS-estimated M2 east OTL displacement residuals based on an elastic PREM Green's function and FES2014b vs. GOT4.10c (top) and FES2014b vs. TPXO8-atlas ocean tide models (bottom). The background map shows the magnitude of the vector difference of the modelled OTL displacement between the two models.

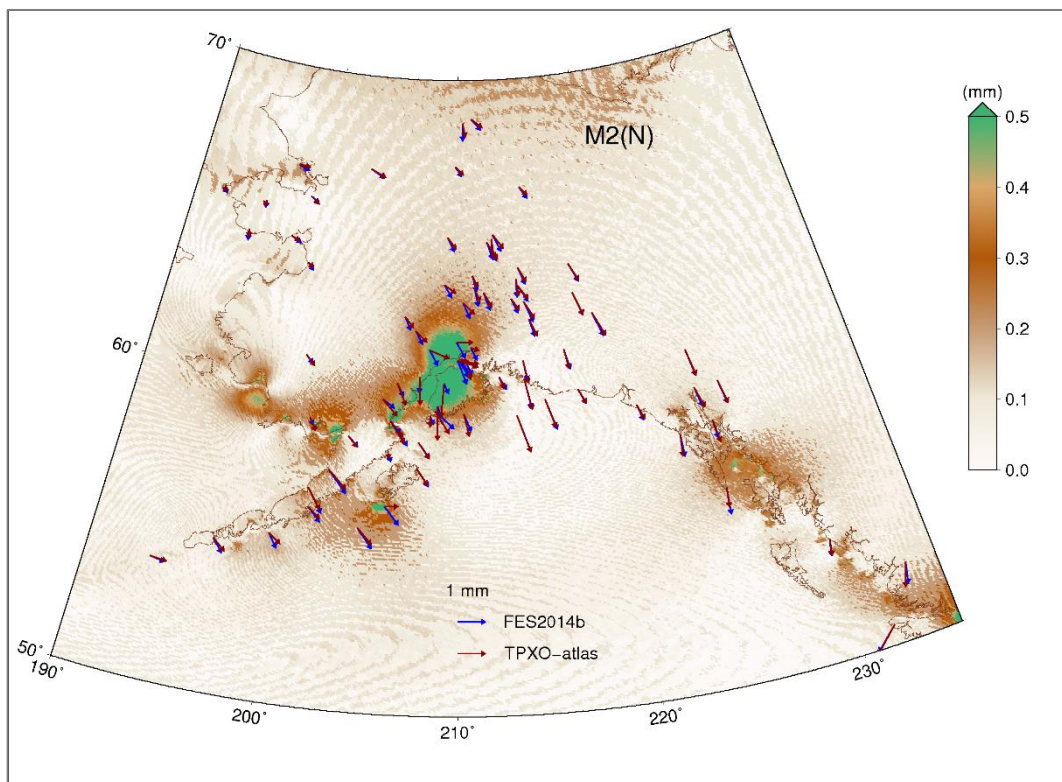
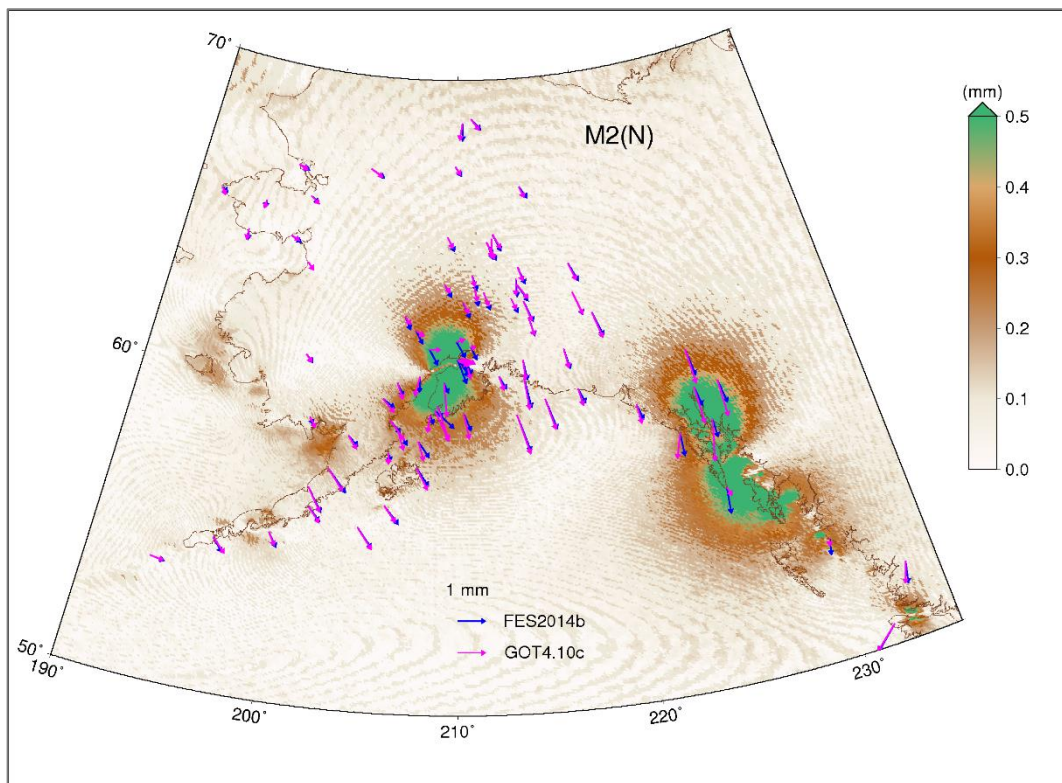


Figure 6.10: Similar to Figure 6.9 but for the north component



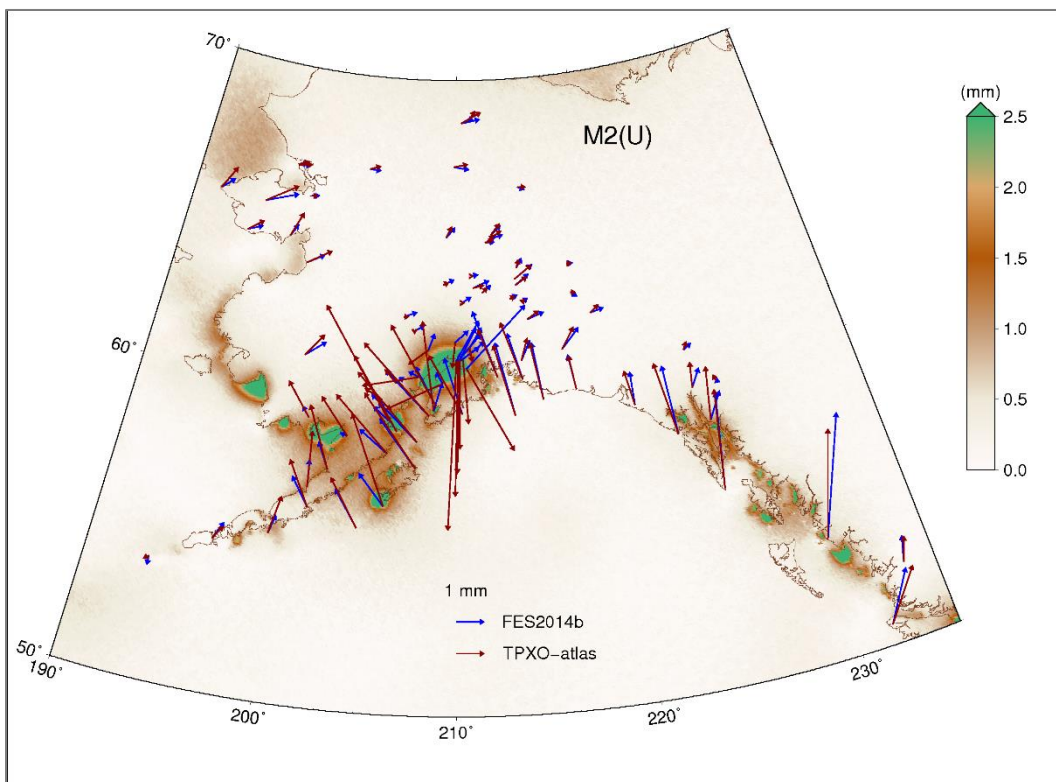
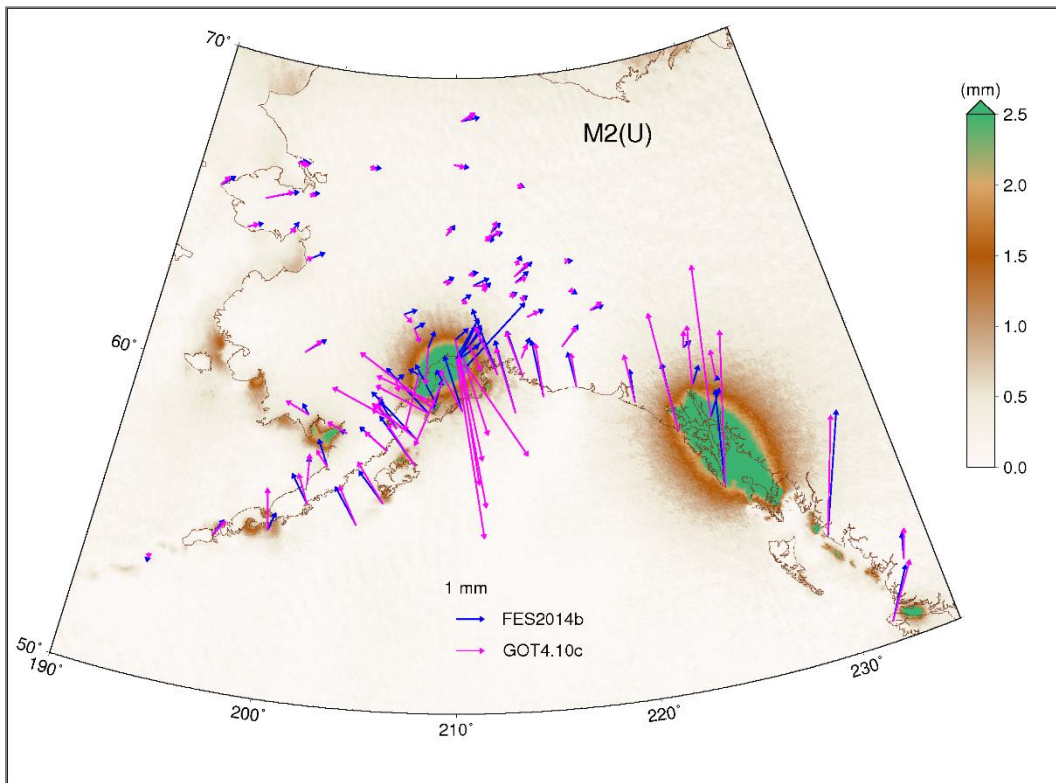


Figure 6.11: Similar to Figure 6.9 but for the vertical component

	<b>FES2014b</b>	<b>TPXO8-atlas</b>	<b>GOT4.10c</b>
<b>A</b>	0.4 (0.4)	0.4(0.4)	0.4(0.5)
<b>B</b>	0.4(0.5)	0.8(1.3)	0.9(1.6)
<b>C</b>	0.4(0.5)	0.5(0.5)	0.4(0.5)
<b>All (A to F)</b>	0.4(0.5)	0.7(0.7)	0.7(0.8)

Table 6.1: RMS and 85th percentile (in brackets) of the GPS-estimated east M2 residuals (in mm) for sub-region A (7 stations), B (26 stations) and C (7 stations), and all sub-regions (51 stations). Individual RMS and 85th percentile in sub-regions D, E, and F are discarded as they include only 4, 5 and 2 stations, respectively.

	<b>FES2014b</b>	<b>TPXO8-atlas</b>	<b>GOT4.10c</b>
<b>A</b>	0.8(0.9)	0.8(0.9)	1.0(1.4)
<b>B</b>	0.6(0.7)	0.7(0.9)	0.7(0.9)
<b>C</b>	0.8(0.9)	0.7(0.8)	0.8(0.9)
<b>All (A to F)</b>	0.6(0.8)	0.7(0.9)	0.7(0.9)

Table 6.2: Similar to Table 6.1 but for the north component

	<b>FES2014b</b>	<b>TPXO8-atlas</b>	<b>GOT4.10c</b>
<b>A</b>	2.4(3.4)	2.4(3.5)	3.9(5.5)
<b>B</b>	1.5(2.2)	2.9(3.5)	2.7(3.8)
<b>C</b>	1.1(1.5)	1.9(2.0)	1.2(1.5)
<b>All (A to F)</b>	1.5(2.1)	2.4(3.4)	2.5(3.8)

Table 6.3: Similar to Table 6.1 but for the vertical component

#### 6.4 Anelasticity effects on the GPS-estimated OTL displacement

In the Section 6.3, it was shown that using the FES2014b ocean tide model leads to the smallest GPS-estimated OTL displacement residuals. However, for several stations with a well-modelled ocean tide, the residuals are still about 1.0 mm larger than the expected  $\sim 0.5$  mm GPS data uncertainty. Therefore, another source of the OTL displacement modelling error, i.e. the Earth's Green's function, should be investigated.

Earth's Green's functions are typically computed from global seismological Earth models. These models are valid for seismic stresses with about 1 Hz frequency, and cannot fully explain the Earth's mechanical behaviour under the lower frequency tidal forces. By applying the dissipation effect to elastic models, Bos *et al.* (2015) concluded about 2-3 mm reduction for the GPS-estimated M2 OTL vertical displacement residuals for stations in Brittany and Cornwall

to 0.2-0.4 mm. Wang *et al.* (2020) also used a similar approach to Bos *et al.* (2015), and found about 1 mm accuracy improvement for the predicted M2 OTL vertical displacement computed by an anelastic Earth model for GPS stations around the East China Sea.

In Section 6.3, the modelled OTL displacement based on different ocean tide models and the purely elastic PREM Earth model were computed. In this section, the asthenospheric anelasticity effect for the PREM and S362ANI (Kustowski *et al.*, 2008) elastic models are considered. Hence, similar to Bos *et al.* (2015) and Wang *et al.* (2020), after refining the global PREM and regional S362ANI models for the asthenospheric anelasticity effect, Machiel Bos computed and provided the relevant Green's functions. The elastic PREM, anelastic PREM and regional anelastic S362ANI are called PREM-EL, PREM-AN, and S362ANI-AL-AN, respectively, for the rest of this chapter.

To assess the refined models against the GPS-estimated OTL displacement, the modelled OTL displacement based on the FES2014b ocean tide model with PREM-EL, PREM-AN and S362ANI-AL-AN Green's functions are computed. Thereafter, the predicted OTL displacement computed by each Green's function is subtracted from the GPS-estimated M2 OTL displacement, as shown in Figures 6.12 to 6.14. The numerical values for the residuals are presented in Appendix G. In Figure 6.12, it can be seen that the effect of the asthenosphere anelasticity cannot be clearly manifested in the east component of the OTL displacement residuals for PREM-AN and S362ANI-AL-AN, but Figure 6.13 indicates that using the anelastic Green's function slightly amplifies the GPS-estimated OTL displacement residuals for the north component. For the vertical component shown in Figure 6.14, the modelled OTL displacements using the two anelastic Green's functions are closer to those estimated by the GPS data than with PREM-EL. This figure depicts that for stations with well-modelled ocean tides, e.g. the southwest coast, the GPS-estimated residuals based on the anelastic Earth models, especially S362ANI-AL-AN, tend to the GPS data noise level.

To quantify the effect of the anelastic Earth model on the OTL displacement forward modelling, the GPS stations are classified as 'coastal' and 'other' stations. The ocean tidal pattern shown in Figure 6.5 indicates a weak tidal current for the west coast, and therefore were grouped based on their distance from the south coastline. Any point within 100 km of the south coastline is considered as a coastal station, and the RMS and 85th percentile of the GPS-estimated OTL displacement residuals in each class are shown in Tables 6.4 to 6.6. For the east component, Table 6.4 confirms that the GPS-estimated OTL east displacement residuals are not large enough to be sensitive to the anelasticity effect, but it can be seen from Table 6.5 that using an anelastic model changes the RMS and 85th percentile for the north component from 1.0 mm

and 1.2 mm, respectively, which is larger than the ~0.2 mm error for the synthetic signal recovery. In Table 6.6, the RMS and 85th percentile of the GPS-estimated vertical OTL displacement residuals for the coastal stations are reduced by up to 0.4 mm and 0.6 mm, respectively. Although this table shows an overall ~1.5 mm discrepancy between the GPS-observed and modelled OTL displacement based on the anelastic Green's functions within the south coast, the bottom panel of Figure 6.14 shows residuals are less than 0.7 mm for the stations along the southwest coast of Alaska which have high quality ocean tide models.

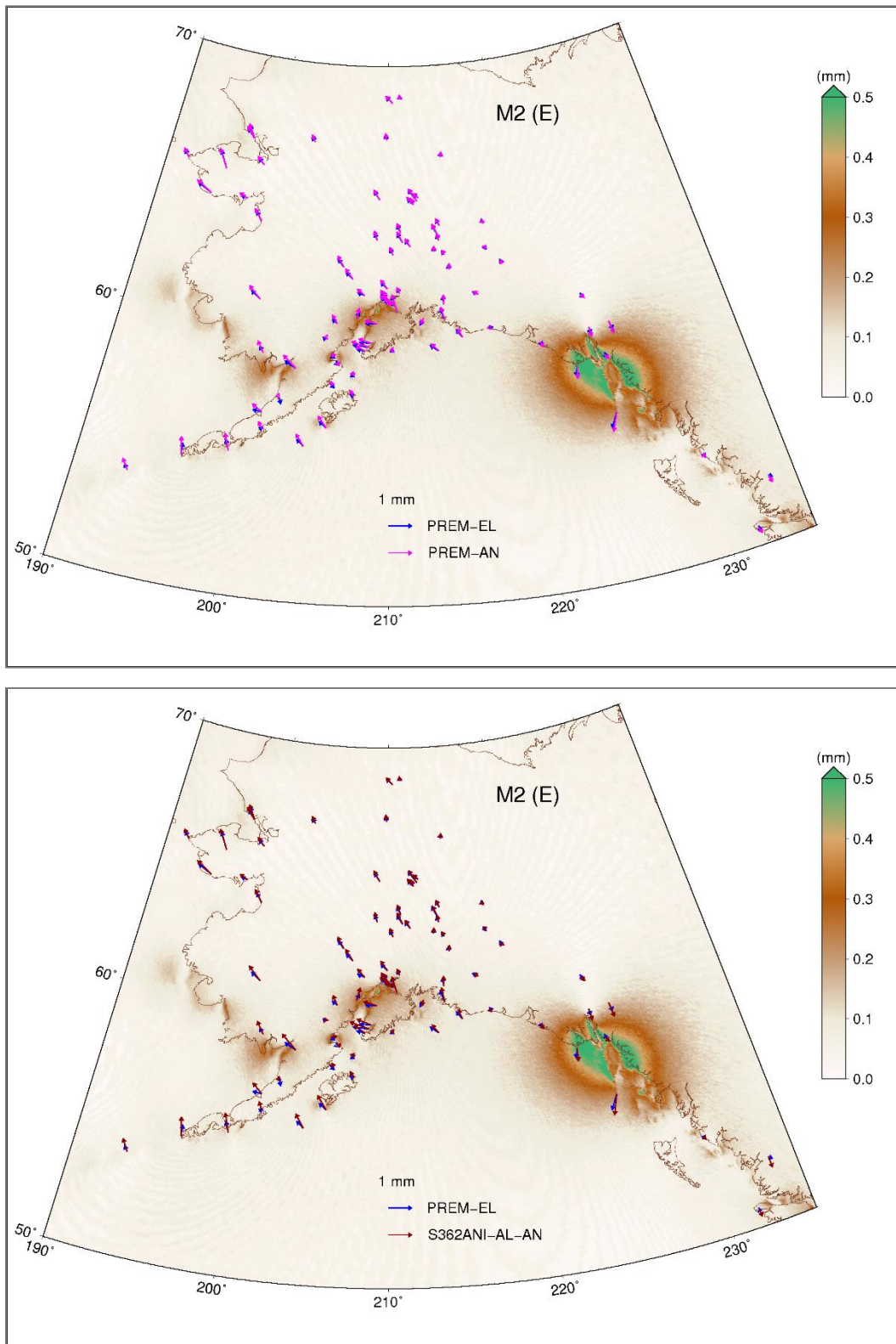


Figure 6.12: GPS-estimated M2 east OTL displacement residuals based on elastic PREM (PREM-EL) vs. anelastic PREM (PREM-AN) Green's functions (top), elastic PREM (PREM-EL) vs. anelastic regional S362ANI (S362NAI-AL-AN) Green's functions (bottom). The FES2014b ocean tide model is used for all computations. The background map shows the RMS agreement of the magnitudes of the vector differences for the predicted OTL displacement (in mm).



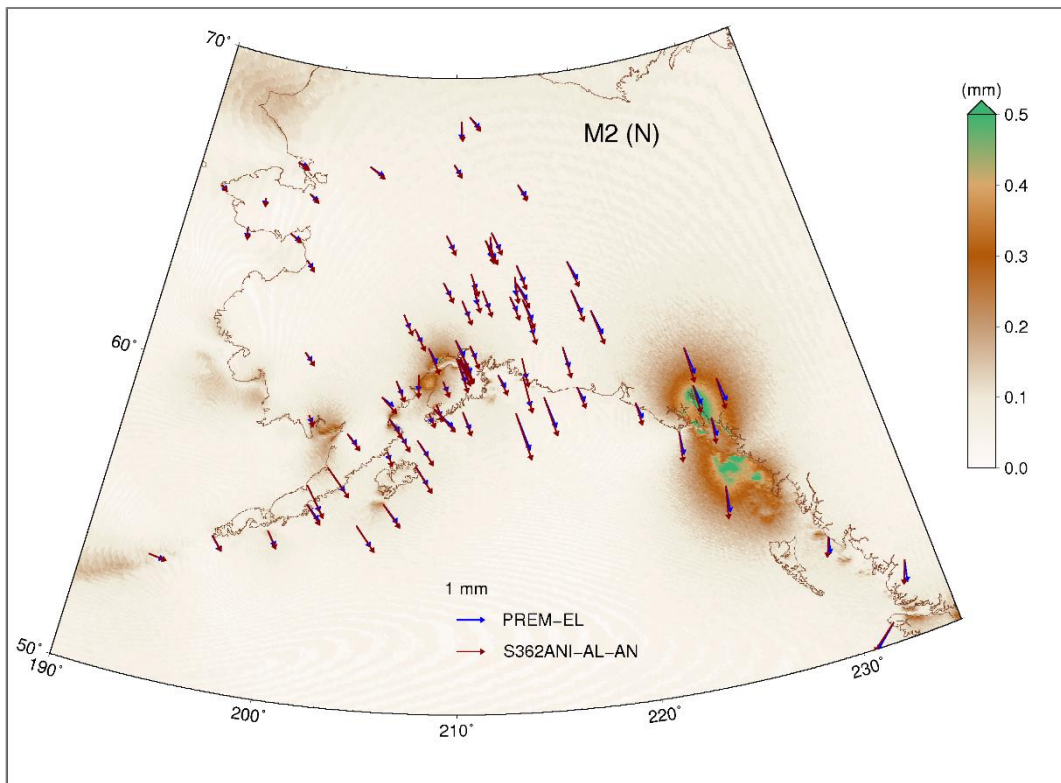
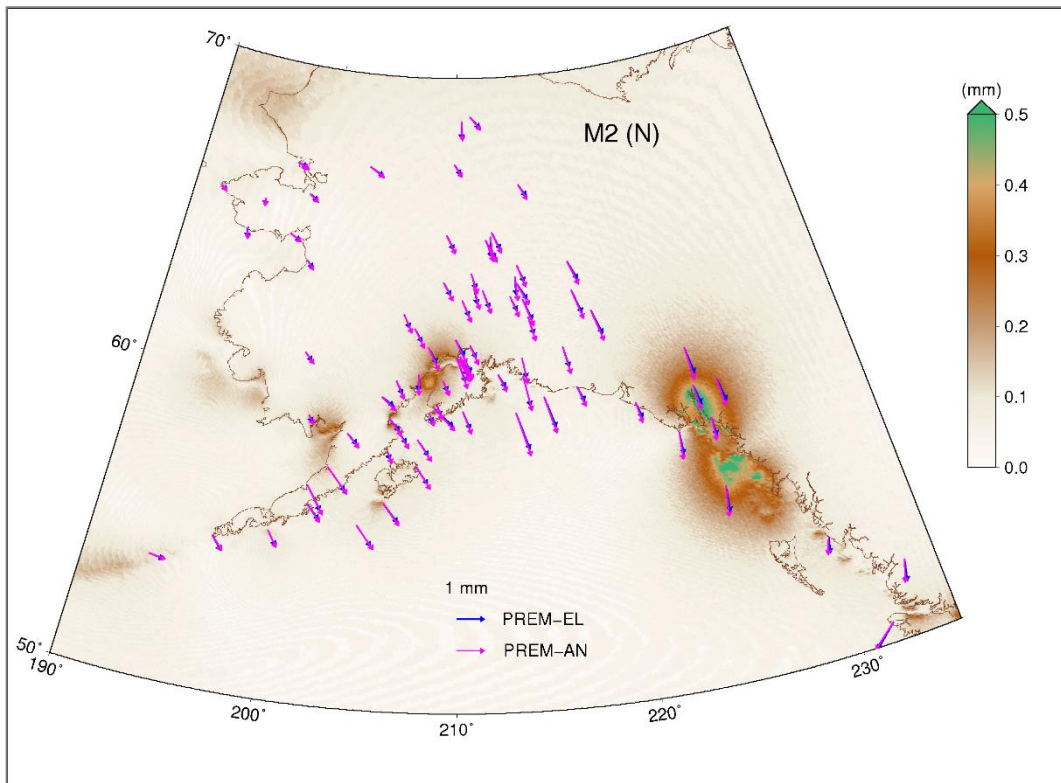


Figure 6.13: Similar to Figure 6.12 but for the north component

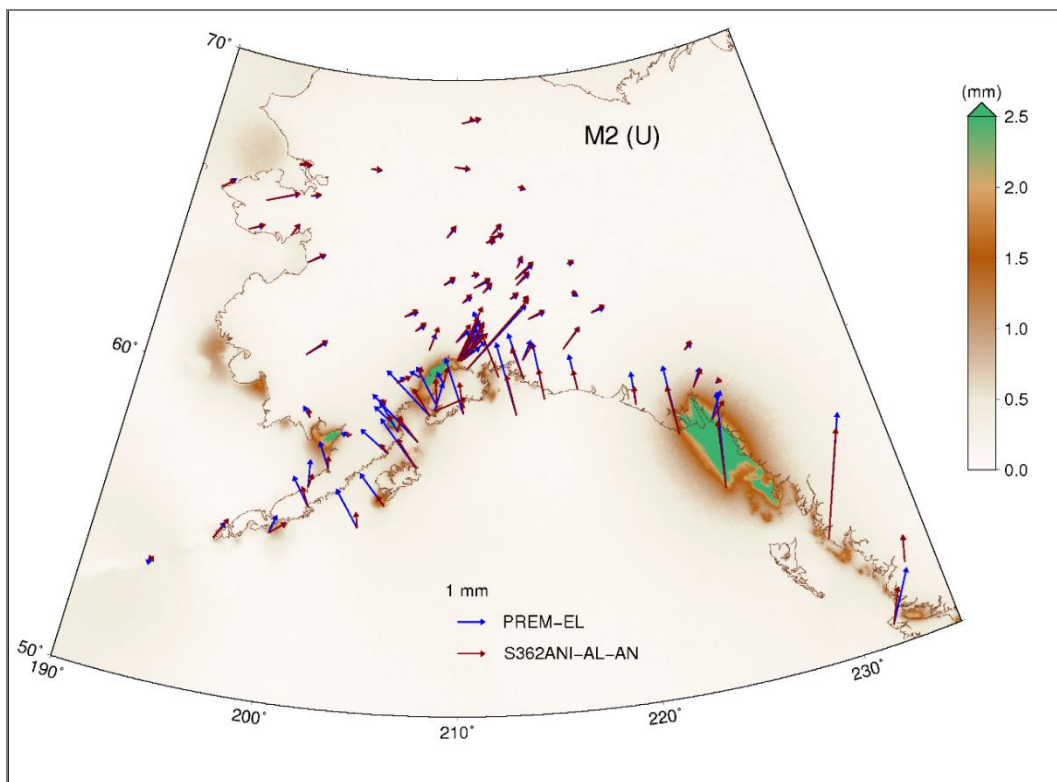
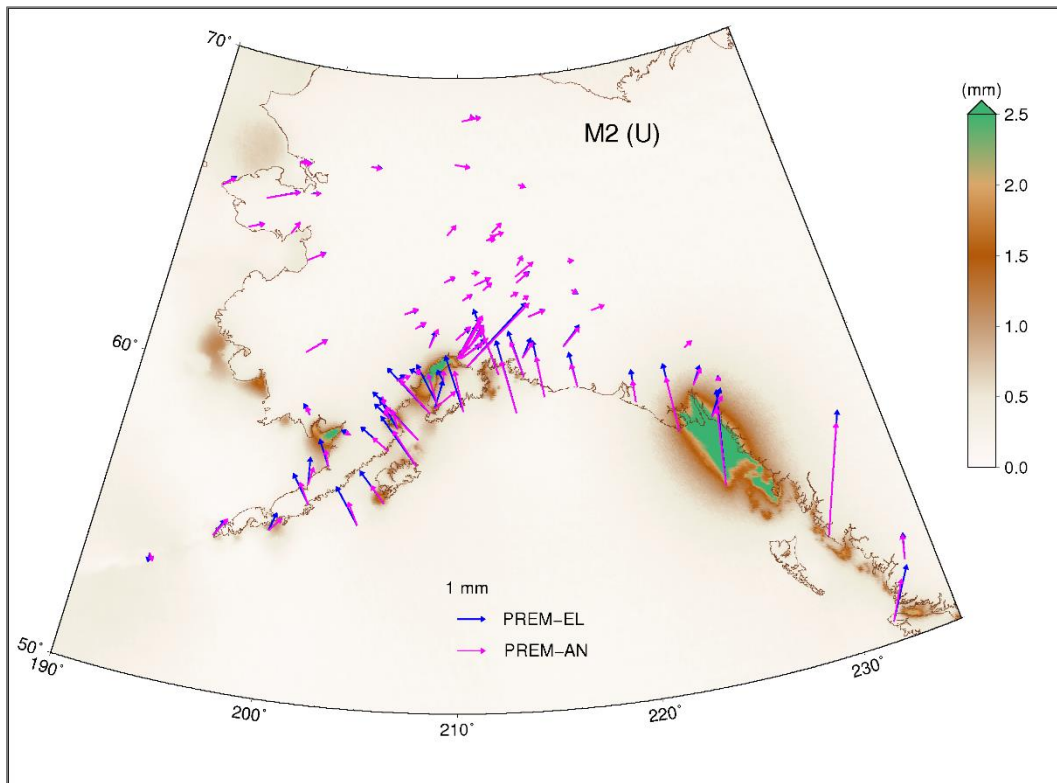


Figure 6.14: Similar to Figure 6.12 but for the vertical component

	<b>PREM-EL</b>	<b>PREM-AN</b>	<b>S362ANI-AL-AN</b>
<b>South coast</b>	0.4(0.5)	0.5(0.6)	0.5(0.7)
<b>Other</b>	0.4(0.5)	0.4(0.6)	0.5(0.6)

Table 6.4: RMS and 85th percentile (in brackets) of the GPS-estimated east M2 residuals (in mm) for the 45 stations within 100 km of the southern coast and 42 stations elsewhere for Green's functions from elastic PREM (PREM-EL), anelastic PREM (PREM-AN) and anelastic regional S362AN (S362ANI-AL-AN) Earth models. For all cases, the FES2014b ocean tide model is used.

	<b>PREM-EL</b>	<b>PREM-AN</b>	<b>S362ANI-AL-AN</b>
<b>South coast</b>	0.7(0.9)	0.9(1.1)	1.0(1.2)
<b>Other</b>	0.6(0.8)	0.8(1.0)	0.8(1.0)

Table 6.5: Similar to Table 6.4 but for the north component

	<b>PREM-EL</b>	<b>PREM-AN</b>	<b>S362ANI-AL-AN</b>
<b>South coast</b>	1.7(2.2)	1.4(1.6)	1.3(1.6)
<b>Other</b>	0.5(0.7)	0.5(0.7)	0.5(0.7)

Table 6.6: Similar to Table 6.4 but for the vertical component

## 6.5 GLONASS and GPS+GLONASS based OTL displacement assessment

There are 22 stations in Alaska with sufficient GPS+GLONASS data from 2016.0 to 2019.0. As explained in Chapter 5, for regions such as Alaska with latitude greater than 50°, at least seven GLONASS satellites are accessible for almost 90% of data collection epochs, which makes reliable GLONASS-only kinematic PPP possible. In this section, to assess the potential GLONASS data benefits for OTL displacement estimation in Alaska, M2 and K1 OTL east, north, and vertical displacement residuals are estimated by GPS-only, GLONASS-only and combined GPS+GLONASS data. The GNSS-derived residual phasors are shown in Figures 6.15 to 6.20, and their numerical values are listed in Appendix G. For the modelled OTL displacement, the FES2014b ocean tide model and anelastic S362ANI-AL Green's function are used, and the GNSS data were processed as described in Chapter 5.

It can be seen in Figures 6.15 to 6.17 that, over almost all stations, the GLONASS-estimated M2 OTL displacement residuals have similar patterns to those estimated by GPS. The RMS and 85th percentile of the M2 OTL displacement residuals are shown in Table 6.7. This table suggests that the east and north M2 OTL displacements estimated by GPS-only, GLONASS-

only and combined GPS+GLONASS data may differ by around 0.1 mm, and for the vertical component, their overall difference is around 0.5 mm.

Figures 6.18 to 6.20 depict that using the GLONASS-only and combined GPS+GLONASS could help overcome the GPS orbit error and multipath problem, especially in the east and north directions, for K1 OTL displacement. In Table 6.8, the RMS and 85th percentile for the estimated K1 residuals from the three data sets are listed. It can be seen from this table that the overall GPS signal multipath and orbit/clock mismodelling error on east and vertical coordinate components is at the same level. For the east component, the RMS and 85th percentile are reduced by more than 1.0 mm when GLONASS were incorporated and the improvement in vertical component was around 0.8 mm for the combined GPS+GLONASS solution with respect to the GPS-only one. The GLONASS-only solution has also slightly smaller RMS and 85th percentile residuals for the vertical component but it is also problematic in many stations. Table 6.8 also shows about 0.3-0.5 mm and 0.8-0.9 mm reductions for the RMS and 85th percentile in the north component, respectively, when GLONASS data has been used for the K1 OTL displacement measurement in Alaska.

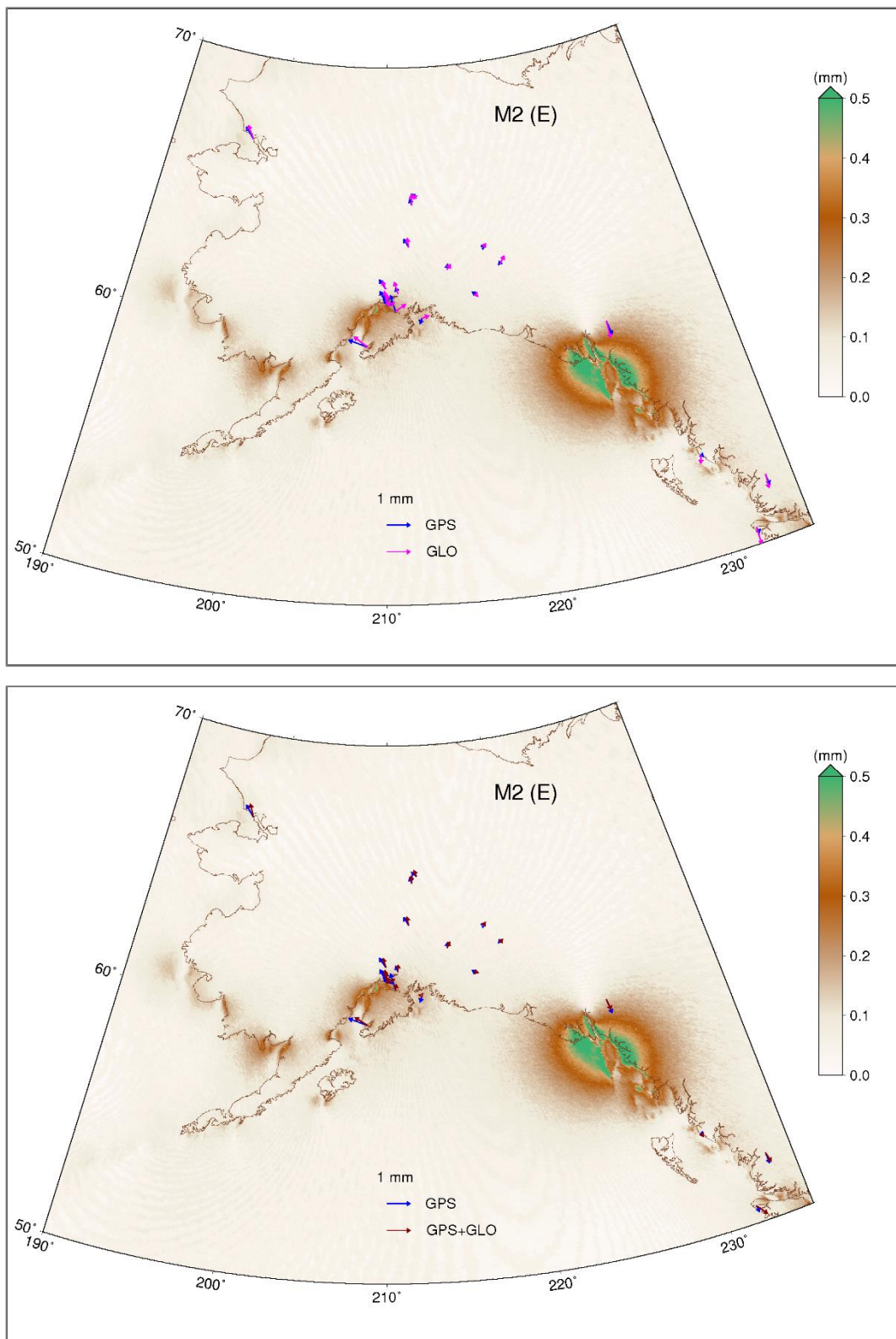


Figure 6.15: M2 OTL displacement residuals for the east component estimated by GPS-only vs. GLONASS-only data processing (top) and GPS-only vs. GPS+GLONASS data (bottom). The priori modelled OTL displacement is computed based on the FES2014 ocean tide model and the anelastic S362ANI-AL Earth model Green's function. The background map shows the RMS agreement of the magnitudes of the vector differences for the predicted OTL displacement based on seven ocean tide models (DTU10, EOT11a, FES2014b, GOT4.10c, HAMTIDE, NAO-global, and TPXO8-atlas)



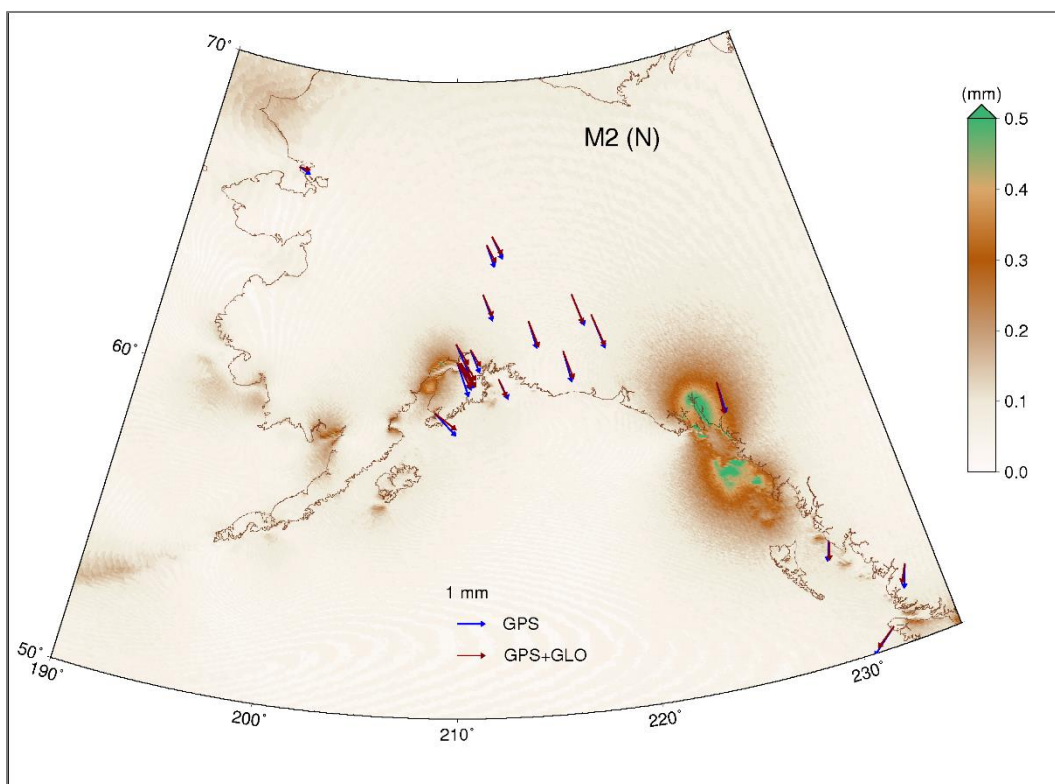
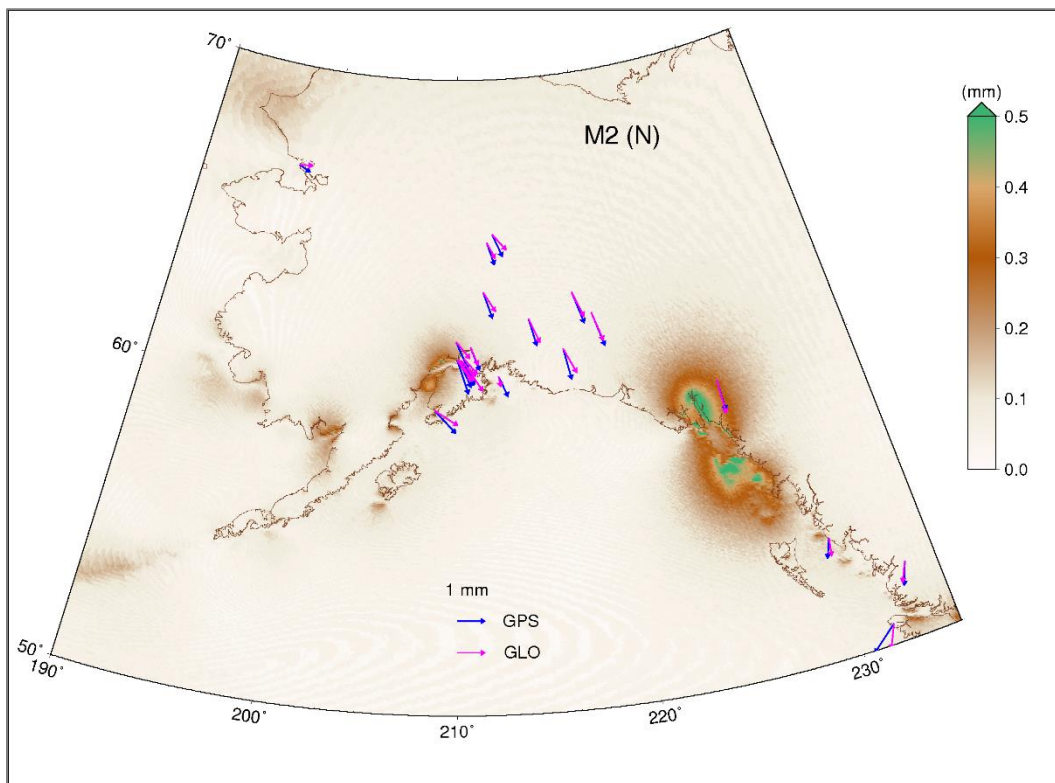


Figure 6.16: Similar to Figure 6.15 but for the north component

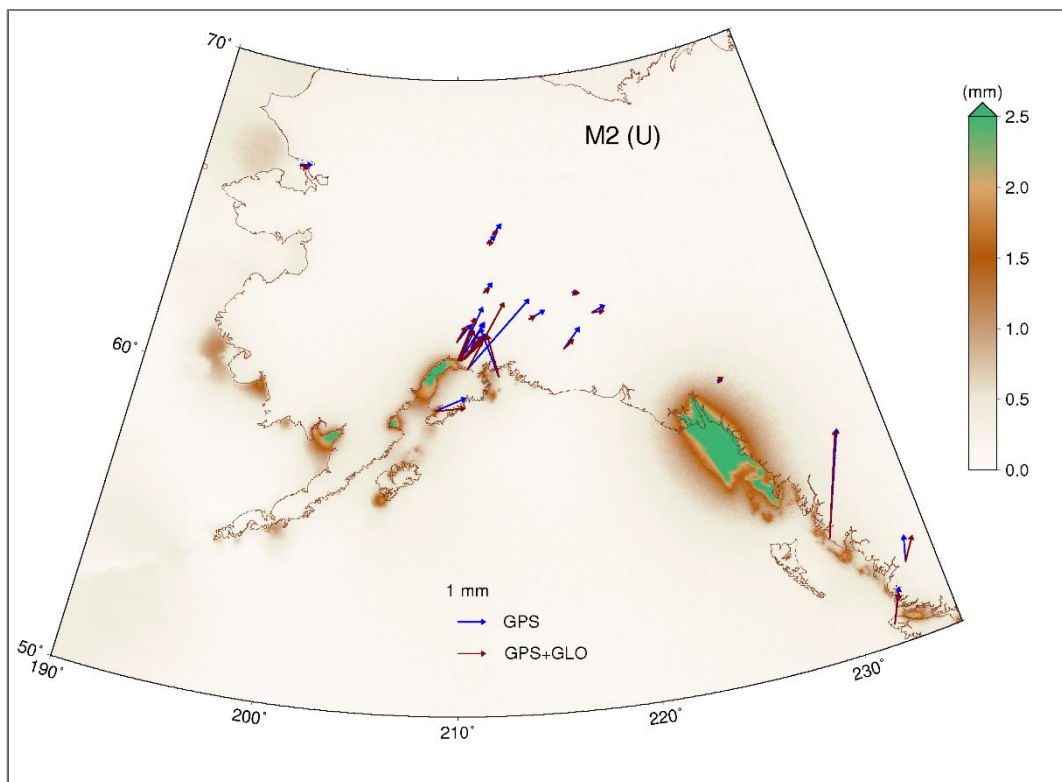
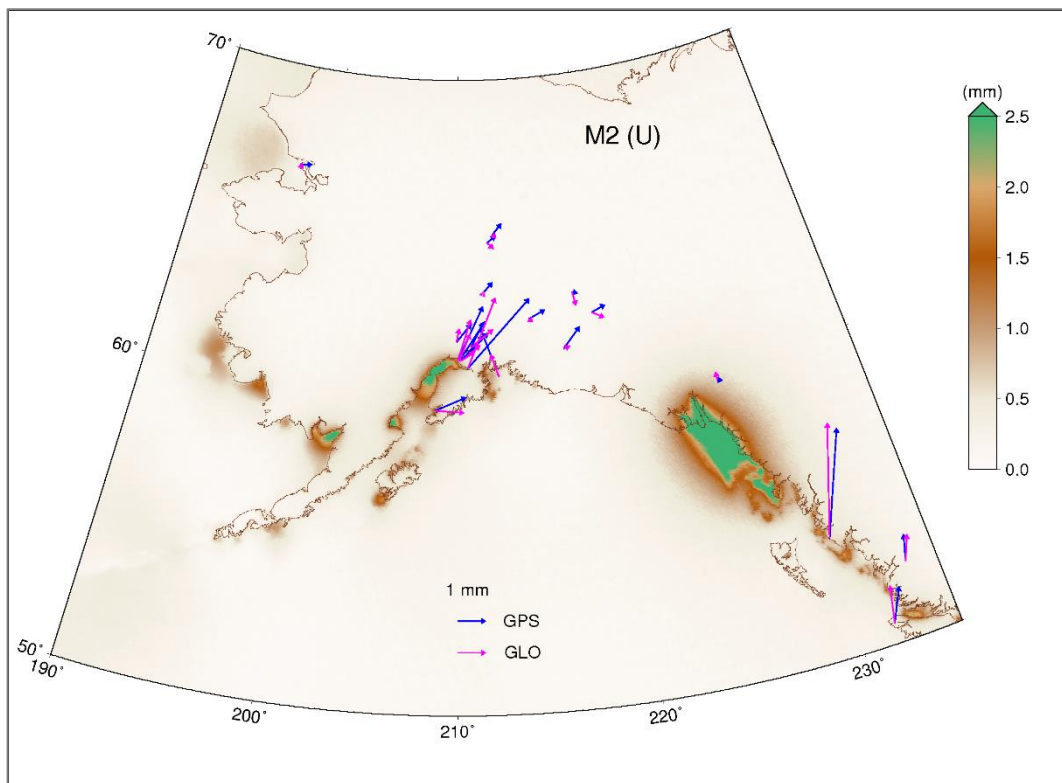


Figure 6.17: Similar to Figure 6.15 but for the vertical component

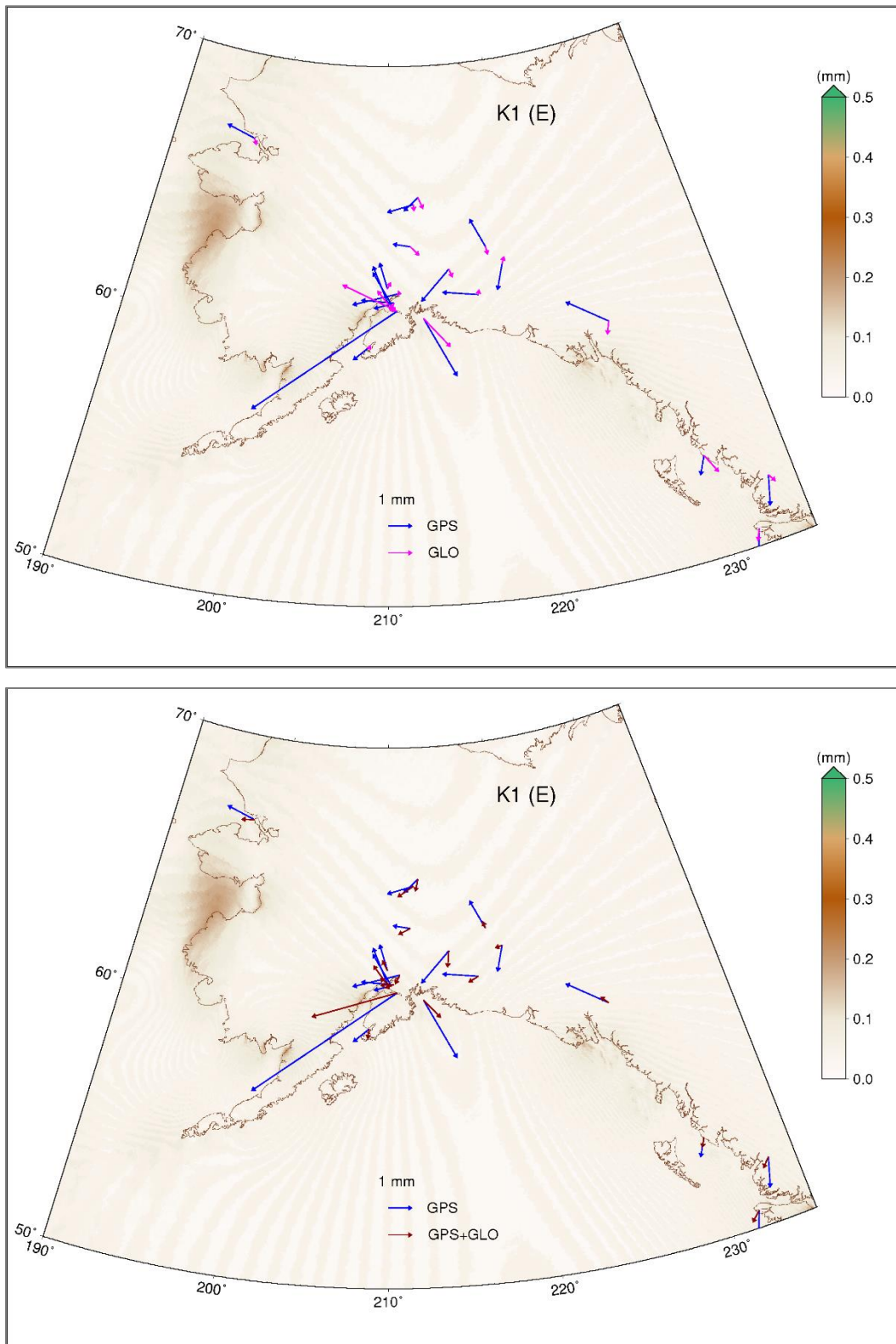


Figure 6.18: K1 OTL displacement residuals for the east component estimated by GPS-only vs. GLONASS-only data processing (top) and GPS-only vs. GPS+GLONASS data (bottom). The priori modelled OTL displacement is computed based on the FES2014 ocean tide model and the anelastic S362ANI-AL Earth model Green's function. The background map shows the RMS agreement of the magnitudes of the vector differences for the predicted OTL displacement (in mm).



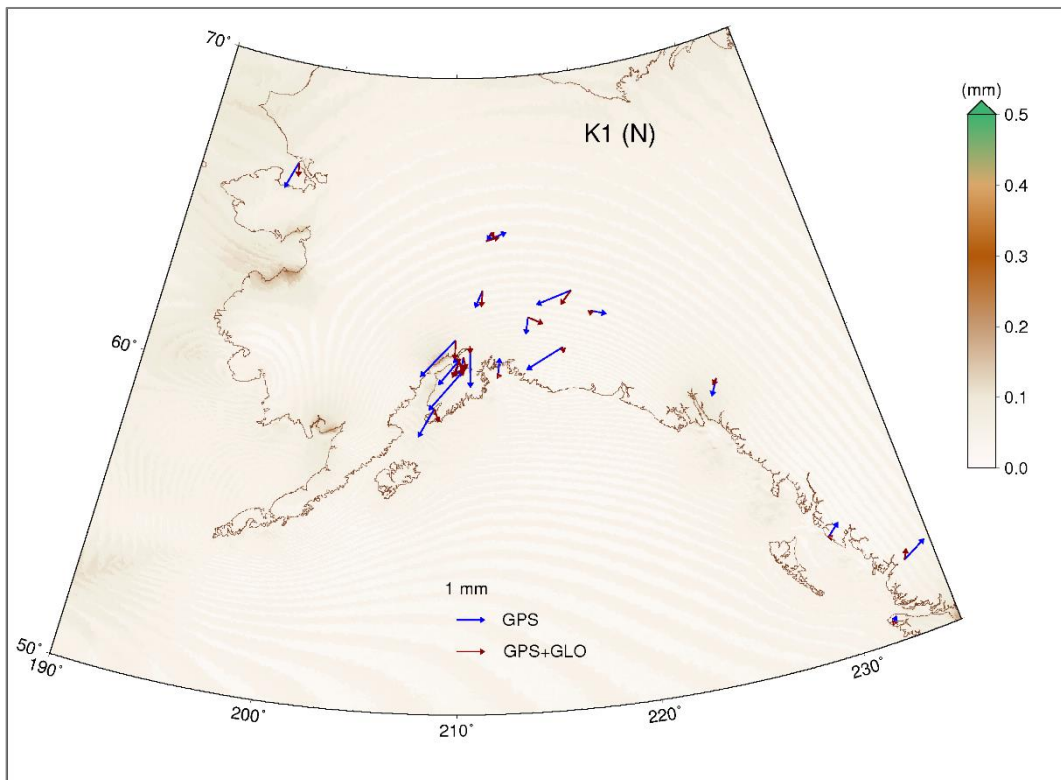
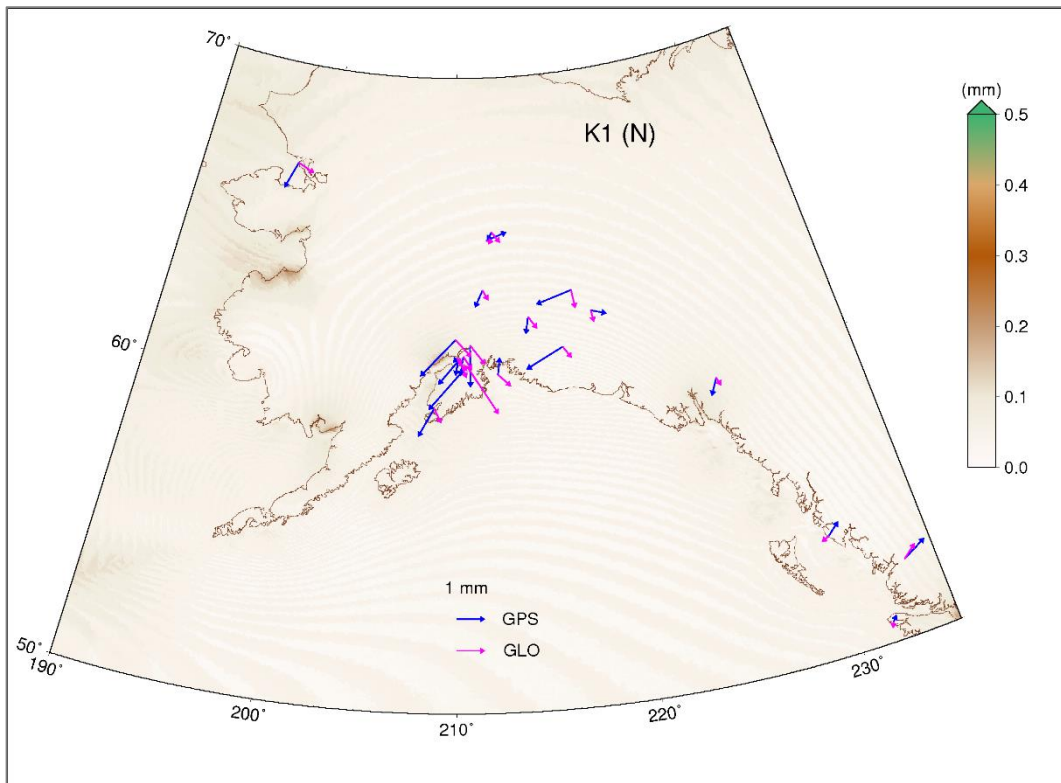


Figure 6.19: Similar to Figure 6.18 but for the north component

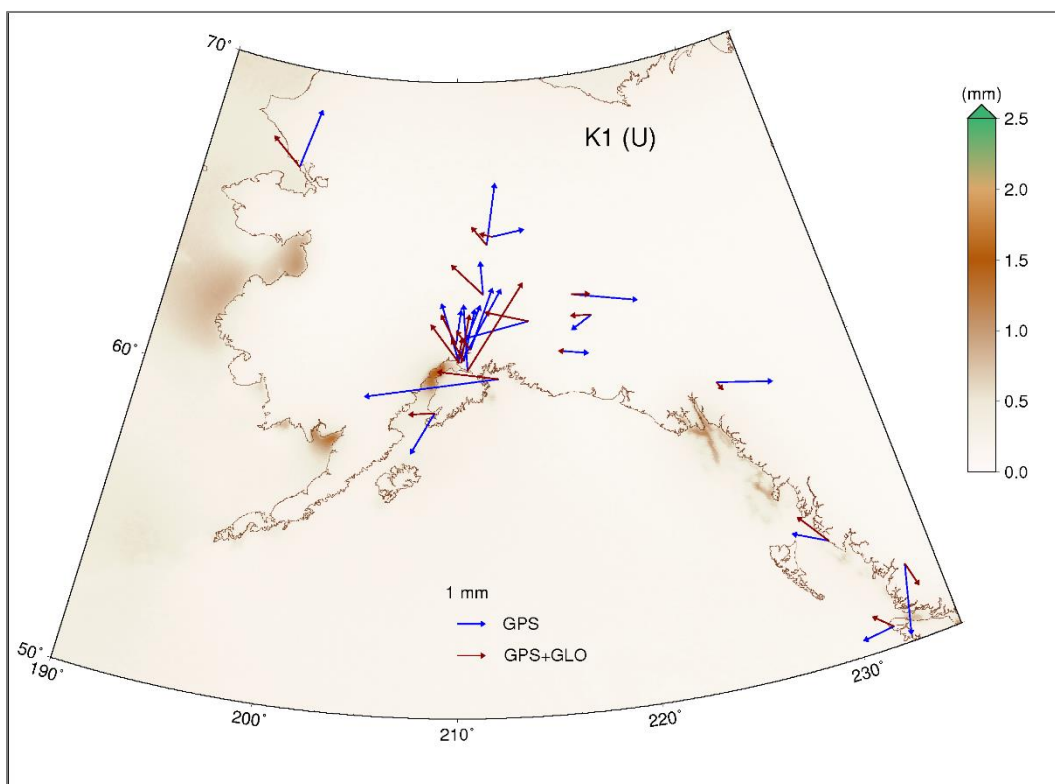
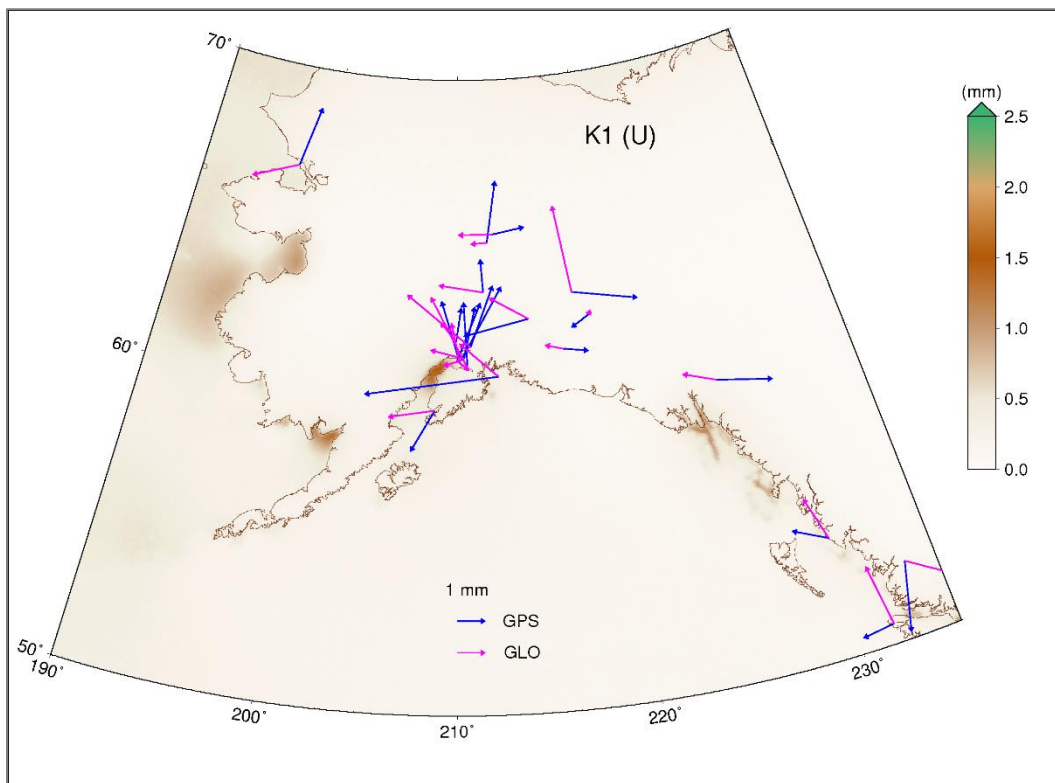


Figure 6.20: Similar to Figure 6.18 but for the vertical component

	<b>GPS</b>	<b>GLO</b>	<b>GPS+GLO</b>
<b>East</b>	0.5(0.6)	0.5(0.6)	0.4(0.6)
<b>North</b>	1.0(1.2)	0.9(1.0)	0.9(1.0)
<b>Vertical</b>	1.5(1.9)	1.3(1.4)	1.3(1.6)

Table 6.7: RMS and 85th percentile (in brackets) of the M2 OTL displacement residuals (in mm) estimated by GPS-only, GLONASS-only and combined GPS+GLONASS data at 22 multi-GNSS stations. The modelled OTL displacement is computed with the FES2014b ocean tide and the anelastic S362ANI-AL Earth model Green's function.

	<b>GPS</b>	<b>GLO</b>	<b>GPS+GLO</b>
<b>East</b>	2.1(2.0)	0.7(0.7)	1.0(0.8)
<b>North</b>	1.0(1.5)	0.7(0.7)	0.5(0.6)
<b>Vertical</b>	2.2(2.5)	1.7(2.3)	1.4(1.7)

Table 6.8: Similar to Table 6.7 but for the K1 constituent.

## 6.6 Summary and conclusions

This chapter has considered the use GNSS-estimated OTL displacement for investigating ocean tide models and asthenospheric anelasticity in Alaska. The larger than 15 mm modelled M2 and K1 OTL vertical displacements near the southern Alaskan coastline led to them being used as candidates for considering GNSS-observable anelasticity effects.

As the modelled M2 OTL displacement computed using different ocean tide models varies up to 0.5 mm and 2.5 mm for the horizontal and vertical components, respectively, to select the most accurate model among the most modern global ocean tide models, i.e. DTU10, EOT11a, FES2014b, GOT4.10c, HAMTIDE, NAO-global, and TPX08-atlas, they were compared with tide gauge data. Furthermore, the predicted OTL displacements using different ocean tide models were compared with those estimated from the GPS data processing. FES2014b has been shown to be the most accurate ocean tide model for Alaska, based on both comparisons.

It was found even at stations with a well-modelled ocean tide, that the predicted OTL displacement based on the FES2014b ocean tide model and the elastic PREM Earth model Green's function, differed from the GPS-estimated one by about 1.5 mm. After modifying the global PREM and regional S362ANI Earth models for the asthenospheric anelasticity effect, a reduction around 0.4 mm and 0.6 mm for the RMS and 85th percentile for the GPS-estimated OTL vertical displacement residuals, respectively, was seen. Hence, similar to western Europe and around the East China Sea, the asthenospheric anelasticity dispersion effect at M2 tidal frequency has been confirmed for Alaska.

Similar to Chapter 5, it has been shown that GLONASS is nearly as accurate as GPS to measure M2 OTL displacement in Alaska, and a data integration from the two systems leads to the most reliable solution. GLONASS-only and mixed GPS+GLONASS data also could partially overcome the GPS problem for K1 OTL displacement estimation.

It has been also shown that there is a common mode GNSS-estimated M2 OTL north displacement residual with around 1 mm amplitude in Alaska. The common mode residual was weakly correlated to the ocean tide model variation, and it was enlarged when an anelastic Green's function was used for the OTL displacement forward modelling. It is speculated that the common mode residuals may be related to the north-dipping subduction zone in Alaska, inferring that a local radial Earth model for that region is somewhat in doubt.

## Chapter 7 Conclusions

Multi-GNSS data has been used in this thesis for OTL displacement measurement as GPS-only data could not accurately determine K1 and K2 OTL displacement constituents, and it was also expected to have a more robust estimation of the GPS-detectable M2, N2, and O1 constituents with multi-GNSS rather than GPS-only solution. Several benefits for the multi-GNSS estimation of the OTL displacement have been found. It has been also shown that Earth's seismological physical models, which are recommended by the IERS Conventions for OTL displacement forward modelling, cannot fully explain the Earth's rheological behaviour when subject to tidal forces. Furthermore, it has been demonstrated that GNSS-estimated OTL displacement is applicable for the enhancement of OTL displacement forward modelling in two ways: ocean tide model validation and Earth model refinement.

### 7.1 Conclusions

The main conclusions of this thesis are summarized as follows:

#### 1. Validation of PANDA software

The ability of the PANDA software for a robust kinematic post-processed PPP of GPS-only, GLONASS-only and combined GPS+GLONASS data, over 49 globally distributed stations with more than three years observations, has been confirmed in two tests: comparison between the power spectral density of the GPS-estimated height time series in PANDA and GIPSY, and recovery of a synthetic tidal displacement signal with GNSS data processing in PANDA. Both tests have verified better than 0.5 mm accuracy for the GNSS observation kinematic PPP in PANDA.

The synthetic signal recovery test used in this thesis may be usable to simulate main orbit mismodelling effects and investigate their impact on the GNSS-estimated parameters either in PPP or relative positioning. It also can be used for the quality check of the precise satellite orbit information generated by different IGS analysis centres.

#### 2. IGS products selection and process noise optimization

By processing 101 globally distributed stations, it has been shown that ESA offers the most accurate satellite clock/orbit products for a global investigation of the OTL displacement through GPS and GLONASS kinematic PPP. It has been also shown that  $3 \text{ mm}/\sqrt{s}$  and  $1 \text{ mm}/\sqrt{h}$  are the optimum station position and ZWD process noise values, respectively, for PANDA kinematic PPP of a continuous GNSS station.

### 3. GLONASS data benefits for OTL displacement measurement

Three main benefits for incorporating GLONASS data for OTL displacement measurement have been found:

- a. Kinematic PPP of the combined GPS+GLONASS data in a float ambiguity solution is as precise as GPS-only fixed ambiguity solution, whilst the former does not rely on the availability of UPD external information.
- b. GLONASS-only float data can measure M2, N2 and O1 OTL displacement almost as accurately as GPS-only float solution. It is also shown that the combined GPS+GLONASS solution provides a robust GNSS-based OTL displacement measurement for the aforementioned constituents.
- c. GLONASS-only and combined GPS+GLONASS measurement could partially overcome the intrinsic GPS problems for measuring the K2 and K1 OTL displacements. However, due to the GLONASS sidereally-repeating station-satellite geometry, unmodeled EBT, surface displacement induced by the Earth's free core nutation, and sub-daily variation of EOPs, the GLONASS-based K2 and K1 OTL displacements were not as accurate as M2, N2, and O1.

### 4. GLONASS satellite availability

It has been illustrated that at around 40% of their data collection epoch per day, stations with absolute latitude less than  $50^\circ$  records data from less than seven GLONASS satellites at above  $10^\circ$  elevation angle. Consequently, the GLONASS-only kinematic PPP for these stations may be less accurate than stations with higher latitude.

### 5. Ocean tide model validation in Alaska

The applicability of GNSS-estimated OTL displacement for the accuracy assessment of the ocean tide models has been confirmed for the M2 and K1 constituents. In Alaska, it has been shown that FES2014b is the most accurate global ocean tide model, as the predicted OTL displacement based on this model had the best agreement with GNSS measurement of OTL displacement. A comparison between the modelled M2 and K1 ocean tide and tide gauge observations also showed FES2014b to be the most accurate model around Alaska.

### 6. Asthenosphere anelasticity in Alaska

It has been shown that modifying elastic Earth models (global PREM and regional S362ANI) for the effect of the asthenospheric anelasticity reduces the discrepancy between the modelled and GNSS-estimated M2 OTL vertical displacement up to 1.2 mm in Alaska. This has

confirmed that the Earth models which are computed by seismic data need to be refined for the dissipation effect within the asthenosphere when they are subjected to the tidal forces which act with a lower frequency than seismic forces.

## 7. Common mode signal for the OTL north displacement across Alaska

A common mode GPS-estimated OTL north displacement residual across Alaska with a magnitude of  $\sim 1.0$  mm was found. As the superimposed error induced by the GNSS data processing and ocean tide modelling was expected to be less than  $\sim 0.5$  mm, it was postulated that the Pacific plate north-dipping motion disturbs the radial symmetry assumption for physical Earth modelling in Alaska.

### 7.2 Suggestions for future work

For future research in this area, the following are suggested:

- The GNSS-estimated OTL displacement in this research can be compared with VLBI-estimates. This is especially useful to interpret the larger K2 and K1 OTL displacement residuals measured by GLONASS-only and combined GPS+GLONASS data.
- With regard to the IGS Multi-GNSS Experiment (MGEX) project, observations from Galileo and BeiDou can also be incorporated for OTL displacement estimation. This can improve the accuracy of the OTL displacement estimation, especially for K2 and K1 constituents.
- Using ambiguity fixed solution for the GLONASS-only and combined GPS+GLONASS kinematic PPP has the potential to reduce the noise level of the GNSS-estimated OTL displacement. Although GPS ambiguity fixed solution is applied in some software packages, e.g. GIPSY, kinematic PPP with ambiguity fixing of GLONASS phase measurement is still an ongoing research topic (e.g. Teunissen and Khodabandeh, 2019)
- It is expected to have more multi-GNSS stations in Alaska in future, and the benefits of using multi-GNSS data for the OTL 3D displacement assessment there, especially for the K1 constituent, can be investigated using a denser network.
- With the increased reliability of the multi-GNSS estimation of the OTL displacement compared to the GPS-only solution, the GNSS-estimated harmonic displacement at inland stations (where OTL displacement is negligible) may be used to investigate the surface displacement induced by the Earth body tide and Earth's free core nutation.
- Similar to the investigation for Alaska, GNSS-estimated OTL displacement can be used for investigating asthenospheric anelasticity in other regions with large predicted OTL

displacements. Eventually, a refined anelastic Earth model can be proposed for the IERS Conventions which currently use a seismological Earth model for OTL displacement prediction.



## References

- Abraha, K.E., Teferle, F.N., Hunegnaw, A. and Dach, R. (2017) 'GNSS related periodic signals in coordinate time-series from Precise Point Positioning', *Geophysical Journal International*, 208(3), pp. 1449–1464.
- Abraha, K.E., Teferle, F.N., Hunegnaw, A. and Dach, R. (2018) 'Effects of unmodelled tidal displacements in GPS and GLONASS coordinate time-series', *Geophysical Journal International*, 214(3), pp. 2195-2206.
- Agnew, D.C. (1997) 'NLOADF: A program for computing ocean-tide loading', *Journal of Geophysical Research: Solid Earth*, 102(B3), pp. 5109-5110.
- Agnew, D.C. (2007) 'Earth Tides', *Treatise on Geophysics*, 3, pp. 163-195.
- Allinson, C.R., Clarke, P.J., Edwards, S.J., King, M.A., Baker, T.F. and Cruddace, P.R. (2004) 'Stability of direct GPS estimates of ocean tide loading', *Geophysical Research Letters*, 31(15)
- Alsop, L.E. (1964) 'The characteristic numbers of semidiurnal tidal components for various earth models', 20, p. 286.
- Altamimi, Z., Rebischung, P., Métivier, L. and Collilieux, X. (2016) 'ITRF2014: A new release of the International Terrestrial Reference Frame modeling nonlinear station motions', *Journal of Geophysical Research: Solid Earth*, 121(8), pp. 6109-6131.
- Alterman, Z., Jarosch, H. and Pekeris, C.L. (1961) 'Propagation of Rayleigh Waves in the Earth', *Geophysical Journal of the Royal Astronomical Society*, 4(S0), pp. 219-241.
- Baker, T.F. (1984) 'Tidal deformations of the Earth', *Science Progress*, 69(274), pp. 197-233.
- Bar-Sever, Y.E. (1996) 'A new model for GPS yaw attitude', *Journal of Geodesy*, 70(11), pp. 714-723.
- Bar-Sever, Y.E., Kroger, P.M. and Borjesson, J.A. (1998) 'Estimating horizontal gradients of tropospheric path delay with a single GPS receiver', *Journal of Geophysical Research: Solid Earth*, 103(B3), pp. 5019-5035.
- Bertiger, W., Desai, S.D., Haines, B., Harvey, N., Moore, A.W., Owen, S. and Weiss, J.P. (2010) 'Single receiver phase ambiguity resolution with GPS data', *Journal of Geodesy*, 84(5), pp. 327-337.
- Bisnath, S. and Gao, Y. (2009) 'Current state of precise point positioning and future prospects and limitations', *Observing Our Changing Earth*, ed. By M.G. Sideris (Springer, Berlin 2009), pp. 615-623.
- Blewitt, G. (1990) 'An automatic editing algorithm for GPS data', *Geophysical research letters*, 17(3), pp. 199-202.
- Blewitt, G. (2008) 'Fixed point theorems of GPS carrier phase ambiguity resolution and their application to massive network processing: Ambizap', *Journal of Geophysical Research*, 113(B12).
- Blewitt, G., Hammond, W.C. and Kreemer, C. (2018) 'Harnessing the GPS Data Explosion for Interdisciplinary Science', *Eos*, 99.
- Boehm, J., Niell, A., Tregoning, P. and Schuh, H. (2006) 'Global Mapping Function (GMF): A new empirical mapping function based on numerical weather model data', *Geophysical Research Letters*, 33(7).
- Bos, M.S. and Baker, T.F. (2005) 'An estimate of the errors in gravity ocean tide loading computations', *Journal of Geodesy*, 79(1-3), pp. 50-63.

- Bos, M.S., Penna, N.T., Baker, T.F. and Clarke, P.J. (2015) 'Ocean tide loading displacements in western Europe: 2. GPS-observed anelastic dispersion in the asthenosphere', *Journal of Geophysical Research: Solid Earth*, 120(9), pp. 6540-6557.
- Cai, C. and Gao, Y. (2007) 'Precise point positioning using combined GPS and GLONASS observations', *Journal of Global Positioning Systems*, 6, pp. 13-22.
- Cai, C. and Gao, Y. (2013) 'Modeling and assessment of combined GPS/GLONASS precise point positioning', *GPS Solutions*, 17(2), pp. 223-236.
- Carrère, L., Lyard, F., Cancet, M., Guillot, A. and Picot, N. (2016) 'FES2014, a new tidal model – Validation results and perspectives for improvements', presentation to ESA Living Planet Conference, Prague 2016, (3), pp. 677-703.
- Carrère, L., Lyard, F., Cancet, M., Guillot, A. and Roblou, L. (2012) 'FES2012: A new global tidal model taking taking advantage of nearly 20 years of altimetry, ' *Proceedings of meeting "20 Years of Altimetry"*, Venice 2012.
- Cartwright, D.E. (1977) 'Oceanic tides', *Reports on Progress in Physics* 40, pp. 655-708.
- Cartwright, D.E. and Ray, R.D. (1990) 'Oceanic tides from Geosat altimetry', *Journal of Geophysical Research: Oceans*, 95(C3), pp. 3069-3090.
- Chen, H., Jiang, W., Ge, M., Wickert, J. and Schuh, H. (2014) 'An enhanced strategy for GNSS data processing of massive networks', *Journal of Geodesy*, 88(9), pp. 857-867.
- Cheng, Y. and Andersen, O.B. (2011) 'Multimission empirical ocean tide modeling for shallow waters and polar seas', *Journal of Geophysical Research: Oceans*, 116(C11).
- Collins, P., Bisnath, S., Lahaye, F. and Héroux, P. (2010) 'Undifferenced GPS Ambiguity Resolution Using the Decoupled Clock Model and Ambiguity Datum Fixing', *Navigation*, 57(2), pp. 123-135.
- Dach, R. and Dietrich, R. (2000) 'Influence of the ocean loading effect on GPS derived precipitable water vapor', *Geophysical Research Letters*, 27(18), pp. 2953-2956.
- Davis, J.L., Herring, T.A., Shapiro, I.I., Rogers, A.E.E. and Elgered, G. (1985) 'Geodesy by radio interferometry: Effects of atmospheric modeling errors on estimates of baseline length', *Radio Science*, 20(6), pp. 1593-1607.
- Desai, S. D. (2002) 'Observing the pole tide with satellite altimetry' *Journal of Geophysical Research*, 107(C11), 3186
- DiCaprio, C.J. and Simons, M. (2008) 'Importance of ocean tidal load corrections for differential InSAR', *Geophysical Research Letters*, 35(22)
- Dick, W. R. and Thaller, D. (2017) 'IERS Annual Report 2017', International Earth Rotation and Reference Systems Service, Central Bureau. Frankfurt am Main: Verlag des Bundesamts für Kartographie und Geodäsie, 2017. 207 p., ISBN 978-3-86482-131-8.
- Dziewonski, A.M. and Anderson, D.L. (1981) 'Preliminary reference Earth model', *Physics of the Earth and Planetary Interiors*, 25(4), pp. 297-356.
- Egbert, G.D. and Erofeeva, S.Y. (2002) 'Efficient Inverse Modeling of Barotropic Ocean Tides', *Journal of Atmospheric and Oceanic Technology*, 19(2), pp. 183-204.
- Elgered, G., Davis, J. L., Herring, T. A., and Shapiro, I. I. (1991) 'Geodesy by radio interferometry: water vapor radiometry for estimation of the wet delay', *Journal of Geophysical Research*, 96, pp. 6541–6555.
- Estey, L. and Meertens, C. (1999) 'TEQC: The Multi-Purpose Toolkit for GPS/GLONASS Data', *GPS Solutions* 3, pp. 42-49.

- Farrell, W.E. (1972) 'Deformation of the Earth by surface loads', *Reviews of Geophysics*, 10(3), pp. 761-797.
- Leon-Garcia, A. (1994) 'Probability and Random Processes for Electrical Engineering'. 2nd ed. Reading, Mass.: Addison-Wesley, 1994. Print.
- Ge, M., Gendt, G., Dick, G., Zhang, F.P. and Rothacher, M. (2006) 'A New Data Processing Strategy for Huge GNSS Global Networks', *Journal of Geodesy*, 80(4), pp. 199-203.
- Ge, M., Gendt, G., Rothacher, M., Shi, C. and Liu, J. (2007) 'Resolution of GPS carrier-phase ambiguities in Precise Point Positioning (PPP) with daily observations', *Journal of Geodesy*, 82(7), pp. 389-399.
- Gendt, G., Dick, G., Reigber, C., Tomassini, M. and Liu, Y. (2003) 'Demonstration of NRT GPS water vapor monitoring for numerical weather prediction in Germany', *Journal of Meteorological Society of Japan*, 82(1B), pp. 360-370.
- Geng, T., Xie, X., Fang, R., Su, X., Zhao, Q., Liu, G., Li, H., Shi, C. and Liu, J. (2016) 'Real-time capture of seismic waves using high-rate multi-GNSS observations: Application to the 2015 Mw 7.8 Nepal earthquake', *Geophysical Research Letters*, 43(1), pp. 161-167.
- Geng, J., Teferle, F.N., Shi, C., Meng, X., Dodson, A. H., Liu, J. (2009), 'Ambiguity resolution in precise point positioning with hourly data', *GPS Solutions*, 13(4), pp. 263-270.
- Godin, G. (1972) 'The analysis of tides'. Toronto, Buffalo: Toronto, Buffalo University of Toronto Press.
- Gong, X., Gu, S., Lou, Y., Zheng, F., Ge, M. and Liu, J. (2017) 'An efficient solution of real-time data processing for multi-GNSS network', *Journal of Geodesy*, 92(7), pp. 797-809.
- Görres, B., Campbell, J., Becker, M. and Siemes, M. (2006) 'Absolute calibration of GPS antennas: laboratory results and comparison with field and robot techniques', *GPS Solutions*, 10(2), pp. 136-145.
- Griffiths, J. and Ray, J. (2012) 'Sub-daily alias and draconitic errors in the IGS orbits', *GPS Solutions*, 17(3), pp. 413-422.
- Guo, J., Xu, X., Zhao, Q. and Liu, J. (2015) 'Precise orbit determination for quad-constellation satellites at Wuhan University: strategy, result validation, and comparison', *Journal of Geodesy*, 90(2), pp. 143-159.
- Hadas, T., Teferle, N.T., Kazmierski, K., Hordyniec, P. and Bosy., J. (2017) 'Optimum stochastic modelling for GNSS tropospheric delay estimation in real-time', *GPS Solutions*, 21, pp. 1069-1081.
- Hartmann, T. and Wenzel, H.-G. (1995) 'The HW95 tidal potential catalogue', *Geophysical Research Letters*, 22(24), pp. 3553-3556.
- Hofmann-Wellenhof, B., Lichtenegger, H. and Wasle, E. (2007) *GNSS-global navigation satellite systems: GPS, GLONASS, Galileo, and more*. Springer, Vienna.
- Hopfield, H.S. (1969) 'Two-quartic tropospheric refractivity profile for correcting satellite data', *Journal of Geophysical Research (1896-1977)*, 74(18), pp. 4487-4499.
- Ito, T., Okubo, M. and Sagiya, T. (2009) 'High resolution mapping of Earth tide response based on GPS data in Japan', *Journal of Geodynamics*, 48(3-5), pp. 253-259.
- Ito, T. and Simons, M. (2011) 'Probing asthenospheric density, temperature, and elastic moduli below the western United States', *Science*, 332(6032), pp. 947-51.
- Jin, S., Wang, J. and Park, P. (2014) 'An improvement of GPS height estimations: stochastic modeling', *Earth Planet Sp* 57, pp. 253-259.

- Khan, S.A. and Scherneck, H.-G. (2003) 'The M2 ocean tide loading wave in Alaska: vertical and horizontal displacements, modelled and observed', *Journal of Geodesy*, 77(3-4), pp. 117-127.
- Khan, S.A. and Tscherning, C.C. (2001) 'Determination of semi-diurnal ocean tide loading constituents using GPS in Alaska', *Geophysical Research Letters*, 28(11), pp. 2249-2252.
- King, M. (2006) 'Kinematic and static GPS techniques for estimating tidal displacements with application to Antarctica', *Journal of Geodynamics*, 41(1-3), pp. 77-86.
- King, M.A., Penna, N.T., Clarke, P.J. and King, E.C. (2005) 'Validation of ocean tide models around Antarctica using onshore GPS and gravity data', *Journal of Geophysical Research*, 110(B8).
- King, M.A., Watson, C.S., Penna, N.T. and Clarke, P.J. (2008) 'Subdaily signals in GPS observations and their effect at semiannual and annual periods', *Geophysical Research Letters*, 35(3).
- King, M.A. and Watson, C.S. (2010) 'Long GPS coordinate time series: multipath and geometry effects', *Journal of Geophysical Research*, 115, B04403.
- King, M. A., Padman, L., Nicholls, K., Clarke, P. J., Gudmundsson, G. H., Kulesa, B., Shepherd, A. (2011) 'Ocean tides in the Weddell Sea: New observations on the Filchner-Ronne and Larsen C ice shelves and model validation', *J. Geophysical Research*, 116, C06006
- Kouba, J. and Heroux, P. (2001) 'Precise Point Positioning Using IGS Orbit and Clock Products', *GPS Solution*, 5(2), pp. 12-28.
- Kouba, J., Lahaye, F. and Tetreault P. (2017) 'Precise Point Positioning. In: Teunissen P.J., Montenbruck O. (eds) Springer Handbook of Global Navigation Satellite Systems. ', Springer Handbook.
- Kudryavtsev SM (2004) Improved harmonic development of the Earth tide-generating potential. *J Geod* 77.
- Kustowski, B., Ekström, G. and Dziewoński, A. M. (2008) 'Anisotropic shear-wave velocity structure of the Earth's mantle: A global model', *Journal of Geophysical Research*, 113(B06306).
- Lagler, K., Schindelegger, M., Böhm, J., Krásná, H. and Nilsson, T. (2013) 'GPT2: Empirical slant delay model for radio space geodetic techniques', *Geophysical Research Letters*, 40(6), pp. 1069-1073.
- Le Provost, C., Genco, M.L., Lyard, F., Vincent, P. and Canceil, P. (1994) 'Spectroscopy of the world ocean tides from a finite element hydrodynamic model', *Journal of Geophysical Research: Oceans*, 99(C12), pp. 24777-24797.
- Lefèvre, F., Lyard, F.H. and Le Provost, C. (2000) 'FES98: A new global tide finite element solution independent of altimetry', *Geophysical Research Letters*, 27(17), pp. 2717-2720.
- Li, X., Dick, G., Lu, C., Ge, M., Nilsson, T., Ning, T., Wickert, J. and Schuh, H. (2015a) 'Multi-GNSS Meteorology: Real-Time Retrieving of Atmospheric Water Vapor From BeiDou, Galileo, GLONASS, and GPS Observations', *IEEE Transactions on Geoscience and Remote Sensing*, 53(12), pp. 6385-6393.
- Li, X., Ge, M., Dai, X., Ren, X., Fritsche, M., Wickert, J. and Schuh, H. (2015b) 'Accuracy and reliability of multi-GNSS real-time precise positioning: GPS, GLONASS, BeiDou, and Galileo', *Journal of Geodesy*, 89(6), pp. 607-635.

- Li, X., Zus, F., Lu, C., Dick, G., Ning, T., Ge, M., Wickert, J. and Schuh, H. (2015c) 'Retrieving of atmospheric parameters from multi-GNSS in real time: Validation with water vapor radiometer and numerical weather model', *Journal of Geophysical Research: Atmospheres*, 120(14), pp. 7189-7204.
- Liu, J. and Ge, M. (2003) PANDA software and its preliminary result of positioning and orbit determination.
- Longman, I.M. (1963) 'A Green's function for determining the deformation of the Earth under surface mass loads: 2. Computations and numerical results', *Journal of Geophysical Research* (1896-1977), 68(2), pp. 485-496.
- Luo, X., Mayer, M., Heck, B. and Awange, J.L. (2014) 'A Realistic and Easy-to-Implement Weighting Model for GPS Phase Observations', in *IEEE Transactions on Geoscience and Remote Sensing*, 52(10), pp. 6110-6118.
- Love, H. (1912) 'Some Problems of Geodynamics', *Nature*, 89(2228), pp. 471-472.
- Loyer, S., Perosanz, F., Mercier, F., Capdeville, H. and Marty, J.-C. (2012) 'Zero-difference GPS ambiguity resolution at CNES-CLS IGS Analysis Center', *Journal of Geodesy*, 86(11), pp. 991-1003.
- Martens, H.R., Simons, M., Owen, S. and Rivera, L. (2016) 'Observations of ocean tidal load response in South America from subdaily GPS positions', *Geophysical Journal International*, 205(3), pp. 1637-1664.
- Mathews, P.M., Dehant, V. and Gipson, J.M. (1997) 'Tidal station displacements', *Journal of Geophysical Research: Solid Earth*, 102(B9), pp. 20469-20477.
- Matsumoto, K., Takanezawa, T. and Ooe, M. (2000) 'Ocean Tide Models Developed by Assimilating TOPEX/POSEIDON Altimeter Data into Hydrodynamical Model: A Global Model and a Regional Model around Japan', *Journal of Oceanography*, 56, pp. 567-581.
- Matsumoto, K., Takanezawa, T. and Ooe, M. (2001) 'GOTIC2: A Program for Computation of Oceanic Tidal Loading Effect', *J. Geodetic Soc. Jpn.*, 47.
- Maymon, G. (2018) 'Chapter 2 - Some Important Statistical Distributions', in Maymon, G. (ed.) *Stochastic Crack Propagation*. Academic Press, pp. 9-18.
- McCarthy, D. D., and Petit G. (2004) 'IERS Conventions 2003', IERS Tech. Note 32.
- Melachroinos, S.A., Biancale, R., Llubes, M., Perosanz, F., Lyard, F., Vergnolle, M., Bouin, M.N., Masson, F., Nicolas, J., Morel, L. and Durand, S. (2007) 'Ocean tide loading (OTL) displacements from global and local grids: comparisons to GPS estimates over the shelf of Brittany, France', *Journal of Geodesy*, 82(6), pp. 357-371.
- Melbourne, W.G. (1985) 'The Case for Ranging in GPS-based Geodetic Systems', *Proceedings of 1st International Symposium on Precise Positioning with the Global Positioning System*, Rockville, MD, USA., pp. 373-386.
- Melchior, P.J. (1966) *The earth tides*. [1st ed.]. edn. Oxford, New York, Pergamon Press.
- Montenbruck, O., Hauschild, A., Steigenberger, P. (2014) 'Differential code bias estimation using multi-GNSS observations and global ionosphere maps', *Navigation*, 61(3), pp. 191-201
- Pan L, Zhang X, Li X, Li X, Lu C, Liu J, Wang Q (2017) Satellite availability and point positioning accuracy evaluation on a global scale for integration of GPS, GLONASS, BeiDou and Galileo. *Adv Space Res* 63(9):2696-2710.
- Penna, N.T. and Stewart, M.P. (2003) 'Aliased tidal signatures in continuous GPS height time series', *Geophysical Research Letter*, 30(23), 2184.

- Penna, N.T., Bos, M.S., Baker, T.F. and Scherneck, H.G. (2008) 'Assessing the accuracy of predicted ocean tide loading displacement values', *Journal of Geodesy*, 82(12), pp. 893-907.
- Penna, N.T., Clarke, P.J., Bos, M.S. and Baker, T.F. (2015) 'Ocean tide loading displacements in western Europe: 1. Validation of kinematic GPS estimates', *Journal of Geophysical Research: Solid Earth*, 120(9), pp. 6523-6539.
- Penna, N.T., King, M.A. and Stewart, M.P. (2007) 'GPS height time series: Short-period origins of spurious long-period signals', *Journal of Geophysical Research: Solid Earth*, 112(B2).
- Penna, N.T., Morales Maqueda, M.A., Martin, I., Guo, J. and Foden, P.R. (2018) 'Sea Surface Height Measurement Using a GNSS Wave Glider', *Geophysical Research Letters*, 45(11), pp. 5609-5616.
- Petit, G. and Luzum, B. (2010) 'IERS Conventions (2010)', IERS Tech. Note 36.
- Petrov, L. and Ma, C. (2003) 'Study of harmonic site position variations determined by very long baseline interferometry', *Journal of Geophysical Research: Solid Earth*, 108(B4).
- Pingree, R.D. (2009) 'The Formation Of The Shambles And Other Banks By Tidal Stirring Of The Seas', *Journal of the Marine Biological Association of the United Kingdom*, 58(1), pp. 211-226.
- Prange, L., Orliac, E., Dach, R., Arnold, D., Beutler, G., Schaer, S. and Jäggi, A. (2016) 'CODE's five-system orbit and clock solution—the challenges of multi-GNSS data analysis', *Journal of Geodesy*, 91(4), pp. 345-360.
- Pugh, D.T. (1987) *Tides, surges, and mean sea-level*. Chichester New York: J. Wiley.
- Rao, K.R. (2010) *Fast Fourier transform algorithms and applications*. Dordrecht, New York: Dordrecht, New York : Springer.
- Ray, R. D. and R. M. Ponte, 2003, "Barometric tides from ECMWF operational analyses," *Annual Geophysics*, 21(8), pp. 1897–1910.
- Ray, J., Dong, D. and Altamimi, Z. (2004) 'IGS reference frames: status and future improvements', *GPS Solutions*, 8(4), pp. 251-266.
- Ray, R.D. (2013) 'Precise comparisons of bottom-pressure and altimetric ocean tides', *Journal of Geophysical Research: Oceans*, 118(9), pp. 4570-4584.
- Ray, R.D., Loomis, B.D., Luthcke, S.B. and Rachlin, K.E. (2019) 'Tests of ocean-tide models by analysis of satellite-to-satellite range measurements: an update', *Geophysical Journal International*, 217(2), pp. 1174-1178.
- Rodriguez-Solano, C.J., Hugentobler, U., Steigenberger, P. and Lutz, S. (2011) 'Impact of Earth radiation pressure on GPS position estimates', *Journal of Geodesy*, 86(5), pp. 309-317.
- Rothacher, M. and Beutler, G. (1998) 'The role of GPS in the study of global change', *Physics and Chemistry of the Earth*, 23(9–10), pp. 1029-1040,
- Rothacher, M. and Schmid, R. (2010) 'ANTEX: The Antenna Exchange Format, Version 1.4', <ftp://igs.org/pub/station/general/antex14.txt>.
- Rothacher, M. and Mader, G. (2003) 'Receiver and satellite antenna phase center offsets and variations', In: Tétreault, P., Neilan, R., Gowey, K. (eds.) *Proceedings of the Network, Data and Analysis Centre 2002 Workshop*, , pp. 141-152.
- Saastamoinen, J. (1972) 'Contributions to the theory of atmospheric refraction', *Bulletin Géodésique (1946-1975)*, 105(1), pp. 279-298.

- Savcenko, Roman; Bosch, Wolfgang (2012): EOT11a - Empirical Ocean Tide Model from Multi-Mission Satellite Altimetry. Deutsches Geodätisches Forschungsinstitut (DGFI), München, 89, 49
- Schenewerk, M.S., Marshall, J. and Dillinger, W. (2001) 'Vertical Ocean-loading Deformations Derived from a Global GPS Network', *Journal of the Geodetic Society of Japan*, 47(1), pp. 237-242.
- Scherneck, H.G. (1991) 'A parametrized solid earth tide model and ocean tide loading effects for global geodetic baseline measurements', *Geophysical Journal International*, 106(3), pp. 677-694.
- Schmid, R., Mader, G. and Herring, T. (2005) 'From relative to absolute antenna phase center corrections', In: Meindl, M. (ed.) *Proceedings of the IGS Workshop and Symposium 2004*, Bern.
- Schuh, H. and Moehlmann, L. (1989) 'Ocean loading station displacements observed by VLBI', *Geophysical Research Letters*, 16(10), pp. 1105-1108.
- Schwiderski, E.W. (1980) 'On charting global ocean tides', *Reviews of Geophysics*, 18(1), pp. 243-268.
- Seeber, G. (2003) *Satellite Geodesy*. Walter de Gruyter.
- Sośnica, K., Thaller, D., Dach, R., Jäggi, A. and Beutler, G. (2013) 'Impact of loading displacements on SLR-derived parameters and on the consistency between GNSS and SLR results', *Journal of Geodesy*, 87(8), pp. 751-769.
- Sovers, O.J. (1994) 'Vertical ocean loading amplitudes from VLBI measurements', *Geophysical Research Letters*, 21(5), pp. 357-360.
- Stakgold, I. (1998) *Green's functions and boundary value problems*. 2nd ed.. edn. New York: New York : Wiley.
- Stammer, D., Ray, R.D., Andersen, O.B., Arbic, B.K., Bosch, W., Carrère, L., Cheng, Y., Chinn, D.S., Dushaw, B.D., Egbert, G.D., Erofeeva, S.Y., Fok, H.S., Green, J.A.M., Griffiths, S., King, M.A., Lapin, V., Lemoine, F.G., Luthcke, S.B., Lyard, F., Morison, J., Müller, M., Padman, L., Richman, J.G., Shriver, J.F., Shum, C.K., Taguchi, E. and Yi, Y. (2014) 'Accuracy assessment of global barotropic ocean tide models', *Reviews of Geophysics*, 52(3), pp. 243-282.
- Stewart, M.P., Penna, N.T. and Lichti, D.D. (2005), 'Investigating the propagation mechanism of unmodelled systematic errors on coordinate time series estimated using least squares', *Journal of Geodesy*, 79(8), pp. 479-489.
- Taguchi, E., Stammer, D. and Zahel, W. (2014) 'Inferring deep ocean tidal energy dissipation from the global high-resolution data-assimilative HAMTIDE model', *Journal of Geophysical Research: Oceans*, 119(7), pp. 4573-4592.
- Tapley, B.D., Ries, J.C., Davis, G.W., Eanes, R.J., Schutz, B.E., Shum, C.K., Watkins, M.M., Marshall, J.A., Nerem, R.S., Putney, B.H., Klosko, S.M., Luthcke, S.B., Pavlis, D., Williamson, R.G. and Zelensky, N.P. (1994) 'Precision orbit determination for TOPEX/POSEIDON', *Journal of Geophysical Research: Oceans*, 99(C12), pp. 24383-24404.
- Teunissen, P. (1995) 'The least-squares ambiguity decorrelation adjustment: a method for fast GPS integer ambiguity estimation', *Journal of Geodesy*, 70, pp. 65-82.
- Teunissen, P.J. (2017) 'Carrier Phase Integer Ambiguity Resolution. In: Teunissen P.J., Montenbruck O. (eds) *Springer Handbook of Global Navigation Satellite Systems*. ', Springer Handbook.

- Teunissen, P.J.G., Montenbruck, O. (2017) Springer Handbook of Global Navigation Satellite Systems. 1. edn. Cham : Springer International Publishing : Imprint: Springer.
- Teunissen, P.J.G. and Khodabandeh, A. (2019) 'GLONASS ambiguity resolution', *GPS Solutions*, 23:101.
- Thomas, I.D., King, M.A. and Clarke, P.J. (2007) 'A comparison of GPS, VLBI and model estimates of ocean tide loading displacements', *Journal of Geodesy*, 81(5), pp. 359-368.
- Tregoning, P. and Watson, C. (2009) 'Atmospheric effects and spurious signals in GPS analyses', *Journal of Geophysical Research*, 114, B09403
- Vaniček, P. (1973) 'Further development and properties of the spectral analysis by least-squares', *Astrophysics and Space Science*, 12(1), pp. 10-33.
- Vaniček, P. (1986) *Geodesy : the concepts*. 2nd ed.. edn. Amsterdam, New York: Amsterdam, New York : North Holland Pub. Co.
- Vey, S., Calais, E., Llubes, M., Florsch, N., Woppelmann, G., Hinderer, J., Amalvict, M., Lalancette, M.F., Simon, B., Duquenne, F. and Haase, J.S. (2002) 'GPS measurements of ocean loading and its impact on zenith tropospheric delay estimates: a case study in Brittany, France', *Journal of Geodesy*, 76(8), pp. 419-427.
- Villiger, A. and Dach, R. (2018) 'International GNSS Service Technical Report 2018 (IGS Annual Report)', IGS Central Bureau and University of Bern; Bern Open Publishing.
- Wahr, J.M. (1981) 'Body tides on an elliptical, rotating, elastic and oceanless earth', *Geophysical Journal of the Royal Astronomical Society*, 64(3), pp. 677-703.
- Wang, J., Penna, N.T., Clarke, P.J. and Bos, M.S. (2020) 'Asthenospheric anelasticity effects on ocean tide loading in the East China Sea region observed with GPS.', *Solid Earth Discuss* pp. 1-22.
- Weiss, J.P., Steigenberger P., Springer T. (2017) 'Orbit and clock product generation In: Teunissen P.J., Montenbruck O. (eds) Springer Handbook of Global Navigation Satellite Systems. ', Springer Handbook.
- Wu, J.T., Wu, S.C., Hajj, G.A., Bertiger, W.I. and Lichten, S.M. (1993) 'Effects of Antenna Orientation on GPS Carrier Phase', *Manuscripta Geodaetica*, 18, pp. 91-98.
- Wübbena, G. (1985) 'Software developments for geodetic positioning with GPS using TI-4100 code and carrier measurements', In *Proceedings of the First International Symposium on Precise Positioning with the Global Positioning System*, 19, pp. 403-412.
- Yuan, L. and Chao, B.F. (2012) 'Analysis of tidal signals in surface displacement measured by a dense continuous GPS array', *Earth and Planetary Science Letters*, 355-356, pp. 255-261.
- Yuan, L., Chao, B.F., Ding, X. and Zhong, P. (2013) 'The tidal displacement field at Earth's surface determined using global GPS observations', *Journal of Geophysical Research: Solid Earth*, 118(5), pp. 2618-2632.
- Yuan, L.G., Ding, X.L., Zhong, P., Chen, W. and Huang, D.F. (2009) 'Estimates of ocean tide loading displacements and its impact on position time series in Hong Kong using a dense continuous GPS network', *Journal of Geodesy*, 83(11), pp. 999-1015.
- Yun, H.-S., Lee, D.-H. and Song, D.-S. (2007) 'Determination of vertical displacements over the coastal area of Korea due to the ocean tide loading using GPS observations', *Journal of Geodynamics*, 43(4-5), pp. 528-541.



- Zhao, Q., Guo, J., Hu, Z., Shi, C., Liu, J., Cai, H. and Liu, X. (2011) 'GRACE gravity field modeling with an investigation on correlation between nuisance parameters and gravity field coefficients', *Advances in Space Research*, 47(10), pp. 1833-1850.
- Zumberge, J.F., Heflin, M.B., Jefferson, D.C., Watkins, M.M. and Webb, F.H. (1997) 'Precise point positioning for the efficient and robust analysis of GPS data from large networks', *Journal of Geophysical Research: Solid Earth*, 102(B3), pp. 5005-5017.

## Appendix A: Satellite availability and GDOP calculation

By having receiver coordinates  $(\varphi_r, \lambda_r, h_r)$  and satellite 3D positions  $(x_s, y_s, z_s)$  in an Earth Centred Earth Fixed (ECEF) frame, the satellite elevation angle can be computed through the following steps:

- 1- Conversion of the receiver curvilinear coordinate to the ECEF Cartesian coordinates

$$N = \frac{a}{\sqrt{1 - e^2 \cdot \sin^2(\varphi_r)}} \quad (\text{A.1})$$

$$x_r = (N + h_r) \cdot \cos(\varphi_r) \cdot \cos(\lambda_r) \quad (\text{A.2})$$

$$y_r = (N + h_r) \cdot \cos(\varphi_r) \cdot \sin(\lambda_r) \quad (\text{A.3})$$

$$z_r = ((1 - e^2)N + h_r) \cdot \sin(\varphi_r) \quad (\text{A.4})$$

where  $a$  and  $e$  are the semi-major axis and eccentricity of the reference ellipsoid, respectively.

- 2- Computation of the receiver-satellite relative vector in the ECEF frame:

$$\mathbf{r}_{r-s} = \begin{bmatrix} x_s - x_r \\ y_s - y_r \\ z_s - z_r \end{bmatrix} \quad (\text{A.5})$$

- 3- Conversion of the receiver-satellite relative vector from ECEF to local (east-north-up) frame

$$\mathbf{r}'_{r-s} = \begin{bmatrix} x'_{r-s} \\ y'_{r-s} \\ z'_{r-s} \end{bmatrix} = P_2 R_2 R_3 \cdot \mathbf{r}_{r-s} \quad (\text{A.6})$$

where  $P_2, R_2$  and  $R_3$  are defined as:

$$P_2 = \begin{bmatrix} 1 & 0 & 0 \\ 0 & -1 & 0 \\ 0 & 0 & 1 \end{bmatrix} \quad (\text{A.7})$$

$$R_2 = \begin{bmatrix} \cos(\varphi_r - 90) & 0 & -\sin(\varphi_r - 90) \\ 0 & 1 & 0 \\ \sin(\varphi_r - 90) & 0 & \cos(\varphi_r - 90) \end{bmatrix} \quad (\text{A.8})$$

$$R_3 = \begin{bmatrix} \cos(\lambda_r - 180) & \sin(\lambda_r - 180) & 0 \\ -\sin(\lambda_r - 180) & \cos(\lambda_r - 180) & 0 \\ 0 & 0 & 1 \end{bmatrix} \quad (\text{A.9})$$

- 4- Elevation angle computation

$$\alpha = \arcsin\left(\frac{z'_{r-s}}{|\mathbf{r}'_{r-s}|}\right) \quad (\text{A.10})$$

Thereafter, the number of available satellites will be found after counting all satellites with elevation angle higher than a pre-defined mask angle.

To compute GDOP, each row (relevant to each satellite above the mask angle) of the design matrix  $A$  in least-square adjustment is constructed as:

$$\left[ -\frac{x_s - x_r}{|\mathbf{r}_{r-s}|} \quad -\frac{y_s - y_r}{|\mathbf{r}_{r-s}|} \quad -\frac{z_s - z_r}{|\mathbf{r}_{r-s}|} \quad 1 \right] \quad (\text{A.11})$$

Then, GDOP can be computed from the cofactor matrix:

$$Q_x = (A^t \cdot A)^{-1} = \begin{bmatrix} q_{xx} & q_{xy} & q_{xz} & q_{xt} \\ q_{yx} & q_{yy} & q_{yz} & q_{yt} \\ q_{zx} & q_{zy} & q_{zz} & q_{zt} \\ q_{tx} & q_{ty} & q_{tz} & q_{tt} \end{bmatrix} \quad (\text{A.12})$$

$$GDOP = \sqrt{q_{xx} + q_{yy} + q_{zz} + q_{tt}} \quad (\text{A.13})$$

## Appendix B: Normal equation manipulation and input/output files in PANDA

### B.1 Normal equation manipulation

In a system of linear equations, with  $n$  unknowns and  $n$  independent equations, it is possible to use one group of equations to write a subset of unknown parameters, say  $[x_1 \ x_2 \ x_3 \ \dots \ x_p]^t$ , as a subject of other parameters  $[x_{p+1} \ x_{p+2} \ x_{p+3} \ \dots \ x_n]^t$ :

$$\begin{aligned}x_1 &= f_1(x_{p+1}, x_{p+2}, x_{p+3}, \dots, x_n) \\x_2 &= f_2(x_{p+1}, x_{p+2}, x_{p+3}, \dots, x_n) \\&\vdots \\x_p &= f_p(x_{p+1}, x_{p+2}, x_{p+3}, \dots, x_n)\end{aligned}\tag{B.1}$$

Then, the above  $p$  equations can be substituted in the remaining  $(n - p)$  equations to eliminate  $x_1, x_2, x_3, \dots, x_p$  and construct a new  $(n - p) \times (n - p)$  system. This technique, which is known as elimination, reduces the size of the coefficient matrix of a linear or linearized system. As a result of parameter elimination, the new (smaller size) coefficient matrix can be inverted more conveniently. After solving the smaller system for one subset of the unknown parameters, they are substituted in the original system to solve the remaining parameters.

In PANDA, the above algebraic manipulation is applied on the normal equations (NEQ) system. Instead of reading all data from an entire data processing session and then applying the parameter elimination, PANDA eliminates its target parameters immediately after reading observations at each single epoch. The eliminated normal matrix at one epoch is merged with the normal matrix which is relevant purely to the observations in the following epoch, and another elimination is then applied on the augmented matrix. This elimination/augmentation continues until the last epoch in the processing session.

For a high rate GNSS data collection, the recorded data in two consecutive epochs may be in one of the following situations:

1. All recorded data in both epochs are from the same phase connected arcs
2. A new set of phase connected arcs is added in the new epoch
3. A subset of the existing phase connected arc disappears in the new epoch
4. Combination of case 2 and case 3

In the following sections, the matrix manipulation for the parameter elimination in each case will be described.

**Case 1: Similar phase connected arc**

To perform the parameter elimination in a GNSS data processing, it is typical to categorize the unknown parameters to two classes: time variant (local) and constant (global). Local and global parameters are shown by  $\mathbf{r}$  and  $\mathbf{b}$ , respectively, for the rest of this section.

By considering equal weights for all GNSS measurements, observation equations at the two consecutive epochs  $i$  and  $j$  can be written as:

$$A_i \mathbf{r}_i + B \mathbf{b} = \mathbf{l}_i \rightarrow [A_i \ B] \begin{bmatrix} \mathbf{r}_i \\ \mathbf{b} \end{bmatrix} = \mathbf{l}_i \xrightarrow{NEQ} \begin{bmatrix} A_i^t A_i & A_i^t B \\ B^t A_i & B^t B \end{bmatrix} \begin{bmatrix} \mathbf{r}_i \\ \mathbf{b} \end{bmatrix} = \begin{bmatrix} A_i^t \mathbf{l}_i \\ B^t \mathbf{l}_i \end{bmatrix} \quad (\text{B.2})$$

$$A_j \mathbf{r}_j + B \mathbf{b} = \mathbf{l}_j \rightarrow [A_j \ B] \begin{bmatrix} \mathbf{r}_j \\ \mathbf{b} \end{bmatrix} = \mathbf{l}_j \xrightarrow{NEQ} \begin{bmatrix} A_j^t A_j & A_j^t B \\ B^t A_j & B^t B \end{bmatrix} \begin{bmatrix} \mathbf{r}_j \\ \mathbf{b} \end{bmatrix} = \begin{bmatrix} A_j^t \mathbf{l}_j \\ B^t \mathbf{l}_j \end{bmatrix} \quad (\text{B.3})$$

To eliminate local parameters from a NEQ at epoch  $i$ , Equation B.2 can be rearranged as follows:

$$A_i^t A_i \mathbf{r}_i + A_i^t B \mathbf{b} = A_i^t \mathbf{l}_i \quad (\text{B.4})$$

$$B^t A_i \mathbf{r}_i + B^t B \mathbf{b} = B^t \mathbf{l}_i \quad (\text{B.5})$$

$$\begin{aligned} (A_i^t A_i)^{-1} \times \text{Equation B.4} &\rightarrow \mathbf{r}_i + (A_i^t A_i)^{-1} A_i^t B \mathbf{b} = (A_i^t A_i)^{-1} A_i^t \mathbf{l}_i \\ &\rightarrow \mathbf{r}_i = (A_i^t A_i)^{-1} A_i^t \mathbf{l}_i - (A_i^t A_i)^{-1} A_i^t B \mathbf{b} \end{aligned} \quad (\text{B.6})$$

After substituting Equation B.6 in Equation B.5,  $\mathbf{r}_i$  is eliminated:

$$B^t A_i \{ (A_i^t A_i)^{-1} A_i^t \mathbf{l}_i - (A_i^t A_i)^{-1} A_i^t B \mathbf{b} \} + B^t B \mathbf{b} = B^t \mathbf{l}_i \quad (\text{B.7})$$

Finally, Equation B.7 can be rearranged to write a NEQ purely for the time-invariant parameters at epoch  $i$ :

$$\{ B^t B - B^t A_i (A_i^t A_i)^{-1} A_i^t B \} \mathbf{b} = \{ B^t - B^t A_i (A_i^t A_i)^{-1} A_i^t \} \mathbf{l}_i \quad (\text{B.8})$$

$$M_i \cdot \mathbf{b} = \mathbf{L}_i \quad (\text{B.9})$$

$$\text{where } M_i = \{ B^t B - B^t A_i (A_i^t A_i)^{-1} A_i^t B \}, \mathbf{L}_i = \{ B^t - B^t A_i (A_i^t A_i)^{-1} A_i^t \} \mathbf{l}_i$$

Now, Equation B.9 can be augmented with Equation B.3, and the following NEQ at epoch  $j$  is generated:

$$\begin{bmatrix} A_j^t A_j & A_j^t B \\ B^t A_j & B^t B + M_i \end{bmatrix} \begin{bmatrix} \mathbf{r}_j \\ \mathbf{b} \end{bmatrix} = \begin{bmatrix} A_j^t \mathbf{l}_j \\ B^t \mathbf{l}_j + \mathbf{L}_i \end{bmatrix} \quad (\text{B.10})$$

It is clear that the estimated global parameters from Equation B.10 employ observations from the two epochs. Similar to epoch  $i$ , the local parameters are eliminated from Equation B.10, and then the eliminated NEQ is merged with the NEQ at the next epoch. This approach is then repeated until the last epoch of the phase connected arc.

### Case 2: Adding a new set of phase connected arc

If a new group of satellites is added at epoch  $j$  (parameters and matrices labelled by a quotation mark below), the NEQ at that epoch can be written as:

$$\begin{bmatrix} A_j \\ A'_j \end{bmatrix} \mathbf{r}_j + \begin{bmatrix} B & 0 \\ 0 & B' \end{bmatrix} \begin{bmatrix} \mathbf{b} \\ \mathbf{b}' \end{bmatrix} = \begin{bmatrix} \mathbf{l}_j \\ \mathbf{l}'_j \end{bmatrix} \rightarrow \begin{bmatrix} A_j & B & 0 \\ A'_j & 0 & B' \end{bmatrix} \begin{bmatrix} \mathbf{r}_j \\ \mathbf{b} \\ \mathbf{b}' \end{bmatrix} = \begin{bmatrix} \mathbf{l}_j \\ \mathbf{l}'_j \end{bmatrix} \quad (\text{B.11})$$

$$\xrightarrow{NEQ} \begin{bmatrix} A_j^t A_j + A_j'^t A_j' & A_j^t B & A_j'^t B' \\ B^t A_j & B^t B & 0 \\ B'^t A_j' & 0 & B'^t B \end{bmatrix} \begin{bmatrix} \mathbf{r}_j \\ \mathbf{b} \\ \mathbf{b}' \end{bmatrix} = \begin{bmatrix} A_j^t \mathbf{l}_j + A_j'^t \mathbf{l}'_j \\ B^t \mathbf{l}_j \\ B'^t \mathbf{l}'_j \end{bmatrix} \quad (\text{B.12})$$

Now, Equation B.9 (eliminated NEQ at epoch  $i$ ) can be combined with B.12 to construct the following form:

$$\begin{bmatrix} A_j^t A_j + A_j'^t A_j' & A_j^t B & A_j'^t B' \\ B^t A_j & B^t B + M_i & 0 \\ B'^t A_j' & 0 & B'^t B \end{bmatrix} \begin{bmatrix} \mathbf{r}_j \\ \mathbf{b} \\ \mathbf{b}' \end{bmatrix} = \begin{bmatrix} A_j^t \mathbf{l}_j + A_j'^t \mathbf{l}'_j \\ B^t \mathbf{l}_j + \mathbf{L}_i \\ B'^t \mathbf{l}'_j \end{bmatrix} \quad (\text{B.13})$$

It can be seen from Equation B.13 that the partition of the NEQ relevant to the common global parameters in the two epochs ( $\mathbf{b}$ ) is updated, and the submatrices in the NEQ which are relevant to the new satellite parameters ( $\mathbf{b}'$ ) is initialized. From epoch  $j$  onwards, as long as the two consecutive epochs have the same number of satellites and they experience no cycle slips, the NEQ manipulation which is explained in Section B.1 is repeated.

### Case 3: A set of phase connected arcs is lost

If a group of satellites disappears from epoch  $j$  (parameters and matrices labelled with an asterisk below), the NEQ at epoch  $i$  can be written as follows:

$$\begin{bmatrix} A_i \\ A_i^* \end{bmatrix} \mathbf{r}_i + \begin{bmatrix} B & 0 \\ 0 & B^* \end{bmatrix} \begin{bmatrix} \mathbf{b} \\ \mathbf{b}^* \end{bmatrix} = \begin{bmatrix} \mathbf{l}_i \\ \mathbf{l}_i^* \end{bmatrix} \rightarrow \begin{bmatrix} A_i & B & 0 \\ A_i^* & 0 & B^* \end{bmatrix} \begin{bmatrix} \mathbf{r}_i \\ \mathbf{b} \\ \mathbf{b}^* \end{bmatrix} = \begin{bmatrix} \mathbf{l}_i \\ \mathbf{l}_i^* \end{bmatrix} \quad (\text{B.14})$$

$$\xrightarrow{NEQ} \begin{bmatrix} A_i^t A_i + A_i^{*t} A_i^* & A_i^t B & A_i^{*t} B^* \\ B^t A_i & B^t B & 0 \\ B^{*t} A_i^* & 0 & B^{*t} B^* \end{bmatrix} \begin{bmatrix} \mathbf{r}_i \\ \mathbf{b} \\ \mathbf{b}^* \end{bmatrix} = \begin{bmatrix} A_i^t \mathbf{l}_i + A_i^{*t} \mathbf{l}_i^* \\ B^t \mathbf{l}_i \\ B^{*t} \mathbf{l}_i^* \end{bmatrix} \quad (\text{B.15})$$

After elimination of  $\mathbf{r}_i$  from Equation B.15, the eliminated NEQ takes the form:

$$\begin{bmatrix} M_i & 0 \\ 0 & M_i^* \end{bmatrix} \begin{bmatrix} \mathbf{b} \\ \mathbf{b}^* \end{bmatrix} = \begin{bmatrix} \mathbf{L}_i \\ \mathbf{L}_i^* \end{bmatrix} \quad (\text{B.16})$$

Then,  $M_i \mathbf{b} = \mathbf{L}_i$  from the above equation which is relevant for the common satellites for the two epochs, is augmented with Equation B.3 to make the new NEQ at epoch  $j$ :

$$\begin{bmatrix} A_j^t A_j & A_j^t B \\ B^t A_j & B^t B + M_i \end{bmatrix} \begin{bmatrix} \mathbf{r}_j \\ \mathbf{b} \end{bmatrix} = \begin{bmatrix} A_j^t \mathbf{l}_j \\ B^t \mathbf{l}_j + \mathbf{L}_i \end{bmatrix} \quad (\text{B.17})$$

It should be mentioned that the blocks of the NEQ in Equation B.17 which are constructed based on the lost satellites at epoch  $j$  should be stored in a file to be retrieved during backward substitution.

***Case 4: A set of phase connected is added and a set of current arcs is lost***

This case is decomposable to the two previous cases, and the matrix manipulation relevant to each case can be applied individually.

**B.2 Local formats in PANDA**

In Table B.1, input and (some typical) output files for a PPP in PANDA are listed. GNSS raw measurements and satellite precise clock/orbit information are in RINEX and SP3 formats, respectively, and systematic error correction tables are prepared in the IGS and/or IERS standard formats. However, PANDA local formats are used for the PPP configuration files and all processing outputs. More detail for the local formats, which is extracted from an unofficial PANDA manual (provided by Jing Guo in a personal communication), is provided in this section.

**Configuration files format**

PANDA reads four configuration files which are called: file\_table, gnss.cfg, gnss.sit, and session.obj. Information about directory address of the configuration files and error correction models are provided in file\_table as shown in Table B.2. gnss.cgf, gnss.sit and session.obj contain information about the session start/end time, parameter estimation temporal resolution, observation weighting, process noise value, etc. which are briefly explained in Table B.3 to Table B.5.

<b>Input files</b>	<b>Output files</b>
GNSS raw measurements	Cycle slip log information
Satellite precise clock/orbit information	Observation post-fit residuals
Systematic error correction	Station coordinates
PPP configuration files	Zenith tropospheric delay
	Statistical summary for the involved satellites

Table B.1: Input/output files for a PPP in PANDA

<b>Keyword</b>	<b>File</b>
Config	gnss.cfg
Object	session.obj
Stacoo	gnss.sit
Satnav	Satellite navigation file
Antnam	Receiver antenna information file
Antpcv	Phase center corrections for receiver and satellite antenna
Gptgrd	Grid file for some atmosphere quantities used by GPT2
Leapsc	Leap second
Ocload	Ocean tidal loading coefficients
Jpleph	Planets ephemerides
ut1t96	Tidal deformation effects on the Earth's rotation in IERS Conventions 1996
ut1t03	Tidal deformation effects on the Earth's rotation in IERS Conventions 2003
ut1t10	Tidal deformation effects on the Earth's rotation in IERS Conventions 2010
paninf	Area and optical property coefficients of satellites viewed as box-wing
panfln	Naming convention of PANDA internal files
polut1	Earth rotation parameters
estf96	Solid Earth tide corrections for geopotential in IERS Conventions 1996
estf10	Solid Earth tide corrections for geopotential in IERS Conventions 2003 & 2010
fest04	FES2004 ocean tide model
optide	Ocean pole tide
s1s2lt	Atmosphere loading tide in S1 and S2 frequency
slrsit	SLR SINEX file containing sites coordinates
EGM	Geopotential coefficients
DCB	Differenced code biases

Table B.2: Content of a 'file\_table' file for PPP in PANDA



<b>Key words</b>	<b>Option and description</b>
Start time& session length	YYYY MM DD HH MIN LEN Start epoch and length for data processing. This option is only valid for post data processing
Processing mode	SMOOTH or FILTER for data processing However, the option is useless
Port	BNC's real-time data output port Only valid for real-time
Interval	Data processing interval Only valid for post-time
Real-time PPP	GAP LG LW Thresholds for data pre-processing
ZTD model	ZTDPWC:XX, ZTD:XX, NONE ZTD estimation as piece-wise constant or random process
ZTD Gradient	GRD:XX or NONE Similar as ZTD model
Frequency used	Format: SYS_FRQ1_FRQ2_FRQ3 SYS: GPS, GLS, GAL, BDS, QZS FRQ: L1,L2,L5,G1,G2,E1,E5a,E5b,E6,B1,B2,B3 The frequency used for data processing
Time for initial clock bias	TIME in second Time length considered for determining the initial clock Only valid for 'ckdrt' module
Ambiguity fixing	YES or NO For PPP or PPP-IAR Only used by real-time PPP
Baseline length limit	LENGTH in meter The threshold of baseline for independent baseline selection used by 'ambfix' subroutine
Minimum common time	TIME in second Minimum common time for forming differenced observations
Cutoff elevation for AR	DEGREE The mask elevation angle for ambiguity
Critical search NL	The maximum and minimum for removed and saved ambiguity
Widelane interval	TIME in second used by 'ambfix' subtoutine for WL ambiguity fixed
Widelane decision	Standard error and probability for WL ambiguity fixed

Narrowlane decision	Standard error and probability for NL ambiguity fixed
Update rate for WL FCBs	TIME in seconds Used by real-time FCB, however the WL FCBs are estimated as epoch wise, so it is useless
BRDC data directory	Directory for navigation file
Rinex data directory	Directory for observations
Station LOG data directory	Directory for data healthy dialog files
IGS sp3 file directory	Directory for orbit and clock products
PANDA tables directory	Directory to save the corresponding file Only used for PANDA Python scripts
Hourly data directory	
IGS snx file directory	
Result data directory	
Products data directory	
Station Sigma scale	Scale factor of sites' coordinates accuracy
GNSS satellite orbit	YES or NO If orbit of GNSS satellites to be determined
Estimate EOP	NONE or CON_WOB_UT1_DWOB_DUT1 If the ERP parameters to be estimated
Wobble Constraint	The pre-constraint for the Earth polar motion and their rate parameters
UT1 Constraint	The pre-constraint for UT1/UTC or LOD parameters
+Force model GPS	The force model options for particular satellites
Integration step etc.	SECOND SECOND NUM The length of integration and output, as well as the order of integration approach.
Gravity model	NUM Maximum degree/order
Solid Earth tides	NONE SUN/MOON/SUN MOON
Ocean tides	NONE or the degree/order (maximum 80)
Point mass	EARTH SUN MOON MERC VENU MARS JUPI SATU URAN NEPT PLUT/NONE The n-body force
Solar radiation	NONE/BERN/BOXW [the parameters to be estimated] BERN: CODE SRP model BOXW: Adjustable Box-wing model
Atmosphere drag	NONE/PAN_DTM94

Relativity	NONE/YES
Earth radiation	NONE/YES
Customer model	NONE/YES [the parameters to be estimated]
Accelerator obs.	NONE/YES Accelerometer data to be used for modeling non-gravitational forces
Variation	NONE/YES If the variation equation is solved with equation of motion
Parameter to be estimated	PXSAT PYSAT PZSAT VXSAT VYSAT VZSAT Satellite position and velocity vectors.
-Force model GPS	End of GPS satellite orbit model.

Table B.3: Content of a 'gnss.cfg' file for a PPP in PANDA

<b>Keywords</b>	<b>Description</b>
XXXX_POS	Initial coordinates, velocities, and accelerations
XXXX_SIG	Standard error of initial coordinates, velocities, and accelerations in meter, and power density of coordinates in $m/\sqrt{s}$
XXXX_ENU	Height of antenna reference point, receiver type, antenna type, reference time of initial coordinates (if the site is used for FCBs estimation)

Table B.4: Content of a 'gnss.sit' file for a PPP in PANDA

<b>Keywords</b>	<b>Description</b>
+Satellite used GNSS	Header line for satellite parameters
PRN	Satellite PRN
TYP	Satellite type, e.g. GPS, GLO, etc.
PCV	PCV estimation or not
CLK	Clock estimation or not
SIG0/m	Standard error of initial satellite clock in meter
PD/m	Power density of satellite clock in $m/\sqrt{s}$
X,Y,Z,VX,VY,VZ	Standard error of satellite initial state vector in m (for position) and m/s (for velocity)
F1~FC	Standard error of other dynamic parameters
+Station used	Header line for station parameters
NAME	Site name
TP	K, F, S Site type K: kinematic, F: Fixed (known), S:Static
PCVs	PCV correction
RCLK	CLK, REF Clock estimation or not
SIG0/m	Standard error of initial receiver clock or ISB in meter
PD/m	Power density of receiver clock or ISB in $m/\sqrt{s}$
ELEV	DEGREE Mask elevation angle
MAP	Mapping function
ZTDS/m	Standard error of initial ZTD in meter
ZTDPD	Power density of ZTD in $m/\sqrt{h}$
GRDS/m	Standard error of initial ZTD horizontal gradient
GRDPD	Power density of GRD in $m/\sqrt{h}$
GRa/m	Standard error for GPS code measurements in meter
GPh/m	Standard error for GPS phase measurements in meter
RRa/m	Standard error for GLONASS code measurements in meter

RPh/m	Standard error for GLONASS phase measurements in meter
ERa/m	Standard error for GALILEO code measurements in meter
EPh/m	Standard error for GALILEO phase measurements in meter
CRa/m	Standard error for BDS code measurements in meter
CPh/m	Standard error for BDS phase measurements in meter
SRa/m	Standard error for SBAS code measurements in meter
SPh/m	Standard error for SBAS phase measurements in meter
JRa/m	Standard error for QZSS code measurements in meter
JPh/m	Standard error for QZSS phase measurements in meter
IRa/m	Standard error for IRNSS code measurements in meter
IPh/m	Standard error for IRNSS phase measurements in meter

Table B.5: Content of a 'gnss.sit' file for PPP in PANDA

### ***Output files format***

By running PPP in PANDA, several output files are generated, and some of them with their format are explained in this subsection. As a convention, 'YYYY' and 'DOY' are used for year and day of year, respectively, and 'stn' is used for the station name in this subsection.

logYYYYDOY\_stn

It is generated by 'qc' program and presents a list of phase connected arcs and removed outliers in PPP as shown in Figure B.1.

resYYYYDOY

This file contains post-fit residuals, estimated 3D coordinates, receiver clock and the estimated residual zenith tropospheric delay. One part of the file is shown in Figure B.2. To extract the station coordinates from this file, the extxyz program should be used in the following form, and a kinYYYYDOY (with the format shown in Figure B.3) will be generated.

extxyz file\_table

Furthermore, extztd program is usable to extract zenith total delay from resYYYYDOY file, and by running it in the form below, a new file which is named ztd\_YYYYDOY is produced (Figure B.4).

extztd file\_table

```

%Start time and interval : 57597 0.000 30.000
%Max ambc in one epoch : 11 30.000
%Old removed epochs : 4802 4802 0 0 0 0 0 0 0
%New removed epochs : 0 0 0 0 0 0 0 0 0
%Existed ambiguities : 50 50 0 0 0 0 0 0 0
%New ambiguities : 0 0 0 0 0 0 0 0 0
%Available epochs : 25229 25229 0 0 0 0 0 0 0
%End of header
AMB G02 1 272 1 RN_OLDAMB
AMB G05 1 445 1 RN_OLDAMB
AMB G06 1 63 1 RN_OLDAMB
DEL G07 1 1486 5 RN_DEL_MIXED
AMB G13 1 487 1 RN_OLDAMB
AMB G15 1 710 1 RN_OLDAMB
DEL G19 1 2019 5 RN_DEL_MIXED

```



 Phase connected arc for satellite G02 from epoch 1 to epoch 272  
 Deleted arc for satellite G07 from epoch 1 to epoch 1486

Figure B.1: Content of a 'logYYYYDOY\_stn' file in PANDA. This file is generated by running 'qc' program.

1 STAPX	1 0 0	2304703.80119	2304703.31867	57598.0000000000	57598.0000000000
2 STAPY	1 0 0	-4874817.72083	-4874817.21380	57598.0000000000	57598.0000000000
3 STAPZ	1 0 0	3395186.78436	3395187.07031	57598.0000000000	57598.0000000000
4 RECCLKG	1 0 0	0.81568	-0.07571	57598.0000000000	57598.0000000000
5 ZTD:60	1 0 2102	0.00000	0.01575	57597.9583333333	57597.9999999999
1 STAPX	1 0 16	2304703.80119	2304703.31867	57597.9996527778	57597.9996527778
2 STAPY	1 0 16	-4874817.72083	-4874817.21380	57597.9996527778	57597.9996527778
3 STAPZ	1 0 16	3395186.78436	3395187.07031	57597.9996527778	57597.9996527778
4 RECCLKG	1 0 16	0.81568	-0.07571	57597.9996527778	57597.9996527778
RES1	57597 86370.00000000 2880	1 30	0.145E-01 0.181E+01	0.62018162D+02 0.62018162D-02	0 13.565 82.268 13.460
RES1	57597 86370.00000000 2880	1 29	0.290E-02-0.628E+00	0.28184879D+03 0.28184879D-01	0 43.717 -60.002 9.996

...

Figure B.2: Content of a 'resYYYYDOY' file in PANDA. Boxes are labelled as 1) estimated parameter name 2) initial value for the parameter 3) adjusted value for the parameter 4) start time (in MJD) for the estimated parameter 5) end time (in MJD) for the estimated parameter. Ellipses are labelled as 1) time tag, i.e. MJD, second of the day, and epoch number, for the post-fit residual 2) station number and satellite number 3) phase residual and code residual 4) weight of phase and code data 5) satellite elevation and azimuth angles

2016 7 28 0 0 0.0	BRMU	2304703.30854	-4874817.15859	3395187.02309	-14.35243	10.89637	-3.53784	32.370399715457	295.303725362986	-11.656196049415
2016 7 28 0 0 30.0	BRMU	2304703.31178	-4874817.15607	3395187.01917	-13.95180	10.61311	-3.82316	32.370399689914	295.303725405555	-11.659049340524
2016 7 28 0 1 0.0	BRMU	2304703.31074	-4874817.16731	3395187.02336	-14.52624	10.44676	-2.77813	32.370399674912	295.303725344517	-11.648598977365
2016 7 28 0 1 30.0	BRMU	2304703.30717	-4874817.16361	3395187.02124	-14.69085	10.52849	-3.30303	32.370399682282	295.303725327027	-11.653847972862

Time tag    Station    Estimated X, Y, Z    Estimated Lat., Lon., H

Figure B.3: Format of a 'kinYYYYDOY' file in PANDA.

2.00	C	RINEX VERSION / TYPE	
3600.00		INTERVAL	
1	ZTD	# / TYPES OF DATA	
END OF HEADER			
BRMU	0.034810	0.575970000000E+05	0.575970416667E+05
BRMU	0.032110	0.575970416667E+05	0.575970833333E+05
BRMU	0.034150	0.575970833333E+05	0.575971250000E+05
BRMU	0.036760	0.575971250000E+05	0.575971666667E+05
BRMU	0.041930	0.575971666667E+05	0.575972083333E+05

Station ZTD    Start time (MJD)    End time (MJD)

Figure B.4: Format of a 'ztdYYYYDOY' file in PANDA.

## Appendix C: CODE, ESA and GFZ products comparison

In Chapter 4, to assess the accuracy of satellite clock/orbit products, the RMS of the GNSS-derived height time series using satellite products prepared by different analysis centres has been considered. Names and coordinates of the involved stations with the ratio of the computed height RMSs (using a pair of products) are listed in Table C.1.

Station	Latitude	Longitude	GPS		GLONASS	
			ESA/COD	ESA/GFZ	ESA/COD	ESA/GFZ
ADIS	9.0351	38.7663	1.00	1.00	1.00	0.85
AREV	-16.4655	288.5072	0.59	0.95	0.61	0.93
ASPA	-14.3261	189.2776	0.99	0.95	0.97	0.89
BARH	44.3950	291.7783	0.85	0.95	0.93	0.83
BJCO	6.3847	2.4500	0.94	0.98	0.97	0.91
BOGT	4.6401	285.9191	0.79	0.97	0.79	0.89
BRST	48.3805	355.5034	1.00	0.94	1.00	0.76
BUCU	44.4639	26.1257	0.99	0.95	0.93	0.84
CAS1	-66.2834	110.5197	1.00	0.96	0.84	0.87
CEBR	40.4534	355.6321	0.95	0.94	0.97	0.79
CEDU	-31.8667	133.8098	0.87	0.94	0.97	0.91
CHTI	-43.7355	183.3829	0.92	1.00	0.92	0.98
COCO	-12.1884	96.8340	1.01	1.01	0.88	0.87
CORD	-31.5284	295.5300	0.53	0.89	0.6	0.84
CUSV	13.7359	100.5339	0.71	0.96	0.89	0.9
DAEJ	36.3994	127.3745	0.99	0.95	0.91	0.9
DARW	-12.8437	131.1327	1.05	1.00	0.87	0.91
DGAV	-7.2697	72.3702	0.62	1.04	0.94	0.92
DRAO	49.3226	240.3750	0.92	1.01	1.02	0.94
FAIV	64.9781	212.5015	0.71	0.94	1.09	0.85
GLSV	50.3642	30.4967	0.96	1.02	0.97	0.93
GODZ	39.0217	283.1732	0.94	0.99	0.94	0.79
GOLD	35.4252	243.1108	0.90	1.01	1.02	0.99



GRAS	43.7547	6.9206	0.99	1.04	1.02	0.92
GRAZ	47.0671	15.4935	1.10	1.01	1.00	0.88
GUAT	14.5904	269.4798	0.97	0.99	0.85	0.92
GUUG	13.4332	144.8027	0.99	0.98	0.99	0.92
HARB	-25.8870	27.7072	1.22	1.07	0.92	0.88
HERT	50.8675	0.3344	1.01	0.99	0.9	0.76
HOB2	-42.8047	147.4387	1.01	0.96	0.94	0.84
HOFN	64.2673	344.8021	0.99	1.00	0.93	0.84
IRKJ	52.2190	104.3162	0.92	0.94	1.07	0.88
ISBA	33.3414	44.4384	1.00	0.96	0.98	0.81
JFNG	30.5156	114.4910	1.04	0.93	0.98	0.85
JOZ2	52.0978	21.0324	1.00	0.97	1.04	0.74
KARR	-20.9814	117.0972	0.99	0.97	1.02	0.92
KERG	-49.3515	70.2555	0.99	0.99	0.91	0.97
KIRI	1.3546	172.9229	0.94	0.91	0.98	0.95
KIRU	67.8574	20.9684	1.01	1.00	0.9	0.71
KOKV	22.1263	200.3351	0.79	0.99	0.94	0.82
KOUC	-20.5587	164.2873	0.98	0.95	0.95	0.86
KOUR	5.2522	307.1940	0.90	0.97	0.84	0.94
LHAZ	29.6572	91.1040	0.97	0.99	0.99	0.87
LPGS	-34.9067	302.0677	0.56	0.88	0.62	0.75
MAL2	-2.9961	40.1941	0.75	0.99	0.92	0.96
MAS1	27.7637	344.3667	0.90	0.99	0.94	0.84
MATE	40.6491	16.7045	0.99	0.98	1.06	0.93
MDVJ	56.0215	37.2145	0.82	0.95	1.06	0.9
MGUE	-35.7774	290.6021	0.64	0.90	0.58	0.88
MKEA	19.8014	204.5437	0.65	0.94	0.83	1.02
NANO	49.2948	235.9135	1.01	0.94	1.01	0.90
NAUR	-0.5517	166.9256	0.86	0.90	0.96	0.86
NICO	35.1410	33.3964	1.00	0.99	1.00	0.82
NKLG	0.3539	9.6721	0.98	0.98	0.93	0.90
NNOR	-31.0487	116.1927	0.81	0.97	1.03	0.96
NYA1	78.9296	11.8653	1.04	1.00	1.01	0.88

OHI2	-63.3211	302.0987	0.64	1.09	0.62	0.95
OUS2	-45.8695	170.5109	0.76	0.94	0.91	0.87
PARK	-32.9988	148.2646	0.89	0.93	0.97	0.89
PDEL	37.7477	334.3372	0.97	0.99	0.92	0.83
PERT	-31.8020	115.8852	1.00	1.01	1.03	0.96
PIE1	34.3015	251.8811	0.83	0.99	1.00	0.95
PIMO	14.6357	121.0777	0.72	0.93	0.99	0.98
PNGM	-2.0432	147.3660	0.96	0.96	1.00	0.96
POTS	52.3793	13.0661	1.02	1.01	1.04	0.82
POVE	-8.7093	296.1037	0.89	0.94	0.78	0.89
QAQ1	60.7153	313.9522	0.83	1.00	1.01	0.89
RDSD	18.4614	290.0887	0.94	0.97	0.9	0.91
RECF	-8.0510	325.0485	0.87	0.98	0.78	0.94
REDU	50.0015	5.1449	0.92	0.95	1.02	0.8
REUN	-21.2082	55.5717	1.01	1.00	0.96	0.89
RIO2	-53.7855	292.2489	0.50	0.98	0.49	0.83
SALU	-2.5935	315.7875	0.83	0.98	0.72	0.83
SAVO	-12.9392	321.5677	0.94	0.97	0.76	0.80
SEYG	-4.6787	55.5306	1.03	0.96	0.89	0.89
SOFI	42.5561	23.3947	1.02	0.98	0.95	0.92
STHL	-15.9425	354.3327	0.78	0.98	0.70	0.79
STK2	43.5286	141.8448	0.93	0.91	0.92	0.77
SUTV	-32.3802	20.8105	0.95	1.04	0.8	0.92
SYOG	-69.0070	39.5837	0.82	0.95	0.68	0.97
THTI	-17.5771	210.3936	0.97	0.98	0.87	0.82
THU2	76.5370	291.1750	0.94	0.95	0.94	0.77
TIXI	71.6345	128.8664	1.04	0.96	1.04	0.97
TLSE	43.5607	1.4809	0.98	0.95	1.02	0.79
TOW2	-19.2693	147.0557	0.75	0.92	1.03	0.90
TRO1	69.6627	18.9396	0.98	1.00	0.93	0.83
TSK2	36.1056	140.0871	0.99	0.97	0.92	0.89
TUVA	-8.5253	179.1966	0.99	0.94	0.98	0.89
TWTF	24.9536	121.1645	1.04	0.97	0.96	0.81

UFPR	-25.4484	310.7690	0.82	0.97	0.62	0.79
ULAB	47.8651	107.0523	0.65	0.90	0.82	0.82
UNSA	-24.7275	294.5924	0.65	0.96	0.94	0.88
URUM	43.8079	87.6007	0.87	0.92	0.96	1.03
UZHL	48.6320	22.2976	1.02	1.01	0.93	0.80
VILL	40.4436	356.0480	0.96	0.97	0.94	0.79
WIND	-22.5749	17.0894	0.79	1.02	0.8	0.86
WTZR	49.1442	12.8789	1.05	0.97	0.94	0.83
XMIS	-10.4500	105.6885	0.98	0.96	0.97	1.00
YEL2	62.4813	245.5192	0.88	1.01	1.02	0.87
ZECK	43.7884	41.5651	0.87	0.95	1.00	0.83
ZIM2	46.8771	7.4650	1.04	0.94	0.97	0.86

Table C.1: IGS GNSS stations used for CODE, ESA and GFZ products comparison with the RMS ratio

## Appendix D: GNSS stations, data availability and modelled OTL displacement used in Chapter 5

In Table D.1, stations which are used in Chapter 5 with their coordinates and data provider are listed, and Figure D.1 represents data availability at each station. In Table D.2 to Table D.6, values of the modelled OTL displacement for different tidal constituents are provided. The disagreement maps (due to using different ocean tide models) for the predicted OTL displacement at different tidal frequencies are provided in Figure D.2 and Figure D.3.

Station	Latitude	Longitude	Data Provider
ALGO	45.9558	281.9286	Canadian Geodetic Survey, Natural Resources Canada
AZRY	33.5401	243.3703	US Geological Survey
BADG	51.7697	102.2350	Institute of Applied Astronomy, Russian Academy of Sciences
CAS1	-66.2834	110.5197	Geoscience Australia
CCJ2	27.0675	142.1950	Geospatial Information Authority of Japan
CEFE	-20.3108	319.6805	Brazilian Institute of Geography and Statistics
CHUR	58.7591	265.9113	Canadian Geodetic Survey, Natural Resources Canada
DAV1	-68.5773	77.9726	Geoscience Australia
DRAG	31.5932	35.3921	Survey of Israel
DRAO	49.3226	240.3750	Geological Survey of Canada, Natural Resources Canada
FAIV	64.9781	212.5015	Jet Propulsion Laboratory, NASA, USA
GODZ	39.0217	283.1732	Jet Propulsion Laboratory, NASA, USA
GOLD	35.4252	243.1107	Jet Propulsion Laboratory, NASA, USA
HEL2	54.1863	7.8765	Federal Agency for Cartography and Geodesy, Germany
HOB2	-42.8047	147.4387	Geoscience Australia
JPLM	34.2048	241.8268	Jet Propulsion Laboratory, NASA, USA
KHAR	50.0051	36.2390	Main Astronomical Observatory, Ukraine
KIR0	67.8776	21.0602	Swedish Mapping, Cadastral and Land registration Authority
KOKV	22.1263	200.3351	Jet Propulsion Laboratory, NASA, USA
MAC1	-54.4995	158.9358	Geoscience Australia
MADR	40.4292	355.7503	Jet Propulsion Laboratory, NASA, USA
MAS1	27.7637	344.3667	European Space Operation Center, European Space Agency
MATE	40.6491	16.7045	Italian Space Agency
MAW1	-67.6048	62.8707	Geoscience Australia

MGBH	-19.9419	316.0751	Brazilian Institute of Geography and Statistics
NYA1	78.9296	11.8653	Norwegian Mapping Authority
OHI2	-63.3211	302.0987	Federal Agency for Cartography and Geodesy, Germany
ONRJ	-22.8957	316.7757	Brazilian Institute of Geography and Statistics
ONSA	57.3953	11.9255	Swedish Mapping, Cadastral and Land Registration Authority
PIE1	34.3015	251.8811	Jet Propulsion Laboratory, NASA, USA
SCLA	-27.7928	309.6957	Brazilian Institute of Geography and Statistics
STK2	43.5286	141.8448	Geospatial Information Authority of Japan
STR2	-35.3162	149.0102	Geoscience Australia
SUTV	-32.3802	20.8105	Jet Propulsion Laboratory, NASA, USA
SVTL	60.5329	29.7809	Institute of Applied Astronomy, Russian Academy of Sciences
SYOG	-69.0070	39.5837	Geospatial Information Authority of Japan
TID1	-35.3992	148.9800	Geoscience Australia
TIXI	71.6345	128.8664	Regional GPS Data Acquisition and Analysis Center on
TOW2	-19.2693	147.0557	Geoscience Australia
TRO1	69.6627	18.9396	Norwegian Mapping Authority
TSK2	36.1056	140.0871	Geospatial Information Authority of Japan
UFPR	-25.4484	310.7690	Brazilian Institute of Geography and Statistics
VARS	70.3364	31.0312	Norwegian Mapping Authority
WARK	-36.4344	174.6628	GeoNet, New Zealand
WHIT	60.7505	224.7779	Canadian Geodetic Survey, Natural Resources Canada
YAR3	-29.0465	115.3472	Geoscience Australia
YCBA	-22.0171	296.3200	German Geodetic Research Institute
YELL	62.4809	245.5193	Canadian Geodetic Survey, Natural Resources Canada
ZECK	43.7884	41.5651	Institute of Applied Astronomy, Russian Academy of Sciences

Table D.1: GNSS stations used in Chapter 5

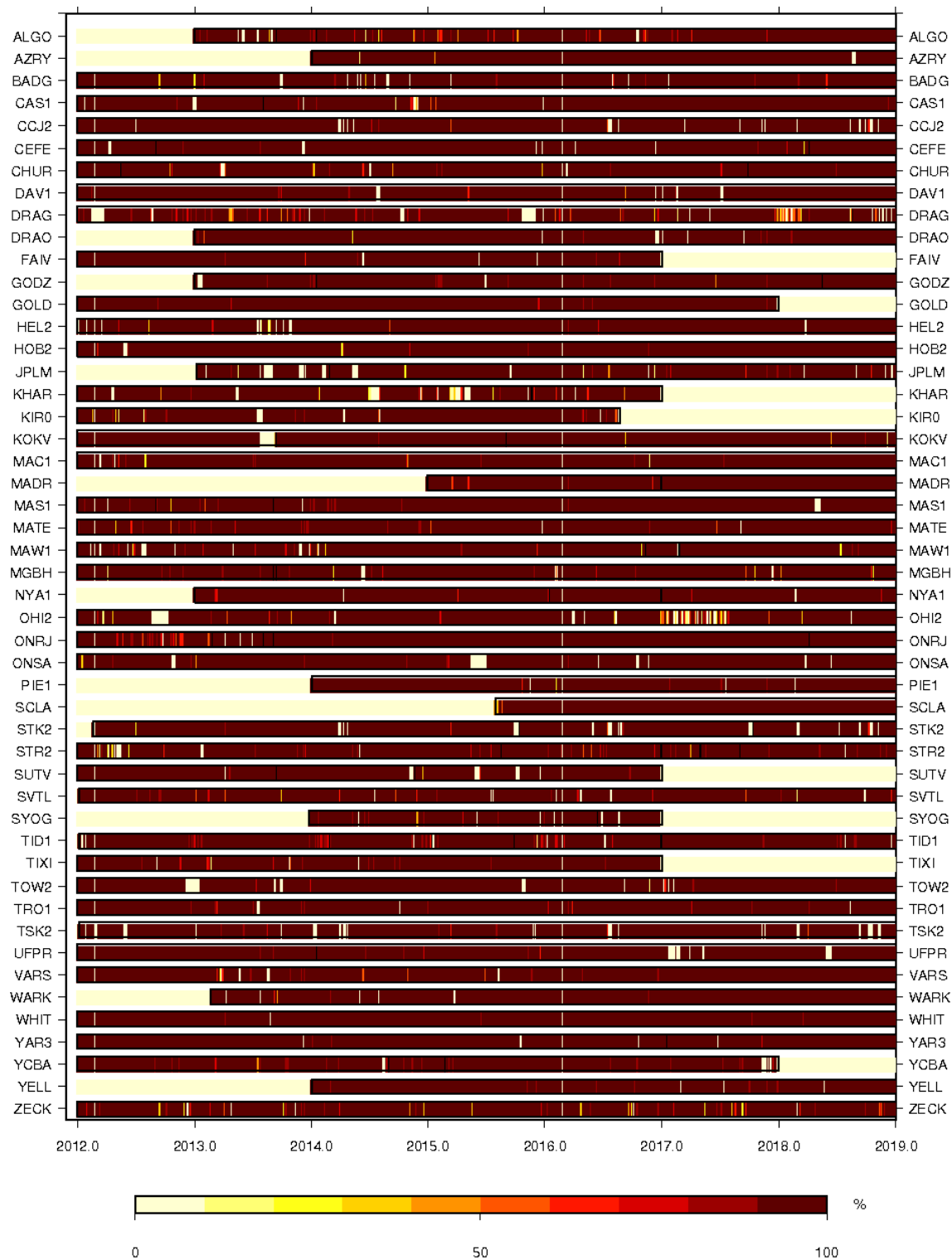


Figure D.1: Processed GNSS data time span with percentage data availability per day at each station.

Station	FES2014		GOT4.10		TPX08		NAO99		HMTIDE		DTU10		EOT11	
	amp	phs	amp	phs	amp	phs	amp	phs	amp	phs	amp	phs	amp	phs
ALGO	5	140	5	139	5	139	5	141	5	139	5	139	5	139
AZRY	3	-39	3	-40	3	-39	3	-40	3	-40	3	-40	3	-40
BADG	1	78	1	79	1	78	1	84	1	82	1	82	1	82
CAS1	8	-31	8	-32	8	-31	8	-31	8	-33	8	-33	8	-33
CCJ2	13	81	13	81	13	80	13	83	13	81	13	80	13	79
CEFE	20	15	20	14	20	14	20	14	20	14	20	14	20	15
CHUR	10	-178	10	-178	10	-178	10	-174	10	-178	10	-177	10	-178
DAV1	6	7	7	5	7	5	6	7	6	6	6	5	6	6
DRAG	3	-73	3	-75	3	-74	3	-74	3	-73	3	-73	3	-74
DRAO	9	84	9	84	9	85	9	84	9	84	9	85	9	85
FAIV	9	99	9	99	9	99	9	100	9	100	9	100	9	100
GODZ	8	154	8	153	8	153	8	155	8	153	8	153	8	153
GOLD	1	9	1	6	1	10	2	11	1	8	1	9	1	8
HEL2	4	146	4	149	4	154	5	138	4	157	4	149	4	155
HOB2	10	153	10	153	10	152	10	154	10	154	10	153	10	153
JPLM	4	-29	4	-29	4	-29	4	-30	4	-29	4	-29	4	-29
KHAR	3	-66	3	-66	3	-67	3	-66	3	-67	3	-68	3	-68
KIRO	3	-175	3	-174	3	-170	3	-177	3	-177	3	-176	3	-174
KOKV	13	-121	13	-121	13	-121	13	-121	12	-121	12	-121	12	-121
MAC1	13	-155	13	-155	13	-155	14	-154	13	-155	13	-155	13	-155
MADR	15	-89	15	-89	14	-90	14	-90	15	-89	15	-89	15	-89
MAS1	22	-142	22	-141	22	-142	22	-141	22	-141	22	-141	22	-141
MATE	5	-79	5	-79	5	-79	5	-79	5	-79	5	-79	5	-80
MAW1	4	-24	4	-22	4	-23	4	-23	4	-26	4	-27	4	-28
MGBH	13	26	12	26	12	26	13	25	13	26	13	26	13	26
NYA1	8	179	8	179	9	-180	7	178	8	178	8	178	8	178
OHI2	22	87	23	87	23	87	22	90	21	87	22	87	22	87
ONRJ	14	17	15	17	14	16	14	16	14	17	15	17	14	18
ONSA	4	-65	4	-64	4	-67	4	-65	4	-62	4	-63	4	-63
PIE1	1	140	1	141	1	137	1	139	1	138	1	140	1	139
SCLA	8	38	8	39	8	38	8	38	8	39	8	38	8	39
STK2	5	21	5	21	5	22	5	25	5	23	5	22	5	22

STR2	9	124	9	124	9	124	9	125	9	125	9	125	9	125
SUTV	21	-134	21	-134	21	-134	21	-134	21	-134	21	-134	21	-134
SVTL	2	-64	2	-63	2	-67	2	-67	2	-65	2	-67	2	-68
SYOG	8	-90	7	-89	7	-89	7	-90	8	-88	8	-89	8	-89
TID1	9	124	9	125	9	124	9	125	9	125	9	125	9	125
TIXI	2	57	2	49	1	59	2	71	2	58	1	58	2	59
TOW2	11	153	11	152	11	153	10	162	11	150	11	152	11	153
TRO1	9	177	9	175	10	-180	10	174	8	174	10	174	8	176
TSK2	8	50	8	50	7	51	7	51	8	51	8	51	8	50
UFPR	9	31	9	31	9	31	9	30	9	31	9	31	9	31
VAR5	11	-74	11	-74	11	-84	10	-79	11	-76	11	-75	11	-75
WARK	26	56	26	58	26	57	26	59	25	59	25	59	25	59
WHIT	14	97	13	96	14	96	14	97	13	97	13	98	13	98
YAR3	3	149	3	148	3	148	3	151	3	149	3	149	3	147
YCBA	5	64	5	64	5	64	5	63	5	64	5	64	5	64
YELL	7	98	6	96	7	97	7	98	6	98	6	98	6	99
ZECK	3	-64	3	-65	3	-65	3	-66	3	-65	3	-66	3	-65

Table D.2: Predicted M2 OTL displacement (amplitude in mm and phase in degree) based on different ocean tide models and an elastic PREM Green's function



Station	FES2014		GOT4.10		TPX08		NAO99		HMTIDE		DTU10		EOT11	
	amp	phs	amp	phs	amp	phs	amp	phs	amp	phs	amp	phs	amp	phs
ALGO	1	125	1	125	1	126	1	130	1	123	1	126	1	125
AZRY	1	-66	1	-67	1	-67	1	-72	1	-67	1	-67	1	-68
BADG	0	102	0	99	0	97	0	96	0	108	0	104	0	109
CAS1	2	-52	2	-52	2	-52	2	-53	2	-52	2	-54	2	-53
CCJ2	2	86	3	85	3	86	3	84	2	84	3	84	3	84
CEFE	4	20	4	18	4	19	4	16	4	18	4	18	4	18
CHUR	2	148	2	147	2	151	2	152	2	146	2	147	2	147
DAV1	2	-24	2	-24	2	-24	2	-22	2	-23	2	-24	2	-23
DRAG	1	-87	1	-89	1	-87	1	-89	1	-88	1	-89	1	-89
DRAO	2	56	2	56	2	58	2	61	2	57	2	58	2	57
FAIV	2	82	2	81	2	82	2	84	2	82	2	84	2	83
GODZ	2	139	2	139	2	140	2	143	2	137	2	139	2	138
GOLD	1	-54	1	-55	1	-54	1	-57	1	-55	1	-55	1	-55
HEL2	0	131	0	166	0	147	0	-142	0	-169	0	169	0	175
HOB2	2	131	2	131	2	129	2	131	2	129	2	131	2	130
JPLM	2	-60	2	-60	2	-60	1	-63	2	-60	1	-60	2	-61
KHAR	1	-81	1	-83	1	-81	1	-79	1	-84	1	-85	1	-84
KIRO	1	164	1	169	1	160	0	166	1	166	1	166	1	169
KOKV	2	-128	2	-128	2	-128	2	-129	2	-128	2	-129	2	-128
MAC1	3	-174	3	-174	3	-175	3	-176	3	-176	3	-174	3	-175
MADR	3	-107	3	-107	3	-107	3	-107	3	-107	3	-107	3	-107
MAS1	5	-154	5	-153	5	-153	5	-154	5	-153	5	-154	5	-153
MATE	1	-91	1	-89	1	-90	1	-91	1	-92	1	-91	1	-93
MAW1	1	-40	2	-39	1	-39	1	-38	1	-38	1	-40	1	-39
MGBH	3	29	3	28	3	29	3	26	3	28	3	27	3	28
NYA1	2	156	2	170	2	156	1	152	2	169	2	162	2	167
OHI2	3	59	3	60	3	61	3	66	3	63	3	63	3	63
ONRJ	3	31	3	31	3	31	3	27	3	30	3	29	3	30
ONSA	1	-89	1	-94	1	-87	1	-91	1	-90	1	-93	1	-89
PIE1	0	-103	0	-106	0	-101	0	-133	0	-99	0	-108	0	-106
SCLA	2	53	2	53	2	54	2	49	2	52	2	52	2	52
STK2	0	27	0	25	0	33	1	36	0	26	0	25	0	30

STR2	2	110	2	110	2	109	2	111	2	108	2	110	2	110
SUTV	4	-145	4	-145	4	-145	4	-146	4	-145	4	-145	4	-145
SVTL	0	-85	0	-85	0	-85	0	-73	0	-89	0	-90	0	-89
SYOG	2	-94	2	-94	2	-92	2	-96	2	-96	2	-97	2	-97
TID1	2	110	2	110	2	110	2	112	2	108	2	110	2	110
TIXI	0	73	0	43	0	67	1	52	0	61	0	55	0	64
TOW2	4	136	4	137	4	137	4	143	3	134	4	136	3	138
TRO1	2	154	2	155	2	152	2	151	2	156	2	154	2	155
TSK2	1	63	1	62	1	66	1	63	1	62	1	60	1	61
UFPR	2	46	2	45	2	47	2	41	2	44	2	44	2	45
VAR3	3	-109	3	-105	3	-117	2	-86	3	-109	3	-105	3	-105
WARK	5	30	5	33	5	31	5	36	4	32	4	33	4	33
WHIT	3	75	3	75	3	75	3	77	2	76	3	78	3	78
YAR3	1	106	1	105	1	107	1	113	1	105	1	109	1	107
YCBA	1	69	1	68	1	69	1	66	1	68	1	67	1	68
YELL	1	77	1	75	1	77	1	80	1	77	1	79	1	79
ZECK	1	-77	1	-81	1	-77	1	-77	1	-79	1	-81	1	-80

Table D.3: Predicted N2 OTL displacement (amplitude in mm and phase in degree) based on different ocean tide models and an elastic PREM Green's function

Station	FES2014		GOT4.10		TPX08		NAO99		HMTIDE		DTU10		EOT11	
	amp	phs	amp	phs	amp	phs	amp	phs	amp	phs	amp	phs	amp	phs
ALGO	1	173	0	173	0	173	0	167	0	174	0	174	0	172
AZRY	1	-92	1	-90	1	-92	1	-94	1	-92	1	-94	1	-97
BADG	0	67	0	67	0	72	0	74	0	81	0	79	0	79
CAS1	1	13	1	27	1	15	1	20	1	22	1	22	1	21
CCJ2	2	88	2	90	2	87	2	91	2	93	2	93	2	87
CEFE	2	21	2	21	2	20	2	19	2	27	2	25	2	17
CHUR	1	-113	0	-112	1	-119	1	-113	1	-133	1	-119	1	-120
DAV1	1	120	1	131	1	116	1	115	1	122	1	121	1	121
DRAG	0	-36	0	-38	0	-38	0	-44	0	-32	0	-33	0	-31
DRAO	1	131	1	130	1	132	1	134	1	140	1	139	1	137
FAIV	1	129	1	129	1	129	1	132	1	137	1	137	1	132
GODZ	1	179	1	180	1	-180	1	171	1	179	1	179	1	180
GOLD	1	-109	0	-107	0	-110	0	-114	1	-111	0	-114	1	-115
HEL2	0	-130	0	-95	0	-108	1	-119	0	-93	0	-123	1	-104
HOB2	0	-126	0	-117	0	-130	0	-111	1	-100	0	-96	0	-104
JPLM	1	-85	1	-83	1	-85	1	-88	1	-86	1	-87	1	-91
KHAR	0	-33	0	-34	0	-32	0	-36	0	-30	0	-31	0	-33
KIRO	0	-131	0	-118	0	-140	0	-154	0	-124	0	-124	0	-141
KOKV	1	-129	1	-129	1	-129	1	-126	1	-121	1	-124	2	-126
MAC1	1	-130	1	-127	1	-129	1	-131	1	-115	1	-117	1	-122
MADR	1	-65	1	-65	1	-65	1	-72	1	-61	1	-62	1	-65
MAS1	2	-126	2	-126	2	-126	3	-127	2	-119	2	-120	2	-124
MATE	1	-63	1	-63	1	-60	1	-77	1	-58	1	-58	0	-54
MAW1	0	-165	1	-169	0	-172	0	176	1	-180	1	-179	0	-177
MGBH	1	32	1	32	1	32	1	31	1	37	1	36	1	28
NYA1	1	-133	1	-122	1	-138	1	-154	1	-132	1	-131	1	-138
OHI2	3	124	3	124	3	124	3	131	3	129	3	126	3	126
ONRJ	2	18	2	17	2	17	2	17	2	23	2	22	2	13
ONSA	0	-41	0	-31	0	-42	0	-66	0	-32	0	-32	0	-44
PIE1	0	-130	0	-131	0	-131	0	-135	0	-130	0	-133	0	-133
SCLA	1	26	1	26	1	28	1	29	1	34	1	31	1	21
STK2	1	51	1	50	1	49	1	54	1	60	1	58	1	53

STR2	0	141	0	149	0	146	0	170	0	180	0	173	0	135
SUTV	3	-113	3	-112	3	-113	3	-114	3	-109	2	-109	3	-112
SVTL	0	-29	0	-26	0	-29	0	-33	0	-26	0	-26	0	-21
SYOG	1	-80	1	-84	1	-82	1	-85	1	-82	1	-82	1	-81
TID1	0	142	0	150	0	147	0	170	0	180	0	172	0	135
TIXI	0	83	0	75	0	88	0	115	0	90	0	78	0	83
TOW2	1	115	1	122	1	117	2	124	1	117	2	118	1	114
TRO1	1	-142	1	-137	1	-149	1	-158	1	-140	1	-141	1	-151
TSK2	1	67	1	67	1	67	1	70	1	73	1	73	1	68
UFPR	1	23	1	23	1	25	1	24	1	29	1	28	1	19
VAR5	1	-30	1	-30	1	-49	1	-33	1	-26	1	-21	1	-28
WARK	2	116	2	122	2	119	2	135	1	140	1	133	1	121
WHIT	1	128	1	128	1	128	1	130	1	137	1	137	1	132
YAR3	0	-113	0	-105	0	-110	0	-95	0	-104	0	-94	0	-128
YCBA	0	68	0	67	0	67	1	61	1	70	0	68	0	65
YELL	1	136	1	133	1	135	1	135	1	143	1	142	1	139
ZECK	0	-32	0	-35	0	-32	0	-36	0	-28	0	-30	0	-32

Table D.4: Predicted K2 OTL displacement (amplitude in mm and phase in degree) based on different ocean tide models and an elastic PREM Greens' function

Station	FES2014		GOT4.10		TPX08		NAO99		HMTIDE		DTU10		EOT11	
	amp	phs	amp	phs	amp	phs	amp	phs	amp	phs	amp	phs	amp	phs
ALGO	3	-4	3	-6	3	-5	3	-5	3	-4	3	-4	3	-4
AZRY	12	39	12	39	12	39	12	39	11	39	11	39	12	39
BADG	2	-118	2	-119	2	-118	2	-121	2	-120	2	-120	2	-120
CAS1	12	59	12	59	12	58	12	58	12	59	12	60	12	60
CCJ2	14	-128	14	-128	14	-127	15	-128	14	-128	14	-128	14	-128
CEFE	1	46	1	46	1	51	1	47	1	46	1	48	1	48
CHUR	3	52	2	53	2	43	2	52	2	53	2	57	3	54
DAV1	10	84	10	84	9	82	10	82	10	83	10	84	10	84
DRAG	1	171	1	171	1	172	1	177	1	168	1	171	1	173
DRAO	8	59	8	59	8	60	8	59	8	58	8	59	8	59
FAIV	5	98	5	97	5	97	6	98	5	98	5	97	5	98
GODZ	3	-5	3	-7	3	-7	3	-4	3	-5	3	-5	3	-6
GOLD	10	43	10	42	10	42	10	42	10	42	10	42	10	42
HEL2	2	-72	2	-73	2	-74	2	-80	2	-75	2	-67	2	-72
HOB2	7	87	7	87	7	88	7	88	7	89	7	88	7	87
JPLM	13	41	13	40	13	40	13	40	13	40	13	40	13	40
KHAR	1	-80	1	-81	1	-85	1	-89	1	-85	1	-83	1	-82
KIRO	2	-49	2	-45	2	-50	2	-49	2	-44	2	-42	2	-38
KOKV	12	61	13	61	12	60	12	60	12	59	12	60	12	60
MAC1	8	49	8	50	7	50	7	52	7	51	8	51	7	50
MADR	2	-68	3	-69	3	-69	3	-70	2	-70	2	-69	3	-69
MAS1	3	-117	3	-115	3	-115	3	-113	3	-116	3	-116	3	-115
MATE	1	-79	1	-80	1	-82	2	-83	1	-81	1	-81	1	-81
MAW1	8	94	8	94	8	93	8	91	8	93	8	93	8	94
MGBH	0	-154	0	-172	0	170	0	-170	0	-161	0	-165	0	-166
NYA1	1	-44	1	31	1	-39	1	-52	1	-46	1	-17	1	-4
OHI2	14	-118	15	-119	15	-119	13	-119	13	-120	14	-119	14	-119
ONRJ	1	-16	1	-7	1	-3	1	-10	1	-9	1	-7	1	-8
ONSA	2	-55	2	-55	2	-57	2	-53	2	-57	2	-51	2	-54
PIE1	6	36	6	36	6	36	6	36	6	36	6	36	6	36
SCLA	1	-105	1	-104	1	-107	1	-109	1	-105	1	-106	1	-106
STK2	9	-146	9	-145	9	-144	9	-145	8	-145	9	-145	9	-145

STR2	3	120	3	120	3	120	3	120	3	123	3	119	3	120
SUTV	0	120	0	109	1	103	1	103	0	78	1	97	0	94
SVTL	2	-66	2	-66	2	-68	1	-67	1	-66	2	-63	2	-60
SYOG	7	124	7	124	7	125	7	121	7	123	7	125	7	123
TID1	3	120	3	119	3	119	3	119	3	122	3	119	3	119
TIXI	2	-153	2	-157	2	-151	2	-164	2	-154	2	-151	2	-157
TOW2	9	-140	9	-139	9	-141	10	-141	9	-140	9	-141	9	-139
TRO1	2	-34	2	-27	2	-34	2	-33	2	-29	2	-24	2	-22
TSK2	11	-138	11	-137	10	-137	11	-137	10	-137	11	-137	11	-137
UFPR	1	-105	1	-103	1	-107	1	-109	1	-104	1	-106	1	-106
VAR3	1	3	1	27	1	0	1	7	2	11	1	20	2	22
WARK	4	-174	4	-174	4	-177	4	-176	4	-175	4	-177	4	-175
WHIT	8	82	8	82	8	81	8	82	8	81	8	82	8	82
YAR3	9	12	9	12	9	13	9	11	9	12	9	12	9	12
YCBA	3	-136	3	-136	3	-137	3	-136	3	-137	3	-136	3	-136
YELL	4	63	4	62	4	62	4	64	3	62	3	62	4	63
ZECK	1	-123	1	-126	1	-128	1	-134	1	-133	1	-128	1	-127

Table D.5: Predicted K1 OTL displacement (amplitude in mm and phase in degree) based on different ocean tide models and an elastic PREM Green's function

Station	FES2014		GOT4.10		TPX08		NAO99		HMTIDE		DTU10		EOT11	
	amp	phs	amp	phs	amp	phs	amp	phs	amp	phs	amp	phs	amp	phs
ALGO	2	-2	2	-3	2	-2	2	-3	2	-2	2	-1	2	-1
AZRY	7	24	7	24	7	24	7	24	7	24	7	24	7	25
BADG	2	-128	2	-129	2	-130	2	-131	2	-132	2	-131	2	-130
CAS1	11	51	11	50	11	51	11	51	11	52	11	51	11	51
CCJ2	11	-148	11	-147	10	-147	11	-147	11	-147	11	-147	11	-147
CEFE	3	-54	3	-54	3	-53	3	-54	3	-55	3	-54	3	-54
CHUR	2	30	2	29	2	30	2	30	2	34	2	35	2	34
DAV1	10	82	10	80	9	81	10	82	10	82	10	82	10	82
DRAG	1	-156	1	-156	1	-160	1	-155	1	-162	1	-160	1	-156
DRAO	5	45	5	45	5	46	5	45	5	46	5	46	5	46
FAIV	4	89	4	89	4	88	4	88	4	90	4	90	4	89
GODZ	2	2	2	1	2	1	2	5	2	2	2	2	2	2
GOLD	7	28	7	28	7	28	7	27	7	28	7	28	7	28
HEL2	1	-53	1	-46	1	-52	1	-45	1	-58	1	-55	1	-56
HOB2	6	57	6	56	6	57	7	57	6	56	7	57	7	57
JPLM	8	26	8	26	8	25	8	25	8	25	8	25	8	26
KHAR	1	-105	1	-106	1	-109	1	-110	1	-110	1	-107	1	-108
KIRO	2	-110	2	-110	2	-111	2	-112	2	-111	2	-109	2	-109
KOKV	7	54	7	55	7	54	7	54	7	54	7	54	7	55
MAC1	7	27	7	26	7	28	8	28	7	28	7	28	7	28
MADR	0	-115	0	-118	0	-117	0	-114	0	-120	0	-112	0	-118
MAS1	2	84	2	83	2	84	2	83	2	85	2	83	2	85
MATE	1	-98	1	-100	1	-101	1	-98	1	-100	1	-100	1	-99
MAW1	9	95	9	94	9	95	9	95	9	95	9	95	9	95
MGBH	2	-75	2	-74	1	-73	1	-74	2	-75	2	-74	2	-74
NYA1	2	-123	2	-120	2	-121	2	-126	2	-126	2	-117	2	-116
OHI2	16	-136	17	-136	16	-138	15	-137	15	-137	16	-137	16	-138
ONRJ	3	-72	3	-72	3	-71	3	-72	3	-72	3	-72	3	-72
ONSA	1	-106	1	-108	1	-106	1	-106	1	-111	1	-107	1	-107
PIE1	4	22	4	22	4	22	4	22	4	23	4	23	4	23
SCLA	3	-107	3	-106	3	-107	3	-107	3	-106	3	-106	3	-106
STK2	7	-164	7	-164	7	-163	7	-163	7	-163	7	-164	7	-163

STR2	3	67	3	67	3	68	3	66	3	67	3	67	3	67
SUTV	2	112	2	112	2	110	2	110	2	114	2	113	2	110
SVTL	1	-105	1	-105	1	-106	1	-108	1	-107	1	-104	1	-104
SYOG	8	125	8	124	8	125	9	125	9	124	9	124	9	124
TID1	3	66	3	66	3	67	3	66	3	66	3	67	3	67
TIXI	2	-168	2	-171	2	-169	2	-173	2	-173	2	-169	2	-173
TOW2	4	-166	4	-165	4	-167	4	-166	4	-165	4	-166	4	-165
TRO1	2	-115	2	-115	2	-113	2	-115	2	-115	2	-112	2	-113
TSK2	8	-156	8	-156	8	-155	8	-155	8	-155	8	-156	8	-155
UFPR	3	-100	3	-99	3	-100	3	-101	3	-100	3	-100	3	-99
VAR5	2	-111	2	-112	2	-111	2	-111	2	-109	2	-106	2	-108
WARK	1	118	1	112	1	117	1	115	1	125	1	119	1	118
WHIT	5	71	5	70	5	70	5	70	5	71	5	71	5	71
YAR3	7	8	7	8	7	9	7	8	7	8	7	8	7	8
YCBA	2	-149	2	-149	2	-149	2	-148	2	-147	2	-148	2	-148
YELL	2	53	2	52	2	53	2	52	2	54	2	55	2	55
ZECK	1	-117	1	-119	1	-122	1	-122	1	-123	1	-120	1	-120

Table D.6: Predicted O1 OTL displacement (amplitude in mm and phase in degree) based on different ocean tide models and an elastic PREM Green's function



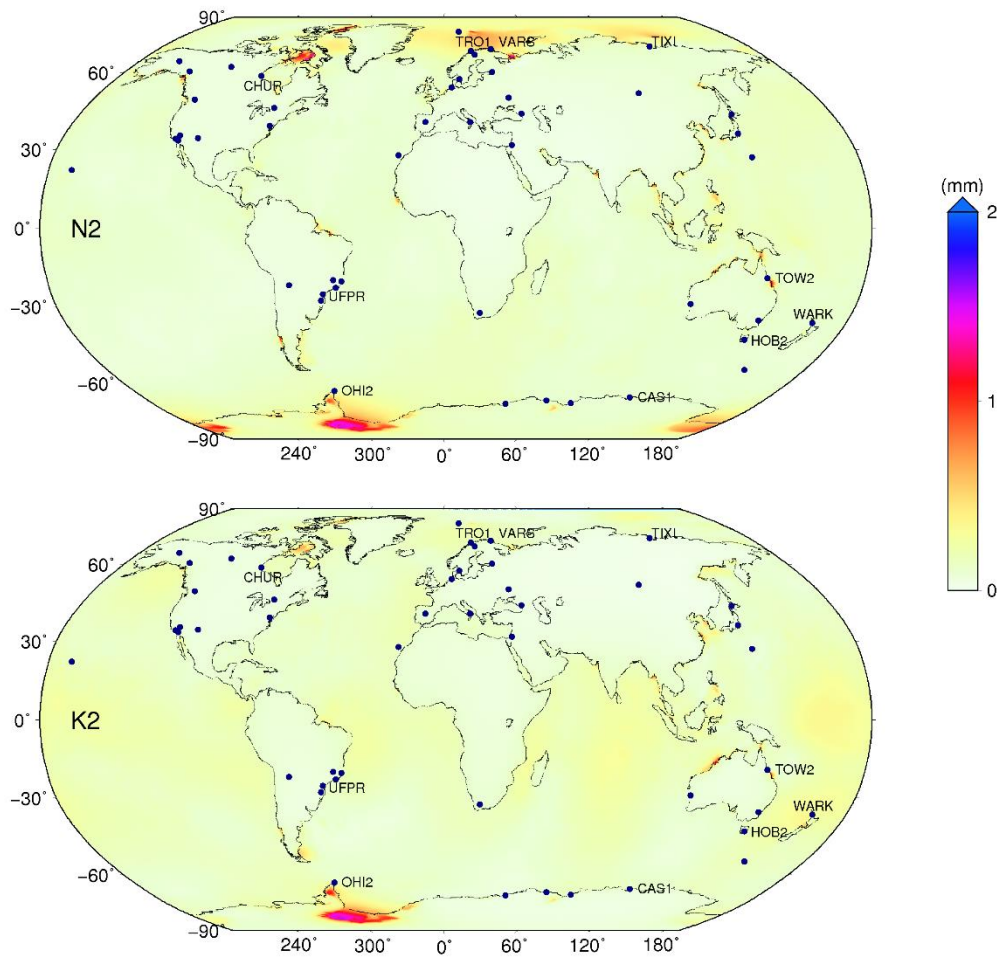


Figure D.2: RMS agreement of the magnitudes of the vector differences for the predicted OTL height displacement (in mm) per cell of a  $0.25^\circ$  global grid for the semidiurnal N2 and K2 constituents based on seven recent ocean tide models (FES2014b, GOT4.10c, TPXO8-Atlas, NAO.99b, HMTIDE11a, DTU10, and EOT11a), with GNSS stations used in this paper shown as dark blue dots.

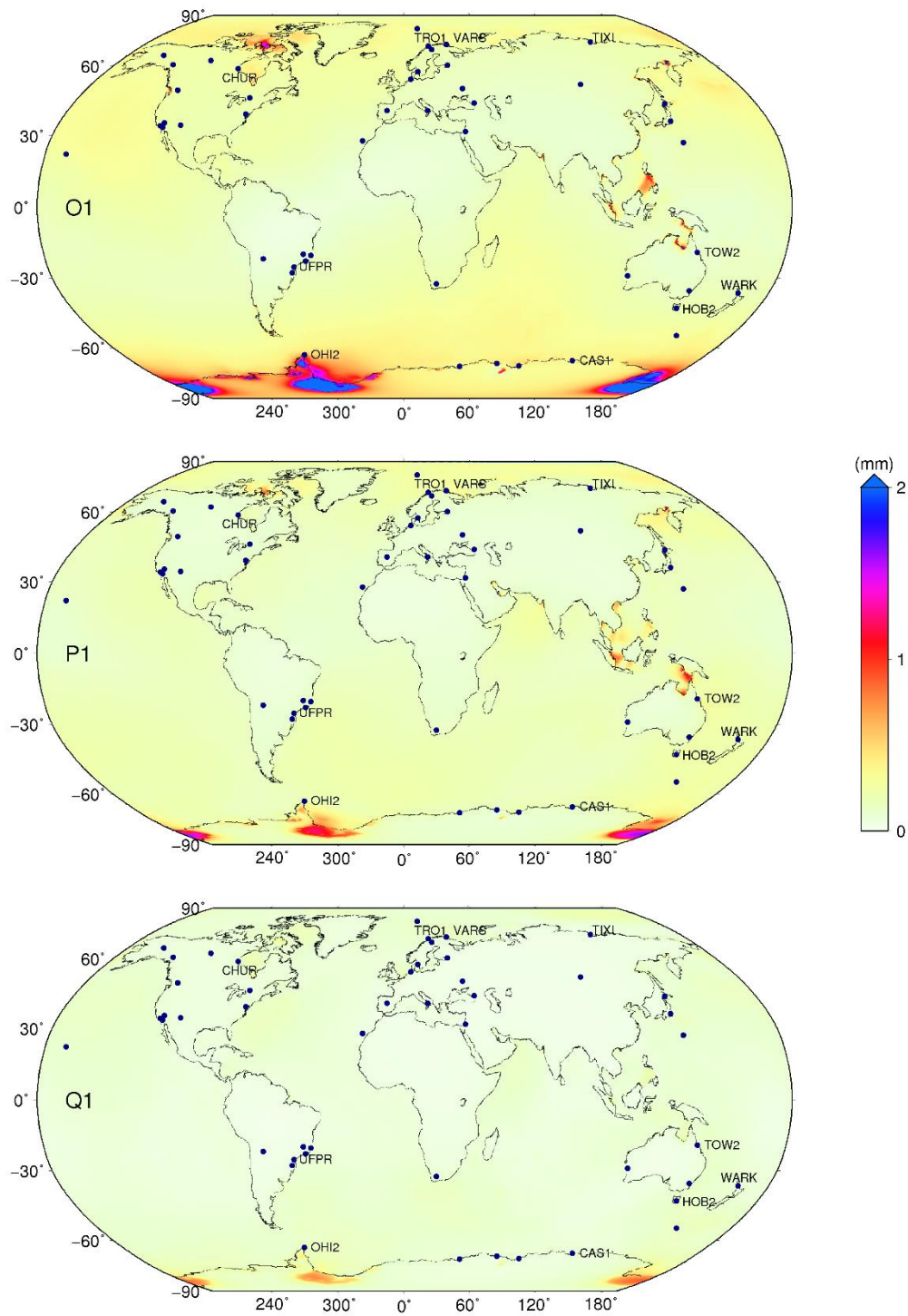


Figure D.3: RMS agreement of the magnitudes of the vector differences for the predicted OTL height displacement (in mm) per cell of a  $0.25^\circ$  global grid for the diurnal O1, P1 and Q1 constituents based on seven recent ocean tide models (FES2014b, GOT4.10c, TPX08-Atlas, NAO.99b, HAMTIDE11a, DTU10, and EOT11a), with GNSS stations used in this paper shown as dark blue dots. The colour scale saturates at 2 mm RMS (maximum RMS for O1 is 3 mm).

## Appendix E: GNSS-derived vertical OTL displacement residuals in Chapter 5

In this section, estimated OTL displacement residuals from GPS-only, GLONASS-only and combined GPS+GLONASS, which are shown in Chapter 5, are listed in Table E.1 to Table E.5. For all constituents, modelled OTL displacement is based on FES2014b ocean tide model and elastic PREM Green's function.

Station	M2					
	GPS		GLONASS		Combined	
	amp	phs	amp	phs	amp	phs
ALGO	0.4	305	0.4	60	0.2	324
AZRY	0.7	341	0.4	354	0.6	334
BADG	0.1	117	0.3	212	0.0	262
CAS1	0.6	261	0.6	249	0.7	260
CCJ2	0.8	121	1.3	130	0.7	127
CEFE	0.6	157	1.4	143	0.6	146
CHUR	0.4	17	0.2	340	0.4	25
DAV1	0.9	213	0.7	217	0.8	215
DRAG	0.5	282	0.3	338	0.3	285
DRAO	0.5	5	0.4	9	0.5	348
FAIV	0.3	211	0.1	261	0.2	216
GODZ	0.3	45	0.5	102	0.2	76
GOLD	0.5	3	0.4	66	0.6	355
HEL2	0.8	89	1.0	66	0.9	75
HOB2	0.2	341	0.1	169	0.2	337
JPLM	0.5	341	0.8	318	0.5	297
KHAR	0.3	251	0.2	300	0.3	266
KIR0	0.1	76	0.4	77	0.2	28
KOKV	0.5	292	0.9	265	0.6	282
MAC1	0.9	346	0.8	5	0.9	350
MADR	0.6	174	0.8	9	0.4	163
MAS1	1.1	355	1.4	342	1.1	350
MATE	0.3	252	0.2	234	0.2	248
MAW1	0.7	218	0.6	199	0.6	209
MGBH	0.5	56	0.5	71	0.5	81

NYA1	1.0	25	0.7	26	0.9	15
OHI2	0.9	131	0.8	109	0.9	126
ONRJ	0.4	201	0.9	211	0.5	181
ONSA	0.4	200	0.2	155	0.1	223
PIE1	1.0	356	0.9	2	0.6	353
SCLA	0.7	81	1.3	78	0.4	99
STK2	0.7	132	0.3	255	0.3	146
STR2	0.4	273	0.3	194	0.4	291
SUTV	0.3	279	0.7	245	0.1	282
SVTL	0.4	251	0.3	274	0.1	329
SYOG	0.2	249	0.3	250	0.3	244
TID1	0.5	310	0.8	285	0.4	291
TIXI	0.7	172	0.2	298	0.5	193
TOW2	1.3	67	1.5	69	1.4	56
TRO1	1.3	40	1.4	45	1.3	37
TSK2	0.5	128	0.4	95	0.5	124
UFPR	0.5	82	1.0	121	0.4	104
VAR5	1.1	280	1.1	270	1.1	276
WARK	1.5	125	1.5	128	1.3	121
WHIT	0.3	198	0.3	185	0.2	199
YAR3	0.3	116	0.3	144	0.2	125
YCBA	0.5	64	0.5	63	0.4	84
YELL	0.3	258	0.4	340	0.1	303
ZECK	0.5	314	0.6	284	0.4	318

Table E.1: GNSS-estimated vertical M2 OTL displacement residuals (amplitude in mm and phase in degree) with respect to FES2014b and the elastic PREM model

Station	N2					
	GPS		GLONASS		Combined	
	amp	phs	amp	phs	amp	phs
ALGO	0.3	167	1.1	131	0.2	126
AZRY	0.3	153	0.7	156	0.1	148
BADG	0.1	285	0.2	292	0.1	359
CAS1	0.1	126	0.3	127	0.2	137
CCJ2	0.2	264	0.1	116	0.2	1
CEFE	0.2	58	0.3	351	0.3	50
CHUR	0.1	310	0.4	323	0.1	339
DAV1	0.1	199	0.3	108	0.2	98
DRAG	0.3	120	0.3	41	0.2	140
DRAO	0.3	188	0.4	226	0.2	220
FAIV	0.2	147	0.3	355	0.1	154
GODZ	0.2	108	0.4	102	0.1	139
GOLD	0.4	210	0.5	167	0.2	227
HEL2	0.2	287	0.2	293	0.1	320
HOB2	0.3	313	0.1	239	0.1	300
JPLM	0.4	161	0.3	201	0.0	161
KHAR	0.4	150	0.3	185	0.2	164
KIR0	0.3	180	0.2	325	0.1	262
KOKV	0.1	110	0.6	158	0.2	170
MAC1	0.2	271	0.3	277	0.2	255
MADR	0.6	140	0.4	15	0.3	164
MAS1	0.2	218	0.2	182	0.3	216
MATE	0.2	130	0.2	307	0.1	24
MAW1	0.2	102	0.1	25	0.1	102
MGBH	0.3	88	0.2	30	0.1	65
NYA1	0.1	299	0.2	335	0.2	294
OHI2	0.3	81	0.1	332	0.1	46
ONRJ	0.4	25	0.2	31	0.1	37
ONSA	0.1	194	0.1	264	0.1	188
PIE1	0.3	179	0.7	138	0.1	114
SCLA	0.1	47	0.4	218	0.2	116

STK2	0.2	23	0.6	122	0.2	84
STR2	0.2	60	0.2	326	0.1	306
SUTV	0.2	252	0.1	94	0.1	173
SVTL	0.3	186	0.1	262	0.2	261
SYOG	0.2	80	0.2	93	0.1	83
TID1	0.3	102	0.3	122	0.2	326
TIXI	0.5	194	0.1	276	0.1	226
TOW2	0.5	272	0.5	268	0.6	267
TRO1	0.1	157	0.1	313	0.1	280
TSK2	0.2	329	0.2	357	0.1	342
UFPR	0.1	83	0.2	304	0.2	71
VAR5	0.3	165	0.4	159	0.3	156
WARK	0.3	54	0.3	22	0.4	20
WHIT	0.1	107	0.2	230	0.2	152
YAR3	0.1	231	0.2	118	0.1	91
YCBA	0.2	194	0.4	143	0.1	195
YELL	0.2	94	0.4	46	0.3	86
ZECK	0.2	153	0.0	308	0.0	204

Table E.2: GNSS-estimated vertical N2 OTL displacement residuals (amplitude in mm and phase in degree) with respect to the FES2014b and elastic PREM model

Station	K2					
	GPS		GLONASS		Combined	
	amp	phs	amp	phs	amp	phs
ALGO	1.1	163	0.9	40	0.2	82
AZRY	2.6	26	0.1	22	1.2	336
BADG	3.4	214	1.3	240	1.7	214
CAS1	1.9	57	0.3	334	1.3	48
CCJ2	1.9	52	0.4	244	1.6	107
CEFE	1.0	50	0.7	129	1.0	91
CHUR	2.0	180	0.5	65	1.0	148
DAV1	2.2	133	0.7	127	1.0	118
DRAG	1.5	33	0.2	10	0.7	316
DRAO	1.1	171	0.6	42	0.4	293
FAIV	1.2	105	1.9	340	0.4	73
GODZ	2.6	304	0.4	84	1.2	284
GOLD	1.5	8	1.2	292	1.1	3
HEL2	4.8	11	0.7	317	1.9	341
HOB2	2.7	155	0.8	15	0.5	193
JPLM	3.1	309	1.6	275	2.0	320
KHAR	5.9	206	1.4	9	2.0	225
KIR0	0.6	107	0.5	7	1.0	111
KOKV	2.8	71	1.4	208	1.4	171
MAC1	1.6	247	0.4	307	1.1	321
MADR	7.3	54	2.6	160	2.3	31
MAS1	1.7	354	0.9	164	1.6	20
MATE	1.4	216	0.8	223	0.5	275
MAW1	1.4	107	0.9	59	0.8	163
MGBH	3.2	134	0.6	169	2.9	120
NYA1	1.0	282	0.4	212	0.2	81
OHI2	1.4	249	0.8	204	0.6	265
ONRJ	2.8	110	0.9	340	1.0	111
ONSA	1.5	4	1.0	292	0.3	163
PIE1	2.9	31	1.9	202	1.2	48
SCLA	2.2	253	0.6	166	0.7	254

STK2	0.9	117	1.6	194	0.4	165
STR2	3.1	104	1.2	65	2.1	102
SUTV	3.2	228	0.5	278	0.6	207
SVTL	2.7	253	0.5	330	1.0	299
SYOG	0.6	326	1.5	354	2.0	315
TID1	1.1	238	1.7	338	0.4	265
TIXI	12.1	244	2.2	32	5.2	281
TOW2	1.3	30	0.7	126	0.4	13
TRO1	1.0	199	0.3	291	0.9	224
TSK2	1.5	80	0.6	225	0.7	103
UFPR	0.4	283	1.2	180	0.6	234
VAR3	0.7	266	0.6	23	0.6	226
WARK	2.9	125	1.4	69	1.1	69
WHIT	2.2	168	2.0	323	1.0	207
YAR3	1.3	327	0.7	80	1.0	44
YCBA	1.5	290	0.5	139	0.2	311
YELL	2.9	8	2.3	358	0.6	38
ZECK	2.5	275	0.4	327	0.9	12

Table E.3: GNSS-estimated vertical K2 OTL displacement residuals (amplitude in mm and phase in degree) with respect to the FES2014b and elastic PREM model



Station	K1					
	GPS		GLONASS		Combined	
	amp	phs	amp	phs	amp	phs
ALGO	2.2	241	1.8	198	1.8	262
AZRY	4.8	9	1.9	113	0.9	71
BADG	1.9	228	1.7	312	1.4	210
CAS1	1.2	344	0.8	215	1.8	297
CCJ2	2.0	294	0.2	273	0.9	56
CEFE	1.4	90	2.2	129	1.7	79
CHUR	0.7	41	1.0	211	0.5	346
DAV1	2.9	342	1.5	158	0.9	299
DRAG	2.7	258	1.9	256	1.4	337
DRAO	3.1	17	1.0	138	0.7	30
FAIV	1.5	242	1.7	135	1.7	165
GODZ	6.0	278	1.9	67	2.8	281
GOLD	1.4	56	1.2	287	0.4	73
HEL2	2.6	127	1.9	249	1.4	126
HOB2	2.2	229	2.7	235	2.1	246
JPLM	0.8	203	1.4	211	1.8	199
KHAR	0.3	96	2.1	305	1.3	332
KIR0	0.9	5	1.4	292	1.5	328
KOKV	0.7	77	1.7	135	1.7	111
MAC1	2.2	81	2.1	250	0.5	226
MADR	2.0	175	2.6	201	1.5	209
MAS1	2.2	134	0.4	260	0.7	113
MATE	2.9	282	2.4	242	1.2	305
MAW1	0.9	132	2.2	162	1.0	181
MGBH	3.5	153	2.7	290	4.6	127
NYA1	1.3	246	0.5	207	0.8	275
OHI2	1.7	131	2.2	33	1.8	69
ONRJ	1.0	273	0.5	285	0.6	98
ONSA	1.9	328	1.1	291	0.6	31
PIE1	1.3	238	1.2	9	1.0	149
SCLA	0.7	179	0.7	122	0.3	110

STK2	2.1	281	1.7	355	0.7	348
STR2	2.8	125	1.9	159	0.8	255
SUTV	2.6	166	1.5	84	1.1	141
SVTL	0.5	213	1.0	259	0.6	254
SYOG	1.4	220	2.3	91	1.1	199
TID1	1.4	27	2.1	115	0.6	231
TIXI	5.1	320	1.2	62	3.9	346
TOW2	2.6	70	0.6	77	1.0	135
TRO1	1.3	296	0.7	305	0.9	319
TSK2	2.5	254	2.0	9	0.3	17
UFPR	3.0	126	0.8	353	1.7	70
VAR3	0.3	267	1.4	298	1.1	331
WARK	1.3	35	2.3	258	0.4	240
WHIT	1.4	88	1.8	163	1.1	151
YAR3	1.3	177	1.9	193	1.0	196
YCBA	1.9	354	1.6	43	0.9	359
YELL	1.7	27	1.7	198	0.7	100
ZECK	1.8	75	1.9	248	0.9	16

Table E.4: GNSS-estimated vertical K1 OTL displacement residuals (amplitude in mm and phase in degree) with respect to the FES2014b and elastic PREM model

Station	O1					
	GPS		GLONASS		Combined	
	amp	phs	amp	phs	amp	phs
ALGO	0.2	281	0.8	360	0.1	213
AZRY	0.4	347	0.5	337	0.2	1
BADG	0.2	225	0.2	183	0.1	241
CAS1	0.5	333	0.6	322	0.4	323
CCJ2	0.3	123	0.5	92	0.4	146
CEFE	0.2	78	0.2	14	0.2	113
CHUR	0.2	223	0.4	286	0.2	265
DAV1	0.5	327	0.7	328	0.5	327
DRAG	0.2	285	0.3	275	0.1	210
DRAO	0.5	341	0.6	291	0.3	298
FAIV	0.1	19	0.3	239	0.3	255
GODZ	0.2	51	0.8	49	0.2	21
GOLD	0.3	319	0.6	309	0.2	291
HEL2	0.2	359	0.2	243	0.1	276
HOB2	0.4	358	0.2	337	0.3	342
JPLM	0.5	318	0.3	19	0.3	225
KHAR	0.2	331	0.2	95	0.1	205
KIR0	0.3	101	0.2	137	0.2	146
KOKV	0.5	4	0.4	137	0.3	32
MAC1	0.5	2	0.3	341	0.3	352
MADR	0.5	61	1.6	109	0.2	93
MAS1	0.3	211	0.4	16	0.2	266
MATE	0.2	200	0.2	156	0.2	230
MAW1	0.2	314	0.4	306	0.3	320
MGBH	0.2	128	0.3	32	0.1	173
NYA1	0.3	146	0.2	174	0.2	184
OHI2	0.6	170	0.3	181	0.5	185
ONRJ	0.2	223	0.9	38	0.2	112
ONSA	0.3	48	0.3	173	0.1	149
PIE1	0.2	270	0.6	21	0.0	307
SCLA	0.3	324	0.2	116	0.1	129

STK2	0.2	193	0.3	338	0.3	215
STR2	0.9	313	0.6	303	0.3	309
SUTV	0.2	289	0.4	253	0.2	267
SVTL	0.1	43	0.3	126	0.2	189
SYOG	0.2	331	0.2	123	0.1	334
TID1	0.7	296	1.0	328	0.5	293
TIXI	0.3	306	0.6	136	0.2	142
TOW2	0.6	11	0.8	30	0.4	357
TRO1	0.2	94	0.1	105	0.2	134
TSK2	0.4	131	0.8	136	0.4	137
UFPR	0.2	174	0.5	194	0.1	135
VARS	0.2	132	0.3	135	0.2	121
WARK	0.5	322	0.5	240	0.4	337
WHIT	0.1	66	0.4	293	0.2	285
YAR3	0.3	273	0.1	218	0.2	234
YCBA	0.4	47	0.5	2	0.3	44
YELL	0.1	58	0.4	3	0.4	343
ZECK	0.4	120	0.1	262	0.4	142

Table E.5: GNSS-estimated vertical O1 OTL displacement residuals (amplitude in mm and phase in degree) with respect to the FES2014b and elastic PREM model

## Appendix F: Modelled and measured (tide gauge) ocean tides in Alaska

To investigate the quality of different ocean tide models in Alaska, the modelled M2 and K1 ocean tidal signals are compared to those observed at tide gauge stations. As the coastline geometry in Alaska varies in different locations, five sub-regions A to E, as shown in Table F.1, are considered, and the difference between the modelled and observed ocean tide, as shown in Table F.2 and Table F.3, are inspected.

Zone	Stn.	Latitude	Longitude	Zone	Stn.	Latitude	Longitude
<b>A</b>	1	57.08	-134.82	<b>B</b>	16	59.77	-149.58
	2	55.08	-132.80		17	58.28	-154.27
	3	55.03	-133.02		18	56.88	-154.23
	4	56.78	-135.38		19	59.77	-151.87
	5	55.20	-132.82		20	59.68	-149.73
	6	55.60	-132.50		21	59.70	-149.78
	7	55.78	-132.18		22	56.58	-153.98
	8	55.12	-131.57		23	56.95	-153.68
	9	56.17	-132.68		24	59.47	-151.55
	10	56.23	-134.63		25	57.72	-152.50
	11	56.90	-134.30		26	60.02	-147.58
	12	57.33	-135.70		27	58.38	-153.95
	13	56.12	-132.07		28	60.05	-151.67
	14	55.35	-132.93		29	57.20	-153.30
	15	57.25	-135.57		30	57.92	-152.48
<b>C</b>	38	54.23	-165.53	31	60.12	-147.38	
	39	54.13	-165.80	32	59.93	-148.22	
	40	53.82	-166.22	33	57.70	-155.38	
	41	54.83	-159.75	34	60.37	-147.70	
	42	54.05	-165.93	35	56.95	-153.25	
	43	55.05	-163.53	36	58.10	-153.33	
	44	54.60	-164.92	37	59.87	-147.40	
	45	56.22	-158.33	<b>D</b>	63	61.52	-166.13
46	55.80	-155.73	64		60.03	-165.67	

	47	56.05	-156.68		65	60.42	-166.17	
	48	55.12	-161.78		66	59.03	-161.82	
	49	54.85	-163.40	<b>E</b>	67	65.38	-167.13	
	50	54.10	-165.65		68	64.48	-165.43	
	51	55.05	-159.42		69	63.32	-168.97	
	52	56.10	-158.58		70	65.72	-168.02	
	53	55.05	-162.32		71	65.25	-166.83	
	54	55.88	-158.82		72	64.37	-161.23	
	55	55.98	-160.57		73	65.55	-167.97	
	56	54.12	-166.08		<b>F</b>	74	66.58	-164.25
	57	54.05	-165.50			75	67.05	-163.32
	58	54.10	-164.93	76		66.08	-162.73	
	59	55.32	-160.50	77		67.72	-164.58	
	60	54.38	-164.73	78		68.33	-166.80	
	61	54.13	-165.52	79		67.57	-164.05	
	62	55.33	-160.62	80		66.25	-166.02	

Table F.1: List of tide gauge stations used in Chapter 6

Zone	Stn.	TPX08		NAO99		HMTIDE		GOT4.10		DTU10		EOT11		FES2014		Tide gauge	
		amp	phs	amp	phs	amp	phs	amp	phs	amp	phs	amp	phs	amp	phs	amp	phs
<b>A</b>	1	159	80	134	80	56	19	110	14	137	332	140	331	178	78	164	81
	2	153	89	123	86	130	89	129	93	131	89	133	89	143	89	151	88
	3	144	89	118	88	126	90	123	92	120	89	122	88	125	90	150	88
	4	108	87	108	85	108	88	111	87	110	85	111	86	108	87	108	87
	5	141	90	120	85	113	89	128	92	130	89	144	87	144	89	153	87
	6	189	90	193	80	70	87	154	90	249	86	255	85	185	87	194	87
	7	201	90	197	80	111	87	158	84	276	86	277	85	194	87	196	88
	8	178	92	181	87	194	94	182	91	196	92	204	92	169	93	181	91
	9	203	89	138	89	194	265	131	70	293	85	291	84	197	86	196	87
	10	130	82	114	89	90	70	120	84	92	79	85	75	127	83	124	84
	11	163	82	132	85	131	359	110	24	127	6	134	1	172	82	162	84
	12	111	86	107	87	105	87	108	86	108	84	100	80	115	84	109	87
	13	204	90	198	81	197	77	137	75	282	86	228	84	169	76	198	88
	14	127	90	119	87	88	89	121	91	142	88	157	87	139	90	113	91
	15	113	86	107	86	103	87	108	85	109	82	97	76	120	83	111	83
<b>B</b>	16	119	72	117	72	118	71	121	71	119	71	119	71	121	72	120	71
	17	133	29	168	34	167	30	159	38	164	38	166	35	162	38	162	37
	18	133	332	121	59	132	55	104	27	106	14	105	13	130	46	135	46
	19	217	23	239	28	206	34	209	25	217	28	208	31	225	26	228	25
	20	121	71	118	72	120	71	122	71	120	71	119	71	123	71	121	72
	21	122	71	118	72	121	71	122	71	120	71	119	71	123	72	122	71
	22	92	47	98	61	93	57	86	50	96	56	95	55	102	53	97	58
	23	70	25	83	62	93	60	81	41	85	50	86	49	105	55	91	61
	24	215	29	213	38	197	39	192	40	215	35	198	37	213	36	223	35
	25	98	52	99	43	101	55	99	51	100	48	104	47	97	53	97	53
	26	137	71	114	69	111	73	121	73	131	70	128	68	125	73	131	71
	27	165	37	171	34	169	35	163	38	170	38	170	36	163	38	162	37
	28	232	358	256	20	213	24	215	16	228	24	218	27	234	7	237	6
	29	99	56	85	60	97	58	94	63	94	59	96	58	96	59	91	61
	30	102	50	116	37	104	54	102	49	103	51	109	50	100	52	97	52
	31	135	71	117	69	119	67	122	72	124	71	122	69	125	72	133	73

	32	118	73	111	69	113	73	114	73	120	74	116	73	118	73	119	74
	33	144	38	146	36	144	40	143	39	145	39	146	39	145	39	143	38
	34	151	68	119	59	137	67	131	71	138	68	136	65	131	71	135	71
	35	91	61	85	61	92	60	92	63	91	61	92	60	92	62	91	61
	36	168	38	172	34	173	37	167	37	167	38	174	37	165	38	166	37
	37	110	72	114	71	109	73	116	73	112	73	110	72	112	73	113	71
<b>C</b>	38	25	285	30	32	14	321	28	34	16	310	17	311	17	294	16	291
	39	26	343	28	33	42	10	32	35	23	350	37	11	28	285	28	279
	40	42	17	28	35	38	25	31	5	23	3	23	6	27	22	42	15
	41	71	38	65	41	67	33	67	36	75	45	69	36	69	41	69	42
	42	40	12	28	33	31	352	36	5	29	351	30	352	34	357	47	15
	43	64	246	71	24	65	248	48	25	57	251	47	261	67	242	71	243
	44	41	294	40	30	40	309	36	30	41	304	43	306	41	299	41	295
	45	91	30	82	27	92	35	84	37	92	37	94	35	89	35	93	36
	46	92	57	90	50	92	52	93	51	93	53	92	53	94	55	90	57
	47	94	42	94	43	96	44	98	44	96	43	96	44	96	44	96	44
	48	66	24	63	22	64	32	60	20	61	23	61	24	71	29	68	34
	49	27	346	74	24	25	348	22	32	44	7	41	351	32	253	23	343
	50	30	359	29	34	38	9	37	7	29	11	30	12	30	354	40	16
	51	77	33	69	37	72	30	71	37	78	41	72	31	72	38	73	38
	52	87	33	81	28	88	36	83	36	83	39	86	37	86	37	81	37
	53	51	11	60	28	57	30	52	27	63	29	64	29	49	22	68	32
	54	82	38	79	35	81	36	81	36	81	39	84	38	80	38	79	38
	55	97	150	92	16	103	157	49	16	106	156	102	163	100	167	103	154
	56	28	292	28	32	24	315	27	34	25	309	25	311	25	314	26	290
	57	51	24	32	35	41	20	44	16	36	16	36	16	49	17	42	19
	58	38	23	40	4	45	25	43	18	33	21	34	19	38	24	45	26
59	81	28	72	36	58	5	56	27	49	3	52	343	78	35	73	38	
60	42	359	38	34	50	6	32	33	49	6	52	6	47	360	51	4	
61	25	355	30	33	32	18	36	7	22	7	23	6	25	360	25	20	
62	81	27	72	35	59	6	55	24	49	335	52	343	80	34	76	36	
<b>D</b>	63	65	81	69	83	59	79	65	88	68	85	61	81	77	84	50	75
	64	79	113	69	11	55	98	70	11	67	115	53	101	82	121	88	118



	65	107	130	88	10	69	104	87	11	88	116	71	105	95	127	94	126
	66	78	196	53	21	80	213	79	21	84	211	82	211	74	221	83	195
<b>E</b>	67	7	159	14	18	12	159	8	19	11	167	12	167	10	169	11	172
	68	10	310	13	33	14	312	9	30	11	316	14	312	9	315	11	322
	69	21	67	18	63	26	66	19	62	25	68	27	68	24	69	29	76
	70	9	144	17	14	14	137	13	14	14	143	14	142	12	143	14	146
	71	7	156	16	21	13	159	8	20	11	168	12	168	10	174	13	173
	72	1	95	13	10	23	118	28	11	22	120	28	118	14	137	18	128
	73	9	150	16	14	13	146	13	16	13	152	12	151	11	153	12	161
	<b>F</b>	74	3	15	18	54	11	12	7	88	11	40	11	39	10	29	11
75		3	344	14	85	4	259	3	12	1	151	1	320	2	189	4	166
76		2	298	22	29	24	285	16	28	18	299	17	299	20	295	21	296
77		2	12	25	66	8	79	11	10	10	89	8	84	9	83	10	91
78		0	149	13	27	6	58	4	24	8	50	6	43	7	52	8	61
79		2	12	23	73	7	80	12	10	9	92	8	85	8	88	7	79
80		5	65	31	10	17	85	15	88	15	92	14	94	15	91	12	95

Table F.2: Modelled and observed (tide gauge) M2 ocean tide in Alaska (amplitude in cm and phase in degree) based on different ocean tide models

Zone	Stn.	TPX08		NAO99		HMTIDE		GOT4.10		DTU10		EOT11		FES2014		Tide gauge	
		amp	phs	amp	phs	amp	phs	amp	phs	amp	phs	amp	phs	amp	phs	amp	phs
<b>A</b>	1	48	96	45	95	3	100	56	86	59	78	60	80	50	96	49	98
	2	48	99	44	96	46	100	46	10	46	98	47	99	48	99	47	97
	3	47	98	44	97	46	100	46	10	45	98	46	99	47	99	46	97
	4	45	99	44	97	46	98	44	93	45	97	47	97	45	99	43	99
	5	47	98	43	96	43	100	46	10	46	97	47	98	48	99	48	98
	6	50	97	50	94	17	99	48	99	53	96	54	97	51	97	53	99
	7	51	97	50	94	22	99	51	96	54	96	55	98	52	97	49	97
	8	49	99	49	97	50	100	50	98	50	98	51	100	49	101	51	102
	9	51	96	43	98	31	278	52	94	55	95	56	97	52	97	54	96
	10	46	97	45	98	48	96	46	97	46	93	47	94	46	97	47	97
	11	48	97	44	97	58	87	55	88	57	86	59	87	49	97	52	97
	12	46	98	45	97	45	98	45	92	44	89	46	91	47	96	48	96
	13	51	97	50	94	54	96	52	94	54	96	47	91	49	85	52	98
	14	46	98	43	96	37	100	46	10	46	97	48	98	47	99	42	97
	15	46	98	44	97	44	98	45	89	43	80	46	83	47	96	44	96
<b>B</b>	16	46	87	44	87	45	89	45	87	45	86	44	88	45	87	48	89
	17	49	67	51	70	51	70	51	74	51	76	51	70	50	75	48	73
	18	51	45	48	89	51	84	43	69	43	59	45	58	49	80	50	80
	19	56	73	61	84	55	74	57	74	55	75	54	71	57	76	57	75
	20	46	87	44	87	44	89	45	87	45	86	44	88	45	87	46	87
	21	46	87	43	87	44	89	45	87	45	86	44	88	45	87	46	87
	22	42	81	45	89	47	88	41	86	44	90	46	89	42	86	36	90
	23	41	70	42	92	45	92	36	77	39	86	41	85	42	86	34	91
	24	55	75	56	86	53	77	54	79	53	71	52	70	55	81	57	82
	25	41	76	39	70	40	82	38	76	40	76	41	76	40	75	40	72
	26	48	87	48	87	47	89	46	86	48	81	48	82	48	89	47	88
	27	51	73	53	70	52	72	51	75	51	77	51	71	50	75	48	72
	28	57	63	65	83	56	67	57	71	57	73	55	69	61	70	60	68
	29	41	83	42	86	44	91	37	91	40	92	42	91	39	86	37	89
	30	42	74	45	68	40	81	39	74	40	77	41	77	40	74	40	75
	31	48	87	48	87	49	86	47	86	47	83	47	84	48	89	50	88

	32	46	87	46	83	45	89	46	88	45	87	45	88	46	87	42	86
	33	50	74	49	74	50	75	51	76	51	75	50	74	49	75	47	74
	34	50	85	47	81	52	87	48	82	50	78	50	78	49	88	51	88
	35	40	86	43	85	43	92	38	90	41	93	43	92	39	88	34	88
	36	52	73	55	71	53	73	53	74	52	75	53	71	51	75	50	74
	37	46	87	48	89	47	89	46	88	46	87	46	88	47	88	47	88
<b>C</b>	38	35	43	43	58	36	56	37	60	34	47	34	47	34	44	32	44
	39	37	56	43	59	39	66	37	63	36	57	38	67	36	43	37	39
	40	41	66	43	62	38	70	38	63	36	58	36	57	35	60	37	72
	41	43	75	41	74	41	73	41	75	43	81	41	77	42	77	41	78
	42	41	65	43	60	38	61	38	66	38	60	38	60	39	65	39	74
	43	47	36	52	38	52	40	49	43	48	40	48	44	51	40	49	38
	44	40	47	44	56	42	54	40	52	42	53	42	53	41	51	40	51
	45	44	69	41	65	45	69	43	72	47	70	46	70	45	71	45	71
	46	45	83	46	81	46	81	47	82	45	83	46	82	47	84	44	83
	47	45	76	45	76	44	76	45	77	44	76	45	76	45	78	43	78
	48	42	67	37	66	44	72	40	65	44	66	45	66	42	71	39	75
	49	43	56	54	38	46	57	45	56	44	64	46	60	47	46	40	52
	50	38	60	43	61	38	65	39	67	36	62	36	63	36	62	37	71
	51	43	72	40	72	39	69	40	74	42	76	40	69	42	72	42	73
	52	43	71	40	65	44	69	43	71	45	72	44	70	44	72	42	72
	53	41	58	39	72	45	67	42	66	44	69	45	69	42	64	42	76
	54	42	73	40	68	42	69	43	71	45	73	43	71	43	72	43	74
	55	65	353	66	35	68	359	52	12	61	0	63	358	64	1	65	356
	56	35	43	42	57	37	54	36	59	37	49	37	48	37	51	34	48
	57	42	71	43	63	39	69	40	71	37	66	37	67	39	75	36	72
58	37	66	43	67	39	68	39	70	35	62	36	63	34	66	37	72	
59	44	70	41	74	39	59	36	61	38	53	38	46	43	72	42	75	
60	41	62	44	64	41	64	40	59	42	66	43	67	42	66	45	68	
61	37	57	43	61	37	65	39	66	34	58	34	58	33	56	33	60	
62	44	70	42	73	39	59	35	60	37	40	38	46	43	72	41	74	
<b>D</b>	63	28	77	29	85	18	49	30	85	31	85	28	82	33	91	25	74
	64	23	168	20	17	21	185	23	16	23	171	21	174	20	169	21	170

	65	21	101	16	12	14	84	25	11	23	108	20	105	25	108	27	98
	66	55	266	64	26	61	271	61	27	61	272	59	273	62	272	57	261
<b>E</b>	67	3	343	7	61	6	263	4	35	2	341	9	320	3	66	4	95
	68	8	247	12	24	7	250	2	12	6	210	4	247	9	214	9	213
	69	8	3	7	11	10	305	7	35	8	354	8	357	9	357	9	353
	70	2	6	6	16	5	255	5	1	4	334	9	315	3	41	3	76
	71	3	336	10	76	7	261	5	4	2	336	8	321	3	71	4	105
	72	7	158	34	24	4	126	35	22	37	239	35	229	43	245	45	248
	73	3	357	5	22	5	261	5	14	3	341	9	317	3	49	4	94
<b>F</b>	74	1	295	10	29	4	180	8	22	7	272	10	265	3	308	4	25
	75	1	267	9	25	3	149	12	19	5	216	8	228	3	270	5	335
	76	1	227	16	28	4	134	16	21	9	225	12	225	5	272	7	356
	77	1	302	4	23	2	163	7	18	4	235	6	251	2	282	4	330
	78	1	312	2	20	2	146	8	17	3	196	4	248	1	265	2	309
	78	1	293	6	23	2	163	8	19	4	241	6	250	2	282	2	275
	80	1	7	8	35	4	217	7	30	6	301	10	295	3	351	4	26

Table F.3: Modelled and observed (tide gauge) K1 ocean tide in Alaska (amplitude in cm and phase in degree) based on different ocean tide models

## Appendix G: GPS/GNSS-derived OTL displacement residuals in Alaska

In Alaska, GPS/GNSS observation have been used for ocean tide model and Green's function investigation. Table G.1 represents GPS/GNSS stations.

GPS-derived OTL displacement residuals based on the elastic PREM Green's function and three ocean tide models, i.e. FES2014b, GOT4.10 and TPX08, are used for the ocean tide models quality assessment and their numerical values are provided in Table G.2. In Table G.3, GPS-derived OTL displacement residuals based on the elastic PREM, anelastic PREM and anelastic S362ANI Green's functions with FES2014b ocean tide models are used for examining the anelasticity effect of the Green's function on the OTL displacement modelling.

A comparison of using GPS-only, GLONASS-only and combined GPS+GLONASS observation in measuring OTL displacement at M2 and K1 periods are shown in Table G.4 and Table G.5, respectively.

Station	Latitude	Longitude	Data	Station	Latitude	Longitude	Data
AB06	54.8853	196.5765	GPS	AC51	61.4981	208.1647	GPS
AB07	55.3493	199.5232	GPS	AC52	57.5672	202.4258	GPS
AB09	65.6150	191.9379	GPS	AC53	61.7690	209.9310	GPS+GLO
AB11	64.5645	194.6265	GPS	AC57	61.1386	214.2573	GPS
AB13	56.3073	201.4962	GPS	AC61	64.0293	217.9242	GPS
AB14	59.1082	200.9085	GPS	AC62	63.0836	213.6873	GPS
AB15	61.0398	200.1216	GPS	AC63	63.5024	214.1528	GPS
AB17	63.8864	199.3053	GPS	AC67	57.7907	207.5746	GPS
AB18	66.8584	197.3865	GPS+GLO	AC70	63.3047	211.8117	GPS+GLO
AB22	59.8993	205.3017	GPS	AC71	64.0493	214.2864	GPS
AB27	67.0559	203.0951	GPS	AC72	63.6951	214.1123	GPS
AB28	62.0938	207.1851	GPS	AC74	63.4644	211.1927	GPS
AB33	67.2510	209.8275	GPS	AC75	62.9993	210.3912	GPS
AB35	60.0791	217.6101	GPS	AC78	63.1135	217.9721	GPS+GLO
AB36	65.0304	209.2560	GPS	ANC2	61.1752	210.0166	GPS+GLO
AB37	62.9673	214.5481	GPS	ATLI	59.5895	226.2855	GPS+GLO
AB39	66.5593	214.7874	GPS	ATW2	61.5978	210.8677	GPS+GLO
AB42	59.3404	221.1012	GPS	AV09	53.8756	193.4582	GPS

AB43	58.1988	223.3592	GPS	BARO	71.3250	203.3323	GPS
AB44	59.5280	224.7717	GPS	BCRK	62.4143	219.1396	GPS+GLO
AB45	68.7605	211.1288	GPS	BLCL	52.3883	233.4107	GPS+GLO
AB48	56.2451	225.3530	GPS	CLGO	64.8738	212.1395	GPS
AB50	58.4168	225.4547	GPS	EYAC	60.5487	214.2501	GPS
AC07	65.9613	198.7134	GPS	FAIR	64.9780	212.5008	GPS
AC08	58.9288	206.3553	GPS	GRNB	53.8468	230.0420	GPS+GLO
AC09	59.8685	215.4761	GPS	GRNX	63.8355	211.0218	GPS
AC13	55.8219	204.3776	GPS	HAAR	62.4074	214.8429	GPS+GLO
AC17	60.6639	207.5962	GPS	HOLB	50.6404	231.8650	GPS+GLO
AC19	62.5192	206.3927	GPS	MCES	59.7461	208.7422	GPS
AC20	60.9292	210.6475	GPS+GLO	OTZ1	66.8873	197.3886	GPS
AC23	60.4751	209.1220	GPS	PFRR	65.1174	212.5669	GPS+GLO
AC24	58.6816	203.3472	GPS	SELD	59.4457	208.2933	GPS
AC26	58.2146	205.8497	GPS	SG27	71.3229	203.3897	GPS
AC27	59.2525	205.8371	GPS	SPIT	59.6081	208.5730	GPS+GLO
AC29	59.4296	213.6600	GPS	SUAF	64.8587	212.1642	GPS+GLO
AC31	64.6380	197.7609	GPS	TBON	61.1797	210.2149	GPS+GLO
AC37	60.4397	206.1346	GPS	TOOL	68.6275	210.4022	GPS
AC39	58.6097	207.6059	GPS	TSEA	61.1873	210.1050	GPS+GLO
AC40	56.9304	201.3814	GPS	WHIT	60.7505	224.7779	GPS
AC43	59.5213	210.3713	GPS	WIKR	63.5527	209.0778	GPS
AC44	61.2422	210.4329	GPS+GLO	WILL	52.2369	237.8322	GPS+GLO
AC45	56.5645	205.8190	GPS	ZAN1	61.2292	210.2197	GPS
AC48	60.6459	212.6570	GPS+GLO	ZINA	61.3835	216.9759	GPS+GLO
AC50	65.5538	195.4334	GPS				

Table G.1: GPS/GNSS stations in Alaska

Stn.	East						North						Up					
	FES2014		GOT4.10		TPX08		FES2014		GOT4.10		TPX08		FES2014		GOT4.10		TPX08	
	amp	phs	amp	phs	amp	phs	amp	phs	amp	phs	amp	phs	amp	phs	amp	phs	amp	phs
AB06	0.5	81	0.6	81	0.5	79	0.6	298	0.7	304	0.6	309	0.7	52	0.7	45	0.6	45
AB07	0.5	102	0.5	90	0.5	79	0.6	295	0.5	292	0.6	315	0.7	65	1.5	90	1.4	69
AB09	0.4	117	0.4	124	0.4	124	0.3	313	0.3	288	0.2	333	0.6	31	0.4	45	0.9	49
AB11	0.7	141	0.7	146	0.7	146	0.4	265	0.4	256	0.3	270	0.6	12	0.4	14	0.7	27
AB13	0.1	156	0.2	153	0.4	146	0.7	307	0.7	304	0.6	315	1.2	115	1.1	105	1.8	109
AB14	0.3	119	0.4	117	0.6	121	0.3	292	0.4	297	0.5	292	0.5	118	0.9	148	1.5	118
AB15	0.5	134	0.6	135	0.6	141	0.4	306	0.4	304	0.5	307	0.9	30	0.7	34	1.0	45
AB17	0.5	118	0.5	112	0.5	127	0.4	305	0.4	304	0.3	315	0.7	22	0.2	27	1.0	24
AB18	0.5	122	0.5	112	0.4	117	0.4	329	0.4	326	0.4	346	0.4	356	0.4	346	0.5	0
AB22	0.2	253	0.4	270	0.3	225	0.5	322	0.6	309	0.8	310	0.2	241	0.7	243	0.7	146
AB27	0.3	119	0.3	108	0.2	117	0.6	325	0.5	323	0.6	329	0.4	351	0.2	333	0.4	14
AB28	0.4	134	0.3	162	0.4	166	0.5	298	0.4	326	0.6	315	0.4	29	0.5	292	0.1	270
AB33	0.2	96	0.3	90	0.3	90	0.4	305	0.4	304	0.4	315	0.6	350	0.4	346	0.5	11
AB35	0.1	247	0.2	117	0.0	180	0.6	300	0.6	288	0.6	301	1.3	104	1.2	100	1.2	104
AB36	0.5	122	0.6	121	0.4	117	0.6	297	0.4	297	0.5	307	0.5	49	0.4	56	0.4	63
AB37	0.2	131	0.4	124	0.3	135	0.8	296	0.8	293	0.7	304	0.3	35	0.1	45	0.1	45
AB39	0.2	86	0.3	90	0.2	90	0.5	306	0.4	297	0.4	315	0.3	339	0.2	333	0.3	0
AB42	0.2	298	0.1	90	0.1	315	0.6	296	0.7	286	0.6	301	1.2	99	1.7	103	1.3	108
AB43	0.4	265	0.4	117	0.3	252	0.8	282	0.9	264	0.8	277	2.5	104	4.3	105	2.7	110
AB44	0.3	287	0.2	297	0.2	297	0.7	295	1.4	287	0.8	300	0.7	73	2.1	95	0.9	96
AB45	0.2	93	0.3	90	0.2	90	0.5	312	0.5	307	0.5	323	0.2	344	0.1	180	0.4	56
AB48	0.7	254	0.2	243	0.7	254	1.0	280	0.4	304	0.7	278	3.4	96	5.5	92	3.5	97
AB50	0.2	349	0.6	309	0.2	0	0.7	288	1.5	274	0.9	291	1.1	74	5.4	97	1.9	96
AC07	0.4	128	0.4	124	0.4	124	0.4	316	0.4	315	0.4	315	0.4	2	0.2	333	0.3	0
AC08	0.1	325	0.1	315	0.2	270	0.6	303	0.7	286	0.3	315	1.2	121	1.1	128	3.1	119
AC09	0.4	130	0.6	121	0.4	124	1.2	293	1.2	290	1.1	292	2.1	102	1.9	99	2.1	104
AC13	0.4	133	0.4	124	0.4	135	0.9	304	0.9	302	0.8	310	1.6	118	1.5	113	2.0	117
AC17	0.3	64	0.5	281	0.5	217	0.6	267	0.7	254	1.0	270	0.4	150	2.1	256	2.0	189
AC19	0.4	125	0.3	135	0.4	146	0.5	293	0.4	304	0.5	307	0.5	18	0.4	315	0.2	0
AC20	0.7	109	2.0	96	1.7	87	0.3	288	0.4	284	0.4	284	3.1	47	3.9	305	3.4	300
AC23	0.5	178	0.4	135	0.3	252	0.4	295	1.2	275	1.2	265	0.5	120	2.5	247	2.2	204
AC24	0.5	146	0.4	146	0.4	166	0.5	310	0.6	301	0.5	307	0.3	155	0.8	150	1.7	123
AC26	0.3	316	0.4	315	0.4	315	0.3	285	0.4	270	0.2	270	1.3	138	1.1	139	2.8	131
AC27	0.2	323	0.1	180	0.7	106	0.6	308	0.9	306	0.9	302	0.8	137	2.3	151	4.7	118
AC29	0.4	147	0.5	127	0.4	146	1.4	291	1.5	290	1.4	291	2.7	106	2.4	107	2.6	108

AC31	0.3	155	0.3	162	0.3	135	0.4	323	0.4	326	0.4	326	0.5	52	0.3	45	0.9	58
AC37	0.3	139	0.2	207	0.4	180	0.5	295	0.6	288	0.9	291	0.4	38	0.4	284	0.6	129
AC39	0.3	216	0.4	214	0.4	243	0.7	304	0.7	286	0.7	304	2.4	133	2.1	141	3.3	130
AC40	0.4	166	0.4	166	0.6	171	1.0	296	1.0	294	0.9	297	1.0	85	1.1	85	2.0	84
AC43	0.2	214	0.1	135	0.2	270	0.7	293	0.9	283	0.8	284	2.1	108	1.7	118	2.4	120
AC44	0.2	217	1.0	96	0.7	82	0.6	296	0.4	333	0.6	329	1.0	39	2.9	288	2.3	275
AC45	0.4	137	0.4	135	0.4	166	0.8	307	0.7	304	0.5	0	1.5	126	1.7	121	3.5	108
AC48	0.3	242	0.1	135	0.0	180	0.5	302	0.5	292	0.4	297	2.5	111	1.9	115	1.8	112
AC50	0.8	106	0.8	104	0.7	106	0.3	258	0.3	252	0.2	243	1.2	10	1.0	11	1.3	23
AC51	0.3	157	0.4	225	0.6	225	0.6	298	0.4	0	0.8	337	0.6	68	1.3	266	0.9	216
AC52	0.3	284	0.4	304	0.5	270	1.1	305	0.9	302	0.9	311	1.0	107	0.7	124	2.4	105
AC53	0.4	136	0.6	121	0.4	104	0.7	299	0.3	18	0.6	0	0.6	42	1.3	283	0.9	264
AC57	0.4	100	0.6	90	0.4	90	0.7	283	0.7	278	0.8	284	0.8	68	0.5	68	0.8	76
AC61	0.1	97	0.2	90	0.1	90	0.7	301	0.7	297	0.7	304	0.2	7	0.1	0	0.2	0
AC62	0.2	93	0.4	90	0.3	90	0.6	297	0.4	297	0.5	307	0.3	28	0.2	27	0.2	27
AC63	0.3	114	0.4	104	0.3	108	0.7	305	0.6	309	0.6	309	0.6	42	0.4	27	0.5	37
AC67	0.2	152	0.2	153	0.1	225	0.8	304	0.9	297	0.7	304	2.2	125	1.8	124	3.2	124
AC70	0.4	129	0.4	117	0.4	124	0.7	292	0.5	292	0.6	301	0.4	41	0.2	27	0.3	45
AC71	0.3	122	0.4	117	0.4	124	0.7	295	0.5	292	0.6	301	0.4	61	0.2	63	0.3	72
AC72	0.5	122	0.7	117	0.5	112	0.6	274	0.6	270	0.6	280	0.8	40	0.7	45	0.8	40
AC74	0.5	122	0.5	112	0.4	117	0.7	282	0.5	281	0.5	292	0.6	25	0.5	0	0.4	14
AC75	0.3	117	0.4	104	0.3	108	0.6	294	0.4	297	0.6	315	0.4	33	0.2	333	0.1	0
AC78	0.1	68	0.2	90	0.1	90	0.9	296	0.9	297	0.9	297	0.3	329	0.1	315	0.2	0
ANC2	0.6	120	2.1	93	1.8	81	0.9	291	0.4	333	0.7	344	1.6	61	6.5	279	6.0	267
ATLI	0.4	297	0.5	292	0.4	297	0.9	295	1.4	287	0.9	297	0.2	338	1.0	101	0.2	117
ATW2	0.2	122	0.8	97	0.6	90	0.5	297	0.2	0	0.3	342	0.8	59	1.0	294	0.5	281
AV09	0.3	115	0.3	108	0.3	108	0.6	338	0.5	338	0.6	342	0.3	258	0.2	270	0.2	207
BARO	0.4	159	0.4	135	0.4	146	0.4	296	0.4	284	0.4	326	0.2	290	0.7	196	0.5	53
BCRK	0.2	119	0.4	104	0.2	117	0.9	297	1.0	294	0.9	302	0.5	21	0.5	37	0.4	45
BLCL	0.2	337	0.2	0	0.3	0	0.8	277	0.8	270	0.9	270	0.9	95	1.1	90	0.9	90
CLGO	0.3	135	0.4	117	0.4	124	0.7	299	0.7	297	0.7	304	0.3	4	0.2	27	0.3	18
EYAC	0.5	113	0.6	108	0.4	104	1.1	285	1.1	280	1.1	285	1.7	109	1.7	111	2.2	112
FAIR	0.6	128	0.7	124	0.6	129	0.7	274	0.7	270	0.7	278	0.5	19	0.4	27	0.5	37
GRNB	0.1	56	0.2	63	0.1	45	0.6	276	0.3	270	0.6	280	4.5	86	4.3	89	3.9	90
GRNX	0.4	118	0.4	104	0.3	108	0.6	288	0.4	284	0.4	297	0.3	10	0.1	315	0.1	0
HAAR	0.2	96	0.4	90	0.3	90	0.6	289	0.6	288	0.7	297	0.6	24	0.4	27	0.5	37
HOLB	0.1	355	0.2	27	0.3	18	1.1	241	1.2	239	1.3	241	2.1	77	2.3	75	2.2	72
MCES	0.5	175	0.6	171	0.4	194	0.5	290	1.3	288	1.2	270	1.6	117	2.3	155	3.3	119



OTZ1	0.5	108	0.6	100	0.5	101	0.4	329	0.4	326	0.4	346	0.3	5	0.3	342	0.4	14
PFRR	0.3	149	0.4	124	0.3	135	0.7	298	0.6	301	0.6	309	0.5	46	0.4	63	0.5	53
SELD	0.4	165	0.4	166	0.4	214	0.3	289	0.6	261	0.4	270	2.2	133	2.1	152	3.5	132
SG27	0.4	122	0.5	112	0.4	117	0.3	305	0.3	288	0.3	342	0.2	333	0.6	190	0.6	51
SPIT	0.7	172	1.0	163	0.8	166	0.9	317	1.2	294	0.9	302	1.1	73	3.3	142	3.2	97
SUAF	0.3	114	0.4	104	0.3	108	0.6	289	0.5	292	0.6	301	0.4	33	0.3	45	0.4	45
TBON	0.4	149	1.6	97	1.3	86	0.7	303	0.4	346	0.6	351	0.8	36	4.6	279	4.0	269
TOOL	0.4	137	0.5	127	0.4	135	0.6	270	0.6	261	0.5	281	0.7	13	0.6	31	0.8	30
TSEA	0.6	120	2.0	93	1.7	83	0.7	300	0.5	349	0.7	352	1.2	50	5.4	281	4.8	269
WHIT	0.1	358	0.1	0	0.1	0	1.0	293	1.3	288	1.0	294	0.4	42	0.6	90	0.3	72
WIKR	0.3	111	0.4	104	0.3	108	0.5	299	0.4	304	0.5	323	0.4	27	0.3	0	0.2	27
WILL	0.3	295	0.3	288	0.3	288	0.9	259	0.9	258	0.9	252	0.3	248	0.2	243	0.2	297
ZAN1	0.5	153	1.6	104	1.3	94	0.7	292	0.4	333	0.7	333	1.2	63	3.8	282	3.2	270
ZINA	0.3	152	0.4	135	0.4	146	0.8	289	0.7	286	0.7	286	1.0	53	0.9	55	0.9	63

Table G.2: GPS derived M2 OTL displacement residuals (amplitude in mm and phase in degree) based on three ocean tide models: FES2014b, GOT4.10c, and TPXO8-atlas in Alaska. Elastic PREM is used for the Green's function.

Stn.	East						North						Up					
	PREM-EL		PREM-AN		S362ANI-AN		PREM-EL		PREM-AN		S362ANI-AN		PREM-EL		PREM-AN		S362ANI-AN	
	amp	phs	amp	phs	amp	phs	amp	phs	amp	phs	amp	phs	amp	phs	amp	phs	amp	phs
AB06	0.5	81	0.8	88	0.8	88	0.6	298	0.7	302	0.7	300	0.7	52	0.8	47	0.9	50
AB07	0.5	102	0.7	100	0.8	98	0.6	295	0.7	295	0.7	294	0.7	65	0.6	41	0.7	30
AB09	0.4	117	0.5	117	0.5	115	0.3	313	0.3	314	0.3	311	0.6	31	0.5	28	0.5	31
AB11	0.7	141	0.8	138	0.8	136	0.4	265	0.4	268	0.5	267	0.6	12	0.6	10	0.6	14
AB13	0.1	156	0.3	114	0.4	106	0.7	307	0.8	304	0.8	302	1.2	115	0.9	110	0.8	106
AB14	0.3	119	0.6	114	0.6	114	0.3	292	0.4	294	0.4	291	0.5	118	0.3	112	0.3	98
AB15	0.5	134	0.7	128	0.8	126	0.4	306	0.5	306	0.6	304	0.9	30	0.9	30	0.9	34
AB17	0.5	118	0.6	117	0.6	116	0.4	305	0.5	303	0.5	302	0.7	22	0.7	22	0.7	26
AB18	0.5	122	0.6	120	0.6	120	0.4	329	0.5	326	0.5	325	0.4	356	0.4	354	0.4	0
AB22	0.2	253	0.1	180	0.1	115	0.5	322	0.7	315	0.8	312	0.2	241	0.3	283	0.2	293
AB27	0.3	119	0.3	116	0.3	115	0.6	325	0.6	322	0.7	320	0.4	351	0.4	348	0.4	356
AB28	0.4	134	0.5	125	0.6	123	0.5	298	0.8	296	0.9	295	0.4	29	0.4	31	0.5	39
AB33	0.2	96	0.3	97	0.3	95	0.4	305	0.5	302	0.6	301	0.6	350	0.6	349	0.6	353
AB35	0.1	247	0.1	299	0.1	308	0.6	300	0.8	295	0.8	293	1.3	104	0.8	106	0.7	104
AB36	0.5	122	0.5	121	0.5	119	0.6	297	0.7	296	0.8	295	0.5	49	0.5	49	0.5	54
AB37	0.2	131	0.2	122	0.2	120	0.8	296	1.0	294	1.1	293	0.3	35	0.3	35	0.3	50
AB39	0.2	86	0.2	84	0.2	83	0.5	306	0.6	302	0.7	301	0.3	339	0.3	337	0.3	347
AB42	0.2	298	0.3	304	0.3	306	0.6	296	0.8	290	0.8	288	1.2	99	0.8	100	0.7	96
AB43	0.4	265	0.5	273	0.6	276	0.8	282	1.0	279	1.1	278	2.5	104	2.0	104	1.8	105
AB44	0.3	287	0.4	288	0.5	289	0.7	295	0.9	289	1.0	287	0.7	73	0.7	66	0.7	67
AB45	0.2	93	0.2	95	0.2	95	0.5	312	0.6	310	0.6	308	0.2	344	0.2	337	0.1	351
AB48	0.7	254	0.8	261	0.9	264	1.0	280	1.1	276	1.2	275	3.4	96	2.8	97	2.4	97
AB50	0.2	349	0.3	321	0.3	314	0.7	288	0.8	283	0.9	280	1.1	74	0.9	64	0.8	58
AC07	0.4	128	0.5	126	0.5	125	0.4	316	0.5	313	0.5	313	0.4	2	0.4	0	0.4	8
AC08	0.1	325	0.1	60	0.2	41	0.6	303	0.8	301	0.9	300	1.2	121	0.7	106	0.6	78
AC09	0.4	130	0.4	120	0.4	115	1.2	293	1.4	290	1.5	290	2.1	102	1.5	102	1.1	102
AC13	0.4	133	0.6	121	0.7	118	0.9	304	1.1	304	1.1	304	1.6	118	0.9	111	0.6	94
AC17	0.3	64	0.4	73	0.5	72	0.6	267	0.7	270	0.8	268	0.4	150	0.2	118	0.4	81
AC19	0.4	125	0.5	118	0.6	117	0.5	293	0.7	293	0.8	292	0.5	18	0.5	21	0.5	28
AC20	0.7	109	0.7	108	0.7	108	0.3	288	0.6	287	0.7	287	3.1	47	3.1	46	3.3	49
AC23	0.5	178	0.5	164	0.6	163	0.4	295	0.6	293	0.6	292	0.5	120	0.4	90	0.6	76

AC24	0.5	146	0.8	133	0.9	130	0.5	310	0.7	308	0.8	306	0.3	155	0.1	215	0.1	244
AC26	0.3	316	0.2	352	0.3	2	0.3	285	0.5	290	0.6	288	1.3	138	0.7	139	0.4	129
AC27	0.2	323	0.2	9	0.3	9	0.6	308	0.8	306	0.8	303	0.8	137	0.4	126	0.2	95
AC29	0.4	147	0.4	136	0.4	131	1.4	291	1.6	290	1.8	289	2.7	106	1.9	106	1.5	104
AC31	0.3	155	0.4	145	0.4	143	0.4	323	0.5	321	0.5	319	0.5	52	0.5	51	0.5	55
AC37	0.3	139	0.4	120	0.5	114	0.5	295	0.7	292	0.8	291	0.4	38	0.5	20	0.6	25
AC39	0.3	216	0.2	180	0.2	169	0.7	304	0.9	303	1.1	302	2.4	133	1.6	134	1.1	128
AC40	0.4	166	0.5	139	0.6	129	1.0	296	1.2	296	1.3	295	1.0	85	0.7	73	0.5	70
AC43	0.2	214	0.2	182	0.2	174	0.7	293	0.9	292	0.9	290	2.1	108	1.5	103	1.1	97
AC44	0.2	217	0.2	196	0.2	207	0.6	296	0.9	293	1.0	292	1.0	39	1.1	38	1.2	48
AC45	0.4	137	0.6	124	0.7	120	0.8	307	1.0	305	1.0	305	1.5	126	0.8	125	0.5	124
AC48	0.3	242	0.3	242	0.3	250	0.5	302	0.7	298	0.8	296	2.5	111	2.1	111	1.9	111
AC50	0.8	106	0.9	107	0.9	107	0.3	258	0.3	263	0.3	265	1.2	10	1.2	9	1.2	11
AC51	0.3	157	0.4	138	0.5	131	0.6	298	0.9	294	1.0	292	0.6	68	0.7	64	0.9	68
AC52	0.3	284	0.1	308	0.1	84	1.1	305	1.2	305	1.3	305	1.0	107	0.6	100	0.5	89
AC53	0.4	136	0.5	128	0.5	126	0.7	299	0.9	295	1.1	294	0.6	42	0.7	43	0.8	51
AC57	0.4	100	0.4	93	0.4	91	0.7	283	1.0	283	1.1	283	0.8	68	0.7	57	0.7	58
AC61	0.1	97	0.1	84	0.1	74	0.7	301	0.9	297	1.0	296	0.2	7	0.2	10	0.2	27
AC62	0.2	93	0.3	89	0.3	86	0.6	297	0.8	294	0.9	293	0.3	28	0.3	28	0.4	40
AC63	0.3	114	0.3	108	0.3	104	0.7	305	0.9	300	1.0	299	0.6	42	0.6	42	0.6	48
AC67	0.2	152	0.3	124	0.3	117	0.8	304	1.0	302	1.1	302	2.2	125	1.5	123	1.3	122
AC70	0.4	129	0.4	123	0.4	120	0.7	292	0.9	291	1.0	290	0.4	41	0.4	42	0.5	49
AC71	0.3	122	0.3	117	0.3	116	0.7	295	0.9	294	0.9	292	0.4	61	0.4	62	0.5	67
AC72	0.5	122	0.5	118	0.5	116	0.6	274	0.9	277	0.9	278	0.8	40	0.8	40	0.9	44
AC74	0.5	122	0.5	118	0.5	116	0.7	282	0.9	284	1.0	284	0.6	25	0.6	26	0.7	31
AC75	0.3	117	0.4	112	0.4	110	0.6	294	0.8	293	0.9	292	0.4	33	0.4	35	0.4	44
AC78	0.1	68	0.1	40	0.1	25	0.9	296	1.1	294	1.2	293	0.3	329	0.2	329	0.2	347
ANC2	0.6	120	0.7	117	0.7	118	0.9	291	1.1	290	1.3	289	1.6	61	1.8	60	2.1	65
ATLI	0.4	297	0.5	294	0.6	294	0.9	295	1.1	289	1.1	287	0.2	338	0.2	324	0.2	355
ATW2	0.2	122	0.3	116	0.3	112	0.5	297	0.8	294	0.9	292	0.8	59	0.9	57	1.0	63
AV09	0.3	115	0.5	111	0.6	108	0.6	338	0.6	339	0.7	338	0.3	258	0.3	289	0.3	304
BARO	0.4	159	0.4	154	0.4	154	0.4	296	0.4	296	0.4	295	0.2	290	0.3	283	0.3	284
BCRK	0.2	119	0.2	116	0.2	110	0.9	297	1.2	294	1.3	293	0.5	21	0.5	21	0.5	30
BLCL	0.2	337	0.4	299	0.5	292	0.8	277	0.9	272	0.9	269	0.9	95	0.9	96	1.0	95

CLGO	0.3	135	0.4	131	0.4	129	0.7	299	0.9	298	1.0	297	0.3	4	0.3	4	0.3	14
EYAC	0.5	113	0.6	108	0.6	104	1.1	285	1.3	285	1.3	285	1.7	109	1.3	111	1.2	112
FAIR	0.6	128	0.6	125	0.6	125	0.7	274	0.9	277	1.0	277	0.5	19	0.5	19	0.5	26
GRNB	0.1	56	0.1	328	0.1	322	0.6	276	0.7	269	0.7	266	4.5	86	4.0	86	3.9	86
GRNX	0.4	118	0.4	112	0.4	110	0.6	288	0.8	288	0.8	289	0.3	10	0.3	10	0.3	25
HAAR	0.2	96	0.2	88	0.2	84	0.6	289	0.9	288	1.0	287	0.6	24	0.6	22	0.7	30
HOLB	0.1	355	0.2	306	0.3	300	1.1	241	1.2	238	1.3	237	2.1	77	1.5	80	1.3	84
MCES	0.5	175	0.6	162	0.7	158	0.5	290	0.6	291	0.7	291	1.6	117	1.1	107	1.0	93
OTZ1	0.5	108	0.6	109	0.7	109	0.4	329	0.4	326	0.4	324	0.3	5	0.3	1	0.3	9
PFRR	0.3	149	0.3	143	0.3	139	0.7	298	0.8	296	0.9	295	0.5	46	0.5	46	0.5	52
SELD	0.4	165	0.5	148	0.6	144	0.3	289	0.5	291	0.6	293	2.2	133	1.6	132	1.1	121
SG27	0.4	122	0.5	121	0.5	120	0.3	305	0.4	304	0.4	302	0.2	333	0.2	321	0.2	322
SPIT	0.7	172	0.8	162	0.9	159	0.9	317	1.1	313	1.1	313	1.1	73	1.0	40	1.2	23
SUAF	0.3	114	0.3	111	0.3	109	0.6	289	0.8	290	0.9	290	0.4	33	0.4	34	0.4	41
TBON	0.4	149	0.4	141	0.4	142	0.7	303	0.9	299	1.0	296	0.8	36	0.9	35	1.2	49
TOOL	0.4	137	0.4	134	0.4	133	0.6	270	0.7	273	0.7	274	0.7	13	0.7	12	0.7	15
TSEA	0.6	120	0.6	116	0.6	118	0.7	300	0.9	296	1.1	294	1.2	50	1.4	49	1.7	57
WHIT	0.1	358	0.2	319	0.3	313	1.0	293	1.2	289	1.3	287	0.4	42	0.4	42	0.4	54
WIKR	0.3	111	0.4	108	0.4	106	0.5	299	0.7	297	0.8	296	0.4	27	0.5	28	0.5	36
WILL	0.3	295	0.5	279	0.6	277	0.9	259	1.0	256	1.0	255	0.3	248	0.3	251	0.3	247
ZANI	0.5	153	0.6	147	0.6	148	0.7	292	0.9	290	1.1	289	1.2	63	1.3	61	1.6	68
ZINA	0.3	152	0.3	147	0.2	147	0.8	289	1.0	287	1.1	286	1.0	53	0.9	50	1.0	54

Table G.3: GPS-estimated M2 vertical OTL displacement residuals in Alaska (amplitude in mm and phase in degree) based on the FES2014b ocean tide model and three different Earth models: Elastic-PREM, anelastic-PREM and anelastic S362ANI

Stn.	East						North						Up					
	GPS		GLO		GPS+GLO		GPS		GLO		GPS+GLO		GPS		GLO		GPS+GLO	
	amp	phs	amp	phs	amp	phs	amp	phs	amp	phs	amp	phs	amp	phs	amp	phs	amp	phs
AB18	0.6	120	0.6	111	0.6	104	0.5	325	0.5	355	0.4	343	0.4	0	0.2	311	0.3	335
AC20	0.7	108	0.5	35	0.2	82	0.7	287	1.0	304	0.7	296	3.3	49	2.7	69	2.7	62
AC44	0.2	207	0.1	285	0.1	273	1.0	292	0.7	312	0.8	301	1.2	48	0.7	41	0.9	44
AC48	0.3	250	0.3	23	0.0	291	0.8	296	0.4	283	0.7	294	1.9	111	0.9	111	1.6	106
AC53	0.5	126	0.4	116	0.4	107	1.1	294	0.8	310	0.9	301	0.8	51	0.5	79	0.7	59
AC70	0.4	120	0.4	100	0.4	103	1.0	290	0.8	303	0.8	294	0.5	49	0.0	69	0.3	35
AC78	0.1	25	0.2	55	0.2	54	1.2	293	1.0	297	1.1	292	0.2	347	0.5	287	0.3	353
ANC2	0.7	118	0.6	101	0.6	99	1.3	289	0.9	305	1.0	298	2.1	65	1.5	72	1.7	68
ATLI	0.6	294	0.7	285	0.5	296	1.1	287	1.2	286	1.1	284	0.2	355	0.3	104	0.2	25
ATW2	0.3	112	0.5	108	0.3	90	0.9	292	0.7	293	0.7	301	1.0	63	1.0	39	0.6	48
BCRK	0.2	110	0.4	65	0.2	52	1.3	293	1.1	294	1.2	294	0.5	30	0.5	338	0.5	8
BLCL	0.5	292	0.6	285	0.5	303	0.9	269	0.8	264	0.7	261	1.0	95	0.9	87	1.0	76
GRNB	0.1	322	0.4	266	0.2	304	0.7	266	0.7	279	0.7	272	3.9	86	4.1	91	3.9	87
HAAR	0.2	84	0.3	57	0.3	65	1.0	287	1.0	296	1.0	292	0.7	30	0.2	320	0.3	25
HOLB	0.3	300	0.8	288	0.6	326	1.3	237	0.9	264	0.9	234	1.3	84	1.4	97	1.1	83
PFRR	0.3	139	0.2	137	0.3	113	0.9	295	0.8	312	0.7	300	0.5	52	0.2	315	0.2	34
SPIT	0.9	159	0.7	143	0.7	147	1.1	313	1.0	327	1.0	322	1.2	23	1.0	356	1.1	5
SUAF	0.3	109	0.5	93	0.3	94	0.9	290	0.7	299	0.7	298	0.4	41	0.3	318	0.2	5
TBON	0.4	142	0.2	156	0.3	126	1.0	296	0.8	314	0.8	301	1.2	49	0.6	33	0.9	50
TSEA	0.6	118	0.4	98	0.5	106	1.1	294	0.9	305	0.9	300	1.7	57	1.0	69	1.2	65
WILL	0.6	277	0.6	266	0.6	276	1.0	255	0.9	257	0.9	259	0.3	247	0.2	164	0.2	230
ZINA	0.2	147	0.1	190	0.2	104	1.1	286	1.0	300	1.1	291	1.0	54	0.3	25	0.5	44

Table G.4: M2 OTL displacement residuals (amplitude in mm and phase in degree) estimated by GPS-only, GLONASS-only and combined GPS+GLONASS with respect to the predicted one based on the FES2014b ocean tide model and anelastic S362ANI Green's function.

Stn.	East						North						Up					
	GPS		GLO		GPS+GLO		GPS		GLO		GPS+GLO		GPS		GLO		GPS+GLO	
	amp	phs	amp	phs	amp	phs	amp	phs	amp	phs	amp	phs	amp	phs	amp	phs	amp	phs
AB18	1.3	152	0.3	285	0.5	178	1.0	240	0.6	325	0.5	268	2.2	68	1.7	192	1.4	129
AC20	7.3	214	2.5	154	3.7	196	2.0	229	2.0	304	0.6	209	2.4	94	2.8	117	3.7	58
AC44	1.4	175	0.3	248	0.6	183	0.7	261	0.6	304	0.4	283	1.9	78	1.2	166	0.9	120
AC48	2.8	300	1.7	314	1.0	315	0.6	85	0.6	319	0.1	122	4.8	187	1.8	140	2.2	173
AC53	1.1	107	0.3	63	0.5	116	1.8	226	0.8	313	0.7	268	1.2	82	0.9	128	1.2	117
AC70	0.7	171	0.5	316	0.6	208	0.7	246	0.4	300	0.6	266	1.2	95	1.6	171	1.6	137
AC78	1.3	120	0.4	286	0.3	111	1.3	202	0.7	283	0.6	234	2.3	355	3.1	103	0.6	1
ANC2	1.7	112	0.7	128	1.1	126	0.2	227	0.6	310	0.5	308	2.2	68	0.6	320	0.9	78
ATLI	2.0	156	0.6	265	0.4	144	0.7	256	0.3	301	0.3	242	2.0	1	1.2	171	0.4	310
ATW2	2.0	194	0.1	348	0.4	243	1.5	271	0.9	309	0.3	272	2.3	71	2.9	140	0.8	127
BCRK	1.1	260	0.3	75	0.3	202	0.6	349	0.4	286	0.2	265	0.9	218	0.2	190	0.7	183
BLCL	1.3	274	0.4	319	0.5	247	1.0	47	0.7	57	0.4	82	2.5	276	1.8	346	0.9	304
GRNB	0.8	261	0.9	312	0.4	261	0.6	58	0.3	221	0.0	165	1.3	169	1.7	123	1.4	143
HAAR	1.8	230	0.4	294	0.7	266	0.6	263	0.5	308	0.6	336	2.4	195	1.6	152	1.6	169
HOLB	1.0	269	0.6	264	0.6	242	0.3	68	0.2	263	0.1	125	1.2	206	2.3	117	0.8	156
PFRR	0.8	224	0.5	295	0.5	259	0.3	241	0.5	310	0.2	298	1.2	13	1.2	181	0.5	167
SPIT	0.9	219	0.1	308	0.4	261	1.1	240	0.6	296	0.5	291	1.7	239	1.7	188	0.9	183
SUAF	1.2	197	0.3	276	0.8	215	0.8	24	0.3	354	0.5	17	2.2	83	0.6	185	0.8	130
TBON	1.6	120	0.3	296	0.6	144	1.2	230	0.2	262	0.7	247	3.0	62	0.7	197	1.7	80
TSEA	0.7	194	0.3	289	0.2	200	0.6	260	0.7	292	0.6	286	2.2	107	1.4	102	1.7	127
WILL	1.3	307	0.6	300	0.3	301	1.2	64	0.2	101	0.3	94	3.4	248	0.7	149	1.0	246
ZINA	1.5	177	0.2	80	0.5	212	1.5	212	0.5	310	0.2	281	0.9	356	0.7	169	0.2	175

Table G.5: K1 OTL displacement residuals (amplitude in mm and phase in degree) estimated by GPS-only, GLONASS-only and combined GPS+GLONASS with respect to the predicted one based on FES2014b ocean tide model and anelastic S362ANI Green's function.